THE INFLUENCE OF TURBULENCE ON A FLAT PLATE AIRFOIL AT REYNOLDS NUMBERS RELEVANT TO MAVs

A thesis submitted in fulfillment of the requirements for the degree of

Doctor of Philosophy

Sridhar Ravi

B.Eng. Aerospace

School of Aerospace, Mechanical & Manufacturing Engineering

RMIT University

Melbourne, Victoria, Australia.

March 2011

To my immediate and extended family

Declaration

Except where due references are made, the work reported in this thesis is solely that of the author alone and has not been submitted or published previously, in whole or in parts, for any academic award.

The work that is reported in this thesis was carried out since the official date of commencement of the program, 03rd of March 2008 at RMIT University.

Sridhar Ravi

14th March 2011

Acknowledgments

The author humbly acknowledges that this work would not have been possible without the support and encouragement received from various quarters.

The author coveys his sincerest thanks to his first and second supervisors, Prof.Simon Watkins and Dr.Jon Watmuff respectively, for their unyielding support and inputs through the various stages of this work. Their encouragement and technical guidance played a pivotal role in the successful completion of this work.

Support offered by AFOSR of the USAF is also gratefully acknowledged.

Sincerest thanks are extended to Mr.Phred Petersen for his assistance in the flow visualization experiments which proved to be one of the highlights of this research.

The author acknowledges the assistance rendered by the work-shop staff at RMIT, in particular Gilbert Atkins. “Interactions” with Gil and Ben will mainly be remembered by the author for their comical value.

Deliberations with Alex Fisher and Matthew Marino over various matters, technical and otherwise, will be fondly remembered and the author looks forward for future encounters. Special mention of the assistance and encouragement extended by Mark Thompson, Edward Cruz and other members of the MAV research group at RMIT also needs to be made.

The author also wishes to convey his humblest gratitude to his immediate and extended family that has stood by through the various endeavors undertaken. The author declares that the inspiration for this work was drawn from the love and affection received from the author’s grandparents, Mr. L.N.Paramasivan and Mrs. Kamala Paramasivan.

Finally, the author thanks all persons who have played an indirect role in the success of this work.

Summary

Micro Air Vehicles (MAVs) are small remotely controlled or autonomous aircraft that fly relatively slowly and very close to the Earth's surface. They are typically used for surveillance and reconnaissance missions where direct line of sight is unavailable. Though the idea of using MAVs was only considered in the 1980s, their potential uses have attracted much interest and accelerated their design and development. However, the deployment of MAVs has been hindered in part due to the lack of understanding of the associated flow dynamics.

MAVs typically fly in the Reynolds number range of 50,000 to 200,000 where the flow usually remains laminar over a large portion of the airfoil. Due to the extended laminar region, Laminar Separation Bubbles (LSBs) tend to form over the airfoil. Previous workers have found that the performance of airfoils reduces significantly in this flow regime primarily due to the influences of LSBs. Though the properties of LSBs have been studied through experimental and numeric approaches, there is still some uncertainty as to their exact influence on the time-varying pressures and performance of the airfoil. The influence of the various other flow structures that develop over the airfoil in this Reynolds number range is also relatively poorly understood.

As well as low Reynolds number effects, MAVs are exposed to the high levels of turbulence present within the Atmospheric Boundary Layer (ABL) which generally extends to several hundred meters above the Earth's surface. MAVs fly in this layer of the atmosphere which is directly influenced by interactions between the natural wind and the structures present over the surface as well as thermal effects, etc. Atmospheric turbulence can be considered to consist of eddies and can be characterized in terms of its intensity and scale. Since MAVs can be exposed to relatively high levels of turbulence, an understanding of the influence of turbulence intensity and integral length scale on airfoil performance is useful. A significant gap in knowledge has been identified in this area, where little is known about the influence of both parameters of turbulence on the flow over the airfoil and on airfoil performance.

The work presented in this thesis aims to increase understanding on the interactions between turbulence and airfoils at Reynolds numbers relevant to MAVs. This was accomplished by measuring the time-varying surface pressures that occurred over a thin flat-plate airfoil with an elliptical Leading Edge (LE) and a tapered Trailing Edge (TE), when exposed to various turbulence conditions including nominally

smooth flow. Turbulence intensity was varied whilst keeping the integral length scale nominally constant and vice versa, to uncover the individual influences of both. Surface pressures were simultaneously measured over a number of spanwise and chordwise locations to identify the pressure and consequently the force and moment fluctuations experienced when exposed to the different turbulence conditions. Velocity measurements and smoke flow visualization were also conducted to augment the pressure measurements.

In nominally smooth flow, separation was found to occur at the LE from an Angle of Attack (AOA) of 4Deg onwards. The pressure measurements provided insights on a number of flow features that formed over the airfoil surface including LSBs, large-scale vortices on reattachment and bluff-body-like vortex shedding at higher AOAs. Various transient properties of the LSB, such as the rate of formation of instabilities in the separated shear layer, shear layer flapping, and reattachment point oscillation length were also identified. These flow features brought about fluctuations in surface pressure and velocity at various frequencies. In the range of AOAs where LSBs formed, it was noted that the airfoil experienced a pseudo-camber effect which resulted in an increased lift and pressure drag.

In elevated levels of turbulence (Ti=7% and 12%), enhanced roll up of the shear layer on separation from the LE was observed. This led to the formation of strong vortex cores which advected downstream imparting large variations in surface pressure and velocity. The rate of vortex core formation was dependent on the AOA of the airfoil. In comparison to smooth flow, a significant delay in stall along with an increase in the maximum lift generated was noticed at higher levels of turbulence. Increasing the turbulence intensity and length scale led to an increase in the maximum lift generated. However, they had an opposing influence on the lift-curve-slope and the moment coefficient of the airfoil. It was also identified that an increase in turbulence intensity and integral length scale resulted in an increased magnitude of pressure and consequently lift fluctuations. Rolling moments however were more influenced by the integral length scale than by the turbulence intensity. Finally, even-though good correlation between incoming turbulence and lift produced was observed, estimation of the time-varying forces over the airfoil based on knowledge of time-averaged airfoil performance data for the flow condition proved to be ineffective. This implied that a suitable aerodynamic admittance function has to be developed to accurately predict the time-varying fluctuations in pressure and forces that the airfoil might experience when exposed to highly turbulent conditions.

Table of Contents

List of Figures

List of Tables

Abbreviations, Acronyms and Symbols

ABL	Atmospheric Boundary Layer
A/D	Analog to Digital
AOA	Angle of Attack
APG	Adverse Pressure Gradient
AR	Aspect Ratio
AWT	Aerodynamics Wind-Tunnel
BL	Boundary Layer
c	Chord
CL,CD and CM	Lift, Drag and Pitching Moment Coefficient
CLmax	Maximum Lift Coefficient
Cp	Pressure Coefficient
D	Grid Width or Blunt Plate Width
Deg	Degree
DFT	Discreet Fourier Transform
DPMS	Digital Pressure Measurement System
DSP	Digital Signal Processing
f	Frequency
FFT	Fast Fourier Transform
fps	Frames Per Second
IFT	Inverse Fourier Transform
Ti_{uvw} or I_{uvw}	Total Turbulence Intensity
IWT	Industrial Wind-Tunnel
HALE	High Altitude, Long Endurance
J	Relative Turbulence Intensity
K-H	Kelvin-Helmholtz
LALE	Low Altitude Long Endurance
LAR	Low Aspect Ratio
LE	Leading Edge

L_R	Location of Reattachment from Leading Edge
LSB	Laminar Separation Bubble
Lxx, Lxy & Lxz	Longitudinal (x), Lateral (y) and Vertical (z) Integral Length Scales along the Longitudinal Axis (x)
MALE	Medium Altitude, Long Endurance
MAV/s	Micro Air Vehicle/s
n	Number of Channels or Frequency
PSD	Power Spectral Density
S	Power
Std.Dev	Standard Deviation
TE	Trailing Edge
TFI	Turbulent Flow Instrumentation
Ti	Turbulence Intensity
UAV	Unmanned Aerial Vehicle
U, V, W	Mean Velocity in the Longitudinal, Lateral and Vertical Directions
u,v,w	Time-varying Velocities in the Longitudinal, Lateral and Vertical Directions
V_R	Resultant Velocity
V_{Veh}	Vehicle Velocity
X	Distance Downstream from Grids
x,y,z	Distances in the Longitudinal, Lateral and Vertical Directions
$\overline{V}, \overline{U}$	Time-Averaged Velocity
α	Best-Fit Constant
τ	Correlation Time Shift
ρ	Density
σ	Standard Deviation
‘	Time-Varying Quantities

CHAPTER 1

Introduction

1.1 A Brief on the Evolution of MAVs

Throughout the evolution of flight, emphasis has been given to the ability to fly fast and carry as much payload (goods or passengers) as possible. Whilst manned flight has always been in the forefront of aviation research, it was not until a few decades ago when the idea of using Unmanned Aerial Vehicles (UAVs) in missions where human piloted crafts were previously used was considered. UAVs may be defined as aircraft that operate autonomously or remotely controlled, without possessing any operational crew on board**.** Since being initially conceived during World War 2, UAVs have reached the stage of technological maturity where they are deployed in a number of missions, ranging from target acquisition to weather reconnaissance. Currently, the largest uses for UAVS are military applications; however this is fast changing with the development of civilian-specific UAVs. Potential civilian applications for UAVs include fire fighting and acting as communication relays.

Due to the large inventory, the US military categorized UAVs into the following four types depending on design and mission profile (Weibel (2005));

1) Micro Air Vehicles (MAV): they are small in size, i.e. less than 1 m span and light weight. Typically these are characterized by having Low Aspect Ratio (LAR) wings, for example the Black Widow.

2) Low Altitude Long Endurance (LALE) or Tactical: GNAT 750 is an example of a LALE UAV, used for reconnaissance purposes. Tactical UAVs are designed for communicating and relay purposes, by loitering in low altitudes.

3) Medium Altitude, Long Endurance (MALE): Cruise between altitudes of 10,000 to 30,000 feet having an endurance limit of around 10hrs to 20hrs. They are characterized by long span, high aspect ratio wings, notable examples are the Predator and Reaper.

4) High Altitude, Long Endurance (HALE): Typically they cruise at an altitude of over 35,000 feet and have an endurance limit of between 30hrs to 48 hours. Similar to MALE UAVs, they also possess high aspect ratio wings. Examples include the Global Observer and Global Hawk.

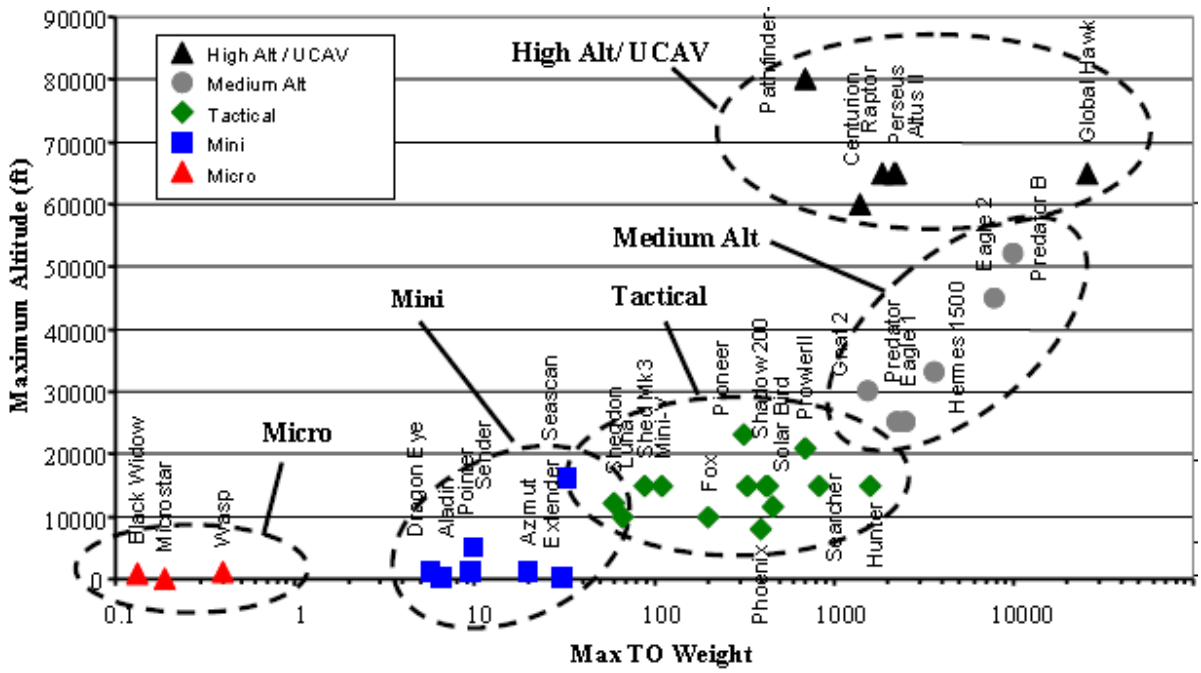

Figure 1: Altitude to maximum take-off weight distribution of the various categories of UAVs, Weibel (2005)

UAVs have become extremely mission specific because of large variations in operational conditions between each category, as seen in Figure 1. For example, a HALE UAV would perform very poorly in the role of a MAV and vice versa. Current research is being carried on the development of multi-role and multi-mission UAVs that are aimed at bridging this operational divide (Sinha & Kusumo (2002) and Hebert (2003)).

For the aerodynamic and other component design of UAVs falling within the latter three categories, there exists a wealth of information, in terms of cruise altitude, speed and size, as they fly within the realms of manned flight. MAVs however fly at Reynolds numbers much lower than manned aircraft and

posses different aerodynamic and propulsive requirements. The origin of MAVs can be traced back to model aircraft builders and hobbyists, therefore conducting a review of the evolution of model airplanes would form a good starting point.

Model airplanes have been in existence from as early as 1804, when Sir George Cayley flew the first model airplane glider (Wragg (1974)). Then, through the 1800s numerous advances were made and by end of the century, rubber band powered model airplanes were commercially available (Wragg (1974)). During the 19th century however, a lag in the development of a suitable propulsion, and communication/remote control system, hindered development of model aircraft. From the turn of the 20th century, when Langley's model airplane was powered by the first small gas engine in 1901, a number of smaller and more efficient engines suitable for model airplane were built (Anderson (1998)). Then by the 1930s, gas engines had become so efficient that they became the preferred choice for propulsion (Wragg (1974)). Alongside the development of the propulsion systems, much had been learnt about the structural layout necessary for model planes. However, suitable transmitting and receiving systems still had to be developed to control the craft in flight. In 1936, the first radio controlled flight of a glider, was conducted both in Germany and America (Good (1986) and Phillips (1927)). Since then, through the efforts of various workers and the accelerated development stages of World Wars 1&2, fully controlled model aircraft were developed by the mid 1940s (Good (1986)). By 1967 electric motors had also become a popular choice for the propulsion system (Aberle (1995)). From early 1970s, along with other aspects of aviation, steady growth has taken place on all fronts of model airplane design and construction (Mueller et al (2007)).

A small remotely controlled airplane is generally considered a MAV when its mission is to retrieve useful data. The idea of using model airplanes for data gathering missions, such as surveillance and reconnaissance, was only explored from around 1975 onwards as part of a US Army, Navy and Air force initiative (Mueller et al (2007)). Through a number of attempts, including a few unsuccessful, the issues and challenges associated with developing MAVs were highlighted (Kellogg et al (2001) and Foch et al (1992)). The state of technology required for MAV development was still unavailable generally up to about 1990, in terms of small sensors, cameras, auto-pilot systems, etc. Then, during the early 1990s, serious consideration was again given to the development of MAVs as completely autonomous systems. In 1995, Defense Advanced Research Projects Agency (DARPA) started a technology feasibility survey on the concept of developing micro air vehicles. DARPA envisioned MAVs as "six-degree-of-freedom aerial robots, whose mobility can deploy a useful micro payload to a remote or otherwise hazardous location

where it may perform any of a variety of missions, including reconnaissance and surveillance, targeting, tagging and bio-chemical sensing" (McMichael et al (1997)). Once it was demonstrated that the idea was feasible, a $35 million research project was initiated in 1997 (Mueller et al (2007)). This project boosted the research and development of MAVs world over. The main goals of the project were to develop MAVs which would be within 6 inches in length and width, carry a day/night camera, have an endurance limit of around two hours, operate with a high degree of autonomity and be cost effective. Aerovironment's Black Widow, NRL's Mite and Lockheed Martin's Microstar, were successful MAVs that fell within the DARPA guidelines (Torres (2002)). Though the mentioned MAVs were built within guidelines, their size constrained their payload and endurance limits, in turn limiting the variety of missions they could carry out. It was found to be more effective to develop slightly larger MAVs that were able to carry a larger array payloads (i.e. cameras, sensors) etc, than building very small MAVs, with very limited payload and endurance limits. DARPA guidelines were then relaxed in 2000 and more-open ended guidelines were put forth (Torres (2002)).

Though no absolute definition for a MAV currently exists, it is generally accepted that an aircraft that has a span less than 1 meter can fall under the MAV category. Since the last decade, a number of private organizations, as well as the defense departments of various nations, have expressed interest in research and development of MAVs. The overriding aim for current research is to develop MAVs that would eventually become a permanent fixture of a soldier's back-pack, so that a solider deployed in the battlefield can launch a MAV on his own, subsequently control it in flight whilst the craft gathers information, and finally land and retrieve it for reuse.

1.2 Issues and Challenges with MAV Flight

The small size and weight of MAVs, along with vastly different ambient conditions due to low flight speeds, raise a number of unique challenges in their design and development. These challenges range from aerodynamic considerations to payload size (as extremely small payloads need to be developed in order to be fitted within a MAV). Some of the unsuccessful attempts at building MAVs in the 1970s were attributed due to lack of sensors and other payload small and light enough to be placed on MAVs (Kellogg et al (2001)). However, considerable progress has occurred on this front, and with the emergence of piezo-electrics, micro-processors and MEMS technology, a number of efficient yet

extremely small and light-weight sensors have been manufactured (Mueller et al (2007)). Similar comments can be made about the propulsive and power plant requirements of MAVs with the development of extremely efficient small motors and high-energy density batteries. Much of the knowledge and technology required for propulsion systems and the structural layout of MAVs has been inspired from model aircraft construction. Newer, more efficient, batteries led to electric motors becoming the preferred propulsion choice over gas engines. If MAVs did not need to hover, a propeller driven MAV was found to be most efficient (Woods & Henderson (2001)).

As for the aerodynamic considerations; the rate of development of MAVs has been hindered due to a lack of understanding of the flow physics associated with MAV flight (Pines & Bohorquez (2006) and Torres (2002)). As shown in Figure 2, MAVs typically fly within Reynolds number ranges of 50,000 to 200,000 and the volume of literature on the flow-field within this range is quite limited (Pines (2006)). At MAV Reynolds numbers, the air flow remains laminar for most part over airfoil surface and as the angle of attack increases, flow separation occurs. The separated laminar shear layer then undergoes transition to a turbulent shear layer that reattaches over the airfoil surface resulting in the formation of a Laminar Separation Bubble (LSB). The presence and structure of a LSB has a significant influence on overall wing performance. Airfoil/wing performance tends to be lower within this Reynolds number range (Mueller (1999)).

At higher Reynolds numbers however, the shear layer undergoes transition to turbulence while remaining attached to airfoil surface and at high angles of attack, only a short bubble forms which has little impact on performance (Mueller (1999)). Detailed review of LSBs and their influence will be presented in forthcoming sections. MAVs also have very small wings generally of low aspect ratios, putting emphasis on aerodynamic efficiency needing to obtain the maximum lift from small wing area**.** MAV designers must therefore choose airfoil/wings platform that are efficient in spite of the reduction in performance due to low Reynolds number effects. This can only be achieved through gaining a better understanding of airfoil/wing performance in low Reynolds number flows.

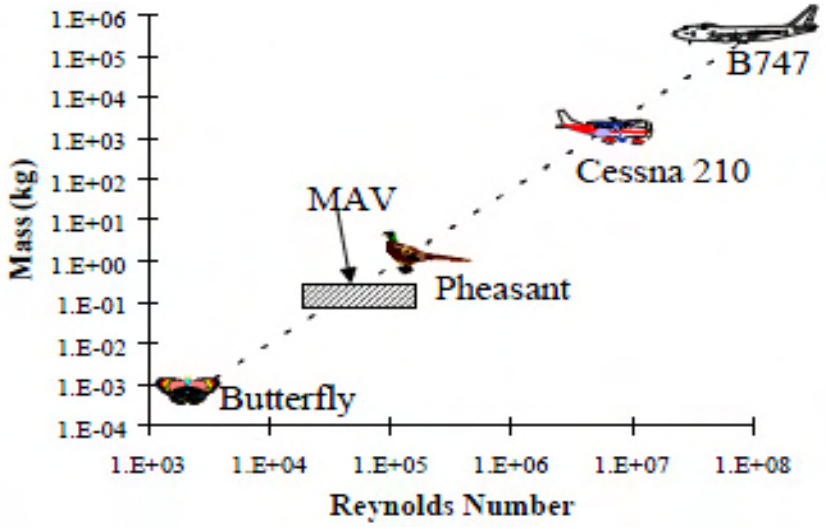

Figure 2: Location of MAVS on Reynolds number versus mass plot. (Meuller et al 2007)

As well as the challenges associated with low Reynolds number effects, MAVs need to fly close to ground in complex terrains such as city canyons or in dense vegetation, where direct line of sight is unavailable. When any appreciable atmospheric wind is present, local obstacles and rough terrains can greatly increase the turbulence and the oncoming flow would be very disturbed. Hence, MAVs need to be able to counteract the combined influence of low Reynolds number flows as well as turbulence. While on their way to the target, MAVs not only need to be stable enough to negate influence of turbulence**,** they also need to have enough control to veer in and out, or around, local obstacles. Since they are most suited for surveillance and reconnaissance missions (Anon (1993)) it is also useful that they maintain steady level flight on reaching their destination.

It is quite easy to imagine the manner in which turbulence or velocity fluctuations can affect a MAV in flight, for example if a MAV were flying level focusing on a ground target as part of its surveillance mission, a gust could render a different lift for each wing causing roll, in turn causing image blurring or the target moving “out of frame”. Even while controlling a MAV with direct line of sight, maintaining steady level flight in turbulence is a considerable task. Similar issues occur when trying to fly a remote controlled aircraft on a breezy day.

Consequently the environment is emerging as a major constraint on the operations of MAVs with an increasing vulnerability to turbulence as size and speed reduces (Spedding & Lissaman (1998)). The ability to hold steady flight can only be achieved with the help of an onboard auto-pilot system that

constantly corrects for turbulence effects. An effective auto-pilot system can best be developed by gaining a sound understanding of airfoil/wing performance at low Reynolds numbers yet immersed in ambient turbulent flows. It is therefore useful to understand the influence of turbulence on the performance of airfoils/wings for making the right choices for various aerodynamic components of a MAV.

In the next sub-section, findings on the properties of the airflow close to the earth's surface will be reviewed. This is important as it provides insight on the size and structure of turbulence MAVs would be exposed to in flight.

1.3 Flow-Field within the Atmospheric Boundary Layer (ABL)

The Atmospheric Boundary Layer (ABL), also known as the planetary boundary layer, is usually defined as the region of the atmosphere which is under the influence of friction and other local effects arising from the Earth's surface. Depending on terrain, the ABL extends from the Earth's surface to a few hundred meters high. MAVs typically fly very close to the ground, hence their flight envelope falls within this region of the atmosphere. In order to understand the flow-field experienced by MAVs in flight, an understanding of the flow-field within the ABL is required. This section will review the various findings on the flow structure within the ABL.

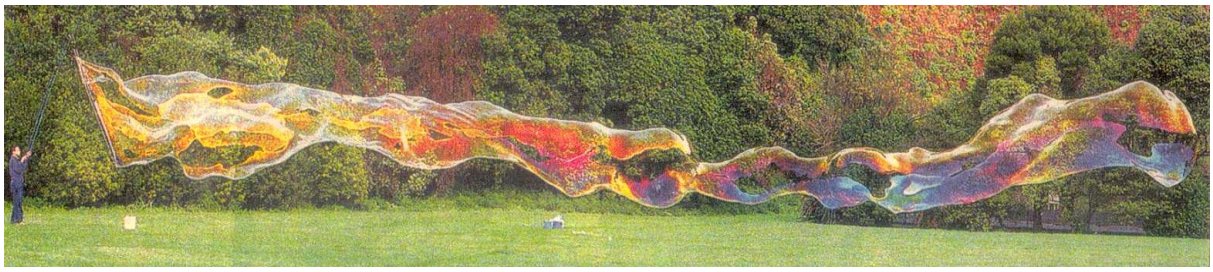

Figure 3: The longest bubble in the world (courtesy Alan McKay, copyright Garry Norman)

The interaction between air flow and local structures on the Earth's surface creates turbulence from mechanical mixing. The photograph of the longest bubble in the world in Figure 3 provides a qualitative idea of the flow-field (i.e. turbulence encountered within the ABL) MAVs would be exposed to. Air flow

within the ABL is rarely smooth but rather a mix of turbulent eddies of varying size and strength. Turbulence in general has been looked at for a number of decades with researchers considering it at a fundamental level. Stochastic theories and chaos theory have been developed to effectively model turbulence. A quest to understand or look for order in the apparent disorder seems to be the primary force behind turbulence research. Thus far, the reason for research in atmospheric turbulence has mostly been for the purposes of aerodynamics relating to building design (wind engineering), meteorological predictions and for design and control of large aircraft flying at high Reynolds numbers.

Before a review of the findings on atmospheric turbulence encountered within the ABL can be conducted, suitable methodologies to characterize atmospheric turbulence must be defined. Through the contribution of a lot of workers, significant advancement in understanding and characterizing atmospheric turbulence has taken place from as early as the 1930s. In 1938 Kolmogrov introduced the law of turbulence decay, where he stated that it would be better to view freestream turbulent flow as a mix of eddies of various sizes. Kolmogrov's spectral law of turbulence decay states that energy from the largest eddy cascades down to smaller and smaller eddies until viscous dissipation takes place. This means that if no external energy is being added to a flow and if no local effects are present, the rate of energy cascade from the largest to the smallest eddy should be the same rate. This is manifested in the -5/3 slope of the Power Spectral Density (PSD) of velocity fluctuations measured in well mixed freestream turbulent flows. G.I Taylor and G.K. Batchelor also made significant contributions to this field; in 1940s the "frozen turbulence" hypothesis was suggested. According to this hypothesis, the structure of turbulence remains largely unchanged if the size of the velocity field (turbulent eddy) is much larger than its mean advection rate, i.e. the turbulent eddy travels downstream as though in a frozen state. This hypothesis was evaluated through various experiments and is now regarded as an accepted property of atmospheric turbulence.

Based on the qualities described, atmospheric turbulence has usually been characterized using three main quantities; i.e. mean and time-varying velocities in the three orthogonal directions, turbulence intensity and turbulence length scales. Velocities in the three orthogonal directions provide a quantitative idea on the magnitude and direction changes of the flow speed. Turbulence Intensity (Ti) may be defined as the ratio between the Standard Deviation (Std.Dev) of the velocity fluctuation to the mean flow speed, see Equation 1. Turbulence length scale is defined as the average dimensions of the largest turbulent eddy within the flow, as stated by Kolmogrov's turbulence decay theory. The integral length scale is a relatively more abstract quantity whereby any given flow contains nine integral length

scales, three for each axis. Based on the velocity fluctuations, Ti and integral length scales, the turbulence within the flow can be well characterized.

Velocities in the orthogonal directions can be measured using suitable velocity measuring probes and they provide time-dependant variations in flow speed and direction. From the collected velocity data, turbulence intensity can be estimated using Equation 1. The turbulence intensity quantifies amount of turbulent energy present within the flow. There are however three main ways of estimating the integral length scale viz. simultaneous velocity measurements, autocorrelation technique and the von Karman spectral fitting method. Further elaboration on each of these methods and the method most suited for this research is provided in Appendix E. The integral length scale ascertains the manner in which the turbulent energy manifests itself within the flow by estimating the average size of the largest or most energetic turbulent eddy.

$$Ti_U = \frac{\sqrt{\overline{u'^2}}}{\overline{V_r}} = \frac{\sigma_U}{\overline{V_r}}, \quad \text{where} \quad \overline{V_r} = \overline{\sqrt{u^2 + v^2 + w^2}} \qquad \text{Equation 1}$$

Where: Ti_U is the turbulence intensity along the longitudinal axis, σ_U is the Std.Dev of the velocity along the longitudinal axis and V_r is the resultant mean velocity.

In strong wind conditions the variation of mean velocity as a function of altitude can be expressed as a power law, see Equation 2 (Holmes (2001)). This is similar to the relationship for boundary layer growth over a flat plate, developed by Prandtl in 1904.

$$\overline{U}_Z = \overline{U}_g \left[\frac{z}{z_g} \right]^{\alpha} \qquad \text{Equation 2}$$

Where; $\overline{U}_Z$ is the mean speed at height z, $\overline{U}_g$ is the mean speed at height z_g known as the gradient height where velocity is unaffected by friction from the ground and α is the best fit constant.

As surface roughness has a significant effect on the flow structure within the ABL, the gradient of the power law changes depending on the surface terrain as shown in Figure 4. Typically, this gradient extends to up around 457 m for large cities, 366 m for typical suburbs, 274 m for open terrain and 213 m for open seas (Chen (1997)). In large built up cities, the presence of manmade structures like buildings block air flow, hence the mean velocity tends to reduce closer to the ground.

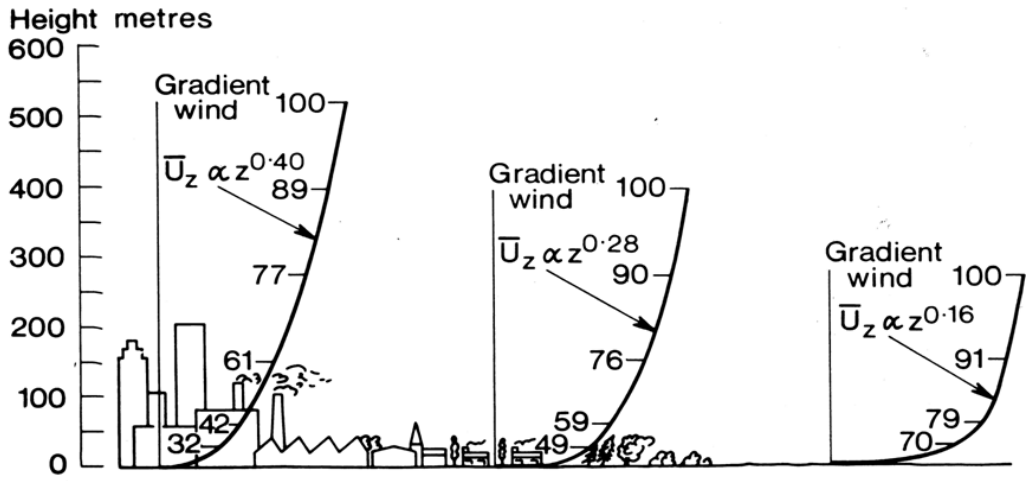

Figure 4: Mean wind profiles as a function of altitude over various terrains, Walshe (1972)

Though the power law is a convenient manner of representing mean flow-field distribution with height within the ABL, it is purely empirical (Ghosal (2005)). However, measurements made in 1961 over open fields fit well with the power law approximation up to 100m after which an almost constant mean velocity was observed (Thuillier & Lappe (1964)). At altitudes very close to the ground, the flow-field seldom resembles the smooth power law approximation. At locations close to ground the surface roughness constituted by local structures have a significantly higher influence on the flow-field. Therefore the power law can be rewritten as follows;

$$\overline{U}_Z = \overline{U}_{10}\left[\frac{z}{10}\right]^{\alpha} \qquad \text{Equation 3}$$

Where, $\overline{U}_{10}$ is the mean speed at a height of 10m, which is usually the height at which anemometers are placed; z is the altitude and α is a terrain roughness factor.

Mean velocity variations at lower altitudes have little significance due to presence of high levels of turbulence and constant changes in flow direction. It is therefore vital that an understanding of the time-varying distribution or flow fluctuations at such altitudes is attained. The time-varying flow close to the surface is primarily governed by local terrain effects like vortex shedding off surface structures. In very low altitudes thermal effects can also be significant. Away from local effects the flow mainly consists of fluctuations of varying magnitude as seen in the photo of the longest bubble (Figure 3). Figure 5 summarizes the time-varying flow fluctuations as a function of frequency and energy.

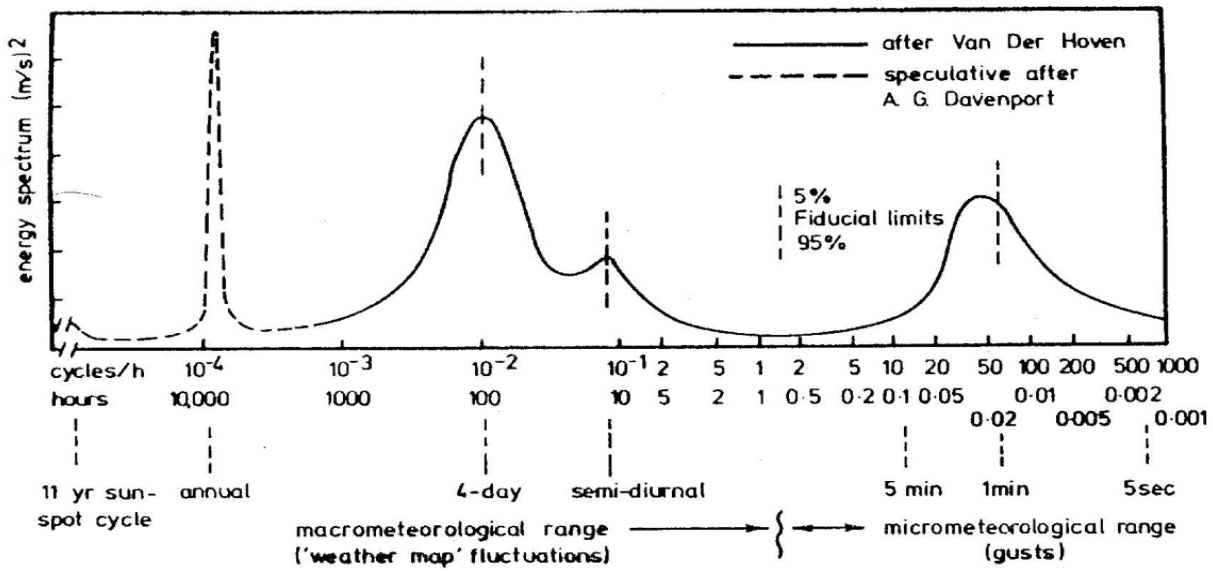

Figure 5: Power spectral density plot of velocity fluctuations occurring within the ABL. Van der Hoven (1957)

The scale and mass of MAVs is such that velocity fluctuations at frequencies lesser than a few Hz can be treated as quasi-static changes in conditions. Therefore, for MAV flight a thorough understanding of the flow on the rightmost side of the plot in Figure 5 is useful.

Engineering Science Data Unit (ESDU) data sheet 74030 provides time-varying wind data at different altitudes from measurements made till the 1970s while the ESDU 85020 data sheets provides revised and summarized wind data based on measurements till the mid 1980s. Though the data sheets provide valuable information of the flow properties within the ABL, their relevance for MAV research is relatively limited. Like most of the research conducted to analyze wind speed and direction fluctuation with spatial variation, measurements in the ESDU data sheets have been made as a function of altitude. For MAV research however, spatial resolution in terms of lateral (i.e. spanwise) separation would be of greater relevance. Moreover, wind data are usually collected using propeller, cup or ultrasonic anemometers placed on top of buildings or masts at various locations of interest. The data collected is well suited for building and road vehicles which are considerably larger than these measuring instruments. The propeller and other anemometers are relatively large and massive compared to the size of MAVs, hence, the spatial and temporal resolution of the collected data is much lower than required to understand the flight environment experienced by MAVs.

1.3.1 Atmospheric Turbulence Relevant to MAV Flight

Data measured with the best spatial resolution appear to be those of Flay (1978) where wind measurements were taken using anemometers spaced apart vertically at approximately 2.2 meters, the results of which were used in ESDU 85020 data sheet. Turbulence measurements taken at two points spaced laterally using Hot Wire Anemometers (HWA) have been taken by Raupach & Thom (1981), however the turbulence was measured over grassy and forest terrains to better understand influence of turbulence on vegetation, rather than in city centers.

Flow-field data that is of most relevance to MAVs were collected by Watkins et al (2006) and Thompson & Watkins (2010). Watkins et al (2006) collected wind data at around 4m above the ground, in an attempt to build a database of outdoor flow-field data relevant to MAV flight. Velocity in the three orthogonal directions was measured at four laterally spaced stations using pressure sensitive probes. The four probes were held various distances apart, the inter-probe spacing ranged from about 15mm to 150mm. Thus the spacing of the velocity measuring probes was of the order of typical MAV spans. Within the ABL, turbulence intensity was measured to be as high as 30% and the integral length scale was found to range from less than a meter to several tens of meters (Watkins et al (2006) and Wordley (2009)). Apart from the high turbulence intensity, the pitch angle, as measured by the ratio of the vertical component of velocity to the relative wind speed, was noticeably different across the four "spanwise" stations even over a small time frame and lateral separations. This implies that if a MAV were flying through the turbulence, different sections of the wing would perceive a different angle of attack, subsequently causing an imbalance of lift distribution resulting in large rolling moments. Wind data and subsequent analysis conducted by Watkins & Thompson (2010) also indicated that destabilization due to rolling formed the most significant disturbing factor when flying outdoors. This fact is well known to model aircraft flyers flying small fixed wing crafts outdoor where considerably more effort is needed to keep the aircraft stable in roll as opposed to pitch and yaw.

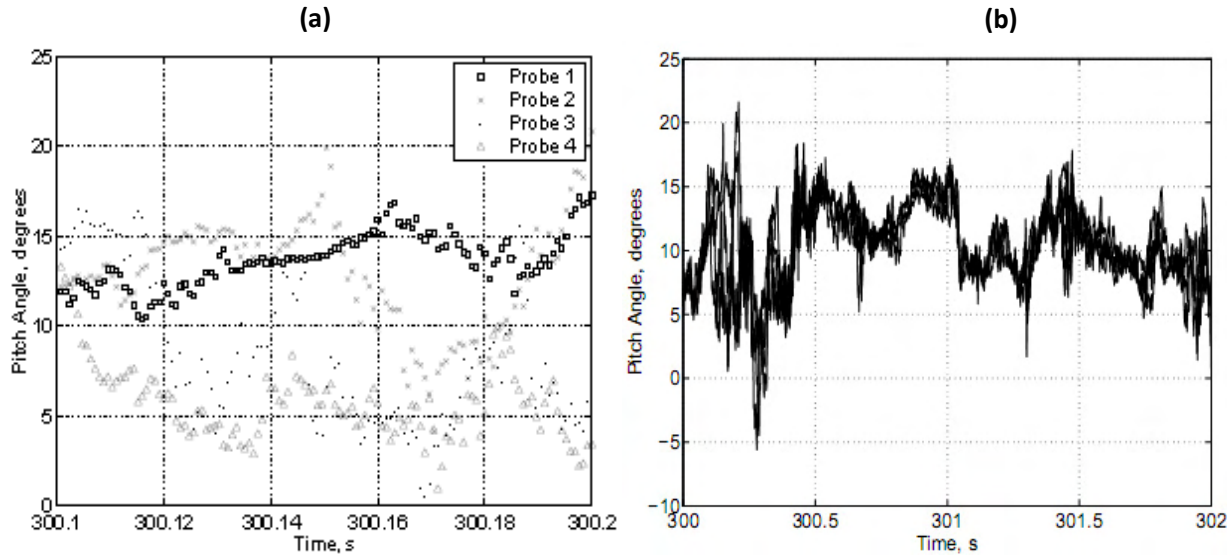

Figure 6: (a) Pitch angle variations as measured by the four probes separated laterally. (b) Pitch angle fluctuations as reported by a single probe. Both figures from Watkins et al (2006)

Up to 10Deg difference in pitch angle over the separated probes was measured within a small time interval of 0.2 seconds, from Figure 6. This implies that the flow over a section of wing would be attached while some distance away, another part of the wing might experience stall. Figure 6 once again highlights the extremely complex and non uniform flow-field MAVs would be exposed to during flight through ABL turbulence. In smooth flow conditions where the flow is largely two dimensional over the airfoil, one chordwise station can be used as a representation of the entire airfoil, however in the case of MAV wing/airfoils exposed to turbulence, each section of the airfoil/wing is under different angle of attack, hence studying a single chordwise station might be inadequate.

Watkins (1990) and Watkins et al (2006) also indicated that the intensity and time scales of turbulence as perceived by a vehicle moving would be considerably different from a stationary one. To gauge the properties of turbulence as viewed by a moving vehicle, velocity of the vehicle is generally added to the respective component in the measured velocities. The turbulence intensity equation is then rewritten as shown in Equation 4. This demonstrates that the perceived intensity and time scale of turbulence reduces as vehicles velocity increase. However the perceived length scale will not change since it is not dependant on the velocity of the vehicle (or observer), refer Appendix E for further details on integral length scales.

$$J_U = \frac{\sqrt{\overline{u'^2}}}{\overline{V_r}}, \quad \text{where} \quad \overline{V_r} = \overline{\sqrt{(u + V_{Veh})^2 + v^2 + w^2}} \qquad \text{Equation 4}$$

Where: J_u is the relative turbulence intensity along the longitudinal axis. V_{Veh} is the mean velocity of the vehicle.

Therefore, if a MAV was hovering at the mean wind speed, it would have zero relative velocity and any fluctuations about the mean would result in infinite relative turbulence intensity as per Equation 4. However, according to Taylor's frozen turbulence hypothesis the fluctuations should be "frozen" since the MAV would be travelling along with the velocity field (eddy) and hence the turbulence intensity should be zero. But as Taylor's hypothesis is only valid for a few length scales downstream, change in velocity will eventually be noticed by the MAV, but as the mean relative velocity is zero in Equation 4, the turbulence intensity tends to infinity. This aspect is seen in Figure 7.

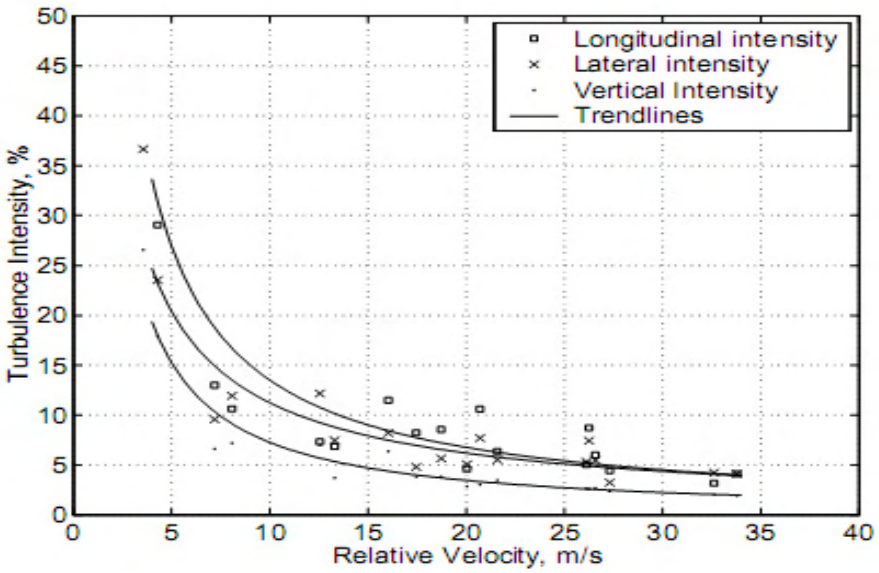

Figure 7: Perceived turbulence intensity as a function of relative velocity, Watkins et al (2006)

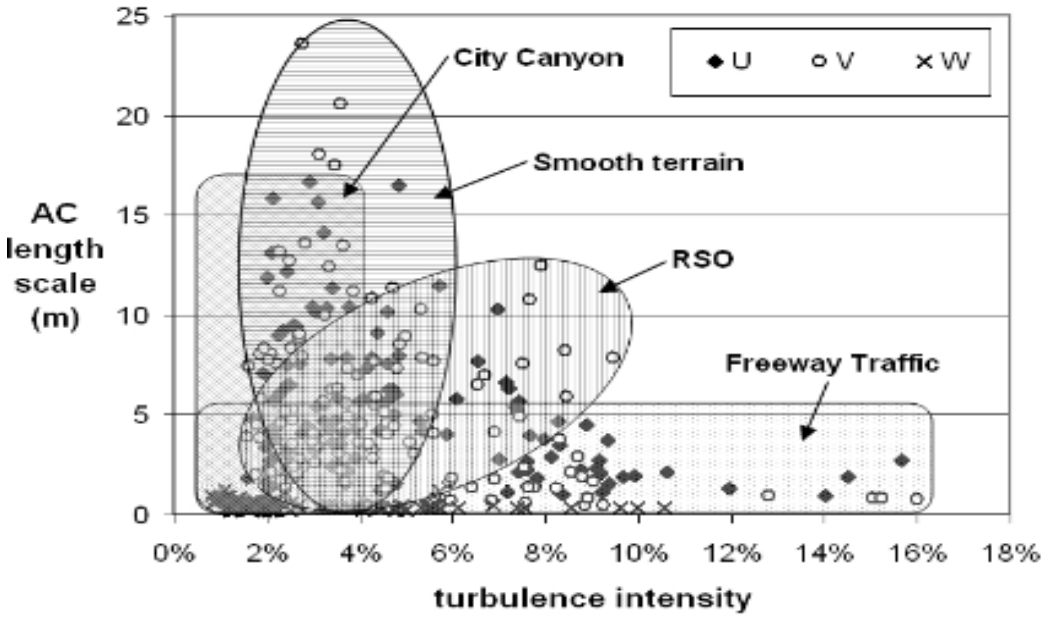

Figure 8: Turbulence intensity versus length scale, measured over various terrains, Wordley (2009)

The measurements made by Watkins et al (2006) concurred well with measurements made by Wordley (2009), who for his PhD also measured velocity fluctuations close to ground over various terrains. Some of Wordley (2009)'s findings are presented in Figure 8. Measurements made by Wordley (2009) were of greater relevance to turbulence encountered by road vehicles as measurements were taken from a vehicle moving at around 100km/hr.

Given that atmospheric flow conditions vary considerably depending on location and ambient conditions, it is important to identify the most critical parameters that would influence MAV flight. In terms of the integral length scales, as MAVs would typically be very small and fly slowly, the changes in flow brought about by very long length scales (tens of meters) can be treated as quasi-static, but eddies present within the larger length scales that are comparable to the size of MAVs would have most impact. Moreover, due to the anisotropy of turbulence present within the ABL, where the lateral length scales are generally much shorter than the longitudinal ones (Flay (1978)), an MAV flying cross-stream would perceive a considerably smaller relative longitudinal length scale. Therefore, insights on the influence of turbulent eddies (integral lengths scales) of the order of the size of MAVs would be very useful. Similarly, since turbulence intensity varies over a wide range, it would be desirable if an understanding of the influence of turbulence intensity across a wide range is obtained.

In order to understand the interaction between turbulence and airfoil performance, a controlled reproduction of turbulence is required. Due to the ever-changing wind speed and direction in the outdoor environment, conducting experiments involving airfoil performance in turbulence outdoors would be highly impractical. Instead, it would be desirable to conduct experiments within a wind tunnel if statistically consistent turbulence of controlled intensity and length scale relevant to MAV flight could be repeatably generated. The forth coming section deals with discussing the various attempts to replicate atmospheric turbulence within a wind tunnel and their associated challenges.

1.4 Replication of Atmospheric Turbulence within a Wind Tunnel

Conducting airfoil or wing testing in outdoor environment within the ABL is very difficult due to the uncontrollability of different turbulence parameters. In order to measure similarity between turbulence within the ABL and within the wind tunnel, it is appropriate to use the same metrics used to characterize turbulence within the ABL. Some of those key metrics being; velocity in the orthogonal directions, turbulence intensity and integral length scale.

For well over half a century a number of researchers have tried to replicate atmospheric turbulence within a wind tunnel facility. In the attempts, various methods have been employed, from active turbulence generation, where energy was added to the flow by the means of stirring the flow using moving components, to passive methods where turbulence was generated by placing stationary obstacles in the flow. This section will review the advantages and disadvantages of the different turbulence generation methods along with choosing the most suitable for MAV airfoil or wing testing.

1.4.1 Passive Grid Generated Turbulence

A number of passive methods have been adopted in order to generate freestream turbulence within a wind tunnel facility. Obstacles are usually placed in the flow-field in an attempt to stir-up the air resulting in homogenous turbulence far downstream. As early as the mid 1930s plane rectangular grids have been used to generate turbulence, the size and location of the grids had a significant effect on the

turbulence properties. Simmons & Salter (1934) conducted a study on turbulence by placing rectangular grids in front of a uniform flow. Batchelor & Townsend (1947, 1948), used four grids made of large circular cylinders in a study of isentropic turbulence. Dryden et al (1936), Grant & Nisbet (1957) and others also conducted research using this method of turbulence generation. Apart from using grids, other methods like placing cylindrical rods in the flow, have also been employed for turbulence generation. Kiya & Sasaki (1983) developed various levels of turbulence intensity and length scales by placing circular rods of various diameters at different distances from their testing specimen.

From previous workers it was found that placing grids within a uniform flow ahead of the test section effectively generates turbulence. However, the flow-field close to the grids consisted mainly of vortices arising from the edges of the grids since they acted like bluff bodies to the oncoming flow. With downstream advection, these vortices decayed as there is no source of turbulent energy along the streamline. Hence, the decay rate of turbulence as it travels downstream was close to the viscous dissipation rate, Figure 9 depicts this transition. The location of the testing area from the grids therefore determines the nature of turbulence experienced in that location. Liu et al. (2004) developed an empirical relation (Equation 5) between turbulence intensity and distance downstream of grids after surveying the flow at different downstream location from perforated plates.

$$\left(\frac{\sigma_u}{\overline{U}}\right)^2 = A\left(\frac{X}{D} - \frac{X_o}{D}\right)^{-n} \qquad \text{Equation 5}$$

"Where A is a universal constant, X is the distance downstream of the plate, D is the width of the grid panel, X_0 is the virtual origin and n varies somewhere between 1 and 1.35 in different studies" Liu et al (2004).

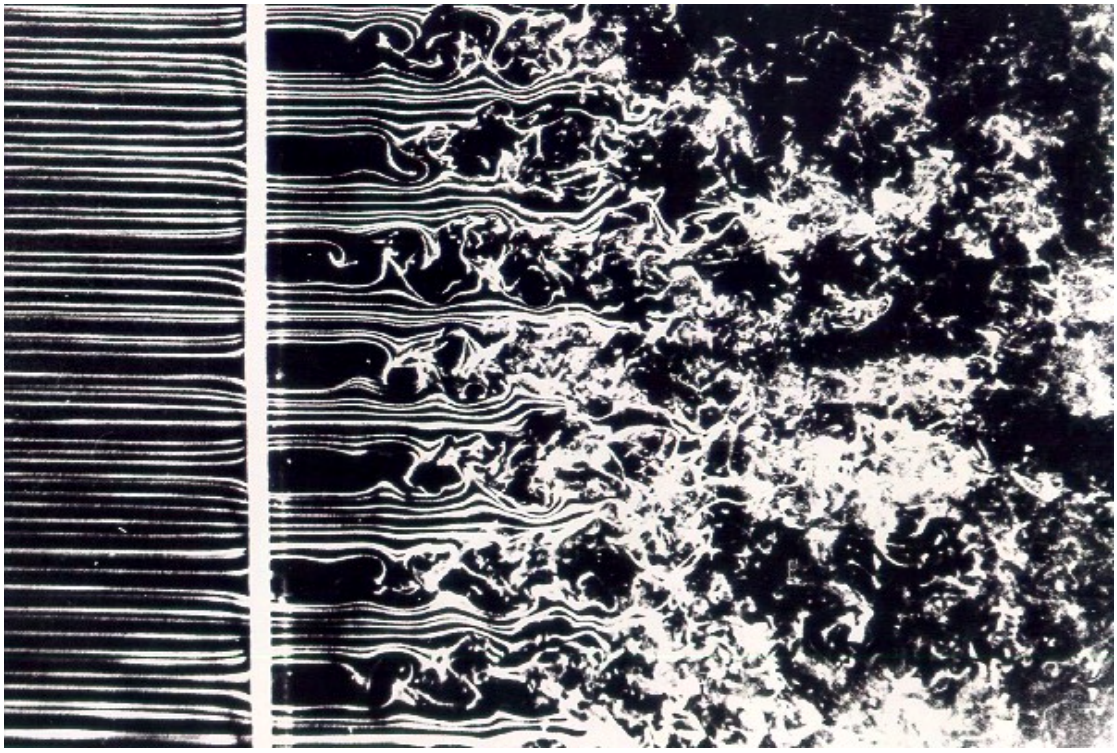

Figure 9: Breakdown of discrete vortices to homogeneous turbulence upstream of grids. (Fluid Dynamics Research Centre, Illinois Institute of Technology).

Comte-Bellot & Corrsin (1966) suggested that turbulence decays to reasonable levels only at a distance of 40-50 grid lengths downstream, while Vickery (1965) suggests only 10-15d is required, where d is the center-to-center spacing of bars on the grid. The differences in the two suggestions lay in the size of grid and on the scale of turbulence being generated. This decay distance can however be greatly reduced by placing the grids upstream of the contraction section of the wind tunnel. Comte-Bellot & Corrsin (1966) placed three different types of grids at various locations upstream (see Figure 10) and downstream of the contraction section of the wind tunnel and studied the turbulence characteristics in the test section as a function of downstream distance from the grids.

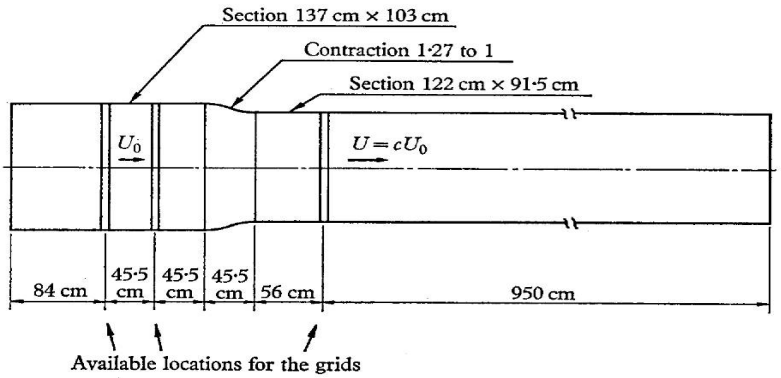

Figure 10: Grids placed at various locations upstream and downstream of the contraction section. Comte-Bellot & Corrsin (1966)

The results indicated that relatively quick decay of turbulence into a homogeneous state is achieved if the grids were placed upstream of the contraction section of the wind tunnel as opposed to just upstream of the test section inlet. Batchelor and Comte-Bellot generated homogeneous and isotropic turbulence in a wind tunnel test section using their respective methods.

1.4.1.1 Turbulence Generation for MAVs and Road Vehicles

Work of particular relevance to turbulence generation with respect to MAVs and road vehicles was conducted by Watkins (1990), Cruz et al (2007, 2008) and Milbank (2005). Through trial and error, Watkins (1990) managed to develop relatively small turbulence intensities of 1.7% to 3.7% by placing planar grids (grids made from plane rectangular panels) on the turning vanes before the contraction section of the RMIT Industrial Wind Tunnel. Milbank (2005) developed a range of turbulence intensities and integral length scales by placing grids within the Monash University Wind Tunnel in Melbourne, which has a top working section measuring 12m x 4m x 30m. Planar grids and different tunnel configurations were used in order to generate various turbulence levels within the test section. The devices used to measure velocity fluctuations, multi-hole pressure sensitive probe and acquisition software, were the same ones used by Watkins et al (2006) for taking outdoor flow-field measurements relevant to MAVs. In Milbank's work, four multi-hole pressure probes were spaced at 150mm and turbulence measurements were taken at different locations within the test section. Due to the very large dimensions of the test section, turbulence intensities as high as 25% were generated with integral

length scales of over 1.5m, these were noted to be well suited MAV airfoil/testing. A comparison of the turbulence generated by Milbank (2005) to outdoor flow-field measurement is presented in Figure 11.

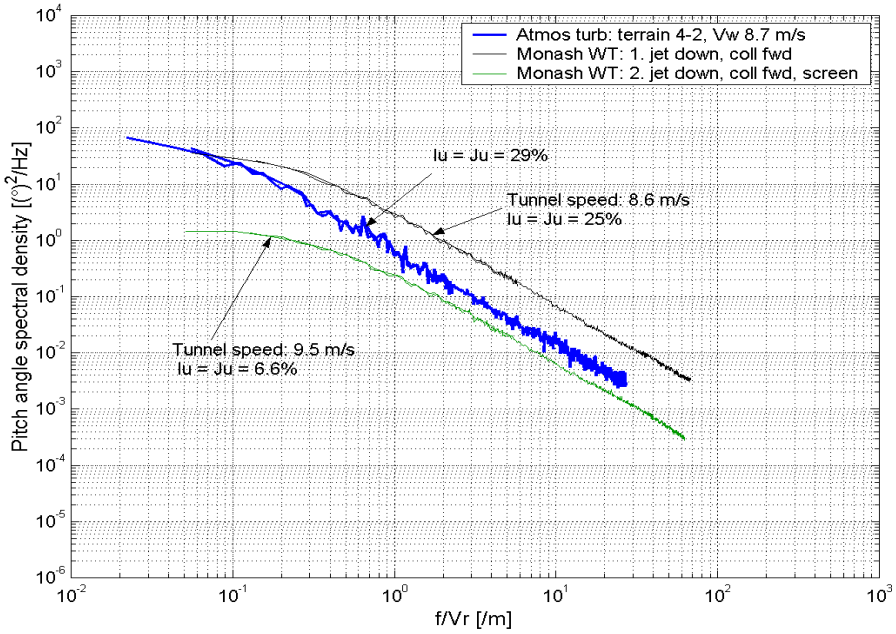

Figure 11: Comparison of spectral plots of pitch angle fluctuation obtained within the ABL and within the wind tunnel, Milbank (2005)

Milbank remarked that "The results obtained from research showed that atmospheric turbulence characteristics for the important roll inputs experienced by MAVs, can be simulated within the wind tunnel facility for the entire relevant frequency range for 150 mm (6 inch) span MAVs, but that 1 m (40 inch) span MAVs might require additional active turbulence generation techniques, as the turbulent eddies do not have enough energy to maintain a larger integral length scale". Milbank's efforts are one of the first to develop turbulence of the required order for MAV research. Grusovin (2006), Cruz et al (2007, 2008) attempted to use a similar method to generate turbulence within the RMIT Industrial Wind Tunnel (IWT) and had good success. Plane rectangular grids of different mesh widths were placed at various locations upstream and downstream of the contraction section of the wind tunnel. They reported that the tunnel had a base turbulence intensity of 1.5% in its clean configuration and it rose to nearly 13% at 7.75m downstream from the grids that were placed at the test section inlet. Integral length scales of a maximum 0.3m and 0.2m longitudinally and laterally respectively were generated

within the facility. By placing a larger version of the same grids just upstream of the contraction, turbulence intensity of around 7.5% and streamwise length scale of 0.22m was generated at the same location in the test section. The turbulence decay rate of both these conditions is presented in Figure 12. Though the generated length scales are much lesser than the length scales present in the ABL, it is comparable to the size of MAVs which is most relevant here, hence offering a starting point to conduct airfoil/wing testing. More information on these grids will be presented in later chapters.

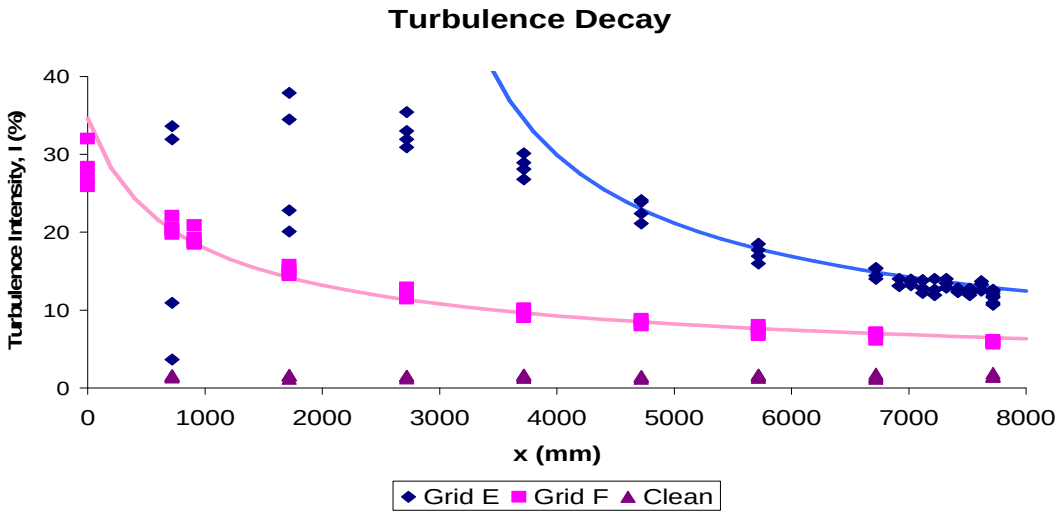

Figure 12: Turbulence intensity measured at various points downstream of grids within test section. Grid E was located at the inlet of the test section while Grid F was placed at inlet of contraction. Cruz et al (2008)

Calibration of a wind tunnel with upstream grids present is significantly more challenging than in smooth flow condition, as a detailed survey needs to be conducted to ensure a consistent intensity and scale of turbulence is present across the region of interest, Grusovin (2006). Close to the boundary walls, the structure of turbulence will be different and fluctuation in the wall normal direction tends to zero resulting in a slight increase in turbulence intensity and length scale in the other directions. Such wall effects are expected and form one of the challenges in generating free stream turbulence within wind tunnels, however in sufficiently large test sections these effects can be neglected if the testing location is well removed from tunnel walls, Grusovin (2006).

From the review of previous attempts to replicate flow experienced in the ABL within a wind tunnel, it was found that success was only partially attained. A wide range of turbulence intensities have been generated but the physical size of the wind tunnel facility and the limitations of turbulence generating

methods render exact length scale replication impossible. Though the replicated scales are smaller in comparison to those observed outdoor, they are comparable to the size of MAVs, which is of particular importance here. Therefore, from the replicated scales and intensity of turbulence generated, it would be possible to identify the influence of each parameter of turbulence, i.e. turbulence intensity and length scale, on airfoil performance.

One disadvantage with grid generated turbulence is that a sufficiently long downstream distance needs to be present between the grids and testing location in order for the wake from the grids to decay into homogenous turbulence. This in turn requires large wind tunnels with long test sections in order to generate turbulent eddies of the order required.

1.4.2 Active Methods of Turbulence Generation

Attempts to generate homogenous turbulence through other techniques e.g. using active grids and using turbulence generating vanes have taken place over the past few decades. Makita (1991), in an attempt to overcome some of the disadvantages of static grid turbulence generation, developed an active method in order to generate turbulence at higher Reynolds numbers. This technique was improved and utilized by Mydlarski & Warhaft (1996). Makita managed to develop relatively large-scale turbulence by controlling the angle of a number of diamond shaped vanes using independently controlled vertical and horizontal bars. Kang et al (2003) used the similar method to generate turbulence in an even smaller wind tunnel facility (0.91×1.22m). Larssen & Devenport (2002) placed such active turbulence generators within a 2.13-m square wind tunnel. The results indicated that a closely uniform mean flow and homogeneous isotropic turbulence was generated around 37 mesh sizes downstream. Wasko (2003) placed an oscillating pendulum upstream within the RMIT Aerodynamics Wind Tunnel and managed to develop reasonable turbulence intensities (Ti around 3.5%) and length scales as large as 0.64m and 0.85m in the longitudinal and lateral directions respectively.

Active turbulence generating methods were generally used to overcome disadvantages encountered when using static grids. However, for the purposes of MAV airfoil/wing testing, static grids can be used to develop various relevant levels of turbulence, unless significantly longer length scales are required, Milbank (2005). Moreover, active turbulence generation methods consist of relatively more elaborate

setup hence they take a lot of time and are not as cost effective. Therefore, for the purposes of MAV airfoil/wing testing, it would appear that in spite of its disadvantages, passive grids offer the easiest and most cost effective manner of turbulence generation within a wind tunnel, as various length scales and a wide range of intensities can be realized.

1.5 Flow at Low Reynolds Numbers

There exists a relatively large knowledge base about flow-field and its influence on airfoil performance from chord Reynolds number 250,000 and higher. This is primarily due to the fact that most conventional aircraft very rarely venture into low Reynolds number flow regime. However, for the purposes of MAV flight an enhanced understanding of the flow below this Reynolds number range and its influences on airfoil/ wing performance is needed. This section would deal with a review of the current body of knowledge on airfoil and wing performance at low Reynolds numbers typically classified between 50,000 < Re < 200,000.

1.5.1 Airfoil Performance in Low Reynolds Number Flows

As the chord Reynolds number decreases below 200,000 a number of non-linear phenomena start to become apparent. Though this type of flow has not been part of active research over the history of aerodynamics, a few researchers have studied airfoil behavior in these conditions. Experiments on Low Aspect Ratio (LAR) wings have however been conducted from as early as the 1930s. Zimmerman (1932) published the results from the experiments conducted on LAR wings with Clark Y airfoil section. The Reynolds number under which the experiments were conducted was around 800,000, well above the typical MAV operating regime. Winter (1936) also conducted experiments and reported his findings on the various aerodynamic properties of thin low aspect ratio wings, however at relatively high Reynolds numbers.

Though a number of different techniques have matured for aerodynamics research (e.g. airfoil force and surface pressure measurements, Particle Image Velocimetry (PIV), and other flow visualization) to study

airfoil behavior over a wide range of Reynolds numbers, testing in the low Reynolds numbers regime has always been more challenging than at higher Reynolds numbers. As the actual magnitude of forces and pressures measured over the airfoil are very small due to the low speeds, it required the use of equipment sensitive enough to enable measurement of force or pressure without influencing the developing flow. With the prevalent use of hot-wire anemometry and the development of other techniques, it is now possible to measure flow properties very close to airfoil surface, shedding light on the flow structure in such Reynolds number regimes.

When an airfoil is inclined to an oncoming smooth flow, depending on the airfoil geometry and the angle of attack, the flow either remains attached or separates. The flow would mostly be laminar near the leading edge and this is consistent through nearly all Reynolds number ranges, except when compressibility effects become a factor. Between the Reynolds numbers of 50,000 to 200,000 however, the laminar boundary layer tends to develop further downstream over the airfoil and in the presence of an Adverse Pressure Gradient (APG), the flow usually separates without transition i.e. laminar separation occurs. Depending on a number of factors, the shear layer later transitions to turbulence while still detached from airfoil surface. The shear layer on transitioning then reattaches further downstream over the airfoil creating a turbulent boundary layer, hence forming a “bubble” between points of separation and reattachment. The bubble is also commonly referred to as the Laminar Separation Bubble (LSB). At higher Reynolds numbers however, this bubble does not form as the boundary layer transitions to turbulent while still attached to airfoil surface. This change in boundary layer structure between high and low Reynolds numbers renders the performance of airfoils in low Reynolds numbers to be significantly different. The anatomy of a typical LSB is seen in Figure 13.

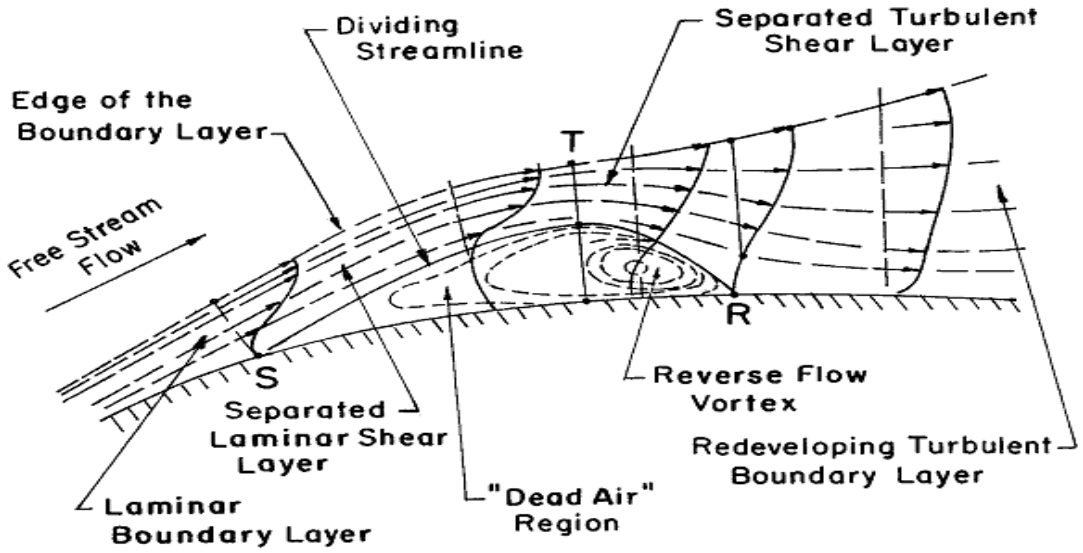

Figure 13: Anatomy of a typical laminar separation bubble. Horton (1968)

Experiments studying LSBs have been conducted since as early as the 1960s. The early work conducted by Gaster (1966) is one of the most substantial studies undertaken in understanding the structure and behavior of LSBs. In his research, Gaster artificially induced LSBs over a flat plate by introducing an APG over the same. By taking velocity and pressure measurements within the bubble over a range of Reynolds numbers, Gaster characterized LSBs into two types, viz. long and short Bubbles. Gaster remarked that short bubbles usually form near the leading edge of the airfoil and have little influence on the overall airfoil performance and pressure fluctuations. However he also found that short bubbles can abruptly burst with slight changes in AOA and Reynolds number to form long bubbles or detached shear layers. Long bubbles extend over a large part of the airfoil chord and have a significant effect on performance. They cause a big drop in the suction hence lead to significant loss in lift. As long bubbles have a significant influence on airfoil performance, their structure needs to be well understood.

Since Gaster's research, a number of other workers like Watmuff (1999), Horton (1968), Burgmann et al (2006, 2008), Pauley et al (1990), Ol et al (2005), Kähler (2003) etc have found key insights on the structure and behavior of the LSBs through both computational as well as experimental means. In their research, Kähler (2003) and Burgmann et al (2006, 2008) found that LSBs are extremely complex and a number of transient features develop as the bubble advects downstream over the airfoil. Even though testing was conducted in smooth flow conditions, the structure of LSB was found to be extremely three dimensional in nature, i.e. large spanwise components of the bubble was noticed. This complex nature

of LSB can be attributed to the process of laminar to turbulent transition of the shear layer. Though a lot of ambiguity still exists about its properties, transition is believed to take place through the amplification of disturbances within the shear layer, Watmuff (1999). Disturbances in the flow amplify instabilities within the detached shear layer to form coherent structures, Watmuff (1999); these are in the form of either Tollmien–Schlichting (T-S) waves or Kelvin-Helmhotz (K-H) instabilities. The separated shear layer usually transitions to turbulence on the formation of either T-S waves or K-H instabilities, however instances have been reported where a combination occurs. These coherent structures re-energize the boundary layer hence tripping the shear layer from laminar to a turbulent profile.

The primary reason for the formations of LSBs is laminar separation and subsequent turbulent reattachment. A number of techniques have therefore been adopted in order to trip the flow from laminar to turbulence before separation occurs. Some of these tripping devices and techniques include; tripwires, tape strips, synthetic jets, bleed air through holes on airfoil surface, etc, (Gopalarathnam et al 2003). They are placed at different locations on the airfoil chord and their primary role is to introduce disturbances in the flow which transmit through the boundary layer enabling the shear layer to transition from laminar to a turbulent profile before separation occurs. Though a turbulent boundary layer creates more drag than a laminar one, this transition is necessary to keep the flow attached longer over the airfoil surface to enhance overall performance. Turbulence is hence considered to have a positive effect since these “flow control” devices are used to introduce “turbulence” into the flow in order to improve overall airfoil performance. However, the scales of turbulence introduced by these devices are significantly smaller than the levels present within the ABL. The use and effectiveness of boundary layer tripping devices is not the subject of research here, hence they will not be discussed any further.

The presence of LSBs over an airfoil can be identified by surveying the velocity distribution over the airfoil. Crompton & Barrett (2000) took velocity measurements within separation bubbles forming behind sharp leading edges between Reynolds numbers 100,000-550,000 and found the velocity to be significantly lesser than the mean flow speed, while the velocity was higher than the mean flow just above the bubble, this is consistent with findings of other workers, see Figure 14. An increase in turbulence was also noticed within the bubble, this was attributed to flow recirculation that occurs within the same. They also found that the structure of separation bubbles originating from airfoil Leading Edges (LE) to be more akin to LSBs that formed behind sharp edges and over forward facing steps.

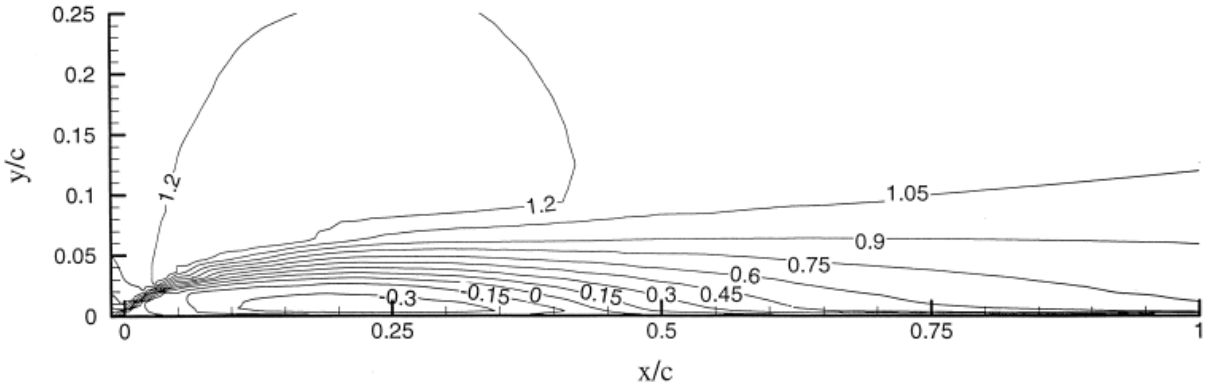

Figure 14: Contours showing normalized velocity distributions within the laminar separation bubble over a flat plate with a sharp leading edge. Reynolds numbers 100,000-550,000. Crompton & Barrett (2000)

The presence of LSBs over an airfoil can also be identified through conducting qualitative studies like smoke flow visualizations or by taking quantitative surface pressure measurements at different points on airfoil chord. A flat region of constant pressure distribution over an airfoil or wing is usually a characteristic sign of presence of LSBs, Crompton & Barrett (2000), Sicot et al (2006), etc. As seen in the pressure coefficient plot in Figure 15, the LSB extends from around x/c of 0.05 till 0.2, Hu & Yang (2008). Figure 15 is of a short bubble forming over a small section of the airfoil chord.

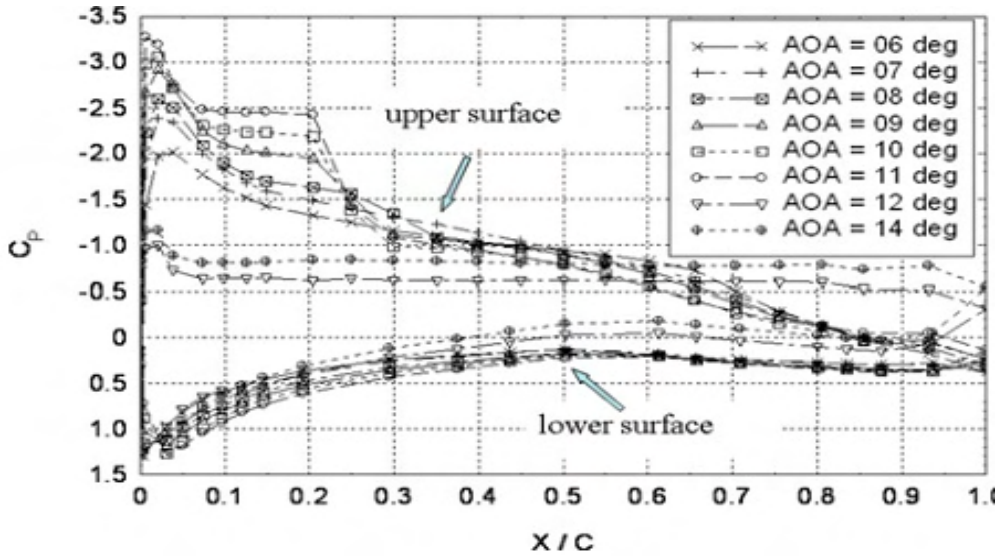

Figure 15: Mean pressure coefficient distribution over a GA(W)-1 airfoil at different angles of attack. Hu & Yang (2008)

It can be seen from Figure 15 that due to a favorable pressure gradient at the bottom surface, no shear layer separation and reattachment occurs, whereby the flow progresses through relatively smoothly. It is also widely accepted that the points of highest standard deviation of the pressure over the airfoil or wing shows the location of separation or reattachment of the shear layer, i.e. the start and finish points of the bubble, Sicot et al (2006) and Melbourne (1993). This is due to the large fluctuations in forces and in turn pressures experienced at the two locations. Figure 16 shows that the location of maximum Standard Deviation (Std.Dev) of pressure coefficient corresponds to location of reattachment. A photo of a LSB occurring over the top surface of a blunt flat-plate along with the Std.Dev of pressures fluctuations occurring over the surface is presented in Figure 16.

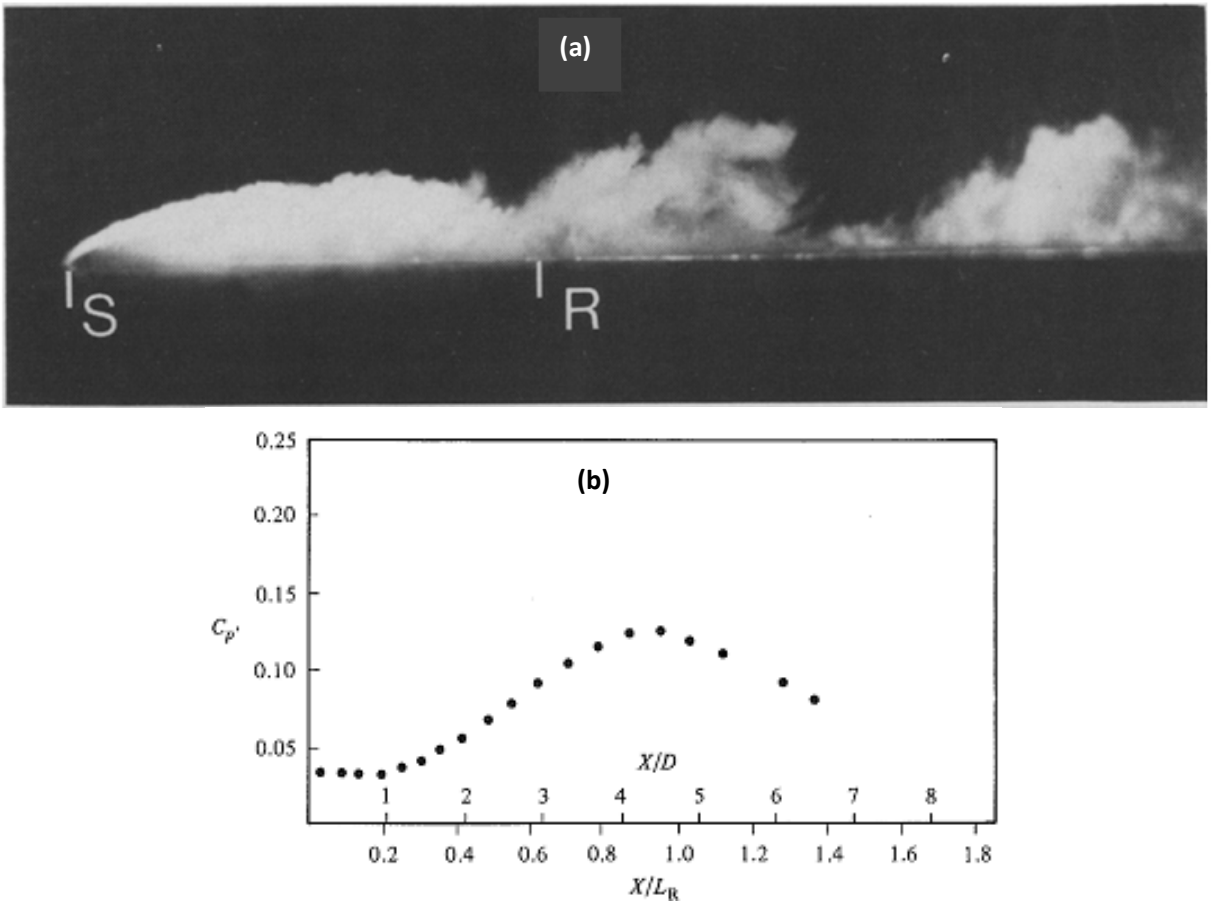

Figure 16: (a) Photograph of a LSB occurring over the top surface of a blunt flat plate, Cherry et al (1983). (b) Distribution of the root mean square of pressure coefficient fluctuations occurring over the top surface of a blunt flat plate, Cherry et al (1984).

At low Reynolds numbers, due to the extremely three-dimensional nature of flow over the airfoil (even at low AOAs in nominally smooth flow testing conditions), Sathaye (2004) found a very non uniform distribution of forces over the airfoil. Given that the suction side of the airfoil or wing is exposed to the forming and bursting of LSBs, it would have a considerable influence on the overall performance of the airfoil. It is more apt if a global perspective is now adopted to understand how all the local complex phenomena affect overall aerodynamic performance.

The survey of airfoils conducted by Carmichael (1981) offers a good review in understanding the performance of airfoil and LAR wings in low Reynolds number flow. Some of the most important conclusions that were derived from the experiments included the following;

- Between the Reynolds numbers range of 30,000 to 70,000 the flow is predominantly laminar with no transition to turbulence occurring over the airfoil, even tripping devices are inefficient and in the absence of transition, no reattachment of the shear layer takes places.
- The type of airfoil also has a significant influence on the aerodynamic performance i.e. thick airfoils become inefficient due to high hysteresis in CL vs. AOA and premature separation. Hence, airfoils that performed well for conventional transport aircraft do not perform well at low Reynolds numbers.
- Between the Reynolds number ranges of 70,000 to 200,000, a larger attached laminar region over the airfoil is obtained leading to an increase in aerodynamic efficiency in spite of the formation of LSBs. However, performance in this regime is also lower in comparison to that at higher Reynolds numbers. Most radio controlled planes and MAVs operate in this region.

Mueller (1999) and Torres (2002) also conducted detailed studies on performance of various airfoils and wings in low Reynolds number flows. Their findings agreed well with the findings of Carmichael in that a drop in performance was noticed at lower Reynolds numbers. Using an airfoil with Aspect Ratio (AR) of 2, Mueller also noticed that end plates had a large influence on the flow-field over the airfoil due to airflow-endplate interaction.

In experiments on LAR wings with different airfoil sections in low Reynolds number flows, by measuring the time-averaged forces like lift, drag and pitching moments, Mueller found thin airfoils to perform better in such flow regimes as opposed to conventional thicker airfoils. Strong influences of AR on the lift generated between airfoil and wings were also noticed, see Figure 17. The airfoil section used in

Figure 17 was a flat plate with an elliptical leading edge. Hoerner (1965) and Hoerner & Borst (1975) also noticed two contributions to the lift generated by LAR wings at low Reynolds number, those being linear and non linear lift. Linear lift is similar to the lift generated by high aspect ratio wings while non linear lift is the lift generated though the formation of low pressure cells from the vortical structures originating from wing tips and leading edges.

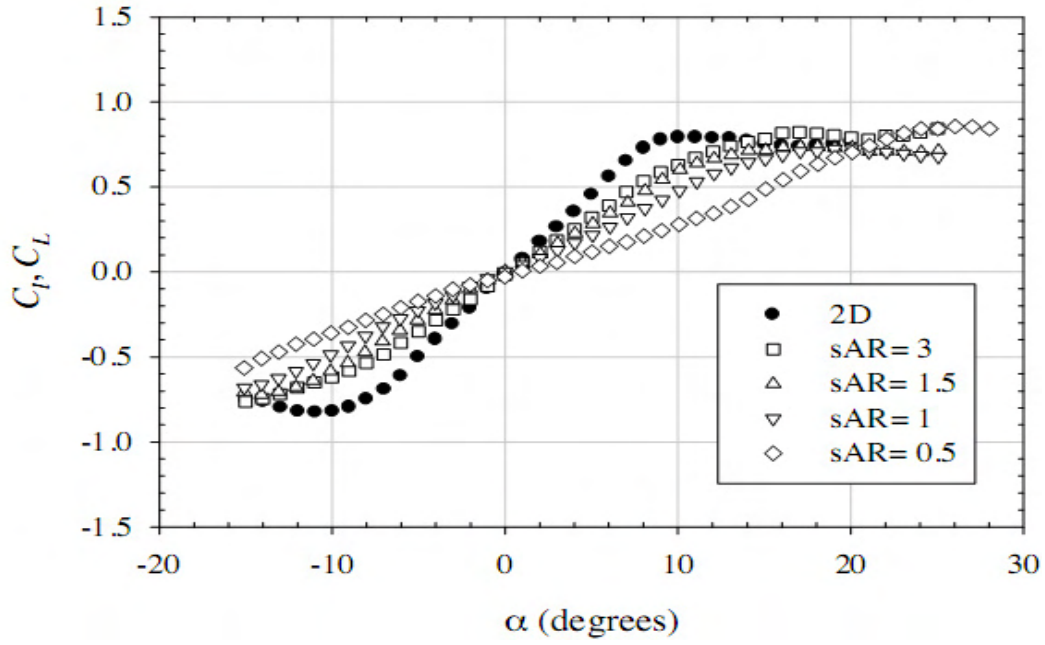

Figure 17: Cl Vs AOA plot for various aspect ratios of a flat plate airfoil. Mueller (1999)

Depending on the airfoil, the location of separation and reattachment of the bubble was found to vary considerably with time. A number of time-varying properties of the bubble have also been identified, like flapping of the shear layer as it reattaches to the airfoil, periodic bursting of the bubble, etc. These periodic changes in the structure of the LSB bring about oscillations in the forces over the airfoil that also results in a drop in airfoil performance. The fluctuations occurring within the bubble bring about other undesirable effects like buffeting and even stall, Roberts (1980). Bastedo & Mueller (1985) reported that the angle at which separation occurs for a particular airfoil at low Reynolds number is lower than that at high Reynolds numbers. This implies that in such flow conditions, LSBs form over airfoil surface at relatively low AOA hence greatly reducing performance. Broeren & Bragg (2001) also

reported a significant drop in the unsteady forces generated over an airfoil by completely eliminating the formation of separation bubbles.

The current state of knowledge indicates that the flow over airfoils at such low Reynolds numbers is very complex indeed. Influences arising from a number of non linear aspects like LSBs and vortical structures render the aerodynamic performance of airfoils and wings in this flow regime to be significantly different to those of higher Reynolds number. Though understanding the structure and dynamics of LSBs have been given special attention by researchers in the field, by no means has a complete picture emerged. The implications of LSBs on airfoil or wing performance is still not entirely clear as further understanding of its influence in the spanwise direction is needed. More experiments must therefore be conducted to shed more light on the structure of the boundary layer and its implications on performance between Reynolds number ranges of 70,000 to 150,000 which is the typical operational regime of MAVs.

1.5.2 Airfoil and Wing Performance in Turbulence

It is important to understand the performance of MAV airfoils and wings under turbulent flow conditions as they would exposed to turbulent flow-fields within the ABL while carrying out their mission. Partly due to the lack of the need in understanding airfoil performance in turbulent flow conditions and also due the various challenges associated with low Reynolds number testing, surprisingly limited experiments have been conducted in this flow regime. Experiments on airfoil performance and flow around bluff bodies in turbulent flows have however been conducted by wind-engineers for a number of years. These experiments are more relevant to design of buildings, bridges, wind mills, etc.

Stack (1931) in as early as the 1930s studied the influence of turbulence on five different airfoil sections in smooth and in grid induced turbulent flows. The scale and intensity of turbulence generated by Stack was however not accurately quantified due to lack of equipment and theoretical knowledge on turbulence at that time. Stack measured the turbulence by estimating the change in drag experienced by a sphere in smooth and turbulent flows. As the boundary layer over the sphere attains transitions much

earlier in turbulent flow as opposed to smooth flow, the shear layer tends to stay attached longer, hence reducing drag. Hoerner (1965) however stated that this means of turbulence estimation can only serve as a qualitative measure as a number of factors including acoustic disturbances, mechanical vibrations, etc. all have an influence in the drag measured. Due to this ambiguity in the flow conditions, Stack's results leave more questions than answers on airfoil performance in turbulence. Some of the results obtained by Stack are presented in Figure 18

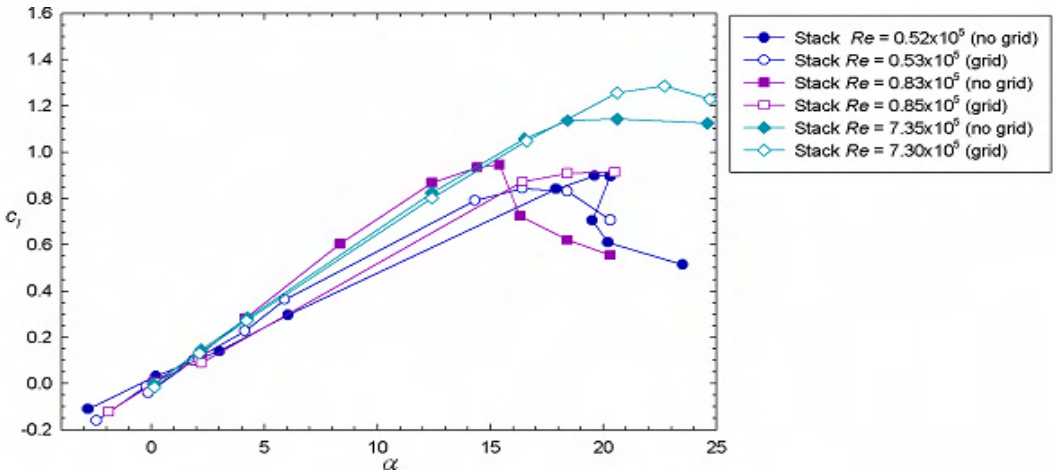

Figure 18: CL vs. AOA for a NACA0006 airfoil at different Reynolds numbers and turbulence conditions. Stack (1931). (Reproduced from Swalwell (2005))

In Figure 18 it can be seen that the influence of turbulence on the lift generated by the airfoil at different Reynolds numbers contradict each other. Stack found the lift curve slope was greater in turbulence than in smooth flow at Reynolds number of 0.83×10^5 while the opposite occurred at Reynolds number of 7.3×10^5. Jancauskas (1983), as part of his PhD, conducted experiments to study the performance of NACA 0006 airfoil in various turbulence intensities and at Reynolds numbers similar to Stack's experiments. Jancaukas's results varied from Stack's in that a delay in angle of stall in turbulent flow was noticed by the former. This trend of a delay in stall was consistent as turbulence intensity was increased from 0.16% to 16%. The variations between Stack's and Jancaukas's findings needs to be further investigated. As seen from Figure 19, the Reynolds number of the experiments conducted by Jancaukas is higher than typical MAV Reynolds numbers hence direct conclusions from these results for the purposes of MAV flight cannot be made. The AR of the wing used by Jancaukas was 2.7 for his experiments in turbulence.

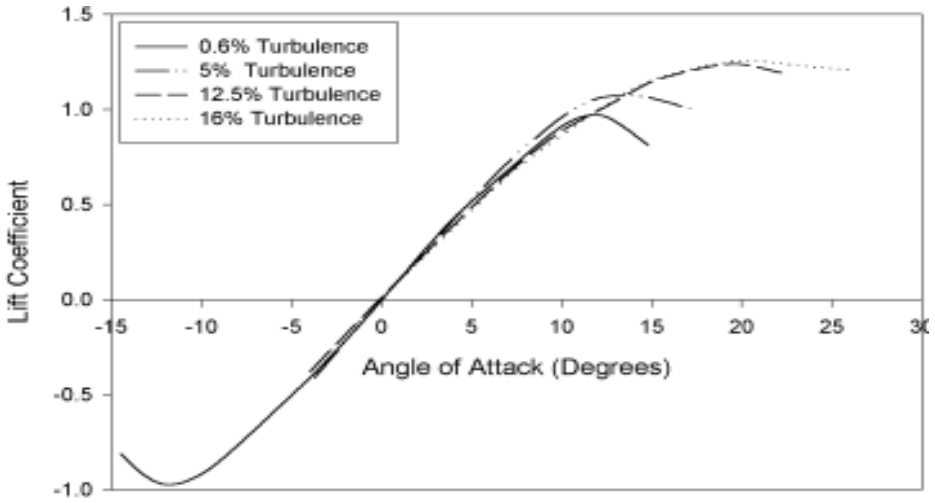

Figure 19: CL vs. AOA plot of NACA 0006 airfoil subjected to various turbulence intensities at Re approx. $2x10^5$, Jancauskas (1983)

Devinant et al (2002) studied the influence of turbulence on NACA 65_4-421 airfoil by measuring both forces as well as surface pressure fluctuations over the airfoil. A range of Turbulence Intensities (Ti) were developed as shown in Figure 20. A maximum Ti of 16% was generated, the integral length scales of the generated turbulence were however not reported. Their results concurred well with the findings of Jancaukas (1983) in that a delay in onset of stall was noticed along with an increase in Maximum Lift Coefficient (CLmax). Through their time-varying measurements, they also identified that the laminar separation bubble constantly changes in size as the point of separation and reattachment keep moving. They concluded that turbulence and Reynolds number have little effect on the oscillation length of the point of separation. The results presented by Devinant et al (2002) are however not entirely relevant as the Reynolds number of their experiments was around 600,000 which is much higher than that of MAVs. Moreover, as length scales were not estimated, it is difficult to ascertain the exact influence of turbulence intensity and length scale on the particular flow phenomena. The experimental setup and some of Devinant et al (2002)'s results are presented in Figure 20. Swalwell (2005) and Swalwell et al (2001) also conducted a number of experiments where pressure fluctuations over three different airfoils were measured when subjected to over 15 different turbulence conditions. While they reported stall to be greatly delayed along with an increase in CLmax in turbulence, the exact influence of length scale could not be conclusively ascertained. All of Swalwell's experiments were at Reynolds number well above 200,000 hence direct inference of results for MAVs was again not entirely possible.

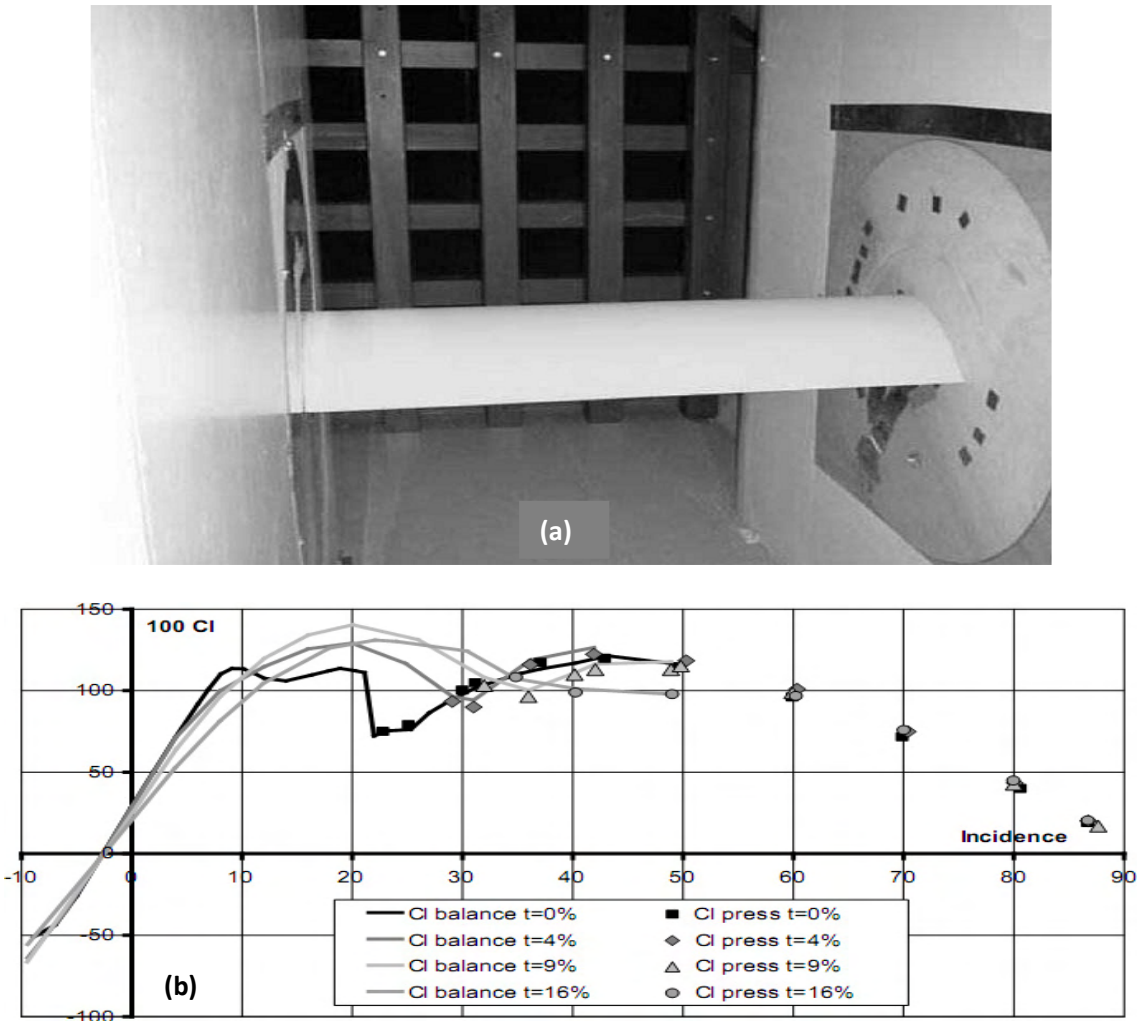

Figure 20: (a) Airfoil setup upstream of grids. (b) CL vs. AOA obtained through force measurement as well as pressure measurement of the NACA 65_4-421 airfoil subjected to various level of Turbulence Intensity (t), Devinant et al (2002)

Experiments at Reynolds number similar to MAV flight were conducted by Li & Melbourne (1999), Saathoff (1988) and Melbourne (1993), where they studied the influence of turbulence on blunt flat plates. Although the experiments they conducted were on bluff bodies, the results offer valuable insight on the structure of the boundary layer in oncoming turbulent flow-fields. By measuring the pressure fluctuations over a blunt flat plate exposed to various levels of turbulence, they studied the influence of turbulence intensity and length scale on LSBs.

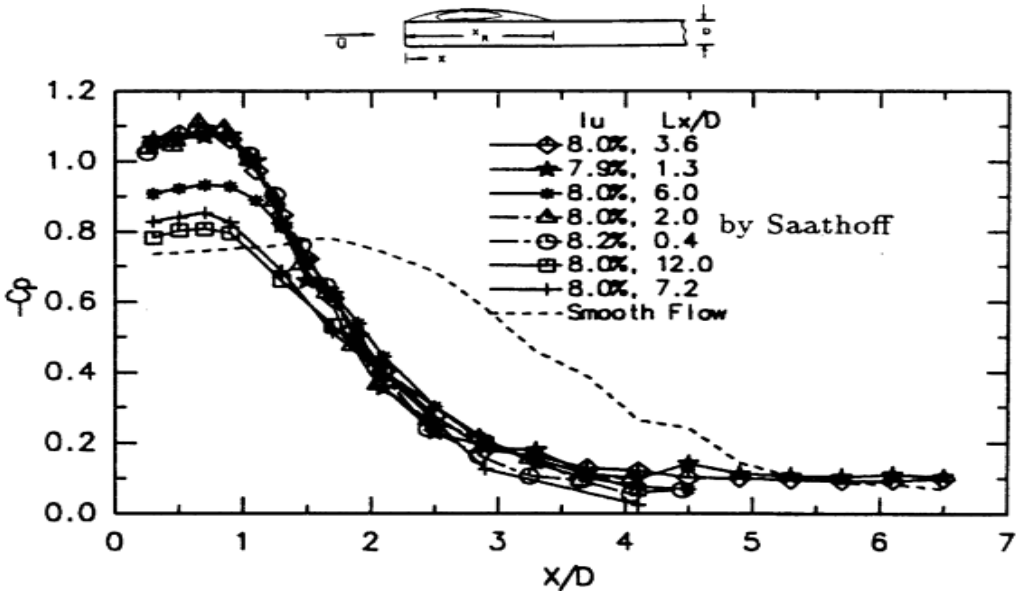

Figure 21: Mean pressure coefficient distribution over the top surface of a blunt plate subjected to different longitudinal integral length scales (Lx) at nominally constant turbulence intensity. Li & Melbourne (1999)

They noticed a reduction in the size of the LSB along with an increase in peak Pressure Coefficient (Cp) as turbulence intensity was increased. However, the Cp distribution at the largest length scales generated most closely resembled the Cp distribution in smooth flow condition, see Figure 21. This suggests that as the length scale increases, the change in velocity due to turbulence can be increasingly treated as quasi-static. Hillier & Cherry (1981) also conducted significant research in this area and their results agreed well with the findings of Melbourne (1993). The work conducted by Li & Melbourne (1999) and Saathoff (1988) is however one of the most comprehensive in studying the individual influence of length scale and intensity on surface pressure fluctuations. Though the results from studying the effect of turbulence on bluff bodies offer valuable information relevant to flow-fields required to test MAV airfoils, the results are not directly applicable since a number of other factors like AOA also need to be considered in the latter case.

Experiments that are of most relevance to testing MAV airfoils or wings in turbulence are that conducted by Cruz et al (2007) and Loxton et al (2009). Cruz conducted a series of tests on a Clark Y airfoil and thin flat plate wing to measure airfoil and wing performance in various levels of turbulence within Reynolds number range of 70,000 to 120,000. The flat plate airfoil was similar to the one Mueller (1999) used for his low Reynolds number smooth flow experiments. By placing grids within a large test

section, Cruz generated different levels of turbulence with highest intensity of around 13% and 0.3m stream-wise length scale. A thin flat plate wing, of AR= 2, was placed over a reflection plane and pressures along the chord at one spanwise location were measured. The experimental setup is presented in Figure 22. Results from Cruz's experiments indicated that similar to high Reynolds number cases studied by wind engineers, the stall angle was considerably higher in turbulence as opposed to smooth flow. Though the experiments conducted by Cruz were extremely relevant to testing MAV airfoils and wings in turbulence, there were still some short comings in that only time-averaged behavior of the airfoils and wings were studied. There exist a number of transient phenomena that occur over the airfoil or wing surface in turbulence as seen in the work of Swalwell, Melbourne, Hillier, Cherry, etc. on bluff bodies immersed in turbulence. Since the focus of the work described later in this thesis is MAV transient aerodynamics, it is important to take time-varying measurements of the flow over the wing/airfoil in order compare and understand the salient flow features that develop in smooth and turbulent conditions.

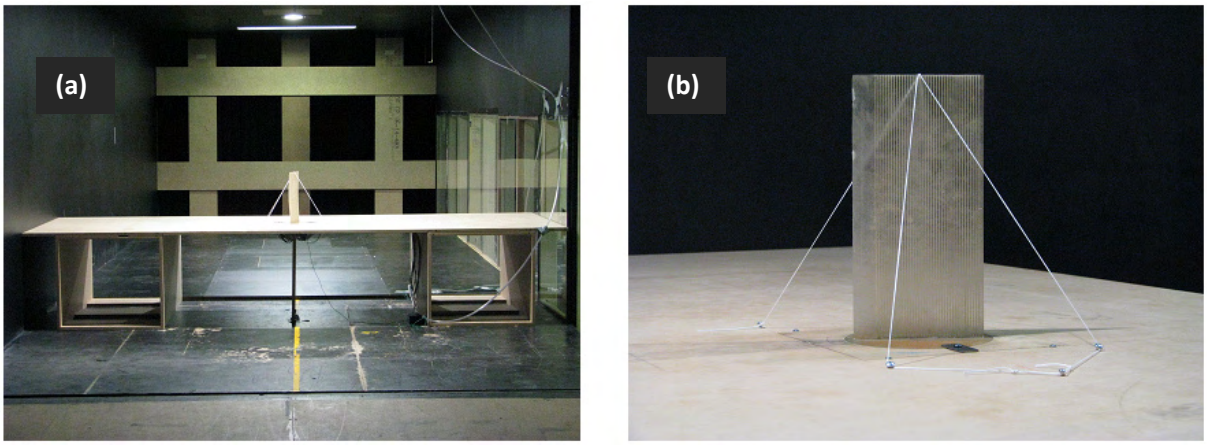

Figure 22: (a) Wing with AR=2 and thin flat plate airfoil section placed on reflective mount upstream of grids within RMIT wind tunnel. (b) Close-up view of the wing and guy wires. Loxton et al (2009)

Loxton et al (2009) measured the time-varying surface pressure fluctuations over the same flat plate airfoil used by Cruz. Loxton also used the same setup as Cruz, seen in Figure 22. The time-averaged results on wing performance agreed well with Cruz's findings however, a substantially higher change in wing performance between smooth and turbulent flow was noticed in Loxton's results. Time-varying flow features like formation, bursting and shedding of the LSB were also identified through Loxton's

research. The experiments conducted by Loxton were however only limited to three turbulence conditions i.e. Ti=1.6% (smooth flow), Ti=7.2% Streamwise Length Scale (Lxx) =0.23m and Ti=13.2% Lxx=0.3m. As both length scale as well as turbulence intensity changed considerably in all three testing conditions, it is difficult to point out the specific influences of each on the wing performance. Apart from that, due to lack of knowledge about airfoil and wing performance in turbulence it is also difficult to disassociate the influence of flow three dimensionality arising from wingtips, on flow over the wing and hence its influence on performance.

Except for the research aforementioned, there has not been any significant work that has been carried out in understanding airfoil performance at low Reynolds number in turbulent flows**.** Though a few experiments have been conducted on the wing performance in turbulence, they are no more than a starting point since a complete picture has not yet emerged in terms of the individual influences of each aspect of turbulence on flow over the wing/airfoil. Airfoil testing should therefore be conducted in smooth and turbulent conditions while taking time-varying data. The airfoil tests must be conducted in facilities where a number of length scales as well as intensities can be generated with control over both such that from the results the influences of either can be understood. Unlike in previous studies conducted by Loxton and Cruz, measurement locations must also be well away from the walls to ensure no distortion of turbulence eddies from flow-wall interactions.

1.6 A Discussion on Existing Literature

Micro Air Vehicles will be exposed to relatively unsteady and turbulent flow-fields that occur within the atmospheric boundary layer on days when substantial wind is present. With potential benefits offered by UAVs and MAVs, there is a real necessity to make them flyable in such conditions. Interest in the performance of wings and airfoils within a turbulent environment has been relatively limited partly due to limited use of MAVs. However, with increasing applications for MAVs in military and civilian missions, a thorough understanding of airfoil and wing performance in flow-fields typically experienced by MAVs is required.

Through contributions from various workers, suitable metrics to quantify turbulence within the ABL in terms of its intensity and scale have been developed. The Turbulence Intensity (Ti) quantifies the

turbulent energy within the flow through the ratio between the Std.Dev and mean of the oncoming flow velocity. The integral length scale provides insight on the manifestation of the turbulent energy through a measure of the average size of the largest turbulent eddy present within the flow. Flow-field measurements within the ABL have revealed that turbulence intensity over 30% can be present while length scales range from a few feet to many tens of meters. It was also identified that a MAV in flight would perceive a smaller Ti due to its mean velocity through a turbulent field while the fluctuations induced by the longest length scales can be treated at quasi-static. Therefore the length scales that would potentially have maximum influence would be of the order of typical MAV chord lengths.

Conducting experiments in order to gauge airfoil performance in turbulence via outdoor measurement were deemed unsuitable primarily due to the inconsistency and uncontrollability of atmospheric flow. Controlled replication of turbulence present in the ABL within a wind tunnel was required to perform airfoil testing. For the range of turbulence intensities and length scales required for MAV airfoil testing, passive grid generated turbulence proved to be suitable. A number of workers adopted this method for testing airfoil and wing performance over a range of Reynolds numbers with good success.

MAVs are exposed to complex influences of low Reynolds number flows as well as turbulence. Airfoil testing at low Reynolds numbers in nominally smooth conditions revealed that the flow over the airfoil in this flow regime was considerable different compared to that at higher Reynolds numbers. Flow separation from airfoil surface occurred while still being laminar (i.e. laminar separation). The separated shear layer later undergoes transition and reattaches downstream over the airfoil as a turbulent boundary layer, forming a LSB between the points of separation and reattachment. The presence of LSBs has a significant influence on the pressures and forces over the airfoil. Therefore, airfoils that performed well at higher Reynolds numbers were found to be inefficient in this flow regime due to influences of LSBs and other phenomena like hysteresis and premature stall. While reasonable interest on the structure and behavior of LSBs in smooth flow has been present, the properties and influence on the time-varying surface pressures and forces over the airfoil and on overall performance is still unclear.

Limited experiments have been conducted in assessing airfoil performance in turbulence in the Reynolds number range that is relevant for MAVs. Experiments on bluff bodies, like blunt flat plates, subjected to higher levels of turbulence have however been conducted by wind-engineers for many decades. The results are more relevant to aerodynamics of large buildings and bridges. A distinct reduction in LSB size over bluff bodies was noticed at higher turbulence intensities along with an increase in the peak suction. Increase in turbulence integral length scale resulted in the pressure distribution over the blunt flat plate

to have closer resemblance to that present in smoother flow conditions. This confirmed that the fluctuations induced at longer length scales can be treated as quasi-steady changes in flow. Airfoil testing in turbulence at higher Reynolds numbers revealed that a delay in airfoil stall occurs and an increase in CLmax was also observed. However, these experiments did not involve the controlled variation of length scale and intensity hence the results consisted of an intermingled influence of both. An understanding of the individual influence of turbulence intensity and length scale is however required to fully understand the influence of turbulence on flow over the airfoil and on its overall performance. Identification and comparison of various salient flow features that develop over typical MAV airfoils when subjected to nominally smooth and turbulent flow of varying length scale and intensity is also required.

1.7 Thesis Aims, Scope and Specific Objectives

From the review of literature it may be deduced that there exists significant gaps in the current body of knowledge. These gaps are particularly in the area of turbulence and its influence on the flow over the airfoil and airfoil performance. Therefore, this research aims to shed more light on the influence of both low Reynolds number effects and turbulence on the time-averaged and time-varying performance of airfoils. The focus of this work would be on obtaining an understanding of the high-energy low-frequency fluctuations that occur over airfoils when subjected to elevated levels of freestream turbulence. This would be accomplished by finding suitable answers for the following research questions, which were devised to form a guide to the research whilst highlighting the key deliverables. The key research questions are;

1) How do the time-averaged and time-varying surface pressures over the airfoil change between smooth and turbulent flows?

2) What are the salient flow features that develop over the airfoil in smooth and turbulent conditions, in particular the LSB?

3) How does the airfoil performance change in turbulence and what is the specific influence of turbulence intensity and integral length scale on the same?

4) How well do upstream velocity fluctuations correlate with surface pressure and lift fluctuations and could upstream velocity measurements could be used as a control input to attain steady level flight?

Suitable answer for these questions would be obtained by measuring the time-varying surface pressures over an airfoil that may be held as a representative of a typical MAV airfoil. The individual influence of turbulence intensity and length scale would be identified by conducting airfoil testing in various turbulence conditions whereby the integral length scale will be varied while keeping the turbulence intensity nominally constant and vice-versa. Airfoil surface pressures would be measured at various spanwise and chordwise stations simultaneously to investigate the time-varying influence of turbulence over the airfoil chord and span. Velocity measurements and flow visualizations will also be conducted to augment the pressure data.

The scope of this research will be limited to experimental work since it is considered that CFD does not yet appear to be sufficiently accurate in replicating small scale atmospheric turbulence and subsequent effects on airfoils at low Reynolds numbers. Since airfoil testing conducted in outdoor atmospheric turbulence are neither controlled nor repeatable, the focus of this work will be limited to testing in replicated passive grid-generated turbulence within wind tunnels. While an infinite number of turbulence intensity and length scale combinations can experienced in the outdoor environment, this research is limited to a few representative turbulence conditions.

CHAPTER 2

Experimental Setup and Instrumentation

In this section the experimental setup along with the instrumentation used to obtain answers for the specific research questions will be described. Firstly, the experimental setup and the airfoil selection process along with details on its manufacturing technique will be presented. It will be followed by an account of the methodology adopted for turbulence generation. It was desirable to obtain a range of turbulence intensities (starting from smooth conditions) and a range of length scales to enable identification of the individual influence of turbulence properties on airfoil performance. A detailed analysis of the different levels and scales of turbulence generated will be presented in the subsequent sections. The characteristics and operational limits of the experiment setup and instrumentation will also be addressed to provide confidence in the data gathered.

2.1 Airfoil

2.1.1 Airfoil Selection

As it would be unrealistic to conduct experiments on all airfoils that would potentially be used for MAVs, a suitable representative airfoil was chosen. Airfoils used in the construction of model airplanes might suit as a good representation of MAV airfoils since model airplanes also fly in similar flight regime. However, given that the airfoil was to be exposed to the combined influences of low Reynolds number effects as well as turbulence, it was important that prior work had been conducted using the airfoil section to form a suitable validation of results. After giving due considerations to various airfoils (e.g. Clark Y, NACA 4 series, etc) the thin flat plate airfoil section, studied by Mueller (1999), was chosen. The

performance of this airfoil in smooth flow conditions has been documented in detail by Mueller (1999) through force measurements. Previous research has also been conducted using this airfoil section within RMIT where Loxton et al (2009) and Cruz et al (2007, 2008) had studied the influence of turbulence on low aspect ratio wings with a similar airfoil section**.**

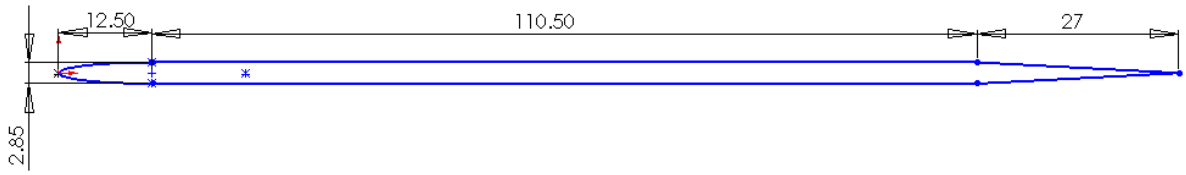

Figure 23: Side view of airfoil section with dimensions in mm.

The airfoil was a non-cambered flat plate and consisted of an elliptical Leading Edge (LE) with a tapered trailing edge. The airfoil had a maximum thickness of 1.9% of chord. A side view of airfoil section is presented in Figure 23. The chord was chosen to be 150mm and was kept constant for all tests. This chord length was found to be most suitable as any smaller would be difficult to place integral pressure channels for pressure measurements, and any larger would require very low velocities to attain the desired Reynolds numbers. To conduct a truly 2D experiment within an unsteady 3D turbulent flow, it was desirable for the airfoil to span the wind-tunnel test section width. However, due to practical reasons this was not possible since very large test sections were required to generate freestream turbulence with long integral length scales. Hence, it was important for the end plates to be as distant as possible to remove end effects. The span was therefore chosen to be at least three times the size of the largest integral length scale (turbulent eddy) in the spanwise direction (see later subsections for details on length of the largest turbulence eddy generated). This resulted in a total span of 900mm, yielding an aspect ratio of 6. This aspect ratio was much larger than the AR used Loxton et al (2009), Sicot et al (2006) and Stack (1931) and it was similar to the AR used by Swalwell (2005) and Jancauskas (1983). For each testing condition, exhaustive calibration was conducted to ensure a reasonably flat velocity and consistent turbulence profile was present over the airfoil location. Results of the calibrations conducted will be presented later in this chapter.

2.1.2 Pressure Tap Location

The rolling moments experienced due to time-varying changes in local pitch angle, as well as ascertaining the scale of three dimensionality of flow over the airfoil in turbulence is of interest here. Taking measurements of pressure fluctuations at two spanwise locations simultaneously would reveal the extent of the three dimensionality of the flow. Integrating the instantaneous pressure distribution over the airfoil chord would result in local lift distributions at the two spanwise stations, from which instantaneous moments could be computed.

Simultaneously pressure measurements were taken at mid-span and 50mm to the right of centerline, viewing from upstream of airfoil. In subsequent experiments, pressure fluctuations were simultaneously measured at 100mm to the left and 100mm right of airfoil mid-span.

A total of 20 pressure taps were placed along the chord at each spanwise measuring location. Each pressure tap consisted of a circular hole on the airfoil surface of 1mm diameter, leading to a pressure channel embedded within the airfoil. Pressure channels started from the pressure tap and terminated at the root of the airfoil. These channels were hollow tubes of 1mm diameter embedded into the airfoil. A CAD model of the airfoil with pressure taps is presented in Figure 24 to assist in visualizing the measuring locations, pressure taps and pressure channel layout.

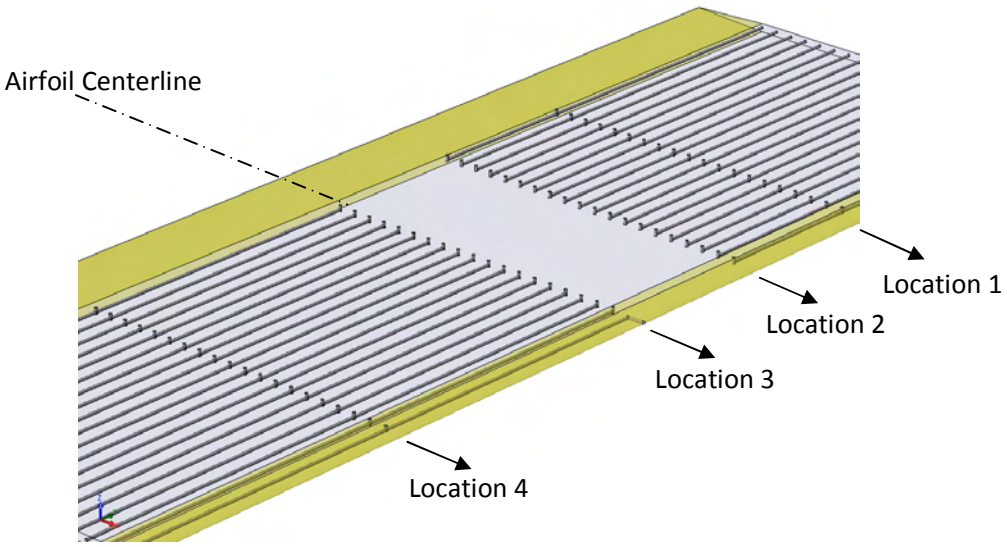

Figure 24: Airfoil section showing the pressures taps and pressure measuring location. Only the central 300mm of the airfoil is presented in this figure

Pressure channels ran from Location 1 and 2 to the right of airfoil, while the channels from Location 3&4 ran to the other end, see Figure 24. This way, tubing length (which has a significant effect on the amplitude and phase response of the tubing system, see later subsections) was kept as short as possible. The first pressure tap at Location 3 was placed exactly on the leading edge of the airfoil and remaining 19 pressure taps started 12mm from LE and were spaced at 6mm inter-tap separations. Therefore the last pressure tap was located 30mm from trailing edge. However for Locations 1&2, all 20 taps were placed at 6mm inter-tap spacing starting 9mm from the LE. Hence the last tap for locations 1&2 was 27mm from trailing edge. A 3mm chordwise offset between pressure taps in Location 1&2 and 3&4 was therefore present. This manner of pressure tap distribution was adopted to ensure pressures over a wider area of the airfoil were interrogated while enabling relative comparisons between different spanwise locations. It was not possible to place pressure taps any closer to the trailing edge due to very small thickness close to the trailing edge.

PVC tubing of 1mm internal diameter was then attached from the end of pressure channels at the airfoil roots, leading to the pressure transducers. To keep constant tubing parameters and obtain best amplitude and phase response, it was important that a constant tube diameter was present, 1mm in this case. The dynamic properties of the tubing system along with the corrections employed to obtain flat frequency response, will be presented in later sub-sections.

Pressure fluctuations were first measured at Location 2&3 by sealing the pressure taps at Locations 1&4. Sealing was necessary because each pressure channel was shared by 2 taps. Taps in Locations 1&2 shared channels on one side while taps at Locations 3&4 shared the channels on the other side, see Figure 24. For the second set of tests, pressure taps at Location 2&3 were sealed, while 1&4 were active for pressure measurement. This implied that whenever pressure measurements were taken at Locations 1&4, 50mm and 100mm of redundant tubing was present respectively as the pressure taps were not located at the end of the channels. Sensitivity studies showed that since the length of this redundant section was much smaller compared to overall tubing length, its influence was quite small. Elaboration on this can be found in Appendix C.

No pressure taps were placed on the underside of the airfoil. Previous research indicated (Cruz et al (2008), Loxton et al (2009)) that pressures on top surface had a governing influence on airfoil performance because of the formation and influences of LSBs, which is of particular importance here. Therefore, to make best use of the available pressure transducers, all pressure measurements were

made on one side of the airfoil. To understand flow structure on the pressure side of the airfoil, the airfoil was inverted to a negative AOA.

2.1.3 Airfoil Fabrication

Having decided on the airfoil section and sized the same, various methods of manufacturing the airfoil were explored. CNC machining the airfoil was not possible as the thickness was very small and it was not possible to drill the pressure channels within. Cutting the airfoil out of foam was also contemplated but with little success as the surface finish was not good and placing the integral pressure taps was very difficult. A stereo lithography technique of rapid prototyping was found to be the most suitable method and a rapid prototyping machine was used to manufacture the airfoil. In this method the model was constructed layer by layer over a platform that kept sinking within a reservoir containing a resin that cured under UV light. A moving head emitted UV rays and cured the resin forming a new layer over the old one, slowly building the model layer by layer. Each layer was of the order of 0.15microns thick with an accuracy of 98%. Refer Figure 25 for schematic of manufacturing technique.

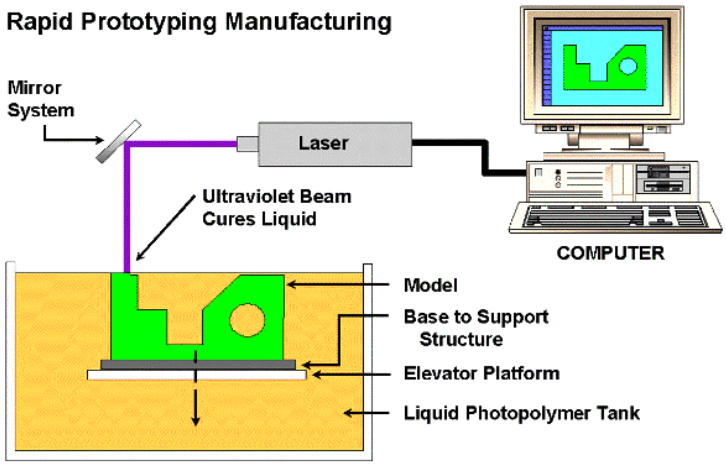

Figure 25: Schematic showing the process of stereo lithography method of rapid prototyping. From, www.rpc.msoe.edu/cbm/about/sla.php, (last accessed: 01/02/2011)

Using this method it was possible to manufacture the airfoil complete with integral pressure taps and channels in a very timely and low cost manner. However, issues with using this stereo lithography technique included problems of "stair-stepping" and structural rigidity. As the model was constructed layer by layer with each layer 15microns thick, the finished airfoil had a slightly coarse finish. Hence the airfoil was sanded down carefully to yield a smooth surface. After sanding, the final thickness of the airfoil was 2.85mm. The machine also had a maximum length limit of 300mm. Since the total span required was 900mm, three airfoils were fabricated individually and then glued together to create the 900mm span airfoil. At the mating ends of the airfoil sections, small adapters were used to ensure a snug and leak-proof bond when the airfoils were glued together. Excess glue at the mating ends of the airfoil sections was wiped and then sanded down to ensure a smooth surface finish.

The UV curing resin used as material for construction was relatively soft and lost most of its rigidity at temperatures over 50Deg Celsius. For this reason, another 20 channels were placed between the channels required for pressure measurement. Steel stiffening rods were placed within the redundant channels to further stiffen the structure. Other precautions, like keeping the airfoil away from direct sunlight and ensuring the airfoil was always placed on a perfectly level surface, were taken to prevent the airfoil from distorting. A photo of the final airfoil is presented in Figure 26.

To ensure a leak proof system and to investigate the dynamic tubing/transducer response, detailed leak check and dynamic tests were conducted**.** Two methods of testing were employed, details of both these methods of testing are available in Appendix C.

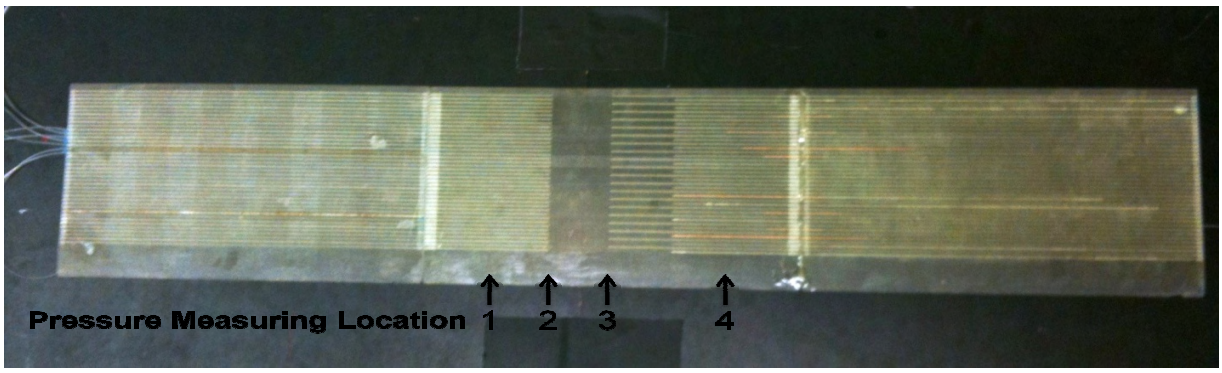

Figure 26: Photograph of the final airfoil with a few PVC tubes attached and some of the reinforcing steel rods placed inside the redundant channels.

2.2 Airfoil Mount

A standalone airfoil mount was designed for easier mobility because different wind tunnel facilities were used in this research. Circular end plates were placed at either ends of the airfoil, to enable pitching about center chord. These circular end plates in turn were fitted into removable rectangular sections that fitted into the walls of the airfoil mount. The airfoil mount consisted of an open-roofed "box" with slots to fit the rectangular sections that housed the airfoil. On one side of the airfoil mount the circular end plate and the rectangular housing were made of transparent Perspex to serve as a chordwise viewing window. Relatively thin horizontal slats were placed on the top of the mount to increase structural rigidity and avoid vibrations when exposed to turbulent flows. To keep the airfoil out of ground-effect, the airfoil was located three chord lengths above the base of the mount and from previous ground-effect research this was found to be a sufficiently well removed distance, Ravi (2007). Side walls of the mount extended to three chord lengths above airfoil location and four chord lengths to the rear of the airfoil to achieve a nominally two dimensional flow around the airfoil, see Figure 27.

In order to reduce the influence of the airfoil mount walls on the oncoming turbulent eddies, the airfoil was placed such that the Leading Edge (LE) was just 70mm from the front edge of the mount. In this setup, it was considered that the turbulent eddies should "impinge" the airfoil well before being significantly influenced by the boundaries of the supporting structure. The pressure measuring locations were also well away from possible separations originating from the front edge of the mount. Whilst the airfoil was made out of a relatively soft material but stiffened by steel rods, it was still found to exhibit slight movement when exposed to high turbulence intensities. Hence, the airfoil was guyed to prevent motion in the vertical axis using high strength Kevlar thread. This was done at three locations over the airfoil span, all these locations were well away from influencing pressure fluctuations at measuring locations, refer Appendix B.

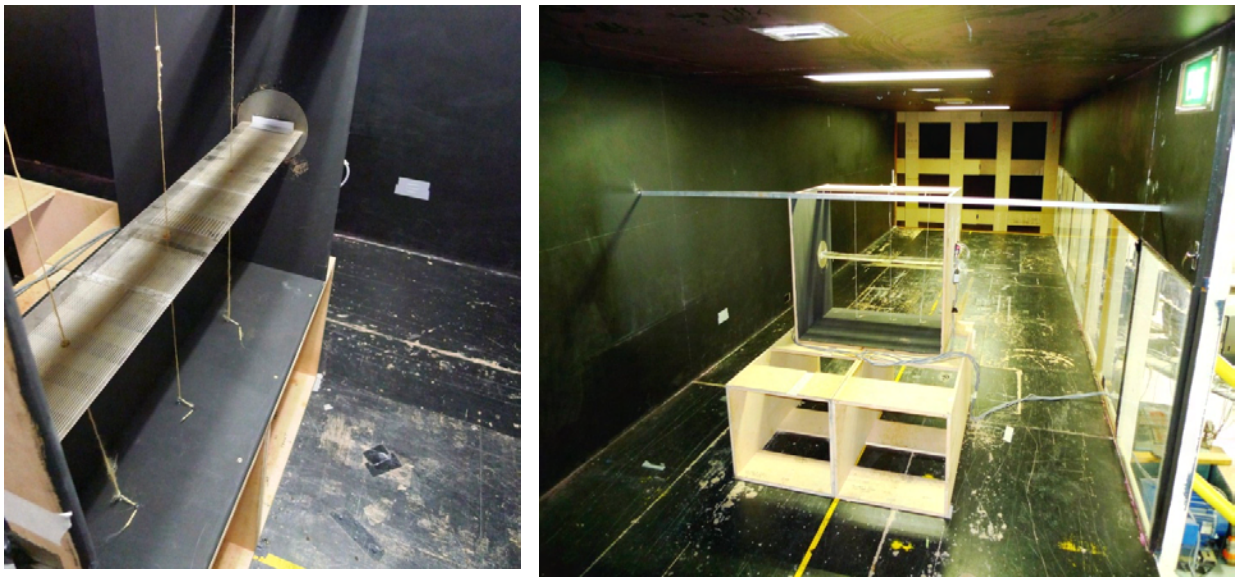

Figure 27: Photographs showing airfoil within the mount along with the guy wires placed to increase structural rigidity and reduce vibrations.

To keep away from boundary layer effects originating from the walls of the wind-tunnel, the airfoil mount was placed over an elevated plane. This also ensured that the airfoil was as close to tunnel centerline as possible, such that the oncoming flow consisted of well-mixed turbulence and away from wall effects. The plastic tubing from the airfoil root was then attached to modules into which pressure transducers were embedded. Once all plumbing was complete and all components firmly restrained, the setup was ready for testing.

2.3 Wind Tunnels & Turbulence Properties

To develop turbulence of different length scales and intensities, three wind tunnel facilities were used viz. RMIT's Industrial Wind Tunnel (IWT), Monash University Wind Tunnel and RMIT Aerodynamics Wind Tunnel. This sub-section details the attributes of the various wind tunnels along with the grids used to generate the turbulence required for testing. Properties of turbulence generated are also presented and discussed.

2.3.1 RMIT Industrial Wind Tunnel (IWT)

RMIT's IWT is a closed-jet wind tunnel, with a test section measuring 2m high, 3m wide and 9m long. A 2:1 contraction is present just upstream of the test section, after a small settling chamber. The wind tunnel schematic is presented in Figure 28. The tunnel is powered by a 225KW Thyristor-controlled DC motor onto which a 6 blade impeller is attached along with 7 flow straightening vanes just upstream of the impeller. The tunnel had very low noise (Vino (2005), Pagliarella (2009)) as it consisted of anechoic turning vanes. Airflow velocity within the test section was changed using the impeller rpm controller, located in the control room. A top speed of 50m/s could be achieved within the test section, however for the current low Reynolds number experiments the maximum testing velocity was only 10m/s. The tunnel was equipped with a MKS differential pressure measuring system, onto which a Pitot-static tube can be connected to interrogate and thus calibrate flow speed at different locations within the test section. The majority of the experiments in this research were conducted within this wind tunnel. By placing grids of different geometric properties at various locations within the wind tunnel, numerous levels and scales of turbulence were generated. These are described in the next four sub-sections.

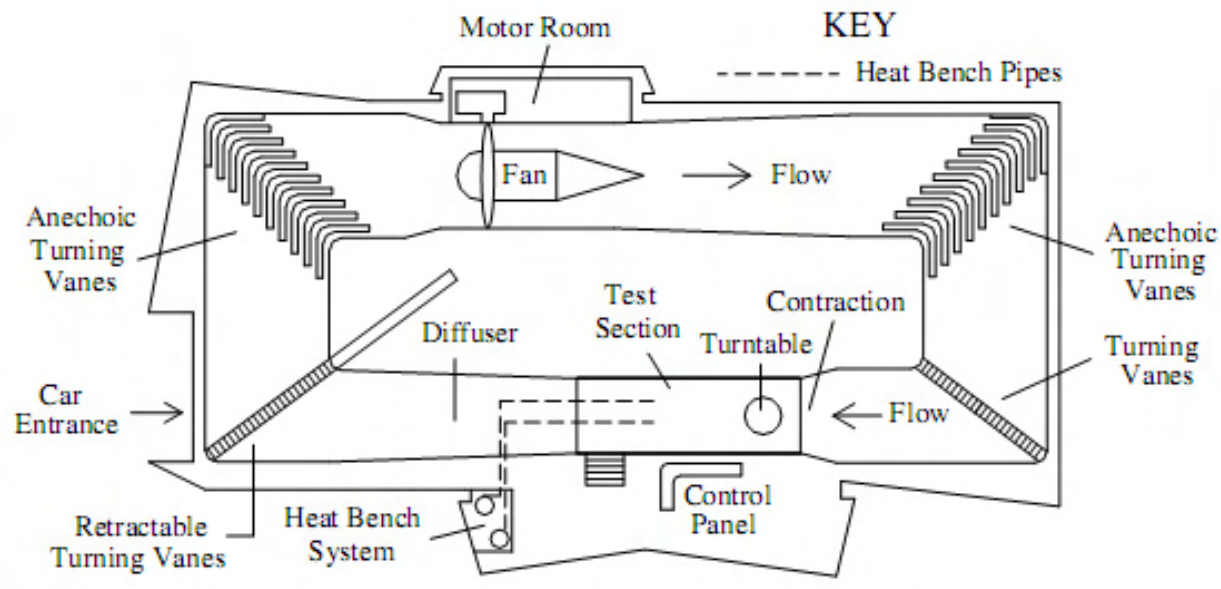

Figure 28: Schematic showing the different sections of the RMIT IWT.

2.3.1.1 Clean Tunnel

In the clean configuration, i.e. without any turbulence generating grids present, the turbulence intensity within the testing chamber was measured to be 1.5% along the tunnel centerline. This was estimated by taking velocity fluctuations in all three orthogonal directions at different points along the test section. Velocity measurements were made using both Pitot-static tubes (for time-averaged measurements) and multi-hole pressure sensitive probes (Cobra Probe for time-varying measurements), more information on the velocity measuring probes and associated data processing will follow later in this chapter. In order to allow for well mixed flow, it was decided to setup the airfoil mount 7.75m downstream from test section inlet. Grusovin (2006) performed an initial calibration of the velocity distribution at this location and found a relatively flat velocity profile and consistent turbulence profile.

Once the airfoil mount was installed, calibrations were carried out to ensure that the presence of the setup did not have an adverse effect on the flow-field. Velocity measurements were taken on the plane of mid-chord of the airfoil at a number of spanwise points at: airfoil location, 100mm above and below the same. Once-again a flat velocity and relatively consistent turbulence profile of intensity 1.2% was noticed within the setup, as seen in Figure 29. Velocity measurements were taken at seven evenly spaced points along the three vertical stations (i.e. total of 21 points within an 800mmx200mm plane were interrogated) during the calibration exercise and it was held constant for the remaining turbulence conditions unless stated. Markers in Figure 29a are placed at locations where velocity measurements were made. To ascertain the influence of turbulence at such small levels, airfoil tests were carried out in the RMIT Aerodynamics Wind Tunnel where the Ti was still lower. More information on the latter tunnel is presented later in this chapter.

(a)

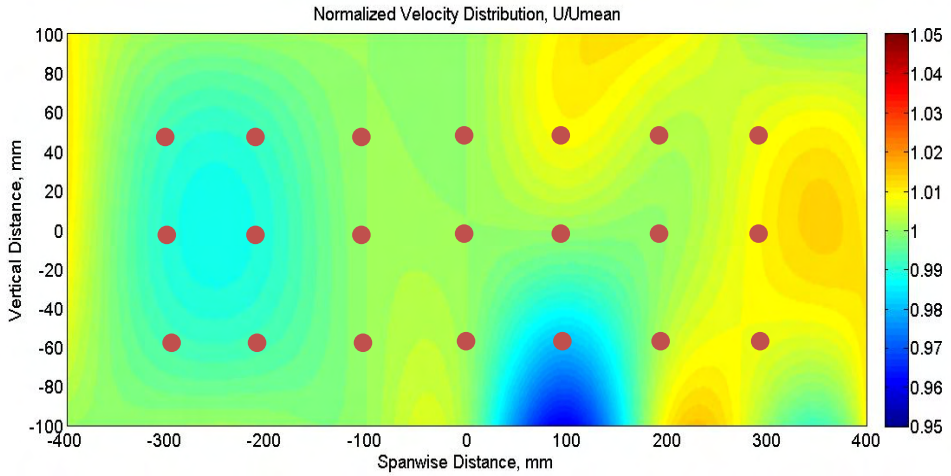

(b)

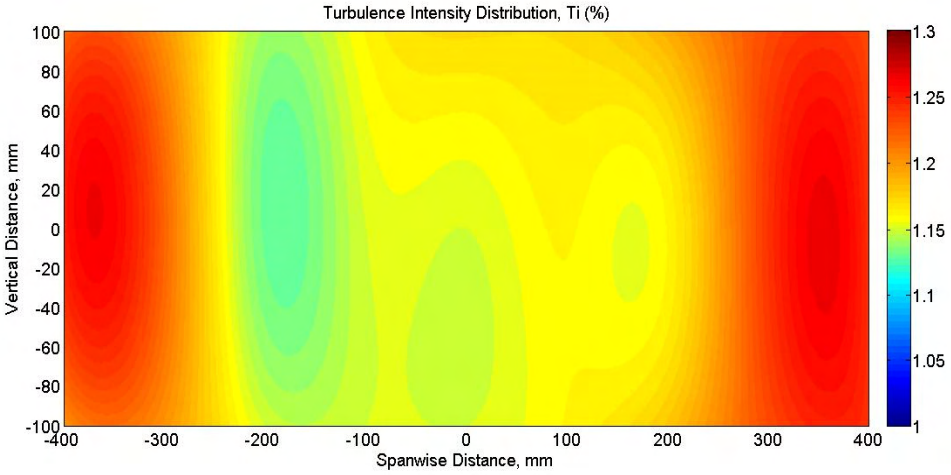

Figure 29: (a) Contour plot showing normalized velocity distribution within airfoil mount, U_{mean}=7 m/s. The markers indicate the locations where velocity measurements were taken. (b) Contour plot showing turbulence intensity distribution of approximately 1.2% within airfoil mount

As the airfoil was placed over a meter above the floor of test section, extensive tunnel boundary layer studies were not conducted. Any minor pitch angularity in the flow was corrected for by adjusting the CL vs. AOA curve of the airfoil, since the airfoil is symmetric, the CL at 0Deg AOA should be zero. It was found that the flow was nominally horizontal as the flow pitch angle was estimated to be around 0.3Deg at a tolerance of ±0.1Deg when the airfoil was held at 0Deg with respect to ground.

2.3.1.2 Grid at Inlet of Test Section

Grusovin (2006) designed planar grids that could be placed at the inlet of the test section in order to generate higher levels of freestream turbulence, see Figure 30. The grids consisted of horizontal and vertical panels made of 6mm thick chip-board with width 300mm and an inter-grid spacing of 600mm. As stated in literature, flow immediately downstream of the grid consisted of discreet jets and wakes originating from the panels. However, the turbulence became more homogenous with increasing distance downstream. It was hence vital that the testing location was as far downstream as possible to obtain consistently mixed turbulence.

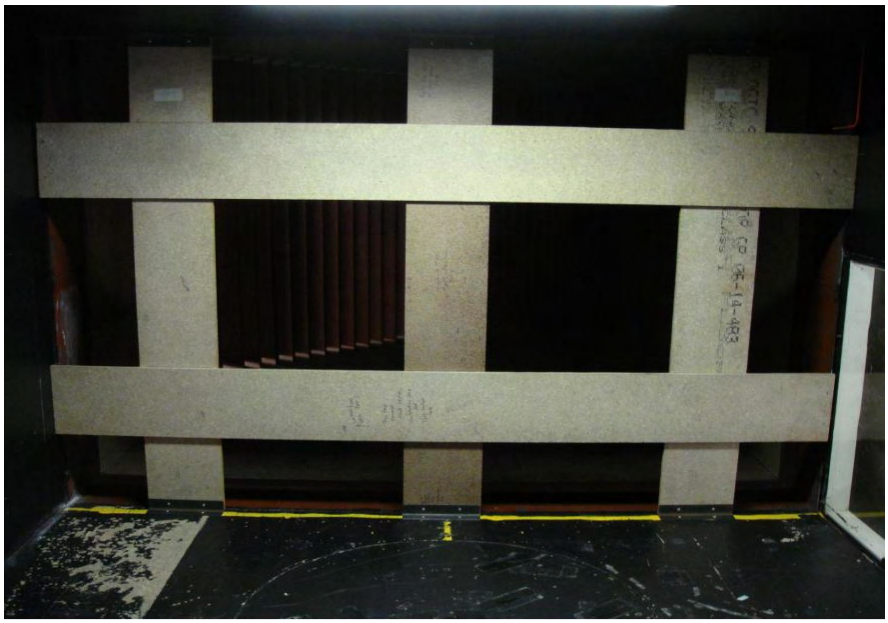

Figure 30: Photo of gird placed at inlet of test section with RMIT's IWT.

The velocity and turbulence properties were measured at different points downstream from the grids and Ti was found to decay nonlinearly, see Figure 31. At 7.75m downstream of the test section the overall turbulence intensity was found to be Ti = 12.9% with the integral length scales in the three orthogonal directions being Lxx=0.31m, Lxy=0.11m and Lxz=0.12m, these were consistent with the measurements made by Grusovin (2006). Further information on data processing is provided later in this chapter and Appendix E provides more information on the method adopted for integral length scale

estimation. Calibration of the plane, 7.75m downstream from the test section inlet, was also done by Grusovin (2006) and it revealed a nominally flat velocity profile as seen in Figure 32.

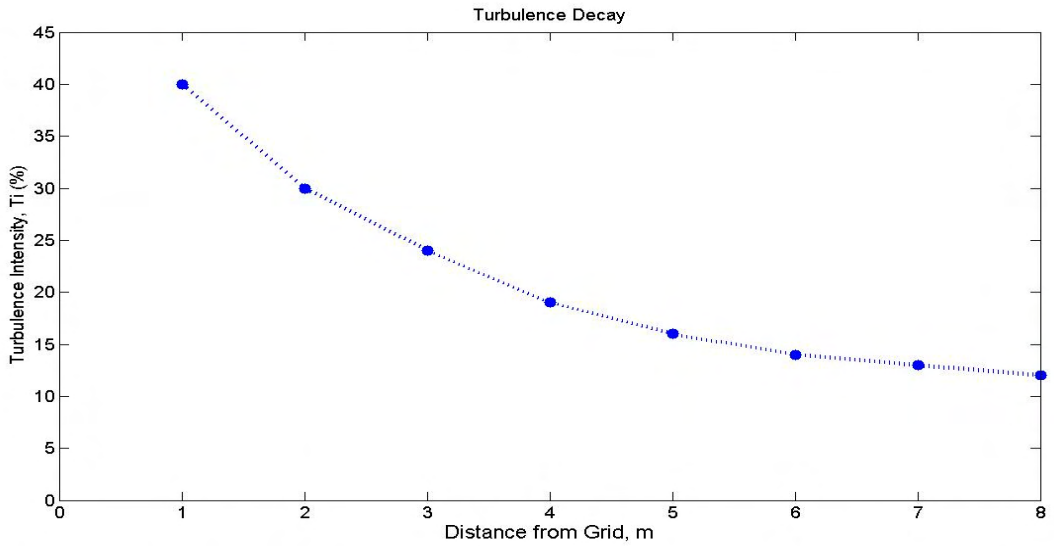

Figure 31: Plot showing decay of turbulence intensity as a function of downstream distance from grids

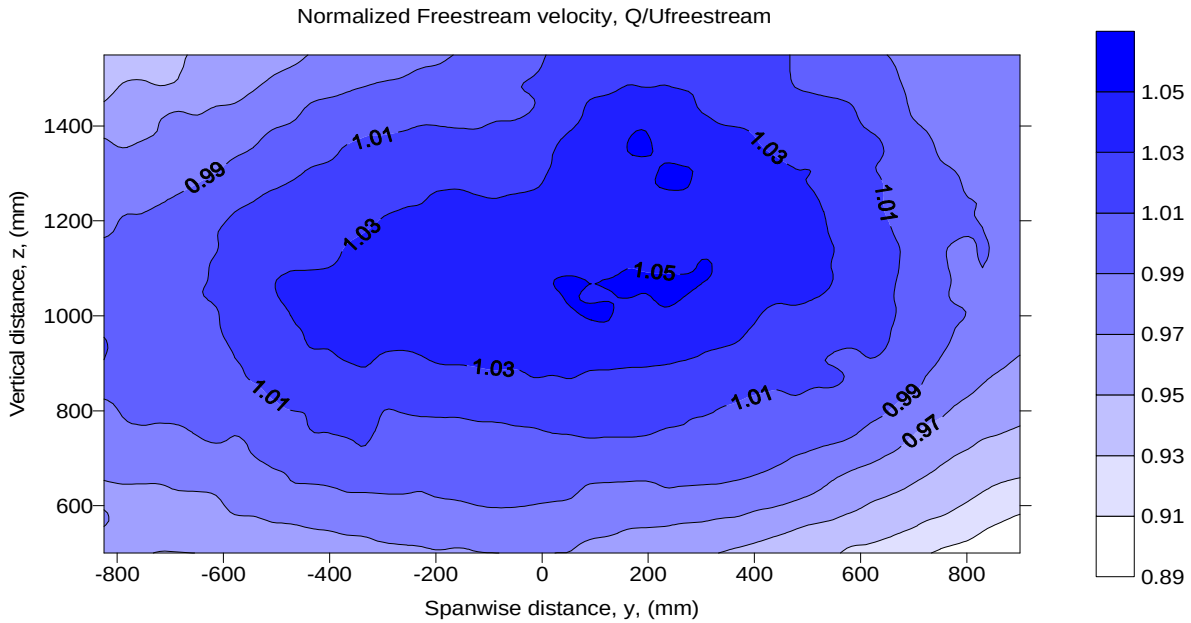

Figure 32: Contour plot showing velocity distribution at 7.75m downstream from grids Grusovin (2006)

(a)

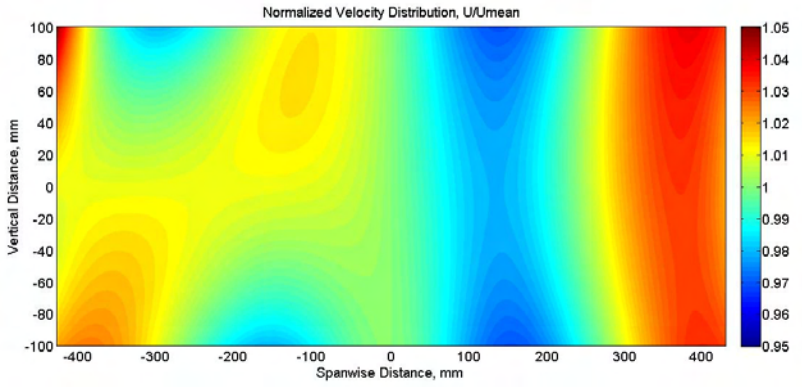

(b)

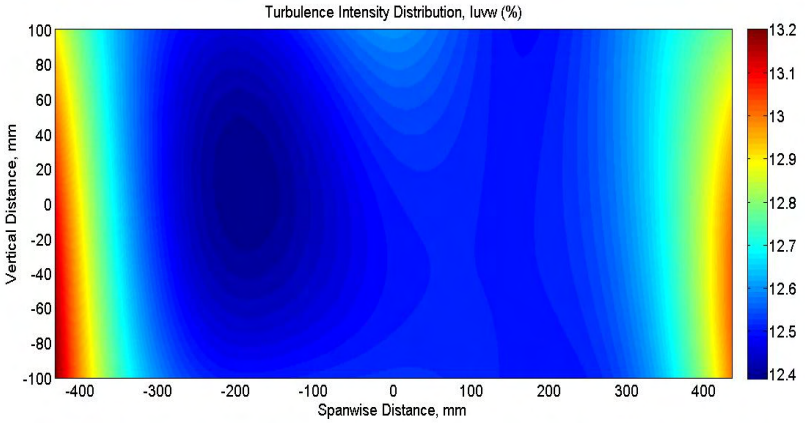

Figure 33: (a) Contour plot showing normalized velocity distribution within airfoil mount, U_{mean}= 7 m/s. (b) Contour plot showing turbulence intensity distribution within airfoil mount. For both figures, test location was 7.75m from test section inlet.

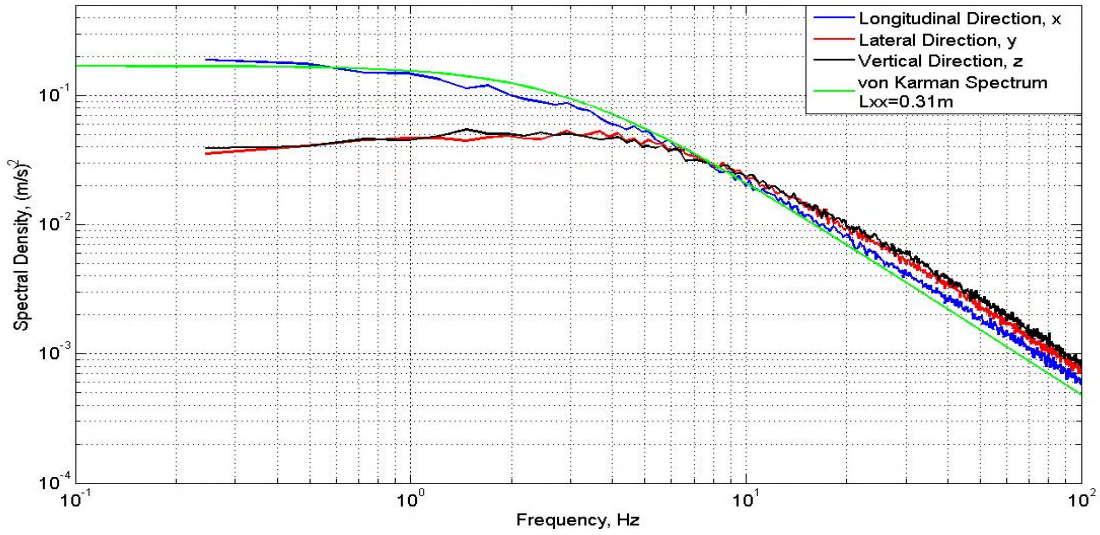

Figure 34: Power Spectral Density plot of velocity fluctuations in the three orthogonal directions measured at mid span location inside the airfoil mount located 7.75m downstream from Grid at inlet of test section. von Karman spectrum is also fitted to ascertain integral length scale.

The airfoil mount was placed 7.75m from the grids and a calibration routine similar to that performed for smooth flow condition was conducted here. As seen in Figure 33, the velocity and turbulence profiles were consistent. The turbulence intensity was measured to be around 12.6% inside the airfoil mount. The -5/3 slope of the PSD plot (Figure 34) indicates that the turbulence is well mixed and follows Kolmogrov's law of turbulence decay. Measurement of flow angularity in turbulence proved extremely difficult however, the time-averaged pitch angle was corrected for using the same method as for smooth flow condition. This angle was again found to be small i.e. <1Deg. As for yaw skewness of the flow, by visually ascertaining the time-averaged position of a moving wool tuft held in the flow, the angle was found to be negligibly small. This location was therefore chosen for conducting further experiments.

2.3.1.3 Grid at Inlet of Contraction

Cruz (2007) and Grusovin (2006) placed grids at the inlet of the contraction section of the wind tunnel, see Figure 35. These grids were made of same material, geometric properties and were thus a larger version of the grids placed at the inlet of test section. The flow was surveyed 1.2m above the ground, at different points along the test section. Figure 36 shows the turbulence intensity variation as a function of downstream distance.

Figure 35: Photo of the grids looking downstream facing its rear

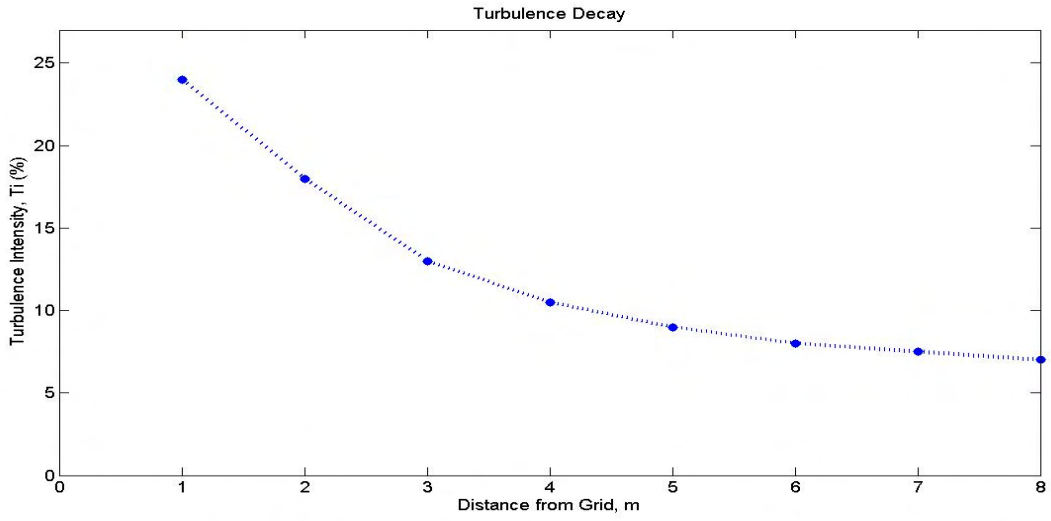

Figure 36: Plot showing decay of turbulence intensity as a function of downstream distance from test section inlet

From Figure 36, it can be seen that at around 3.5m downstream from test section inlet, the turbulence intensity was similar to that noticed 7.75m downstream when grids were placed at test section inlet. The setup however had to be moved slightly along the tunnel centerline and through trial and error it was determined that at 2.75m downstream of inlet, the turbulence intensity was closest to that

observed using the previous grids. A detailed survey of the flow at different locations within the airfoil mount was conducted. A Relatively flat velocity profile across the airfoil location was present, see Figure 37. Integral length scales measuring Lxx=0.15m, Lxy=0.10m, Lxz=0.09m and turbulence intensity of 12.3% was found consistent within the regions of interest (see Figure 38). While nominally similar turbulence intensity was present between this and the previous grid, the longitudinal length scale was only half. Pitch angle of the flow was found to be small and was corrected for as in previous cases, the flow appeared to be un-skewed in the yaw plane.

(a)

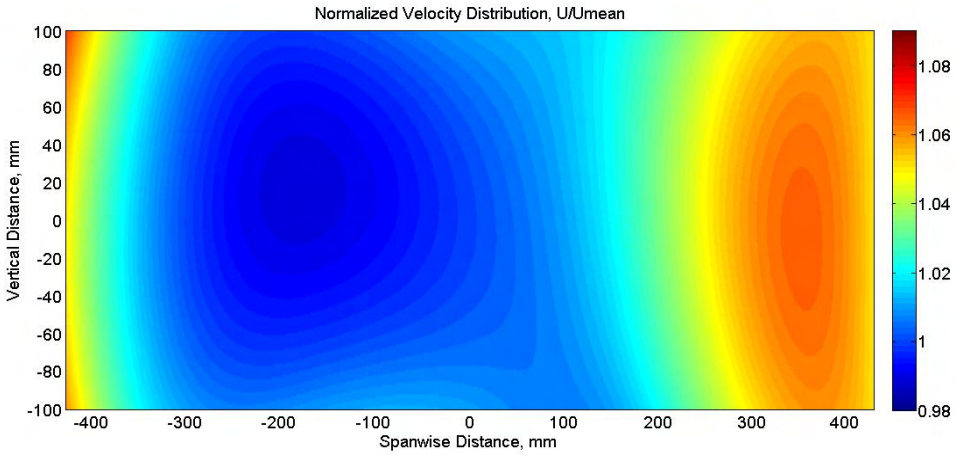

(b)

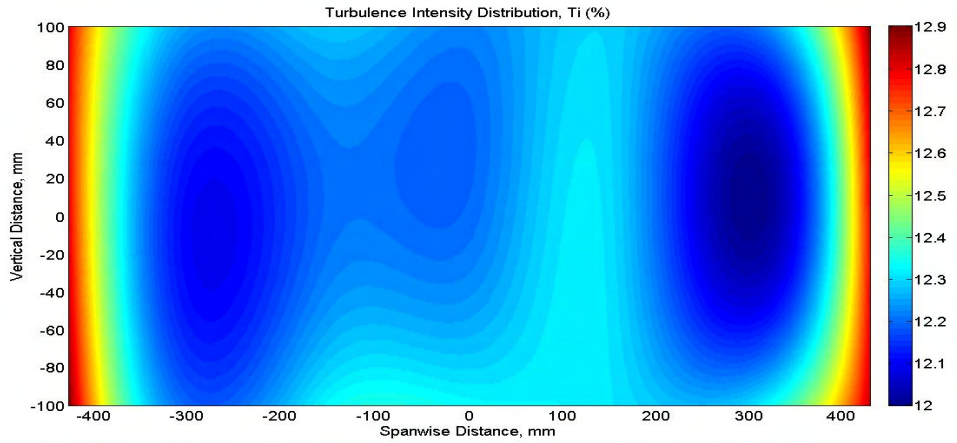

Figure 37: (a) Contour plot showing normalized velocity distribution within airfoil mount, U_{mean}= 7m/s. (b) Contour plot showing turbulence intensity distribution within airfoil mount. For both figures, test location was 2.75m from test section inlet for grids placed at inlet of contraction.

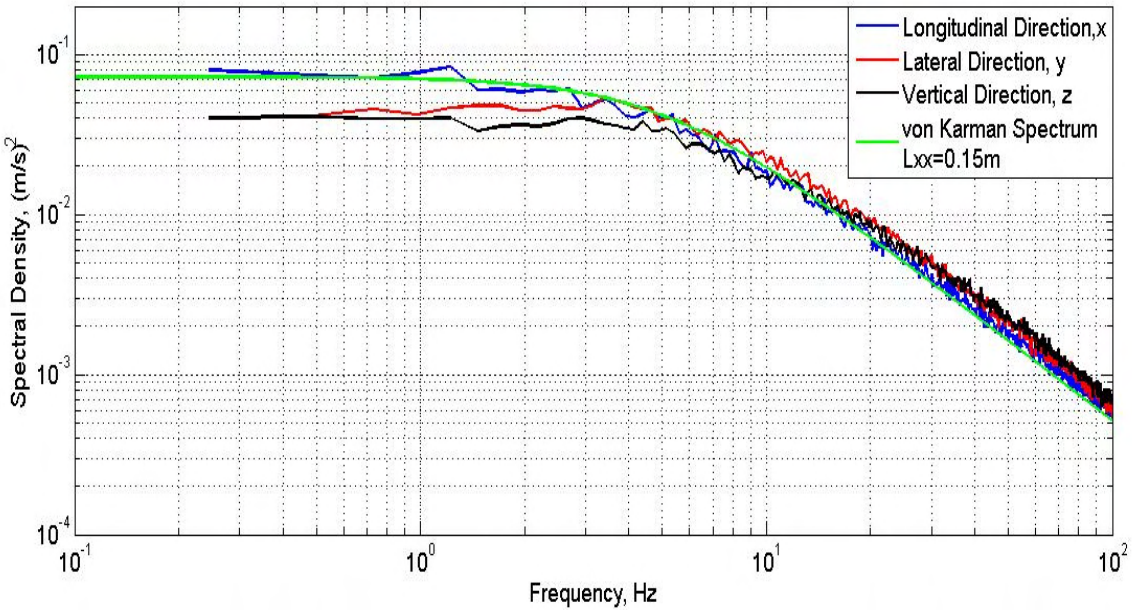

Figure 38: Power Spectral Density plot of velocity fluctuations in the three orthogonal directions measured at mid span location inside the airfoil mount located 2.75m downstream from Grid at inlet of contraction. von Karman spectrum is also fitted to ascertain streamwise integral length scale.

The flow-field 7.75m downstream from test section inlet with the current grid was also interrogated. As seen in the Figure 39, the results of the flow survey that was conducted within the airfoil mount showed that a nominally flat velocity profile and consistent turbulence intensity of 7.3% was present. The drop in turbulence intensity from 12.3% to 7.3% along the test section can be attributed to energy losses due to viscous interactions between the turbulence eddies, friction, etc. PSD plot of velocity fluctuations also exhibited the -5/3 slope indicating that the turbulence was well mixed, see Figure 40. Integral length scales were measured to be Lxx=0.22m, Lxy=0.13m and Lxz=0.11m (see Figure 40). Yaw and pitch angularity was found to be similar to the ones obtained 2.5m from inlet, appropriate corrections were therefore incorporated. Even though the length scales at this location was not similar to both of the previous turbulence conditions, this location offered another base turbulence condition to conduct further tests.

(a)

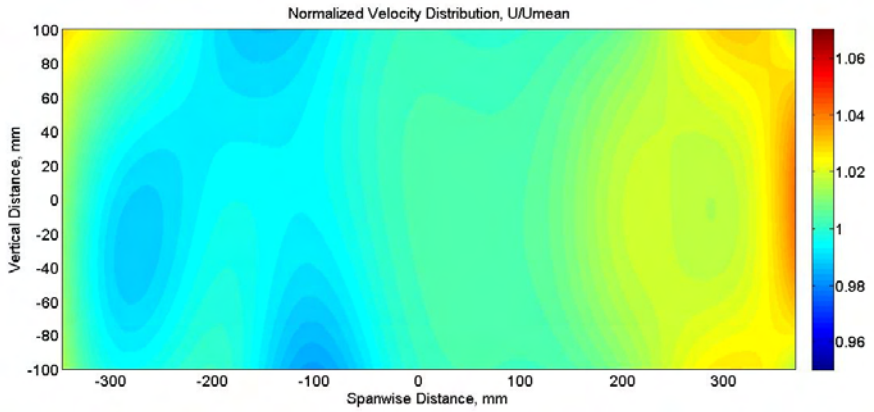

(b)

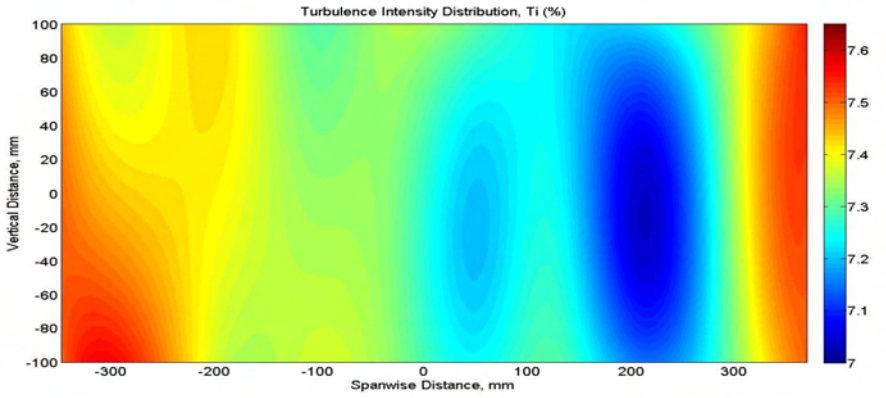

Figure 39: (a) Contour plot showing normalized velocity distribution within airfoil mount, U_{mean}= 7m/s. (b) Contour plot showing turbulence intensity distribution within airfoil mount. For both figures, test location was 7.75m from test section inlet for grids placed at inlet of contraction.

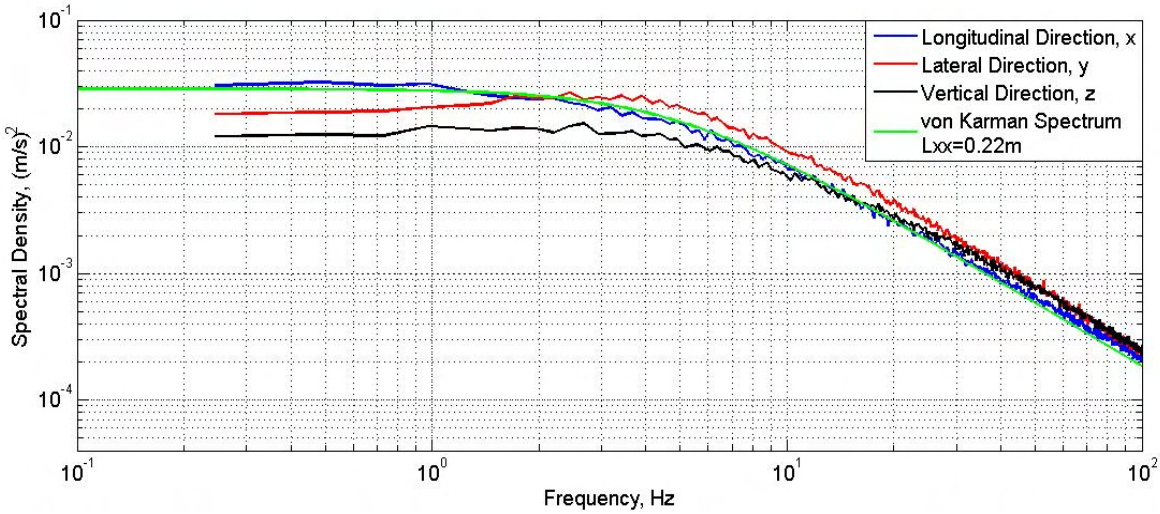

Figure 40: Power Spectral Density plot of velocity fluctuations in the three orthogonal directions measured at mid span location inside the airfoil mount located 7.75m downstream from Grid at inlet of contraction. von Karman spectrum is also fitted to ascertain streamwise integral length scale.

2.3.1.4 Finer Mesh Grid at Inlet of Test section

It was desirable to generate turbulence that would effectively form a link between the 12% and 7% turbulence intensities in terms of integral length scale comparison. The objective therefore was to generate turbulence of the same nominally 7% turbulence intensity but with integral length scale similar to either of the 12% intensity cases i.e. Lxx=0.15m or 0.31m. That way, influence of turbulence intensity on the airfoil's performance can be uncovered while the new turbulence length scale at 7% intensity offered another turbulence condition for validating the influence of length scale.

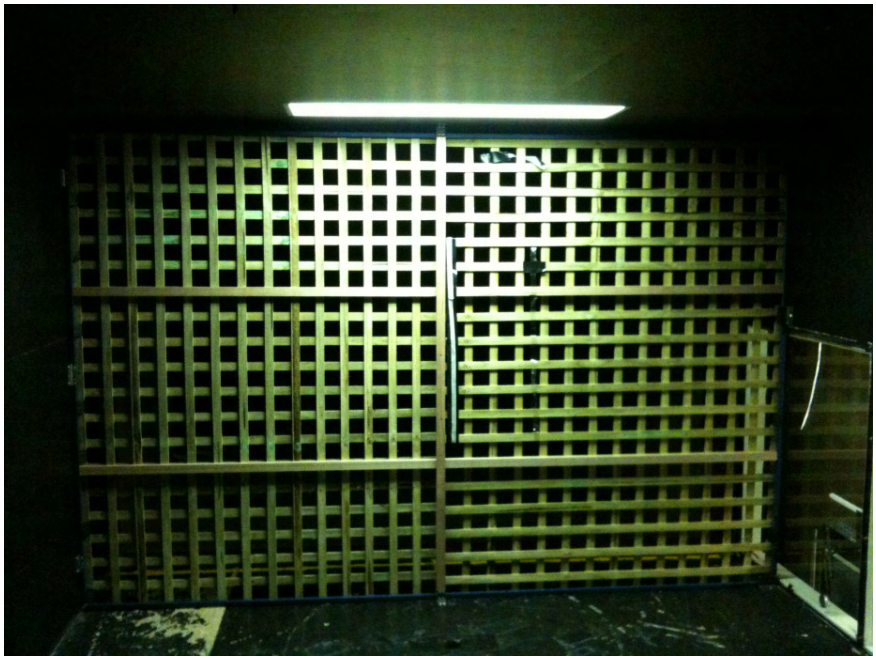

Figure 41: Photo of the finer mesh grid placed at inlet of test section.

A turbulence intensity of 7.15% with integral length scale of Lxx=0.14m, Lxy=0.06m and Lxz=0.08m was generated. The new gird was made from pine, with panels of 1'' width. A photograph of the grid is presented in Figure 41. Decay of turbulence along the test section was first plotted then the most suitable position for testing was ascertained. 5.5m downstream from the grids was found to be the most suitable location where the turbulence intensity experienced was nearly the same as the prior grids (12.3%) but with much shorter length scales. Contours of velocity and turbulence intensity indicated that the flow was nominally consistent through the airfoil span, see Figure 42. The spectra of velocity

fluctuations measured at mid-chord showed that the turbulence was again well mixed (refer Figure 43). The pitch angle of the flow was found to be around 2Deg in this case and was duly corrected for, while the yaw angularity was negligible.

The turbulence generated here was suitable for comparison between previously generated turbulence conditions. A nominally consistent distribution of flow properties was also experienced over the airfoil section. Therefore, this location/turbulence condition was chosen for conducting further airfoil experiments.

(a)

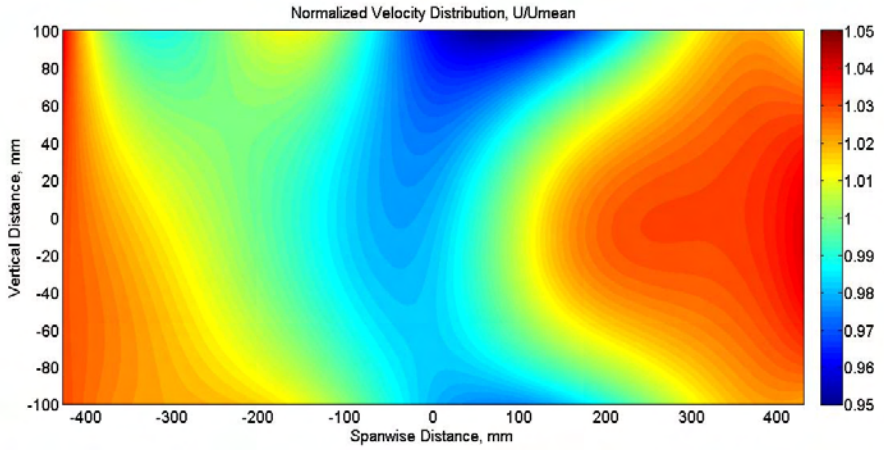

(b)

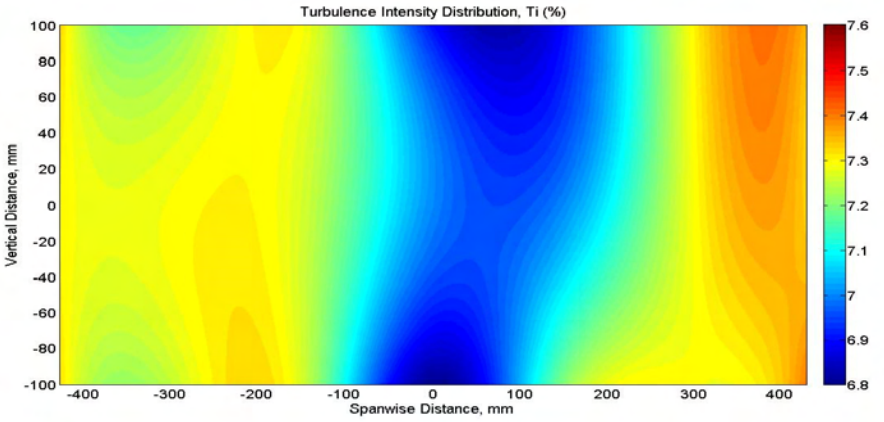

Figure 42: (a) Contour plot showing normalized velocity distribution within airfoil mount, U_{mean}= 7m/s. (b) Contour plot showing turbulence intensity distribution within airfoil mount. For both figures, test location was 5.5m from test section inlet for grids placed at inlet of test-section.

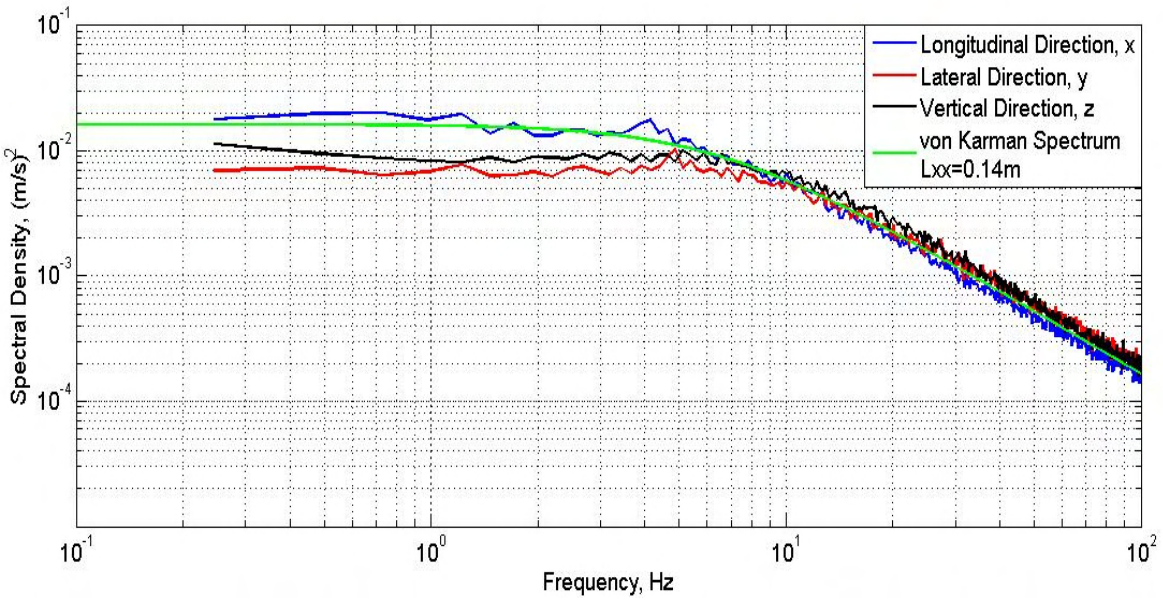

Figure 43: PSD of velocity fluctuations measured at mid span location inside the airfoil mount located 5.5m downstream from the grid at inlet of test section. von Karman spectrum is also fitted to ascertain streamwise integral length scale.

2.3.3 Monash University Wind Tunnel

The wind tunnel at Monash University in Melbourne was also used for some of the experiments in this research, see Figure 44. It has a variety of test-sections and is powered by two 1.5MW DC motors. The tunnel consists of a wind engineering test section at the top level and on the lower level an open jet test section (used primarily for automotive research) and a high Reynolds number closed jet test section. The open-jet automotive aeroacoustic test section provided a low turbulence level area for testing in relatively smooth air (i.e. longitudinal turbulence intensity of 1.5%). For the current research however, the wind engineering test section was used due to its large size, (12m wide, 4m high and 30m long) and ability to generate large integral length scales.

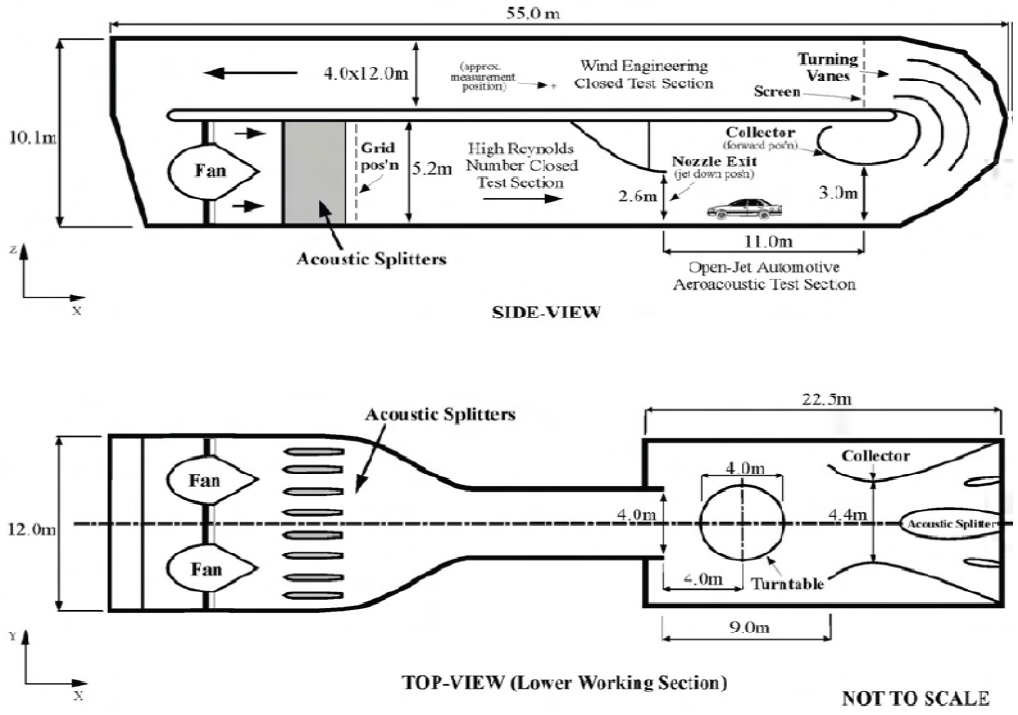

Figure 44: Schematic showing the various sections of the Monash University wind tunnel

The wind-engineering test section could be configured to generate a wide range of turbulence by changing the screens and grids at the entrance of the section, combined with changes to the lower part of the tunnel. As well as the conventional method of utilizing grids, other changes included varying the nozzle exit elevation and the collector position, see Figure 44. These changes permitted the generation of turbulence with intensities up to 25% in the wind engineering test section, with longitudinal integral length scales of up to 1.7m as reported by Milbank (2005). The long test section aids in the development of large turbulence intensity/length scale combinations. To maintain a suitable comparison with results obtained from the RMIT Industrial Wind Tunnel, it was desirable to generate turbulence of intensity closest to either 7% or 12% with much longer integral length scales.

Figure 45: Experiment setup in Monash University wind tunnel. The diagonal guy thread seen in the photo is located at the rear end of the airfoil mount.

To allow for proper mixing of turbulence and generation of large turbulence eddies, the testing location was chosen towards the rear of the test section. After conducting a survey of various planes along the test section, 21m from test section inlet was chosen as suitable. The airfoil mount was placed 2m offset from test section centerline. In this condition, the airfoil mount was around 4m away from the side wall, still staying well away from wall effects. The setup was also placed over an elevated plane with the airfoil located 2m above the ground. This kept the airfoil almost at tunnel center height, well away from boundary layer influences from the wind-tunnel walls. The experiment setup can be seen in Figure 45. The plot in Figure 46 presents variations in mean velocity and turbulence intensity across the airfoil mount. A nominally flat velocity profile was present and turbulence intensity can be seen to be around 7.2% at the measuring locations. In Figure 47 the power spectral density of the velocity measured at leading edge of airfoil is presented. It shows that compared to the spectra obtained in prior turbulence conditions the energy decay begins from a much lower frequency here, however at the same rate (-5/3). This is indicative of the significant increase in the integral length scale. The length scales here measured Lxx=1.3m, Lxy=0.35m and Lxz=0.37m.

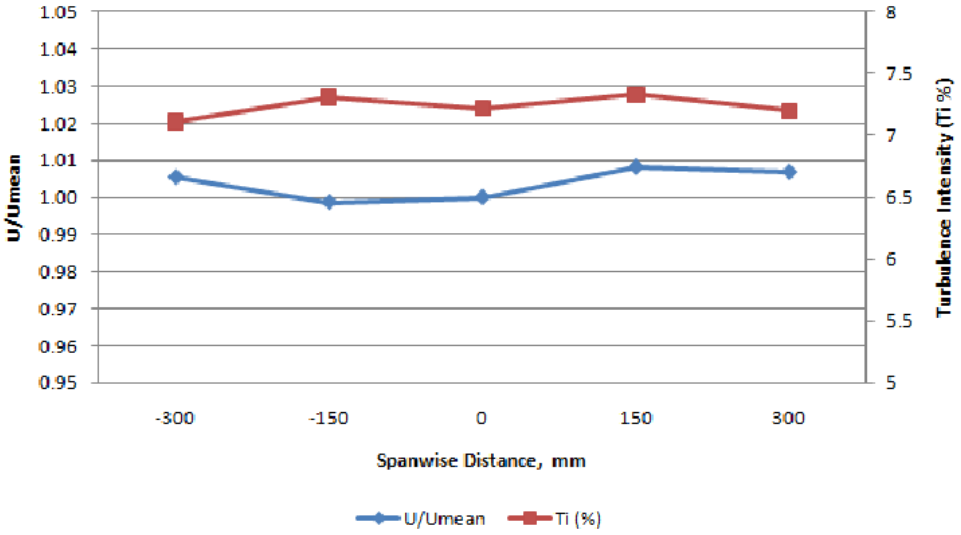

Figure 46: Normalized velocity and turbulence intensity variation across the airfoil span in the Monash University wind tunnel. Measurements were taken only at airfoil location.

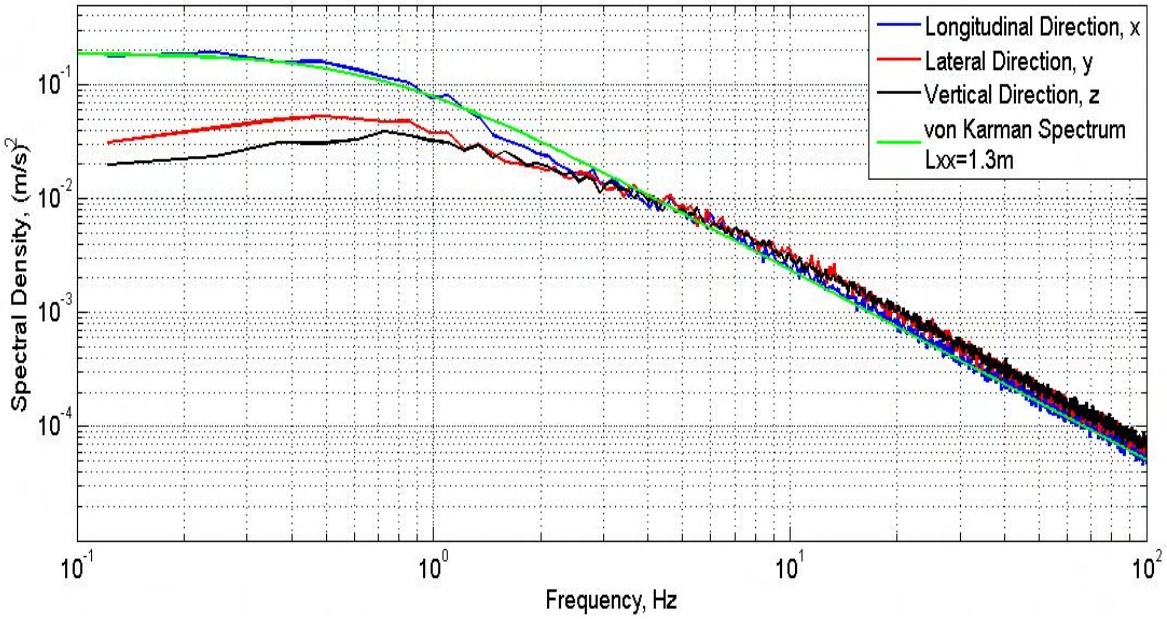

Figure 47: Power Spectral Density plot of velocity fluctuations in the three orthogonal directions measured at mid span location inside the airfoil mount at the Monash University wind tunnel. von Karman spectrum is also fitted to ascertain streamwise integral length scale.

2.3.3 RMIT Aerodynamics Wind Tunnel (AWT)

Traditional aerodynamic testing has mostly been conducted in very smooth flow (Ti<0.1%). The focus of this research was to examine the influence of higher levels of turbulence on airfoils. However to check the influence of "aeronautically" low levels of Ti, limited experiments were conducted within a traditional aerodynamics wind-tunnel. The AWT at RMIT was also used for these experiments. This wind tunnel was also a closed circuit tunnel and powered by a 380 kW DC motor. The test section is hexagonal, measuring 1.37m wide, 1.08m high and 2m long. A photo of the tunnel test section is presented in Figure 48.

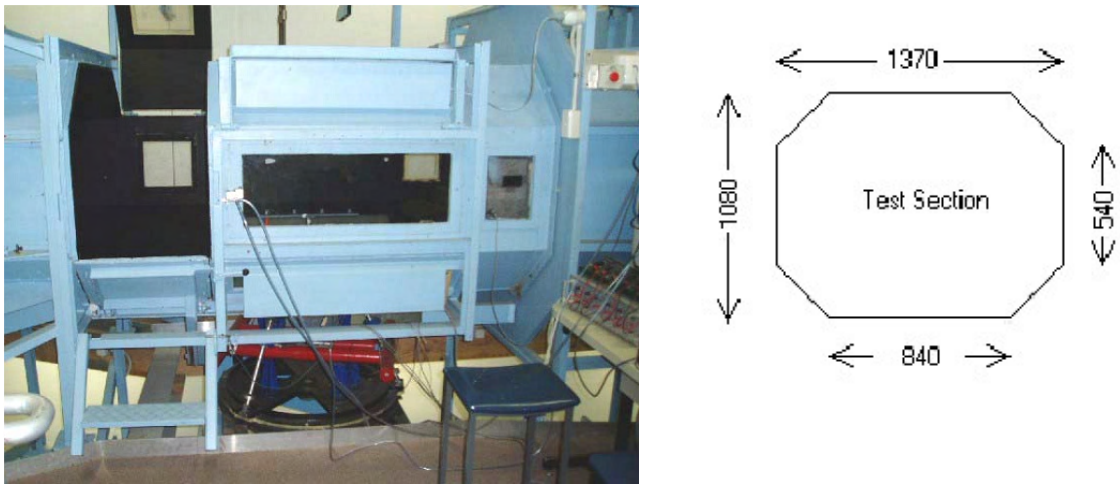

Figure 48: Photo and schematic of the RMIT Aerodynamics wind tunnel test section and its dimensions in mm.

For the tests within this facility, the airfoil span was reduced to 300mm and mounted within a custom made contraction placed in the test section. The contraction gradually reduced the test section width from 1.37m to 0.3meters, as shown in the Figure 49. For 2D tests in very smooth flow the span is generally considered not very important so long as the boundary layer from the side walls do not have a significant influence.

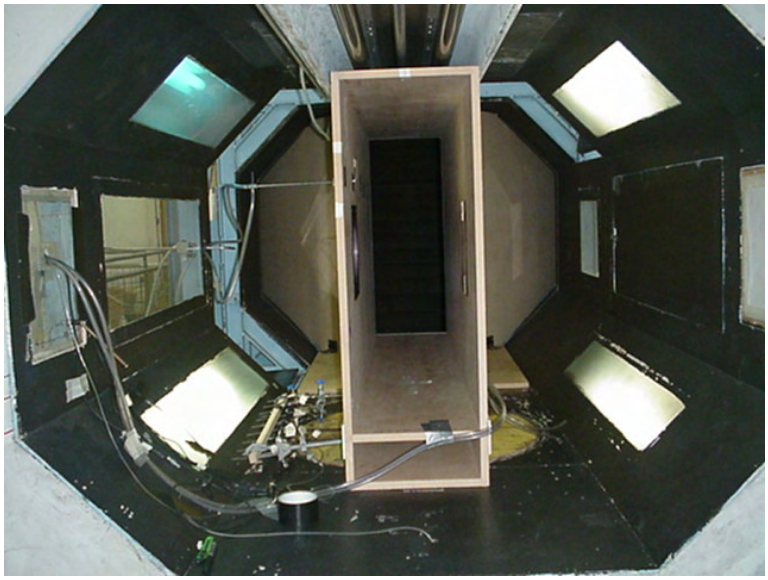

Figure 49: Photo of specially fitted contraction in RMIT Aerodynamics Tunnel, upstream view from the diffuser (Courtesy, Edward Cruz)

The flow within this contraction was surveyed and the turbulence intensity was found to be 0.5%. This was less than half the Ti experienced within the RMIT IWT. The plot in Figure 50 shows a nominally flat velocity profile, along with consistent turbulence intensity distribution present across the testing plane. Pitch and yaw angularity of the flow were insignificant (±0.2°) and hence no corrections were made.

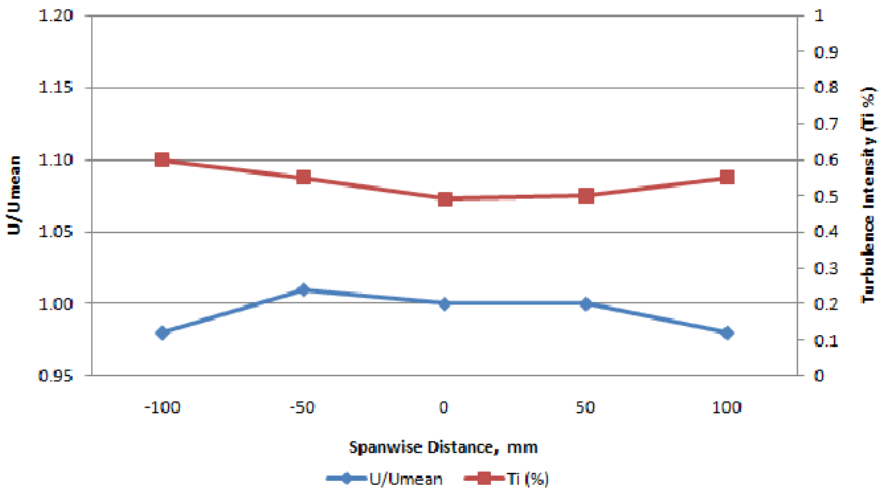

Figure 50: Normalized velocity and turbulence intensity variation across the airfoil span in the RMIT AWT. Measurements were taken only at airfoil location.

2.4 A Summary of Turbulence Conditions

A summary of the properties of various levels of turbulence generated is presented in Table 1.

Test Facility	Grid Properties	Distance from Test Section Inlet	Turbulence Intensity (%)				Integral Length Scale (m)		
			Ti_U	Ti_V	Ti_W	Ti (Overall)	Lxx	Lxy	Lxz
RMIT Aerodynamics Wind Tunnel	No Grid	2m	0.7	0.4	0.3	0.5	NR	NR	NR
RMIT Industrial Wind Tunnel	No Grid	7.75m	1.3	1.1	1.1	1.2	NR	NR	NR
	Large Grid at Test Section Inlet	7.75m	13.6	12.2	12.3	12.6	0.31	0.11	0.12
	Large Grid at Contraction Section Inlet	2.75m	12.9	12.2	12.1	12.3	0.15	0.10	0.09
		7.75m	7.6	7.3	7.0	7.3	0.22	0.13	0.11
	Finer Grid at Test Section Inlet	5.5m	7.7	7.1	7.2	7.2	0.14	0.06	0.08
Monash University Wind Tunnel	No Grid	21m	8.0	7.2	6.8	7.2	1.3	0.35	0.37

Table 1: Summary of different flow properties at the various turbulence conditions generated. NR=Not Relevant

Airfoil testing was conducted within a total of seven turbulence conditions, the properties of each turbulence condition is presented in Table 1. Conducting airfoil testing at the lowest Ti conditions (Ti=0.5% & 1.2%) would provide insight on the influence on turbulence at comparatively reduced levels of turbulence. The table also shows that turbulence of nominally same longitudinal length scale (Lxx=0.15m & 0.14m) and varying intensity (Ti=12.3% & 7.2%) was generated. Similarly turbulence of

varying longitudinal length scale (0.14m, 0.22m & 1.3m) at nominally same intensity (Ti=7.2%, 7.3% & 7.2%) was also generated. The turbulence conditions with properties Ti=12.3% Lxx=0.31m and Ti=12.6% Lxx=0.15m enabled the influence of turbulence length scale at nominally similar higher turbulence intensity to be investigated. In the Figure 51, spectra of all the turbulence conditions are presented. The change in spectral energy across the different conditions can be seen.

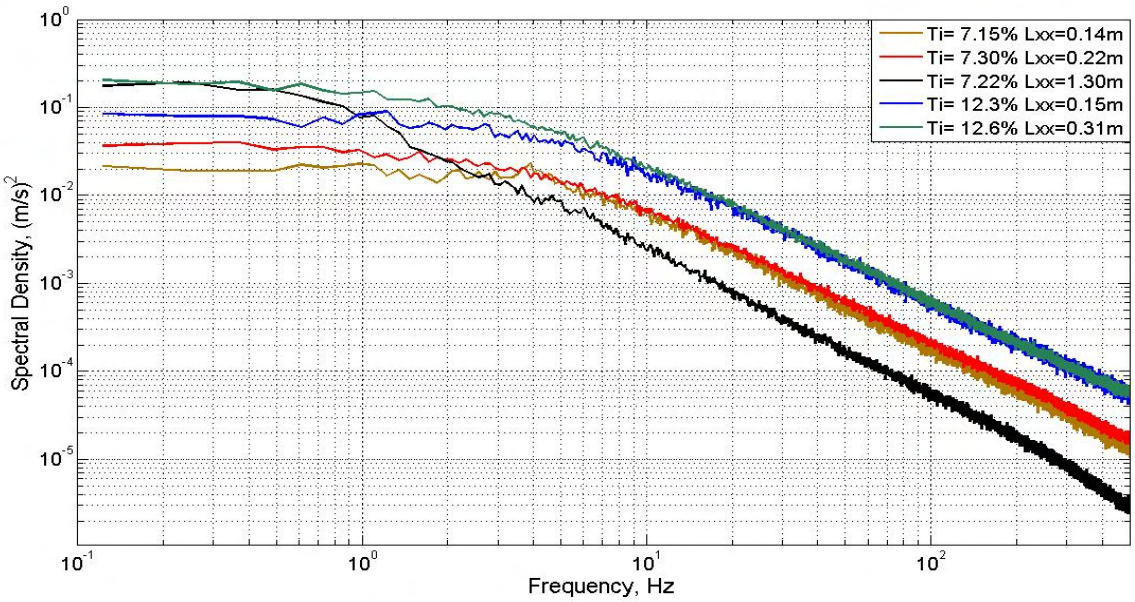

Figure 51: Spectra of the velocity fluctuations in different turbulence conditions.

2.5 Digital Pressure Measurement System (DPMS)

A Digital Pressure Measurement System (DPMS) was used for measurement of the time-varying pressures over the airfoil surface. The DPMS was designed, manufactured and calibrated by Turbulent Flow Instrumentation (TFI). The system at RMIT consisted of four modules and an interface box, where each module housed 15 pressure transducers. These modules were connected to the interface box which in turn was connected to an Analog-to-Digital (A/D) converter located inside a suitable computer. Photos and layout schematic of the system are presented in Figure 52 and Figure 53, respectively.

Figure 52: A DPMS Module alongside the interface box

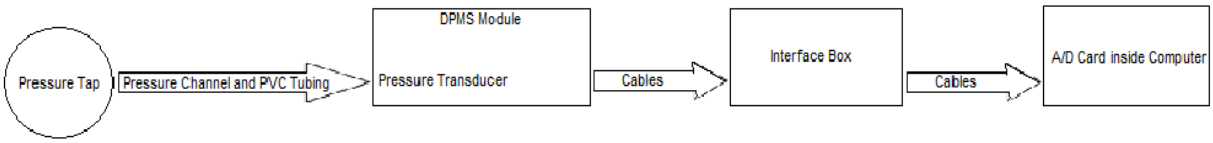

Figure 53: Pressure measurement system layout

A number of tubing types (silicone, PVC, etc.) were considered to connect the airfoil to the DPMS modules. Due to increased confidence on tubing radius and its relatively higher resistance to deformation, PVC tubing was chosen. As stated earlier, PVC tubing of 1mm Internal Diameter (ID) was connected from airfoil root to the various ports on the DMPS modules, for practical purposes this tubing length varied between 150mm to 200mm depending on the pressure measuring location. 42 transducers were used on the DPMS as only 40 pressure taps were present on airfoil and 2 transducers were for reference stagnation (Pitot) and static (static) pressure measurements.

TFI proprietary software was used to run the DPMS. The software let the user choose the sampling rate and time. For all pressure measurements here, sampling rate was set to 2000Hz and sampling time was limited to 300secs. Tubing parameters and ambient conditions (pressure and temperature) were input within this software and a data block-size was also chosen. As time-varying pressures were of particular interest, the tubing system's dynamic response had to be known. Based on the parameters input, an amplitude and phase response for the tubing system was generated by the software. Once analogue data from DMPS module was converted to pressures, the data-set was broken to blocks of size specified by user. Tubing response correction was then applied to these data-blocks using the Inverse Fourier Transform method (IFT). In this method each data block was transformed to the frequency domain by taking the Fourier transform of the same. The software generated amplitude and phase response for the

tubing system, which was also in the frequency domain, was inverted and multiplied with each data set, in the frequency domain. The inverse Fourier transform of the resulting operation gave the amplitude and phase corrected pressures.

2.5.1 Tubing Response and Dynamic Correction

Iberall (1950) first developed a theoretical method of estimating the amplitude and phase response of tubing systems of finite length. This method was then refined to a more definite form by Bergh & Tijdeman (1965). They derived the frequency and phase response equations for tubing systems of various geometries, based on the Navier-Stokes, continuity and state equations. This method of correcting pressures measured in tubing systems with finite length with or without cavities is still widely used, Holmes & Lewis (1987a) & Walter et al (2007). A number of workers have successfully used this method of correction, where the tubing properties such as length and ID were very similar to the tubing system used here, Loxton et al (2009), Vino (2005), Pagliarella (2009), etc.

For each of the four spanwise pressure measuring locations on the airfoil, tubing properties were computed and are presented in Table 2. The software used to run the DPMS generated the tubing and phase response for the input tubing parameter based on the work conducted by Bergh and Tijdeman (1965). As it was difficult to conduct accurate dynamic calibration of the airfoil tubing system (although this was attempted, see later and Appendix C), the measured pressures were theoretically corrected using this method to obtain a flat response.

Measurement Location	Tubing Length	Tubing Diameter
Location 1	550mm	1mm
Location 2	600mm	1mm
Location 3	600mm	1mm
Location 4	500mm	1mm

Table 2: Tubing properties for each pressure measuring location

The frequency and phase response of the uncorrected tubing system here was generated using this method and it is presented in Figure 54. The figure shows that for the longest tubing length i.e. 600mm, the system observed its first resonance at around 110Hz. Since the highest frequency of interest here was around 100Hz, the measured pressures had to be corrected to obtain accurate estimates of the time-varying pressures. In generating the tubing response and correcting the measured pressures, the DPMS software also took into account the fact that the pressure transducer is of finite volume, ($0.2mm^3$) and the tubing was connected internally to the transducer via a tube with ID 0.8mm and 6mm long. This small tube also has an effect on the overall response properties of the system. The software applied this correction (Figure 54) to each data block-set before displaying the final measurements, resulting in a flat frequency response for a range well above the frequencies of interest.

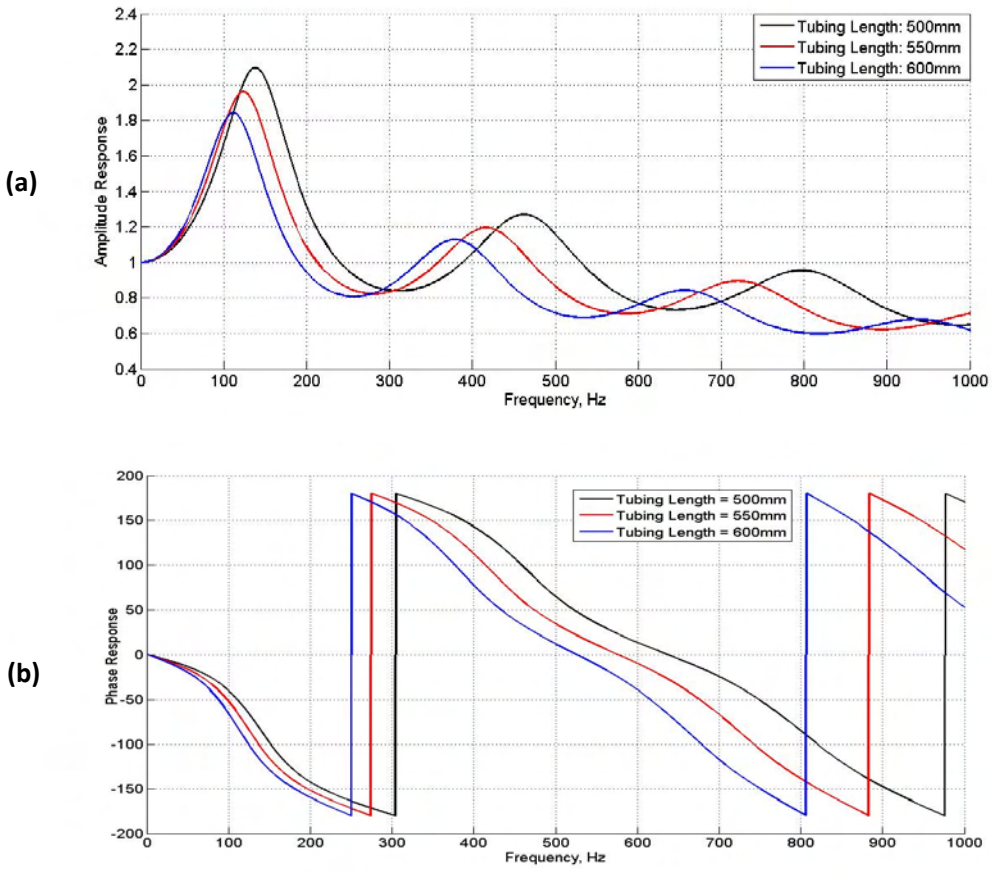

Figure 54: Amplitude (a) and phase (b) response for the tubing systems at all pressure measuring locations based on the Bergh & Tijdeman (1965) estimation

As tubing length for each spanwise pressure measuring location was different, the data from each location was corrected for by applying its unique frequency and phase response, from the unique tubing parameters input for each pressure measuring location. Some of the most sensitive parameters in the dynamic response of tubing system included diameter and tubing length, plots below show the degree of sensitivity of each parameter. The baseline conditions in the plots in Figure 55 correspond to tubing length of 600mm, 1mm ID and ambient temperature of 25°C.

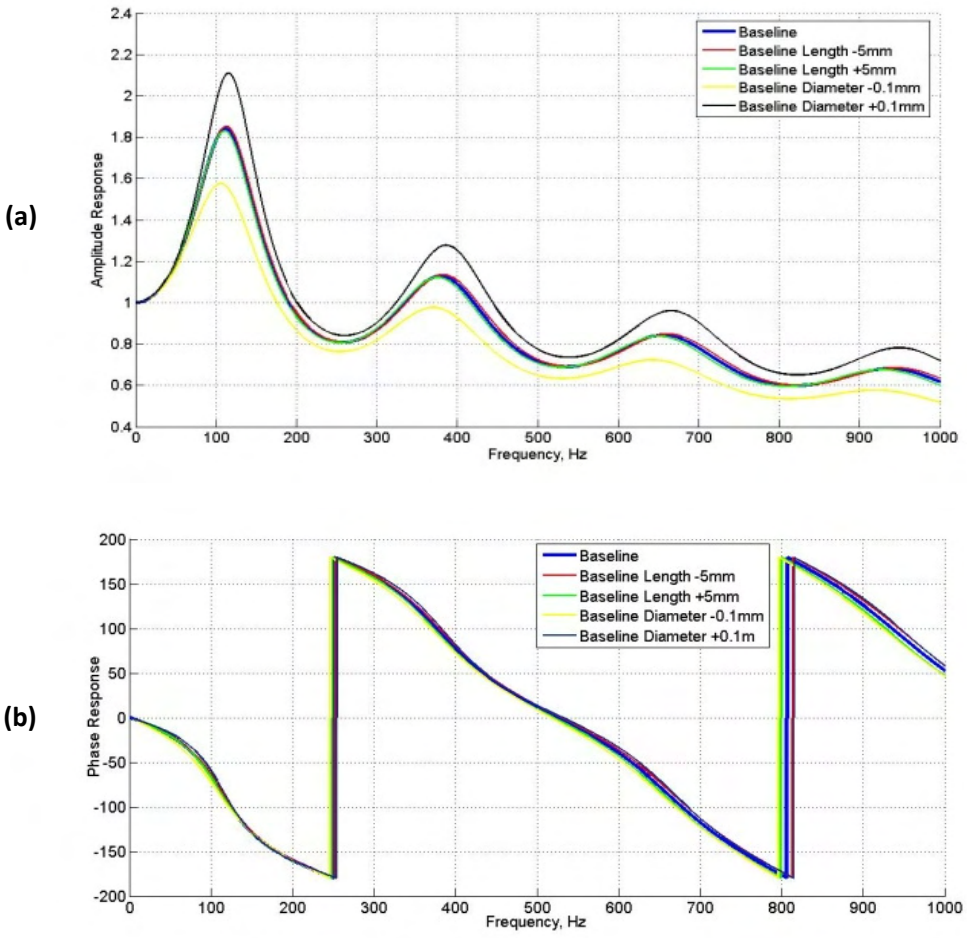

Figure 55: Changes in amplitude (a) and phase (b) response of tubing system due to slight variations in tubing and ambient parameters

As seen in Figure 55, tube internal diameter was the most influential parameter hence great care was taken to ensure consistent tubing diameter and length through all pressure measuring channels. The

ambient temperature and pressure were also regularly updated through the course of the experiment to keep response as accurate as possible.

To validate the use of the Bergh & Tijdeman (1965) method for correcting the frequency and amplitude response of the tubing system, a dynamic validation was conducted. In the dynamic validation, the airfoil was subjected to acoustic excitations at various frequencies and the pressures measured at the pressure taps were compared to the pressures at a reference point with and without tubing correction added. The results from the validation showed that the response of the tubing system followed the response derived by the Bergh & Tijdeman (1965) method. Details on this exercise are available in Appendix C.

2.5.2 Multiplexing and Inter-Channel Delay

Each DPMS module contained 15 high frequency pressure transducers. All transducers were connected on one side with a common reference pressure port while the interrogated pressure could be connected on the other side. The interface box was connected to a National Instruments 6034E A/D card located within the wind tunnel computer. National Instruments 6034E card is a common A/D converter consisting of 16 input channels all leading to a single 16bit A/D converter through a multiplexer. The A/D card also has an aggregate sampling limit of 200kS/sec. Interface Box of the DPMS system contained four more multiplexers rendering the total available channels to 64. Each module requires 15 channels, 1 for each transducer; hence 60 channels were used by all 4 modules. Four extra channels were available on the interface box for auxiliary inputs.

Multiplexing is a common technique used to measure inputs from various channels using a single A/D converter. The system here used the "Round Robin" method of multiplexing, where each channel was sampled one at a time in a sequence. Hence, there existed a (relatively short) time delay and phase lag between samples from each channel. Time delay between samples from each channel could be estimated as follows;

$$\Delta t = \frac{1}{\text{Number of Channels} \times \textit{Sampling rate}} \qquad \text{Equation 6}$$

Where: Δt is the time difference in seconds

The time delay between samples from each channel is around 7.8μsec. This delay for the purposes of this research (which mainly focuses on the lower frequency high-energy oscillations over the airfoil) can be treated as negligible. Due to this time delay, there was a slight phase lag also present. The phase delay between samples from each channel could be estimated using Equation 7.

$$\beta = \Delta t \times f \times 360$$
$$\beta = \frac{\Delta n}{128000} \times f \times 360$$

Equation 7

Where: β is the inter channel phase lag, f is the frequency of interest and n is the queue between the channels.

The denominator in the above equation is the total number of samples measured in one second, i.e. 64 channels at 2000samples/sec in each channel. Since the sampling frequency is much higher than the highest frequency of interest this phase lag due to multiplexing (15Deg approx.) was also considered negligible.

2.6 Cobra Probes

All time-varying velocity measurements were taken using pressure sensitive probes called Cobra Probes manufactured by TFI. The Cobra Probe system consisted of the probe which was connected into a breakout box, which in turn was connected to the A/D convertor within a suitable computer. RMIT possesses four such probes that can run simultaneously using the same A/D card. A photo of the Cobra Probe connected to a breakout box is presented in Figure 56. The probe's head measured 3mm in length and had 4 faces at different angles. Pressures were measured on each face of the head through pressure transducers embedded into the body of the probe. The barrel of the probe housed 4 pressure transducers which were connected to each of the 4 faces. All pressure transducers were connected on one side by a single reference static port. By measuring the pressure variations across the faces, time resolved velocity measurements in the three orthogonal directions were ascertained. The probes also had a ±45Deg cone of acceptance limit, whereby they did not record any velocity (0m/s) if the airflow was more than ±45Deg offset from probe head orientation.

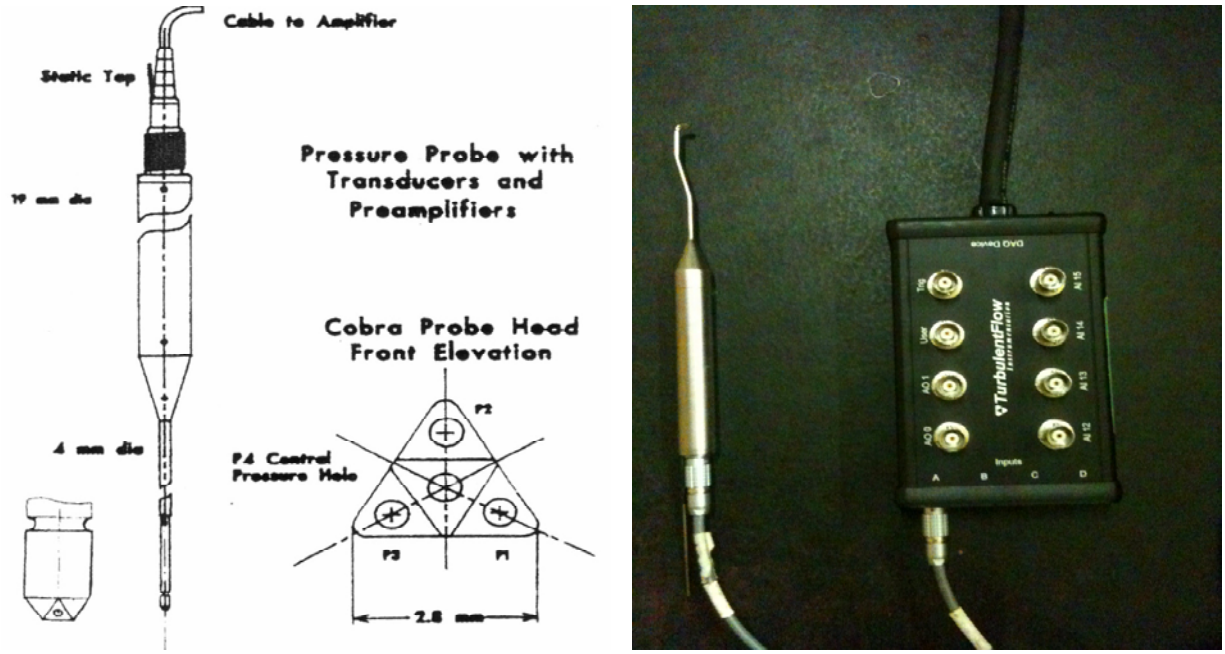

Figure 56: The Cobra Probe system

As early as 1970s work on the development of pressure sensitive probes for velocity measurement have been conducted. The Cobra Probes were a result of further research and development of the idea. Probes similar to the Cobra Probes were used by other researchers (Sims-Williams & Duncan (2002) and Yang et al (2006)), but these were not commercially available and do not have a frequency response as high as Cobra Probes. The Cobra Probes were calibrated for their dynamic response by the manufacturer and have a relatively flat response up to 2.5kHz. These probes have also be been tested and validated in a variety of flow conditions (Chen et al (2000), Hooper & Musgrove (1997) and Mousley (1998)) and were deemed sufficiently validated hence in this research no dynamic calibration or validation exercises was undertaken. However, time-averaged checks were conducted by placing the probe alongside a Pitot-static tube. Further information on this exercise is presented in Appendix A and in other doctoral theses Vino (2005), Pagliarella (2009), etc.

The software which was used to run the DPMS was also used for running Cobra Probes. Here too the user chose a sampling rate, time and data block-size. Sampling rate was set at 2000Hz for all measurements while the time varied from 60secs to 300secs. Inverse Fourier Transform method was employed by the software (in a similar manner to the DPMS software) to correct for phase and amplitude distortion due to tubing and transducer response. The tubing and phase response for the

Cobra Probe was determined experimentally by the manufacturer. Figure 57 shows the effectiveness of the correction factor.

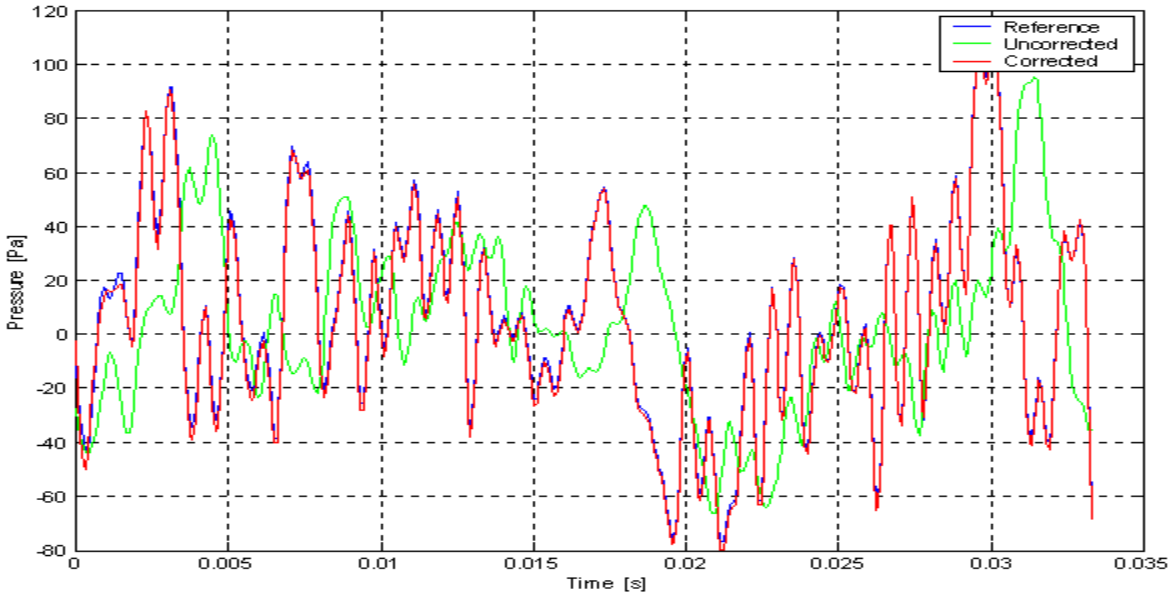

Figure 57: A comparison of the velocity measured by a Cobra Probe with and without tubing correction. Watkins et al (2002)

The probes being extremely robust and insensitive to ambient noise, offered an efficient replacement to other conventionally used time-varying velocity measuring devices. Being plug-and-play systems, they took very little time to setup, unlike hot wire anemometers (HWA) which are considerably more laborious to operate. For the requirements of this research, the Cobra Probes also offered a frequency response well above highest frequency of interest. However, some short comings of the probes included the ±45Deg cone of acceptance, hence they were not used in locations of high reverse flow e.g. within the laminar separation bubble. When velocity was measured along the separated shear layer over the airfoil and in the airfoil wake, instances occurred when the flow direction momentarily fell outside the acceptance cone. In such cases, the data series were appropriately truncated such that all analysis was conducted on data with no or extremely limited drop-outs (i.e. drop-out <0.05% of total sample length). In spite of the disadvantages, the benefits of using Cobra Probes over HWA were considered to far overweigh the disadvantages. They were hence chosen as the preferred means of velocity measurement.

2.7 Flow Visualization

Flow visualization experiments were conducted to obtain a qualitatively understanding of flow over the airfoil using smoke and high-speed photography.

2.7.1 Smoke Flow Visualization

To understand the influence of turbulence on flow-field over airfoil, smoke flow visualization was conducted here**.** A new airfoil was constructed for these experiments. The new airfoil was of the same dimensions but made of aluminum. It was also painted black to obtain best contrast when exposed to white smoke. The same airfoil mount was used.

2.7.1.1 Smoke Generator

RMIT's smoke generator system (Figure 58) was used to produce smoke for the experiments. Mineral oil was poured into the base unit which pumped it to a wand. The wand consisted of a tube through which the oil flowed to a heater at the tip. White smoke was generated by burning the mineral oil at the tip. The produced smoke was dense enough to enable visualization through high-speed photography. In turbulent flows, the smoke was found to diverge very quickly hence, the wand had to be placed close to airfoil leading edge to ensure most of the smoke particles followed the streamline. The wand's tip was placed 70mm upstream of the leading edge of the airfoil such that the produced smoke is carried by the streamline over the airfoil.

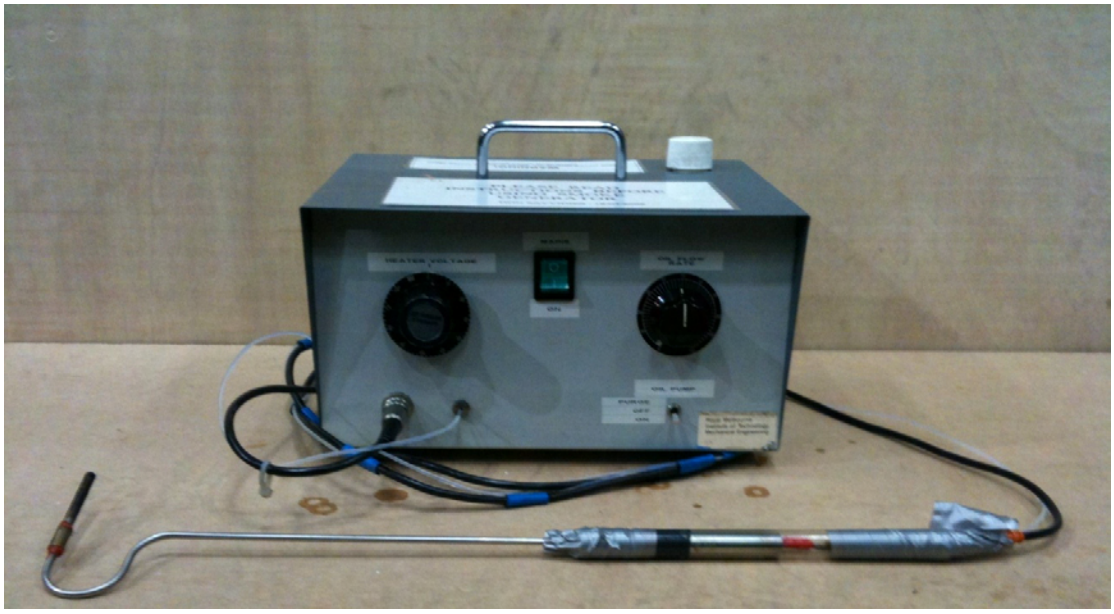

Figure 58: RMIT's smoke generator

Sensitivity studies were conducted to ascertain the influence of the smoke wand on the pressure fluctuations over the airfoil, as it was very close to airfoil leading edge (thus generating its own turbulence). In smooth flow conditions, it was found that the presence of the wand did have an influence on the pressure fluctuations, but the influence was limited only to the pressure fluctuations near the leading edge. Pressures over the majority of the airfoil however remain nominally unchanged. This was believed to be because the wand injected high frequency low energy perturbations into the flow which diffused into the shear layer just upstream of leading edge. In turbulent flow conditions however, the presence of the wand had an insignificant influence on the pressure fluctuations over the airfoil as the perturbations arising from the wand diffused much earlier in the presence of higher ambient turbulence. Elaboration on this sensitivity study can be found in Appendix C.

2.7.1.2 High-Speed Camera and Lighting

A high-speed camera was used to capture the path of the smoke, over the airfoil. The camera used was Phantom V4.2 manufactured by Vision Research. The camera has a maximum frame rate of 90,000fps however, for the current experiments, as the frequencies of interest were not very high and to obtain

good resolution the frame rate was set to 1000fps at a resolution of 800x600 pixels. To capture the salient features of the flow in both chordwise and spanwise directions, visualization was conducted from three different locations as shown in Figure 59.

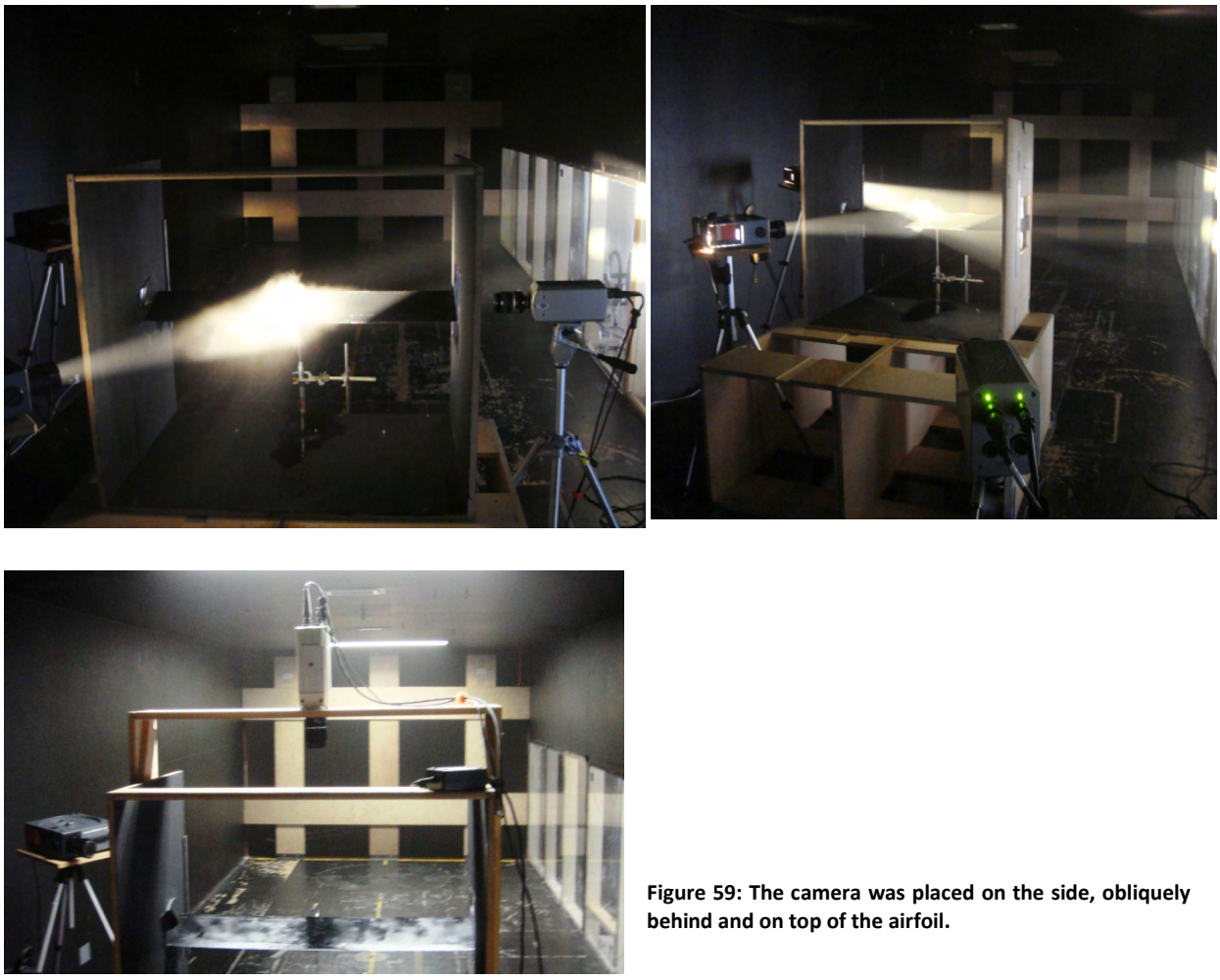

Figure 59: The camera was placed on the side, obliquely behind and on top of the airfoil.

For top view shots, the camera had to be placed directly over and orthogonal to the airfoil. A camera mount was therefore designed which enabled pitching the camera so it stayed directly overhead and focused over the airfoil centerline. For the other viewing locations, the camera was placed on tripods anchored to the ground. Slide projectors were used as a suitable light source as they offered very concentrated light over a small area. A total of two slide projectors and two spot lights were used to generate required lighting. A quick flow survey was conducted to ensure the flow-field within the airfoil

mount was unaffected due the presence of the camera or lights. No notable change in flow conditions was found.

2.8 Analysis of Experimental Data

A number of statistical techniques and processes were adopted for the analysis of data obtained from the experiments such that the various flow features over the airfoil and their influences could be effectively highlighted. The statistical processes and techniques used will be introduced and discussed in this sub-section.

2.8.1 Converting the Mean and Time-Varying Pressures to Pressure Coefficients

To study the pressure distribution over the airfoil, Pressure Coefficients (Cp) were calculated. The pressure coefficient at a point is defined by the ratio between the difference of local and ambient static pressures, and the ambient dynamic pressure. The pressure coefficient was calculated using Equation 8.

$$Cp' = \frac{P' - P_\infty}{1/2 \times \rho \times V^2} \qquad Cp = \frac{P - P_\infty}{1/2 \times \rho \times V^2} \qquad \text{Equation 8}$$

Where; P' and P are the local fluctuating and mean pressures, P_∞ is the mean ambient static pressure, ρ is density of the flow and V is mean velocity.

The dynamic measurements permitted analysis of the mean and time-varying pressure and velocity fluctuations over the airfoil. The highest frequency of interest in this work was only around 100Hz hence before any analysis was conducted all time-varying pressures were passed through a 200Hz second order Butterworth low-pass filter. A linear de-trending was also applied to eliminate very low-frequency (<0.1Hz) effects, but since such effects were not very prevalent in turbulence generated within wind-

tunnels (but are generally considerable in ABL data), the de-trending did not make a significant difference. Since the Cobra Probe had a flat frequency response up to 2.5kHz, the velocity data were not filtered.

For analysis of the mean and Std.Dev of pressures over the airfoil, all the filtered time-varying pressures were non-dimensionalized to time-varying pressure coefficients (Cp') then the average and Std.Dev of the same was computed. Comparisons were also made with the photos from the smoke flow visualization experiments and they provided key insights about the flow structure. Composite plots of the mean and Std.Dev of the pressures over the airfoil chord and span were also created. More information as to the manner of interpretation of the composite plots will be presented in the next chapter. Some of the flow properties that were deduced from the mean and Std.Dev distribution of pressures included: the length of the LSB, the region of recirculation under the LSB, the reattachment point oscillation length, location of maximum fluctuations, etc.

2.8.2 Spectral Analysis of Pressure and Velocity Data

To uncover any repeating fluctuations in pressure and velocity over the airfoil, the spectra of the fluctuations were also computed. This involved converting the pressures at each chordwise and spanwise stations from the time domain into the frequency domain by taking their Fourier transform. The Welch method of Fourier transform was used and further elaboration on this method is available in Appendix F. The spectra of the pressures revealed the rate and energy of fluctuations of a number of flow structures, including flapping of the shear layer, bluff-body-like vortex shedding, etc in nominally smooth flow and vortex core formation rate at higher levels of turbulence. Composite plots of the spectra of pressures over the chord were created and they provided visualization of the fluctuations that occurred. Comparisons were also made between the composite spectra plots and smoke flow visualization to correlate the pressure fluctuations to the flow features observed in the latter. Further information on the manner of interpretation of the composite plots will be provided in the coming chapters. Spectra of the velocity fluctuations revealed oscillations that occurred at significantly higher frequencies (e.g. the rate of instability formation in the separated shear layer and rate of oscillation of the TE streamline at lower AOAs).

2.8.3 Correlation and Coherence Analysis of Fluctuations

The degree of similarity between fluctuations at one location with respect to another were of interest here as they assisted in estimating the size and rate of advection of flow structures over the airfoil chord and the extent of flow two dimensionality over the span. The normalized correlation and coherence coefficients were therefore computed for the fluctuations in pressure and velocity measured. For details on the functions used, refer Appendix F. It was observed that the rate of translations of the different flow structures was relatively low hence inter-channel-delay and associated phase-lag in the A/D card was considered to have a negligible impact. By tracking the time-shift required to attain maximum correlation between pressure fluctuations at each chordwise station and the pressures measured at the shear layer reattachment point, the size and rate of advection of vortices and eddies over the airfoil chord was gauged. Composite plots of the correlation and time-shift with respect to each chordwise station provided a realistic visualization of the advection of flow structures over the chord. The time-shift in the composite plots was non-dimensionalized with respect to the mean freestream velocity and chord. More information on the composite correlation plots will follow in later chapters.

Calculating the normalized coherence and correlation between the pressures measured at each spanwise station over the chord provided insights on the degree of flow two-dimensionality over the span. They also assisted in identifying flow features that were influenced by local effects and others which were much larger over the span and were more influenced by large-scale changes in the flow.

2.8.4 Calculation of Mean and Transient Lift, Drag and Moment Coefficients

The mean pressure Cp distributions over the airfoil chord were appropriately resolved and integrated to estimate the time-averaged CL and lift/unit span respectively. The lift produced by the suction and pressure sides of the airfoil was also individually presented to provide insights on the influence of Ti and length scale on the either sides of the airfoil. Since pressure measurements were taken over the airfoil, only pressure drag was estimated. The pitching moment coefficient (CM) with respect to the quarter-chord was also calculated from the mean Cp distributions.

Integrating the instantaneous pressure distribution over the chord permitted analysis of the lift fluctuations on either side of the airfoil. Similar to the analysis of pressure fluctuations; spectra, spanwise correlation and coherence were computed during the analysis of the time-varying lift coefficient (CL) fluctuations as well. Histograms were used to statistically compare the lift fluctuations at different turbulence conditions and Angles of Attack (AOAs). The individual influence of turbulence intensity and length scale on the mean and time-varying lift, drag and pitching moment were identified through this analysis.

Comparisons between the instantaneous lift at spanwise stations separated by 50mm and 200mm respectively were conducted to study the rolling moments experienced in different turbulence levels. The rolling moment per unit span and unit moment arm was calculated to effectively highlight the change in rolling moment between the two spanwise separations (50mm and 200mm) only due to influences from the flow and not due to change in moment arm-length. The sensitivity of the magnitude of rolling moment to: separation distance, Ti and length scale was successfully gauged through this analysis. Spectra of the rolling moments assisted in identifying any repeating trends in the fluctuations.

A variety of statistical techniques and processes were therefore employed to effectively analyze the pressure, velocity and visual data gathered. More information on the manner of interpretation of certain plots is provided in later chapters and more information on the statistical processes is available in Appendix F.

CHAPTER 3

Mean and Standard Deviation of Pressures over the Airfoil

In this chapter, mean and standard deviations of the pressure fluctuations over the airfoil when exposed to various flow conditions will be presented. This information will be useful in assessing the influence of low Reynolds number flow effects, turbulence length scale and intensity on airfoil performance.

3.1 Pressure Distribution in Smooth Flow

The time-averaged properties and Standard Deviation (Std.Dev) of the fluctuating pressures measured when the airfoil was exposed to the lowest turbulence intensities generated (Ti=0.5% and Ti=1.2%) will be analyzed in this sub-section. It should be noted that majority of the results presented here are from the testing conducted in the Ti=1.2% condition as only a few tests were conducted when Ti=0.5%. The tests conducted in the lower Ti condition were only to determine the influence of Ti at such low levels on the pressures over the airfoil. As will be seen later, the difference in pressures between the two conditions was quite small.

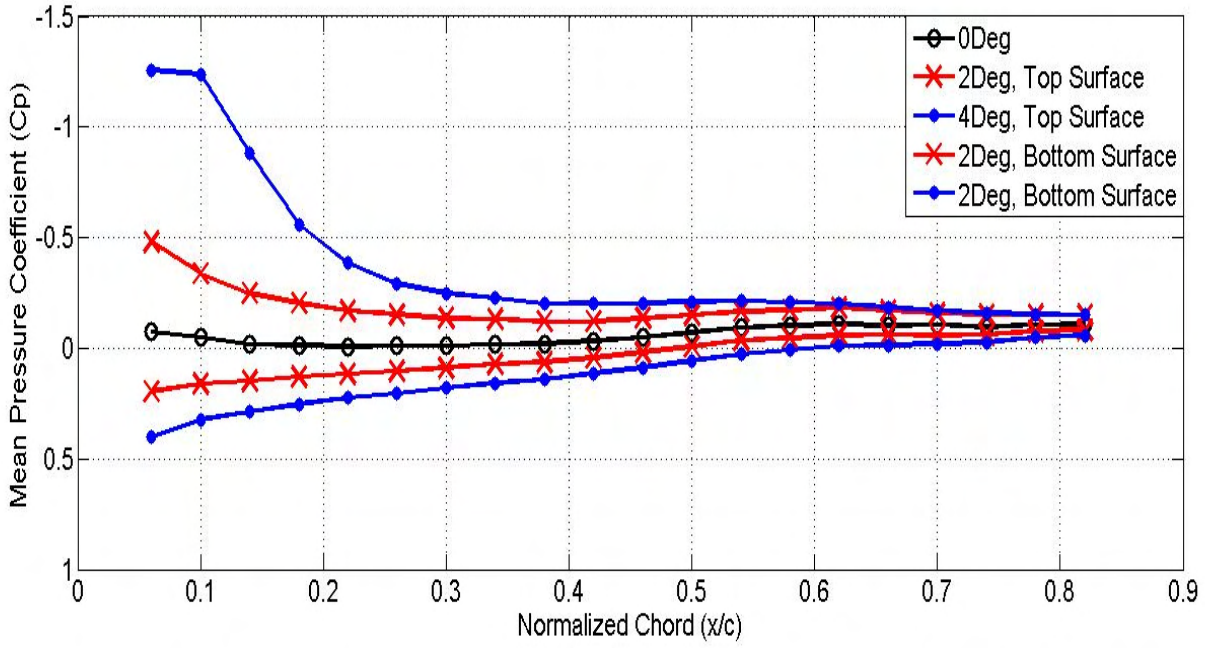

Figure 60: Time-averaged pressure distribution over top and bottom surfaces of airfoil at 0Deg, 2Deg and 4Deg AOA. Ti=1.2% and Re =75000.

Time-averaged distributions of pressure over the airfoil between 0Deg to 4Deg AOA are presented in Figure 60. The figure shows that the suction peak is located on the top surface very close to the leading edge of the airfoil. Immediately after the suction peak a rapid increase in Cp takes place due to the ensuing pressure recovery. This implied a drop in velocity from the location of maximum suction, as expected. At 4Deg AOA, close to the Leading Edge (LE) a small region of constant Cp is noticed which suggests that a small separation bubble may be present. This however cannot be determined with high certainty as the spatial resolution is limited to only two points in this region. But literature suggested that in this Reynolds number range, LSBs do form and can be typically identified from the presence of a region of constant mean suction over the airfoil.

Plotting the Std.Dev of the time-varying pressures over the airfoil could provide insight on the locations where maximum fluctuations take place which assist in identifying key features in the flow, such as the location of reattachment of the shear layer. Until 2Deg AOA, maximum fluctuations are seen to occur close to the peak suction location, see Figure 61. Figure 61 also indicates that at 4Deg AOA fluctuations increase considerably over the entire airfoil, suggesting a change in flow structure occurs at this AOA. Based on the presence of a region of constant mean Cp and the point of maximum fluctuations moving

downstream at this AOA, it can be professed with good certainty that at 4Deg AOA leading edge separation occurs and consequent reattachment takes place at around 0.18(x/c). As large transient pressures are experienced at the point of reattachment of the shear layer, the region of maximum Std.Dev of Cp generally corresponds to the point of reattachment, Cherry et al (1983), Loxton et al (2009), Sicot et al (2006), etc.

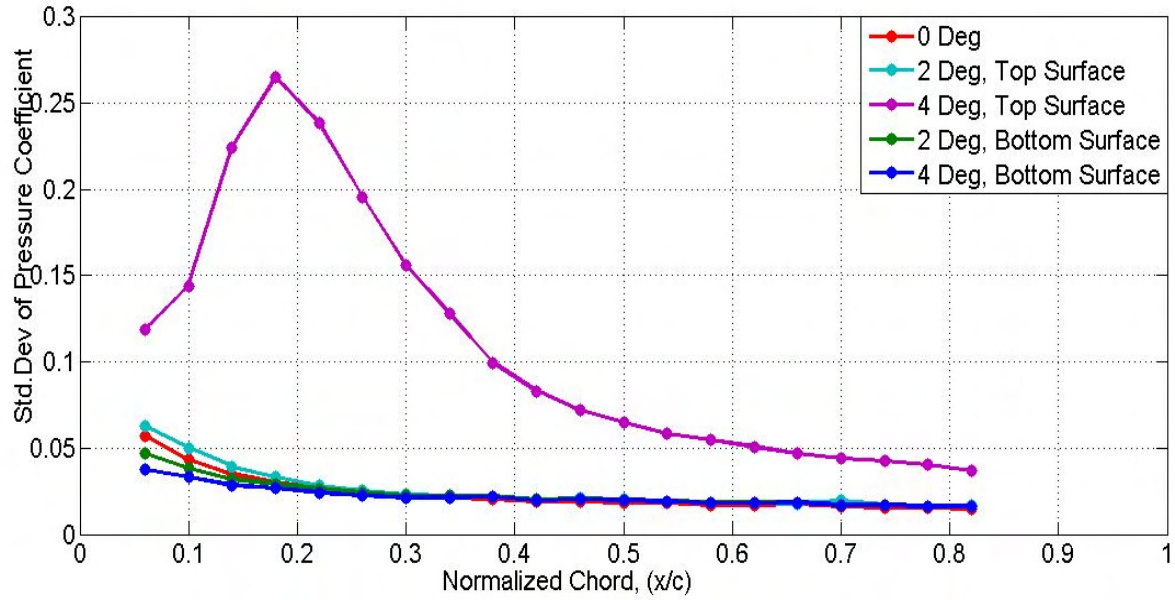

Figure 61: Standard deviation of the pressure fluctuations over top and bottom surfaces of airfoil at 0Deg, 2Deg and 4Deg AOA. Where Ti=1.2% and Re =75000.

At these low AOAs, the flow is mainly two-dimensional (only chordwise) as can be seen from the smoke flow visualization patterns in Figure 62. Figure 62a shows the top view of time-averaged smoke flow pattern over the airfoil at 2Deg and here the flow can be seen to travel only chordwise without any significant spanwise components. Figure 62a was derived through overlapping photos acquired over a period of 0.5secs, from the smoke flow visualization experiments. A side view showing the instantaneous path of the smoke over the airfoil in Figure 62b confirms that the flow remains fully attached at 2Deg.

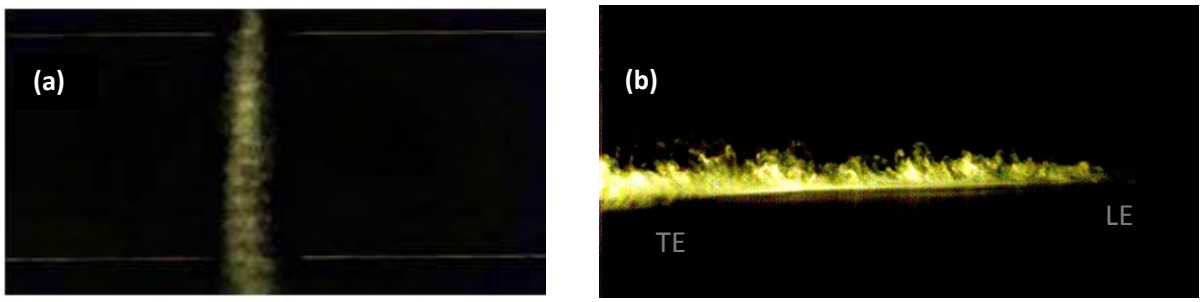

Figure 62: (a) Top view of the time-averaged smoke flow over the airfoil at 2Deg AOA, created by overlapping 0.5secs of smoke flow visuals. (b) Side view of Instantaneous smoke flow over the airfoil at same AOA. Ti=1.2% and Re=70000

At AOAs higher than 4Deg, a distinct region of constant negative Cp is present at the location of maximum suction, see Figure 63. This region of constant mean Cp grows considerably in length as the AOA changes from 4Deg to 8Deg, implying an increase in bubble length originating from the leading edge. With increase in AOA the location of maximum Std.Dev of Cp also moves downstream indicative of the point of reattachment shifting rearwards, see Figure 64. This distribution of Std.Dev and mean Cp till 8Deg is similar to the one presented by Cherry et al (1983) from his research on blunt flat plates, see Figure 66. This suggested that the flow structure over the thin airfoil is very similar to that present over blunt flat plates with sharp edges. In comparison to Figure 66, the difference in sectional geometry is believed to be the reason for the increased magnitude of fluctuations noticed here.

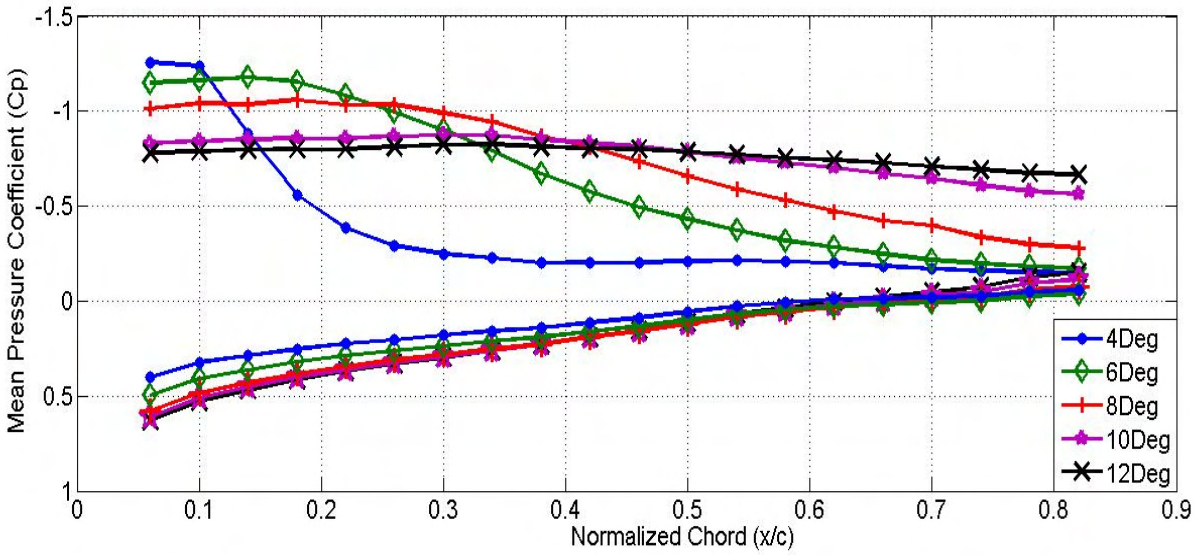

Figure 63: Time-averaged pressure distribution over top and bottom surfaces of airfoil from 4Deg to 12Deg AOA. Where Ti=1.2% and Re =75000.

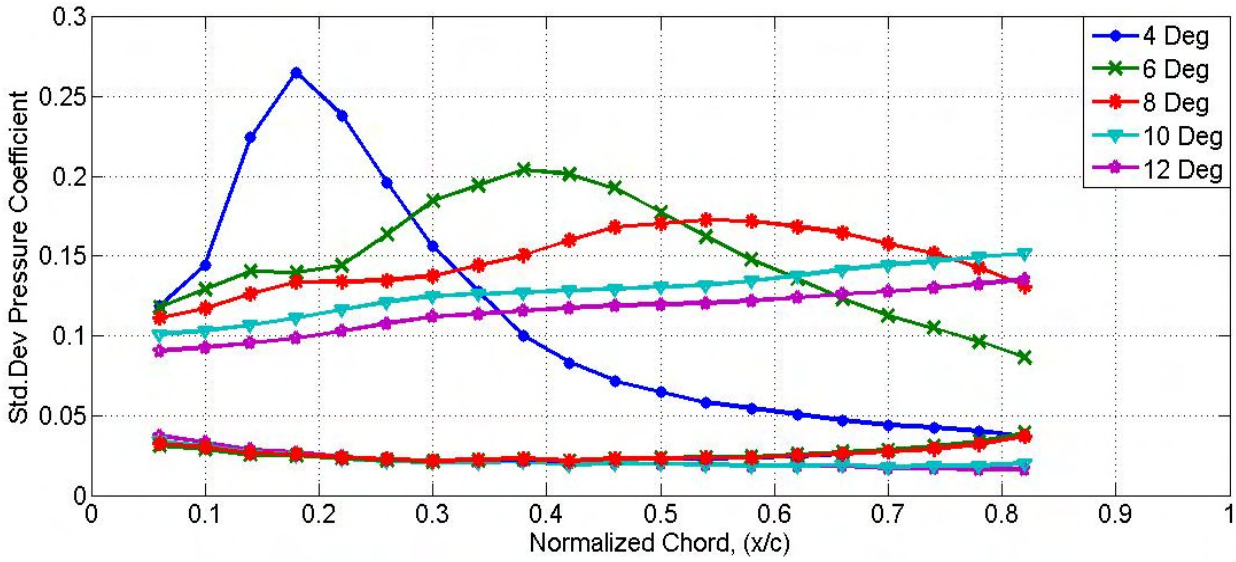

Figure 64: Standard deviation of the pressure fluctuations over top and bottom surfaces of airfoil from 4Deg to 12Deg AOA. Where Ti=1.2% and Re =75000.

The length of the separation bubble is generally defined as the distance between the point of separation to the point of reattachment of the shear layer. As per Figure 64, this length is approximately 0.4(x/c) when the airfoil is at 6Deg AOA. This estimation is however considerably larger than the region of

constant mean Cp, approximately 0.17(x/c) from Figure 63, which is sometimes used as a metric for bubble length, Crompton & Barrett (2000). Smoke flow visualization for this AOA showed that the location of reattachment corresponded well with the region of maximum Std.Dev as seen in Figure 65. This implied that the region of constant Cp is not necessarily the length of the laminar separation bubble, but rather it is the region of recirculation within the bubble which is least affected by the disturbances induced by the shear layer reattaching. As a corollary, time-averaged measurement of the pressures over the airfoil would be inadequate to accurately estimate LSB length hence time-varying measurements must be taken in order to gauge true bubble length.

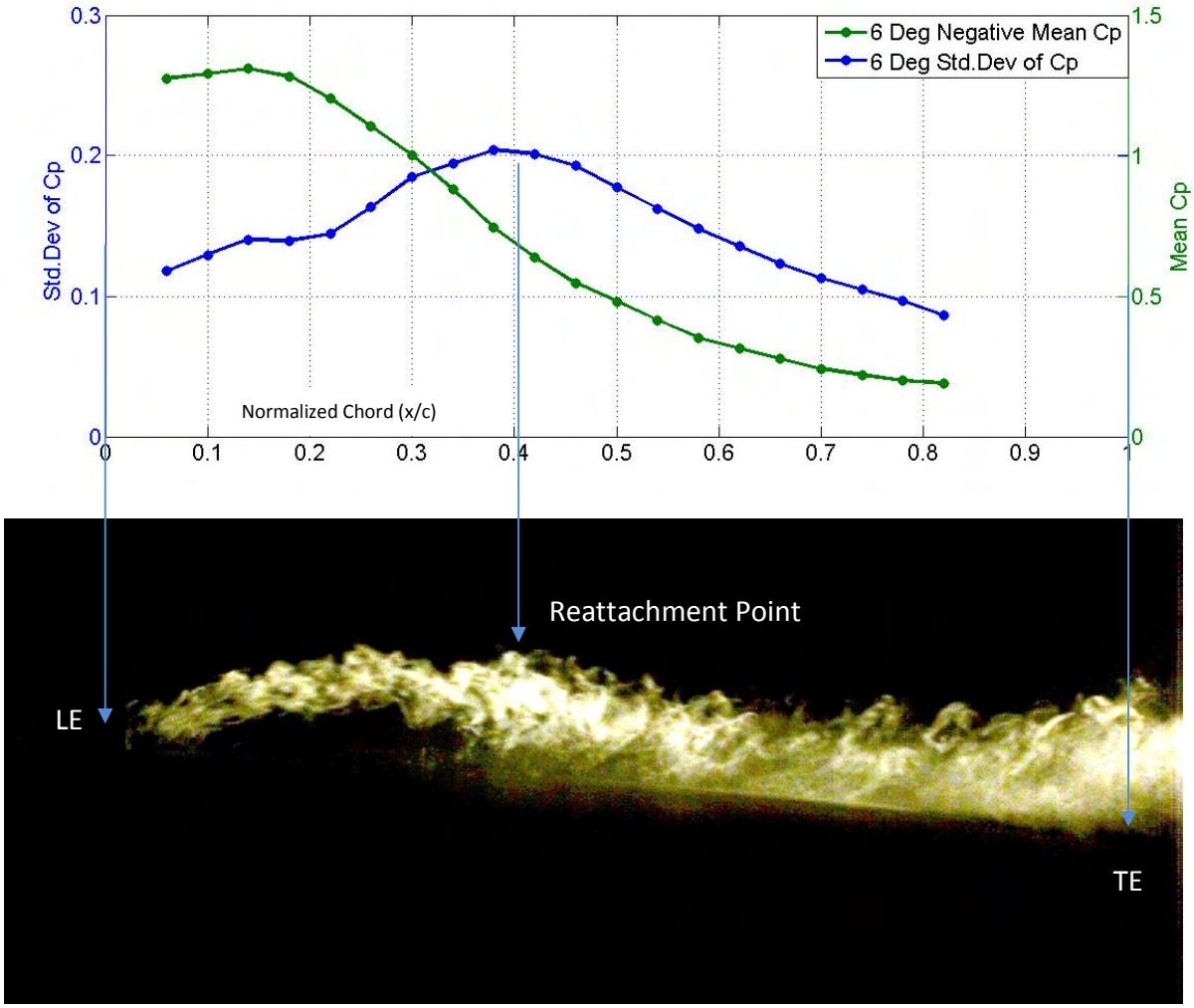

Figure 65: Mean and Std.Dev of Cp over the airfoil at 6Deg AOA is plotted on the same graph. Side view of instantaneous smoke flow over the airfoil at same AOA. Ti=1.2%

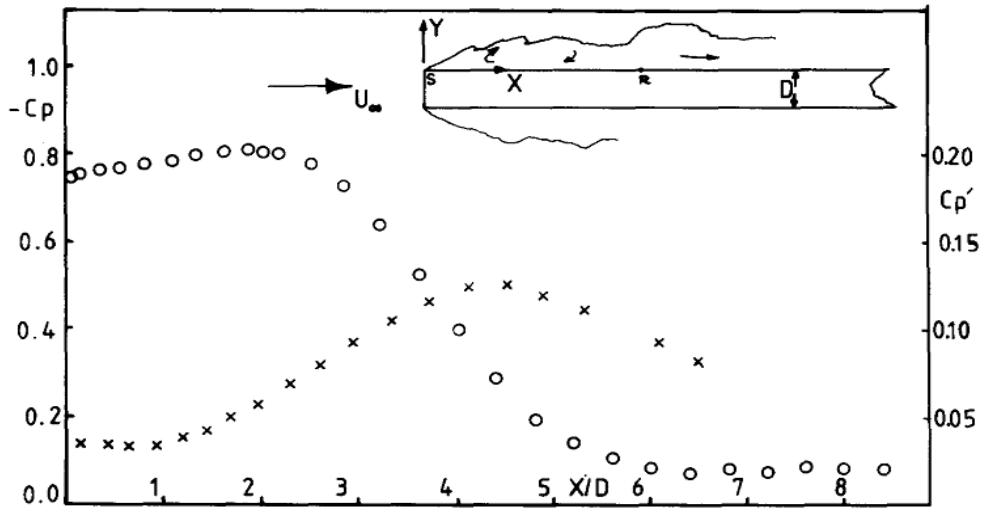

Figure 66: Mean and Std.Dev of Cp over a blunt flat plate in smooth flow. Cherry et al (1983)

Literature suggested that the velocity within LSBs is much lower compared to the free stream velocity, Gaster (1966). However, in spite of the reduced velocity within the bubble, considerably high suction is experienced as inferred from the regions of constant high negative Cp in Figure 60 and Figure 63. The high suction experienced under a LSB in spite of the reduced velocity within the same is due to the flow in the upper region of the shear layer accelerating to a velocity higher than the freestream flow speed, (Gaster (1966), Zhang et al (2008) and Li & Melbourne (1999)). The acceleration of the flow just above the LSB creates the noticed suction acting over both the LSB as well as the airfoil.

As for the pressures over the airfoil bottom surface (pressure side), a steady increase in the mean Cp is noticed close to the LE with increase in AOA while the Std.Dev changes to a relatively limited extent, see Figure 63 and Figure 64. The increase in mean Cp is due to the underside offering a stronger favorable pressure gradient with increase in AOA. Similar to that noticed over the suction surface, on the pressure side the magnitude of pressure fluctuations reduces slightly as AOA increases to 4Deg after which it remained nominally unchanged, refer Figure 61 and Figure 64.

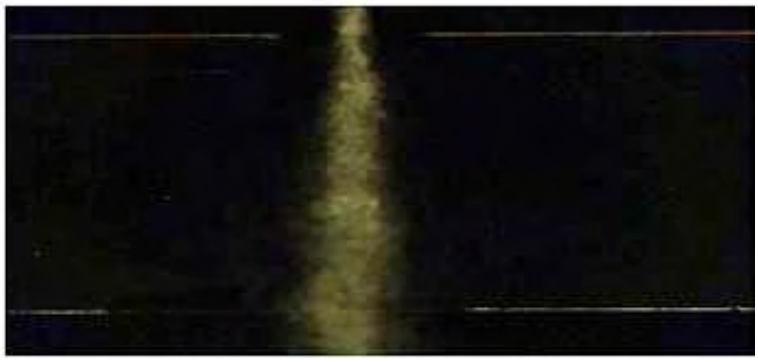

Figure 67: Top view of the time-averaged smoke flow over the airfoil at 6Deg AOA. Ti=1.2% and Re=75000

The mean Cp distribution in Figure 63 is similar to the measurements made by Crompton & Barrett (2000) on a flat plate airfoil with a sharp leading edge, see Figure 68. Unlike in the case of the airfoil used in this research, the formation of LSBs was detected from AOA as low as 1Deg by Crompton & Barrett (2000). This change can be attributed to the difference in LE geometry between the airfoils. The relatively more streamlined LE profile here appears to delay the formation of LSBs. Crompton & Barrett (2000) also detected two counteracting recirculating regions under the reattached shear layer, flow visualization conducted in this research however indicated that only one recirculation region was present under the separated shear layer.

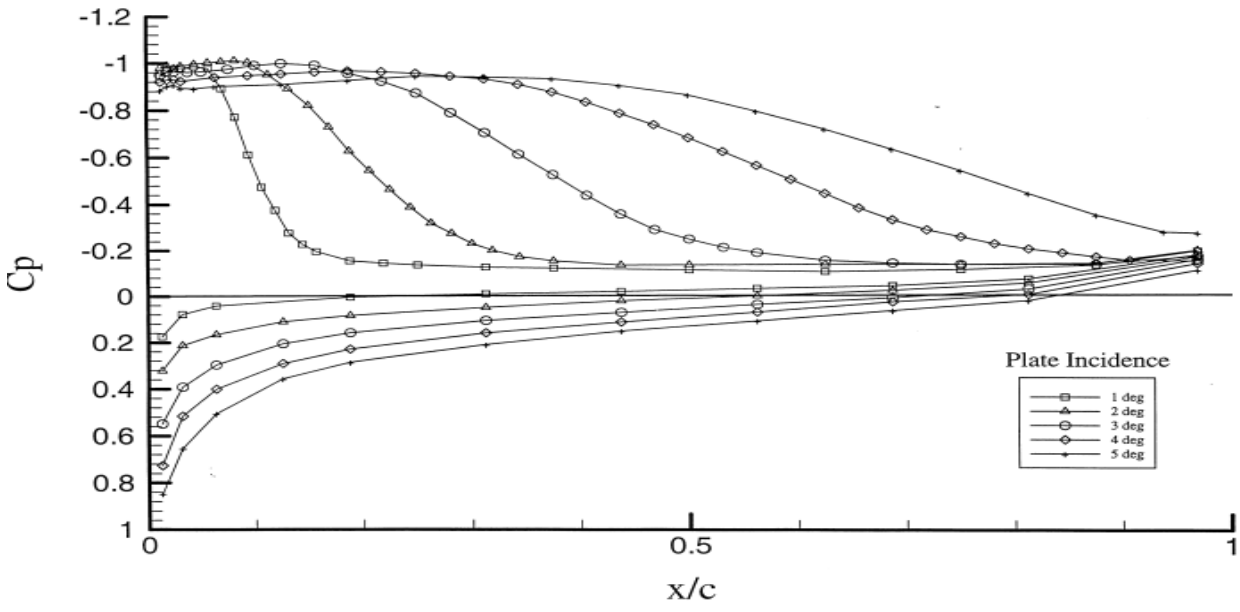

Figure 68: Mean Cp distribution at different AOAs over flat plate airfoil with sharp LE, Crompton & Barrett (2000)

Considerably higher spanwise dispersion of smoke was noticed as the AOA was increased above 4Deg, refer Figure 67, which was also created by time averaging smoke flow visuals similar to Figure 62a. The smoke dispersion at 6Deg in Figure 67 highlights the presence of small spanwise components within the shear layer. The instantaneous smoke flow visualizations (Figure 65) show that only sections of the shear layer undergoes transition and roll up as recirculating fluid, while some of the fluid in the shear layer pass over the bubble following its contour, see Figure 65.

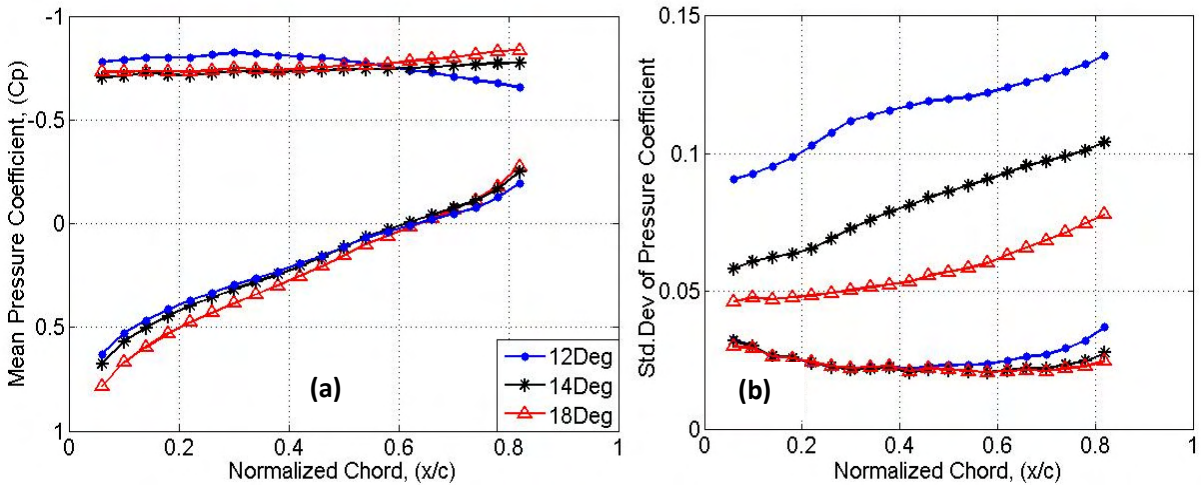

Figure 69: Mean (a) and Std.Dev (b) of Cp over the airfoil top and bottom surface at 12Deg, 14Deg and 18Deg. Ti=1.2% and Re=75000

At 10Deg AOA, from the mean Cp plot the length of the LSB was estimated to be around 0.4(x/c), refer Figure 63, while the Std.Dev of the Cp showed the point of reattachment of the shear layer to be very close to the trailing edge, Figure 64. It was found from flow visualization that at 10Deg and beyond, the shear layer failed to reattach onto the airfoil i.e. the airfoil stalled, see Figure 71. Past this angle, the pressure remained constant over entire chord while the Std.Dev of the fluctuations increased only marginally towards the trailing edge. After stall, the airfoil began displaying bluff-body-like characteristics, see Figure 71.

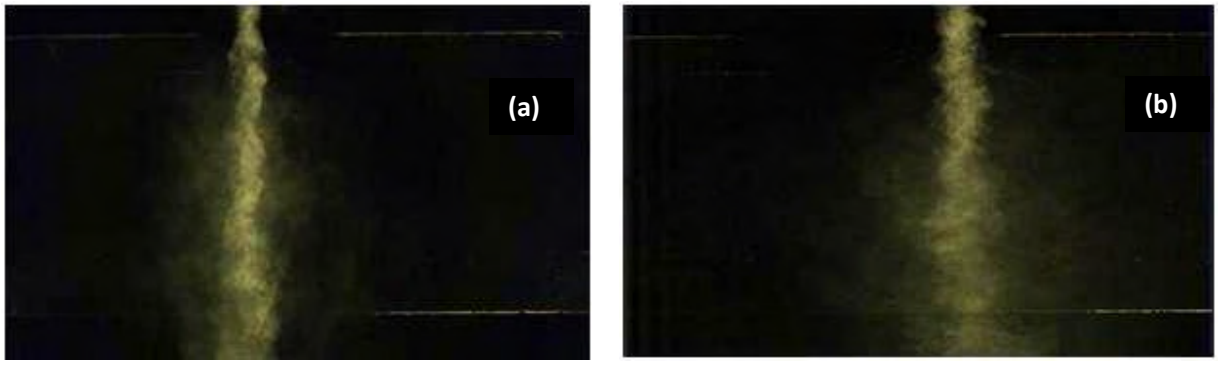

Figure 70: Top view of the time-averaged smoke flow over the airfoil at 10Deg (a) and 14Deg (b) AOA.

The time-averaged smoke flow at AOA=14Deg (Figure 70) also showed lateral smoke dispersion, implying the presence of strong spanwise flows. These flow patterns maybe attributed to the increased vulnerability of the shear layer to transition to turbulence as angle of attack increased, whereby instances occurred when flow reattachment occurred earlier at certain sections of the airfoil as compared to other locations, creating time-varying non-uniform flow across the span. While the manner in which transition occurs cannot be determined with absolute certainty using the data gathered, transition has been reported to be extremely complex, three dimensional and AOA dependant (Kähler (2003) and Burgmann et al (2006, 2008)). The presence of the smoke-wand upstream is also believed to have an influence, however small, on the observed flow structure. Refer Appendix C for further elaboration on the influence of the upstream smoke-wand on the flow over the airfoil.

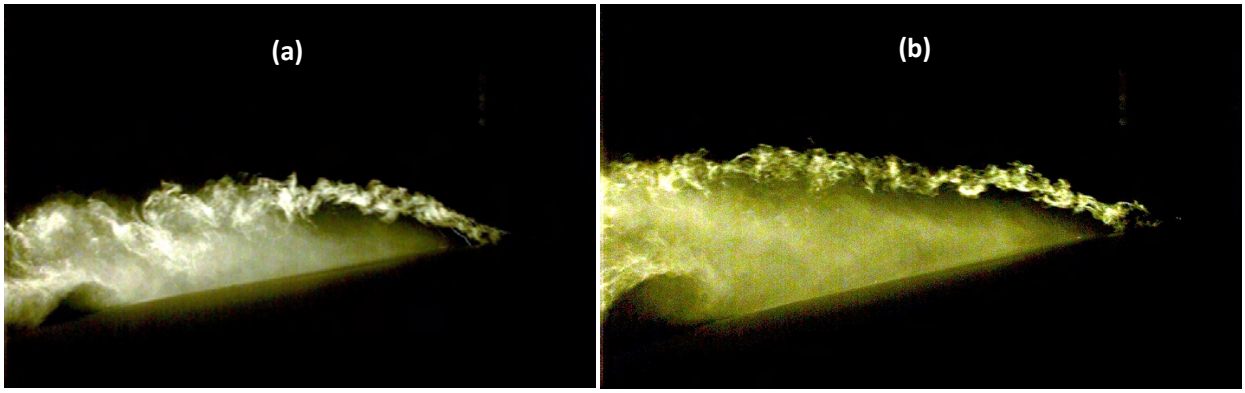

Figure 71: Instantaneous flow visualization when AOA=10Deg (a) and 14Deg (b), showing the airfoil in a stalled condition. Characteristic bluff-body-like vortex shedding can also be seen at the TE. Ti=1.2% and Re=75000.

All the pressure measurements presented thus far were from the measurements made along the chord at one spanwise station. However, to investigate the lateral flow effects, measurements were taken at four spanwise stations for each angle of attack. These measurements were brought together to provide an idea on the time-averaged structure of the flow over the airfoil span.

Figure 72 shows the variations of mean and Std.Dev of Cp over the airfoil span at various AOAs. Figure 72 is to be interpreted as follows; depending on the figure, the negative mean or Std.Dev of Cp at each chordwise (y axis) and spanwise (x axis) location is plotted on the x-z plane with the color intensity representing the magnitude. The rapid growth of the bubble is clearly captured here. In the figures it can be seen that the region of reattachment or elevated fluctuation (high Std.Dev) followed immediately after the region of recirculation or constant mean Cp. A nominally 2D time-averaged pressure distribution can also be observed. The reasons for small spanwise variations in the pressure distribution in the figures are addressed in Appendix B.

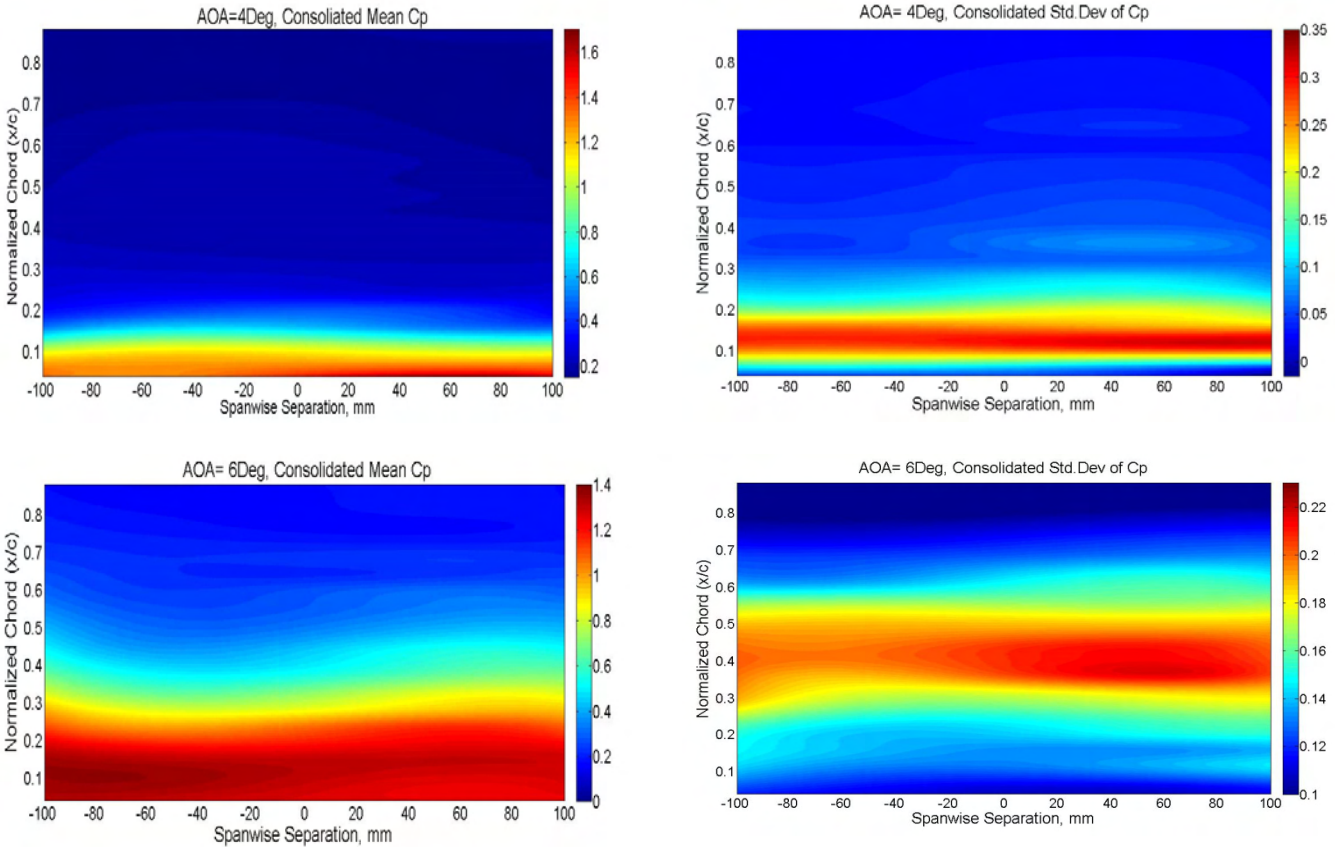

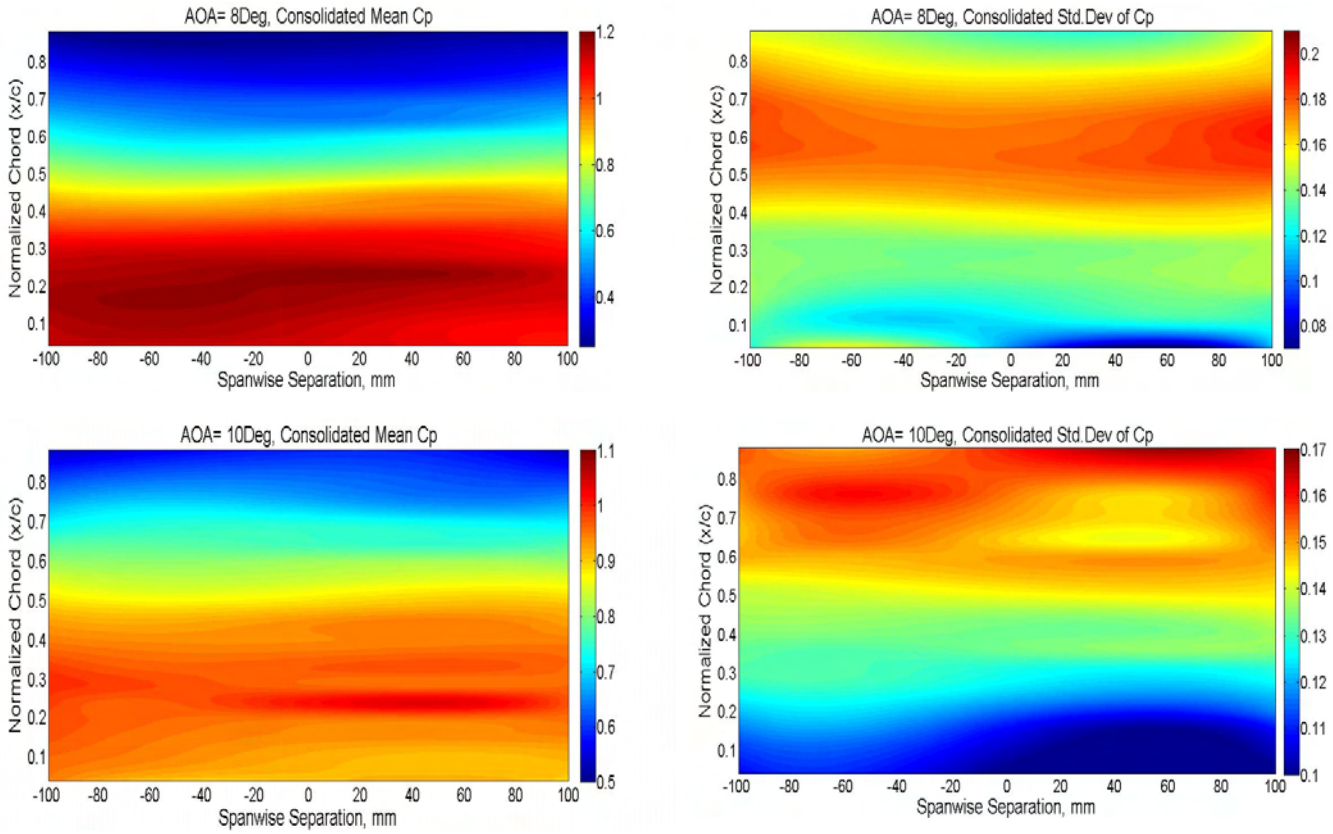

Figure 72: Series of plots showing spanwise distribution of inverted mean and Std.Dev of Cp at various AOA when subjected to nominally smooth conditions, i.e.Ti=1.2%. Refer plot title for AOA and pressure property.

3.2 A consolidated View of Pressure Distribution in Smooth Flow

Attempts were made to obtain a suitable non-dimensional relation such that all mean and Std.Dev of Cp over the range of AOAs would collapse to a universal relationship, however these were futile. As the flow over the airfoil passed through three distinct phases viz. fully attached, with LSB and fully detached conditions, it was not possible to obtain a universal expression for mean Cp distribution across all AOAs. However, for the AOAs where LSBs were present (between 4Deg to 10Deg) the mean Cp collapsed into a nominally similar trend as seen in Figure 73. The plot indicated that the length of the recirculation region within the bubble that is least influenced by the disturbances induced during reattachment was usually around 40% of the total bubble length.

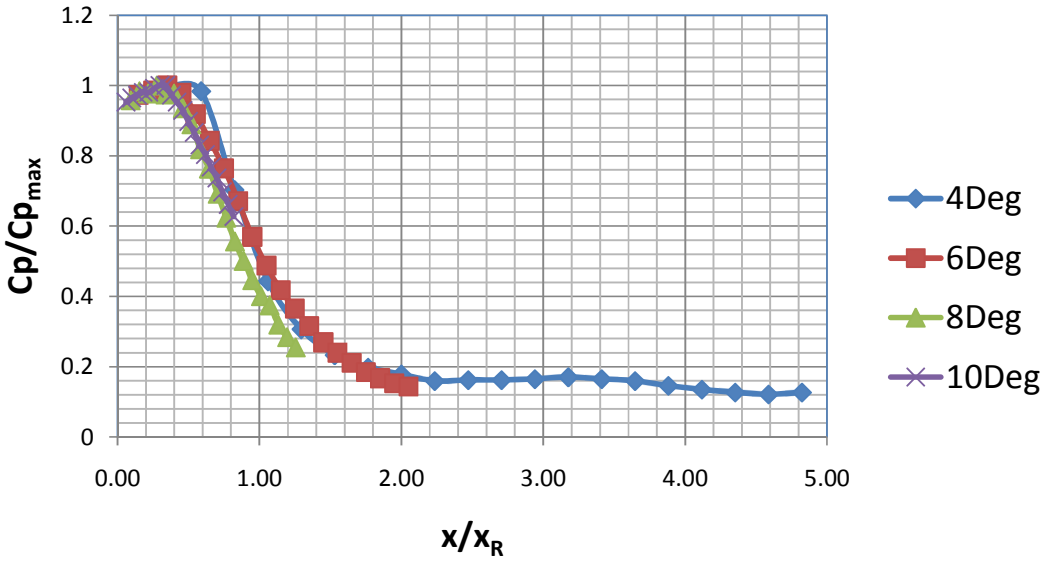

Figure 73: Mean Cp distribution over the airfoil between 4Deg to 10Deg AOA. Local Cp is normalized against maximum suction Cp and pressure tap location normalized against point of reattachment.

The Std.Dev of Cp generally increased along the chord until the point of reattachment where it was highest. The Std.Dev of Cp on reaching the maximum then appeared to stabilize for a short distance after which it decreased. The location of reattachment of the shear layer did not remain constant with time and this region of high Std.Dev represented the region over the airfoil where the point of reattachment oscillated as also noted by Devinant et al (2002). From Figure 74, the oscillation region can be seen to increase quite rapidly with increase in AOA. This might due to the fact that, as length of the bubble increased, it became more susceptible to disturbances which greatly influenced the shear layer's ability to undergo transition and reattach, consequently the location of reattachment varied considerably. The length of the bubble, as estimated from the point where maximum Std.Dev of Cp occurs or the center point on the oscillation region plateau, can also been seen to grow rapidly with AOA. In the same figure, the length of constant mean Cp is also plotted and it also increases non-linearly but not as greatly as the oscillation length. The increase in length of region of constant mean Cp gives an idea on the size of the recirculation region within the bubble.

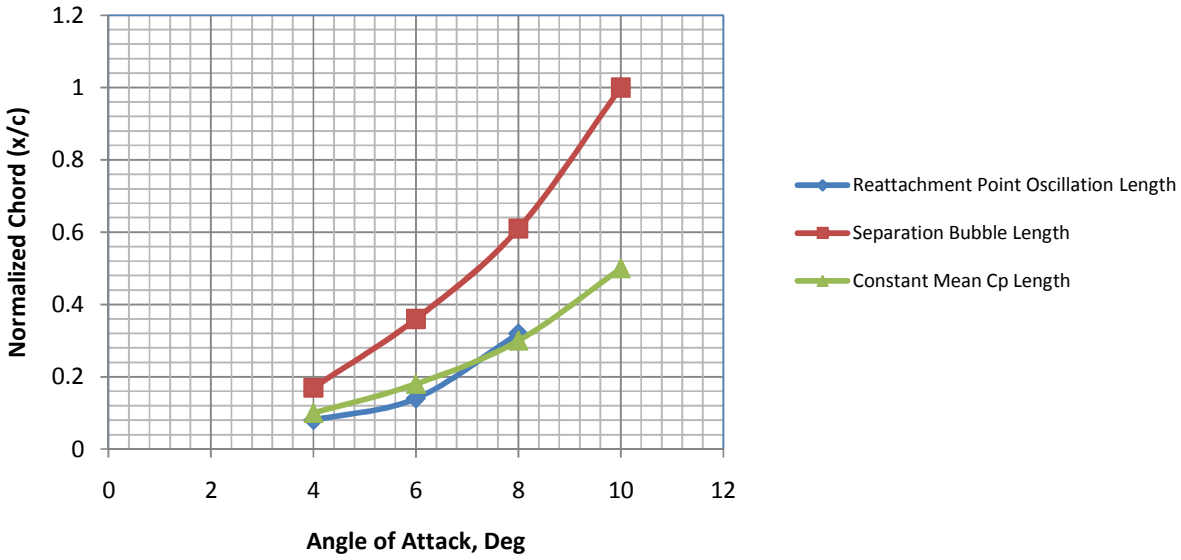

Figure 74: Various quantitative characteristics of the LSB between 4Deg and 10Deg AOA

As the bubble got longer and larger with increasing AOA, the strength of recirculation appears to decrease. This can be inferred from the reduction in the maximum Std.Dev of Cp and the continual rise in surface pressure as AOA increases see Figure 75. At the onset of bubble formation (AOA=4Deg onwards) significant change in both quantities (Mean and Std.Dev of Cp) can be noticed, while at stall (AOA=10 Deg), a slight change is seen in the minimum mean Cp however the maximum Std.Dev follows the same decreasing trend (Figure 75). This may be due to instances when increased ambient disturbances render the shear layer reattach near the airfoil trailing edge, increasing the fluctuations experienced by the airfoil. At 14Deg AOA however, a relatively higher drop in maximum Std.Dev of Cp is evident implying that the shear layer was unable to resist the Adverse Pressure Gradient (APG) and thus remained fully detached at all times from this AOA onwards.

NB. The inferences made here are based on trends that are well above the range of variation of the quantities due to errors in the setup, instrumentation and data processing. Refer Appendix A for further information.

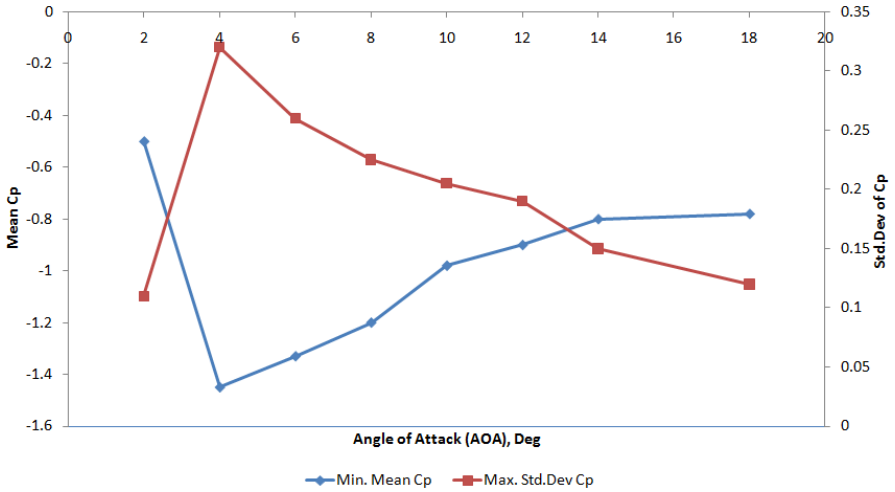

Figure 75: Variation of minimum mean Cp and maximum Std.Dev Cp with AOA. Ti=1.2%

Figure 76 presents a consolidated perspective of the mean and Std.Dev of pressure distributions over the airfoil for the different AOAs at the lowest turbulence intensities tested. The results from Loxton's experiments using the same airfoil section on a wing of AR=2 are presented in Figure 77. The plots are interpreted as follows; for each angle of attack (along x axis), depending on the figure, the distribution of inverted mean Cp or Std.Dev of Cp over the airfoil chord (y axis) is plotted across the x-z plane, with color intensity representing the magnitude. The small discontinuities ("troughs") seen between 2Deg and 6Deg in all the plots are due to large changes in the pressure distribution. It was concluded that these might be an artifact of the contouring routine used, however they are also exhibited in Loxton's findings.

In comparison to Loxton's findings (Figure 77), standard deviation plots indicated that a slightly longer bubble was present over the airfoil. This change in bubble length is believed to be due to the wing tip vortices present in Loxton's 3D airfoil experiments. It is strongly believed that these vortices increased the disturbances in the flow and rendered earlier reattachment of the shear layer hence shortening the bubble present over the wing. Shortening of the bubble would have an influence on the overall performance and this will be discussed in detail in forthcoming chapters. The color-bar on Loxton's Std.Dev plot represents the actual Std.Dev of pressures and not of the Cp hence magnitude comparisons between plots cannot be easily made.

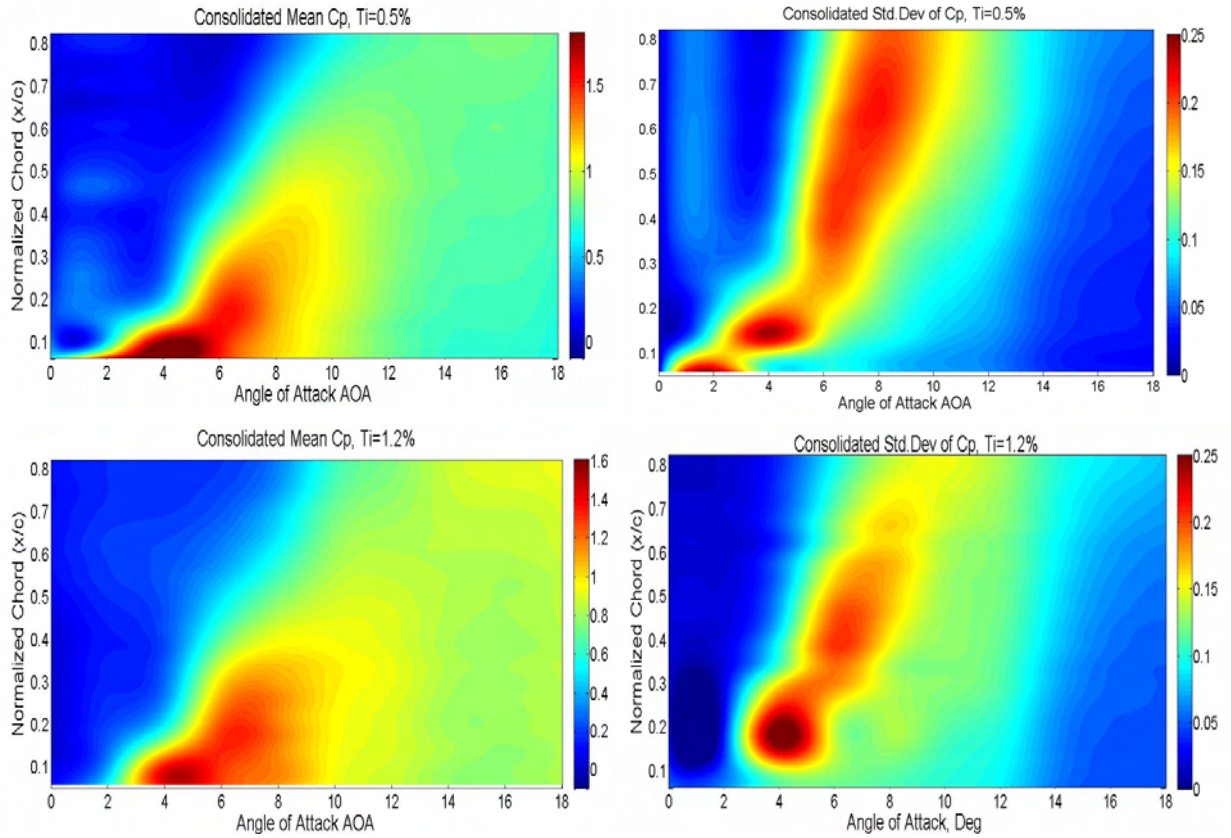

Figure 76: Consolidated view of inverted mean and Std.Dev of Cp over airfoil at different levels of low turbulence intensities, i.e. nominally smooth flow. Refer plot title for AOA and pressure property.

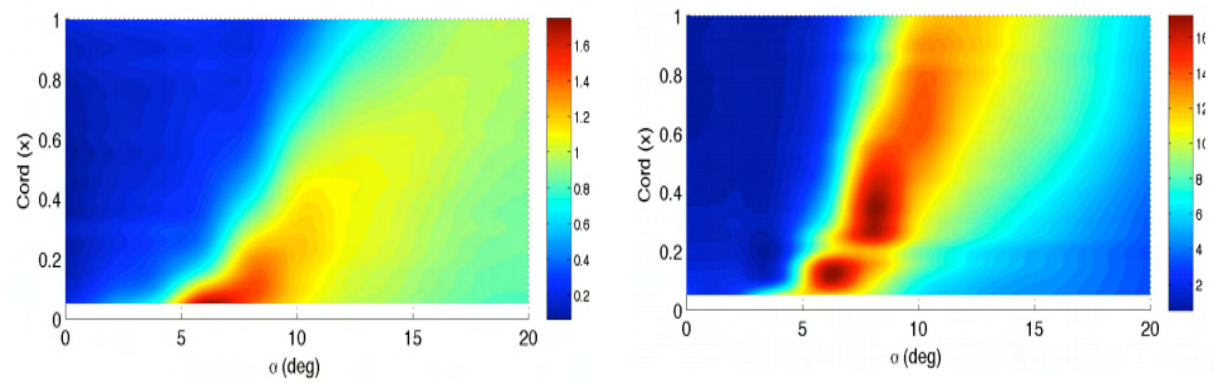

Figure 77: Consolidated view of inverted mean and Std.Dev of Cp over wing at Ti=1.4% i.e. nominally smooth flow. The wing had an AR=2. Refer plot title for AOA and pressure property. Loxton et al (2009).

Although the influence of significantly raised levels of turbulence will be examined in subsequent sections, it is worth noting that only a small difference between the pressures measured in the 0.5% and

1.2% turbulence intensity cases can be seen from the plots in Figure 76. At the lowest turbulence intensity, the growth of bubble seems slightly more rapid along with a marginal increase in suction. Mueller (1999) also found only a small influence of turbulence at such low levels on the mean forces and moment over the airfoil. A slightly higher suction was generated at the lower Ti condition along with a longer separation bubble. The lower level of turbulence meant the shear layer took longer to undergo transition and reattach. The higher Std.Dev of pressures noticed when Ti=1.2% is believed to be due to the increase in ambient disturbances in the flow resulting in an increase in the fluctuations experienced. From the airfoil and wing surface pressure measurements (Figure 76 and Figure 77), the LSB is seen to grow rapidly and nonlinearly in nominally smooth flow. Peak suction however appears to drop slightly as the turbulence level was raised from around 0.5% to 1.2%.

3.3 Pressure Distribution in Turbulence

Similar to the analysis conducted with measurements in nominally smooth flow, in this subsection the influence of varying elevated levels of freestream turbulence on the surface pressure distributions is presented and discussed. As both turbulence intensity and length scale are important metrics of turbulence, individual influence of each on the pressures in both chordwise as well as spanwise directions is analyzed.

3.3.1 Influence of Turbulence Intensity on Pressure Distribution

To understand the influence of relatively higher levels of turbulence intensity on the time-averaged pressure distribution over the airfoil, the results obtained from airfoil testing conducted in flow with freestream turbulence properties; Ti=7.2% Lx=0.14m and Ti=12.3% Lx=0.15m, will be compared. As the length scales in both the turbulence conditions was nominally the same and all other parameters were unchanged, any differences in the pressure distribution may be attributed to the influence of change in turbulence intensity.

At low AOA (AOA=0Deg-4Deg), the influence of turbulence intensity on the mean Cp distribution is hardly noticeable as seen in Figure 78. A small influence can however be noticed at 0Deg and -2Deg but this was only marginal. At 4Deg AOA, higher suction is created close to the leading edge in the 7.2% turbulence condition while pressure distribution over majority of the airfoil remains similar. In both cases however, the suction created is significantly lower than in smooth flow where the minimum mean Cp created at the same AOA was around -1.4 for this AOA.

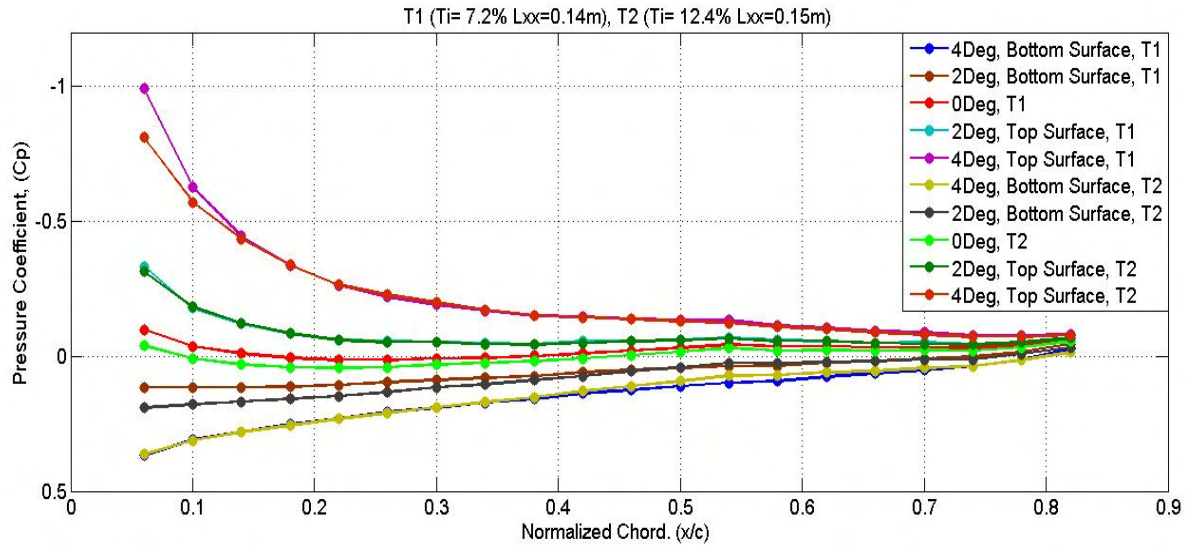

Figure 78: Mean Cp distribution over airfoil at 0Deg, 2Deg and 4Deg AOA with Ti=7.2% and 12%. Lxx=0.15m and 0.14m respectively, Re=75000

The standard deviation of Cp distribution presented in Figure 79 however shows considerable differences in the fluctuations occurring over the airfoil in the two turbulence conditions. Between 0Deg-4Deg AOAs, the standard deviation is much higher close to the leading edge when Ti= 12.3% as opposed to the Ti=7.2% case. However the Std.Dev near the Tailing Edge (TE) is slightly lower in the former. Similar to that noticed in smooth flow, a considerable increase in fluctuations is noticed at 4Deg AOA in both turbulence cases but at Ti= 12.3%, the rate of increase is higher. As turbulence intensity increased from 7.2% to 12.3% the ambient disturbances increased significantly, hence the magnitude of fluctuations across all AOAs also increased as shown in Figure 79.

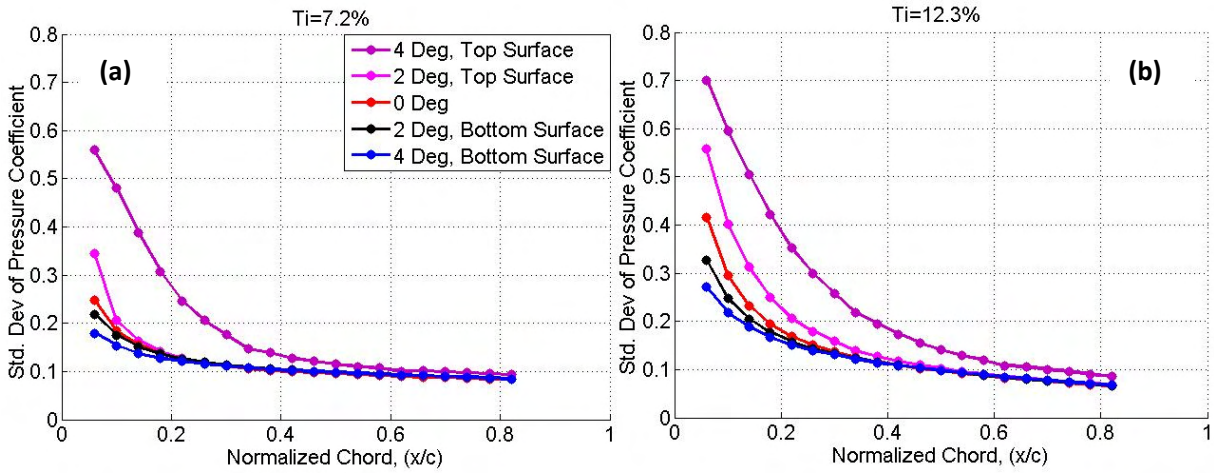

Figure 79: Std.Dev of Cp over the airfoil top and bottom surface at 0Deg, 2Deg and 4Deg. When (a) Ti=7.2% and (b) 12.3%. Lxx=0.15m and 0.14m respectively, Re=75000.

In nominally smooth flow, as well as at both the turbulence intensities, the pressure fluctuations experienced on the bottom surface at 0Deg AOA is more than that experienced at lower angles of attack; see Figure 61 and Figure 79. This trend suggests that as AOA increases, the changes in oncoming flow have little influence on the pressure distribution on the pressure side of the airfoil.

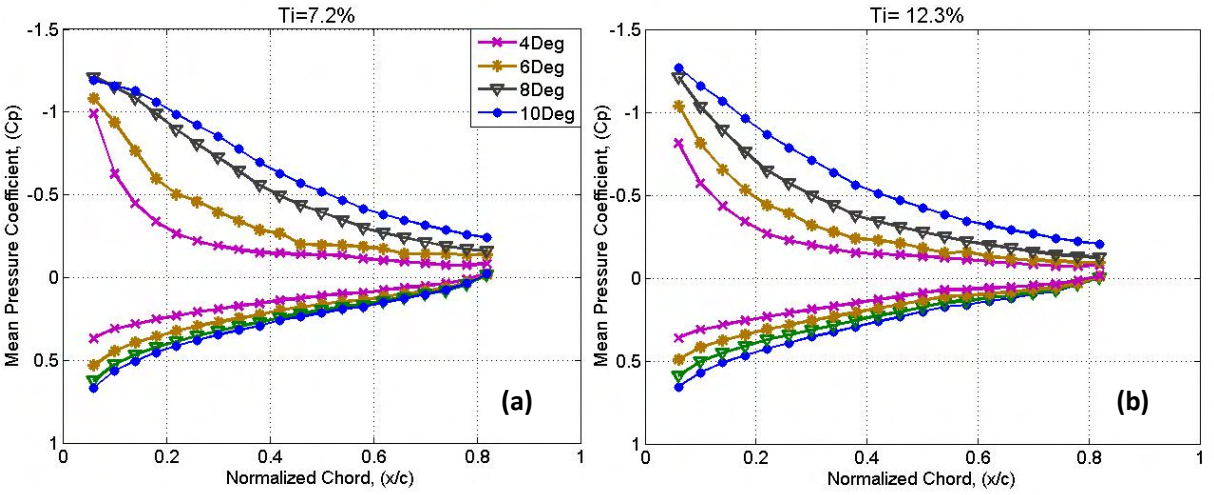

Figure 80: Mean Cp distribution over the airfoil top and bottom surface between 4Deg and 10Deg. When Ti=7.2% (a) and 12.3% (b). Lxx=0.15m and 0.14m respectively, Re=75000.

The region of constant mean Cp near the LE found in tests conducted in nominally smooth flow (Figure 63) is absent in both the higher turbulence intensities, which indicated that the flow remained fully attached over the airfoil, refer Figure 78. However, at higher AOAs (AOA>8Deg) when Ti=7.2%, a small region of constant mean Cp is noticed while fully attached flow still appears to be present at even 10Deg AOA when Ti=12.3%, see Figure 80. The plot of the Std.Dev of Cp at the same AOA (Figure 81) suggests that a small bubble may be present at 6Deg which keeps increasing with AOA when Ti=7.2%. A similar trend is noticed in the Ti=12.3% condition however only after 8Deg AOA.

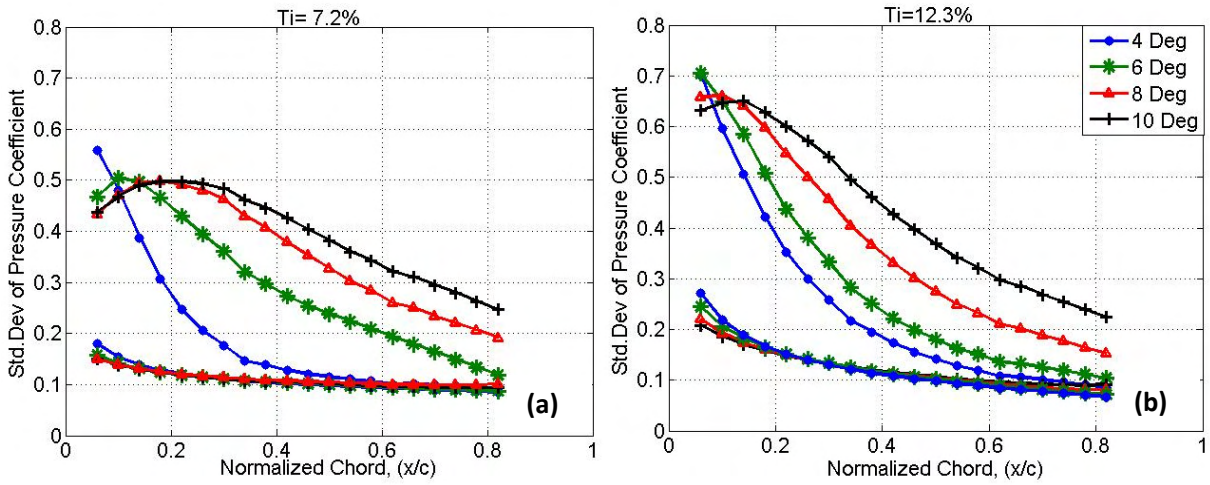

Figure 81: Std.Dev of Cp distribution over the airfoil top and bottom surface between 4 and 10Deg. When Ti=7.2% (a) and 12% (b). Lxx=0.15m and 0.14m respectively, Re=75000.

The absence of a region of constant mean Cp and the location of maximum Std.Dev staying close to leading edge till around 6Deg implies that the shear layer undergoes transition to turbulence even before separation occurred, a feature that happens at higher Reynolds numbers. However, smoke flow visualization revealed that large bubbles formed even at low angles of attack (AOA<6Deg) when high freestream turbulence was present, see Figure 82. The formation of LSBs even at low AOAs can be attributed to the local pitch angle fluctuations experienced due to turbulence. A sample time history of freestream local pitch angle fluctuations experienced when Ti=7.2% and Ti=12.3% is presented in Figure 83. Due to the large variation in pitch angle experienced by the airfoil in turbulence, the flow over the LE passes through times of fully attached to fully detached conditions, even when the airfoil is set at a low

AOA. These transitions become more frequent when turbulence intensity increases, hence the fluctuations in pressures thus also increase significantly.

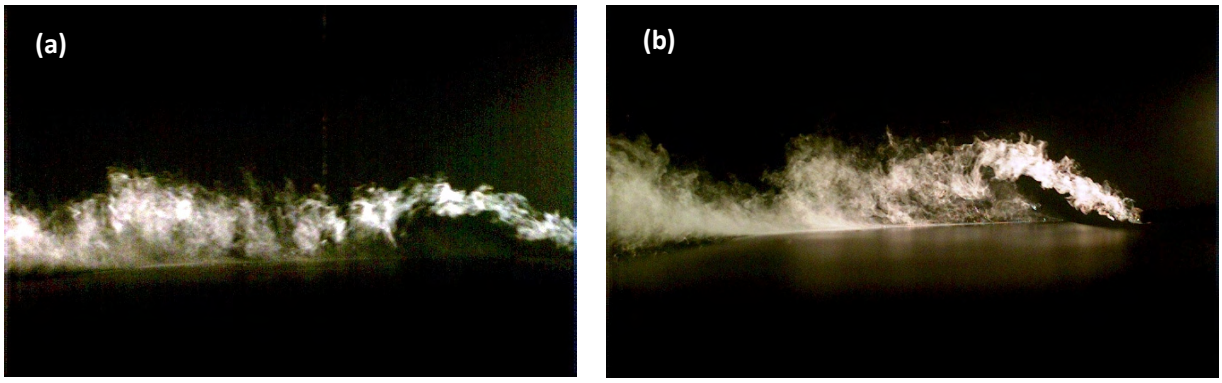

Figure 82: Side view of instantaneous smoke flow over the airfoil at 2Deg AOA, with freestream properties of Ti=7.3% Lxx=0.22m (a) and Ti=12.6% Lxx=0.31m (b). Re=75000 for both cases.

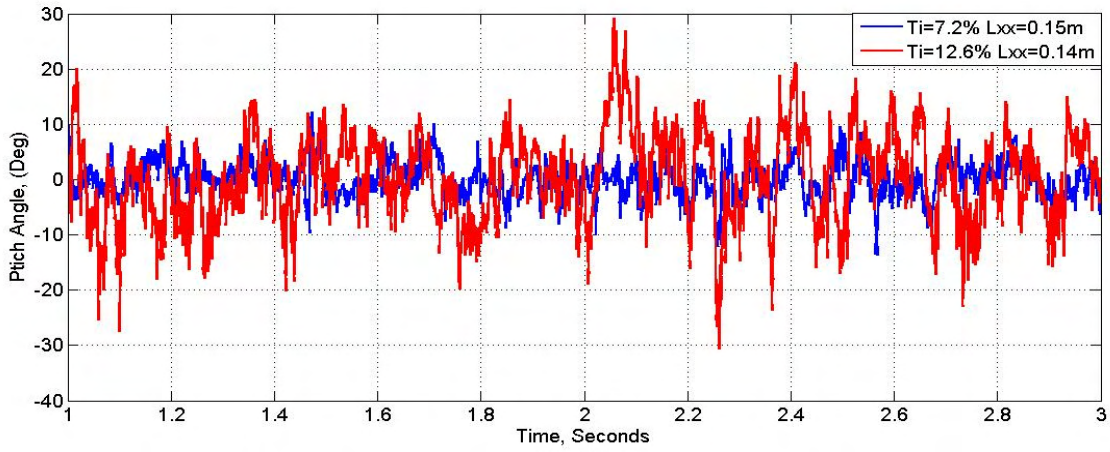

Figure 83: Sample time series of typical pitch angle fluctuations measured in flow with turbulence properties, Ti=7.2% Lxx=0.15m and Ti=12.6% and Lxx=0.14m.

Flow visualization revealed that in high levels of turbulence, when the LE encountered a sudden increase in pitch angle, flow separation occurred from the LE similar to smooth flow conditions. But unlike in smooth flow, due to the increased levels ambient unsteadiness when Ti was high, the shear layer appeared to attain transition much earlier and due to further amplification of disturbances, an enhanced roll up of the shear layer was observed. This enhanced roll-up could be seen to lead to the formation of vortical cores which advected downstream over the airfoil (Figure 84). The vortical cores were different

compared to LSBs in that, it would appear that significantly higher flow circulation and pulsating cycles of rapid growth and dispersion was noticed in the former. In smooth flow conditions, vortex cores never formed, as only sections of the shear layer rolled up as recirculating fluid, while some of the fluid proceeded over the bubble. Inside the LSB, fluid entrainment and circulation appeared to be relatively mild, as shown in the instantaneous photo of smoke flow in smooth condition (Figure 65) where very limited smoke is noticed within the LSB.

It is considered that the vortical cores promoted significant mixing within the Boundary Layer (BL) leading to a reduction in suction produced over the airfoil. With an increase in Ti, the periods of vortical core formations became more frequent rendering further reduction in suction. This was evident by comparing mean Cp distribution in smooth flow and in both the turbulence intensities tested (Figure 63, Figure 78 and Figure 80). At AOA<10Deg, consistently greater suction pressures were created over the airfoil with a decrease in turbulence intensity. In spite of the increased mixing within the boundary layer at higher Ti, a high nominally constant suction was seen to be present close to the LE at higher AOAs. This indicated that (similar to smoother flow conditions) the top region of the separated shear layer accelerates rendering its velocity to be nominally greater than the mean flow speed even in elevated levels of turbulence. During shear layer rollup and on reattachment, due to the enhanced mixing, a relatively larger reduction in velocity ensued. Hence the region of high nominally constant suction was considerably shorter than that noticed in smooth flow. The formation, growth and advection of these vortical structures along with their influence on the time-varying oscillations occurring over the airfoil will be addressed in detail in the next chapter.

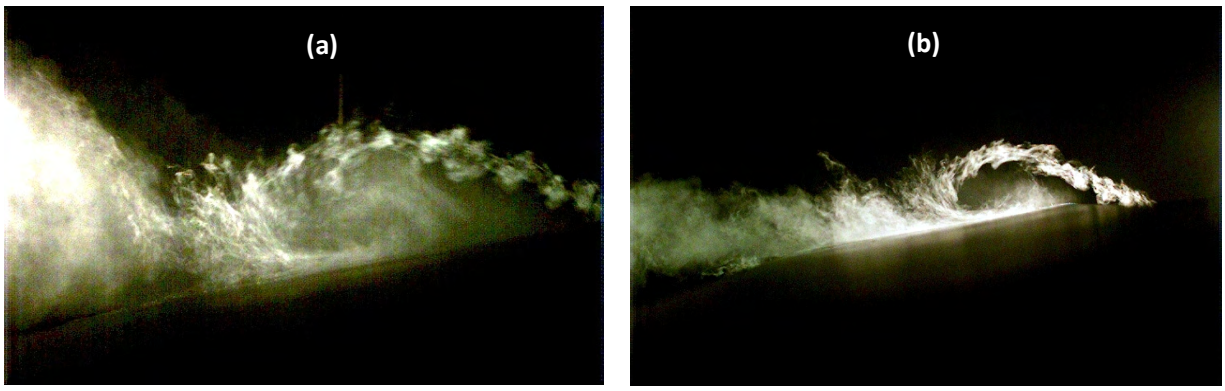

Figure 84: Side view of instantaneous smoke flow over the airfoil at 10Deg AOA showing the formation of vortical cores, when Ti=7.2% Lxx=0.15m (a) and Ti=12% Lxx=0.14m (b). Re=75000 for both cases.

At higher AOAs (AOA>10Deg) however, from Figure 63, Figure 69 and Figure 85 it can be seen that the peak suction increased as Ti increased. As freestream Ti increased it was considered that the airfoil experienced longer periods of attached flow condition through the formation the large vortex cores. The greater resistance offered to the APG by the shear layer and closer proximity of the shear layer to the airfoil surface in elevated levels of turbulence (due to what appeared to be earlier transition and vortex core formation) rendered a greater suction than that experienced when the shear layer remained fully detached (i.e. stalled condition).

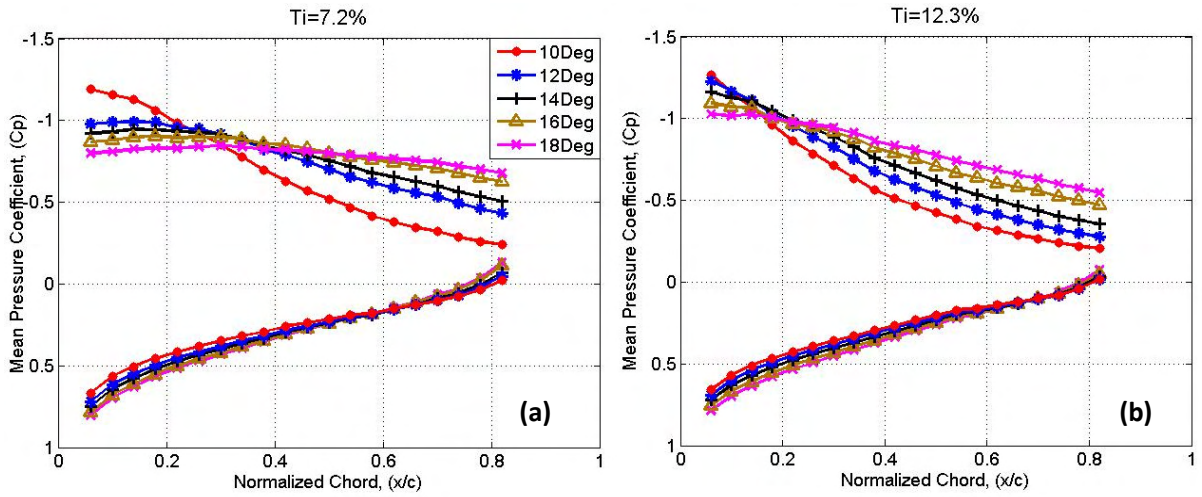

Figure 85: Mean Cp distribution over the airfoil top and bottom surface between 10Deg and 18Deg. When Ti=7.2% (a) and 12.3% (b). Lxx=0.15m and 0.14m respectively, Re=75000.

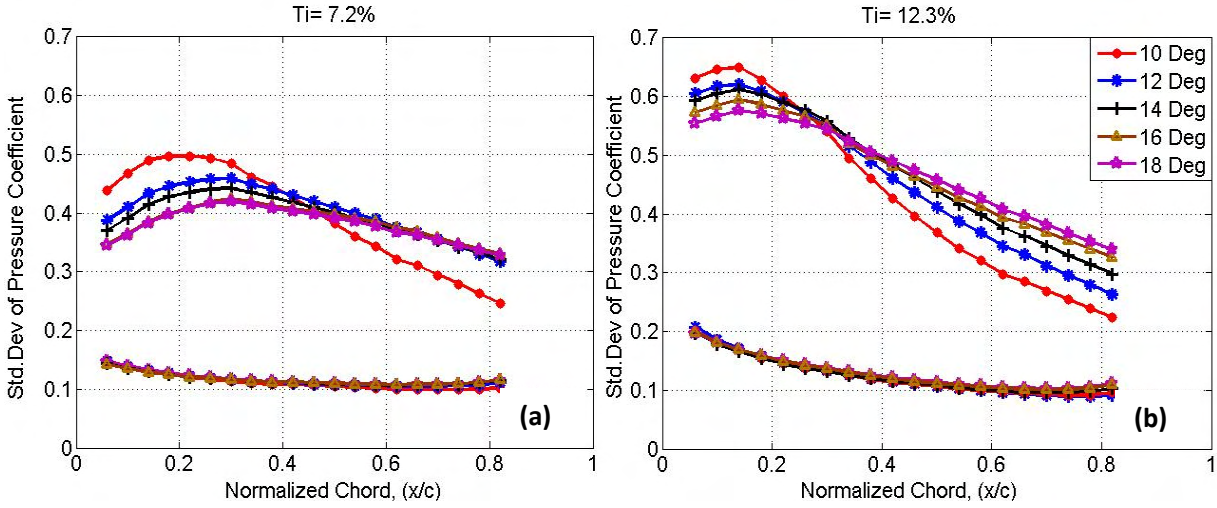

Figure 86: Std.Dev of Cp distribution over the airfoil top and bottom surface between 10Deg and 18Deg. When Ti=7.2% (a) and 12.3% (b). Lxx=0.15m and 0.14m respectively, Re=75000.

Analyzing the mean and Std.Dev of Cp at Ti=7.2% in Figure 85 and Figure 86, with increase in AOA past 10Deg, a steadier region of constant mean Cp was present. The airfoil seems to stall at around 14Deg whereby the mean Cp was relatively constant over the entire chord from that AOA onwards. This is considerably higher than the stall angle in smooth flow (10Deg). The Std.Dev plot (Figure 86) however indicated that the location of maximum fluctuation moves downstream only marginally with increase in AOA. Unlike in smooth flow, where at stall AOA the location of maximum Std.Dev was near the trailing edge, here, at 14Deg, it is located at around 0.3(x/c). In turbulence therefore, the location of maximum Std.Dev correlated with the region where vortex cores formed. The peak in Std.Dev became less acute with increase in AOA implying that the location where the vortical cores formed oscillated over a greater region at higher AOAs.

In comparison, at the higher turbulence condition (Ti=12%, see Figure 85 and Figure 86), a drop in min mean Cp is noticed as AOA increases, however the region of peak suction remains near the leading edge, throughout the range of AOA presented. Even when AOA=18Deg no sign of stall was present with the location of maximum Std.Dev remaining close to leading edge. The increased Ti seems to amplify the formation of these vortical cores, further delaying stall and increasing the fluctuations experienced.

In both smooth and turbulent flow, the mean and Std.Dev converged to a similar distribution on the pressure side, refer Figure 63, Figure 64, Figure 80 and Figure 81. While the mean Cp distribution was also very similar in all flow conditions (i.e. smooth and turbulent), the Std.Dev increased to around 0.15 Cp in 12% turbulence intensity from the 0.02 Cp in smooth flow. The lack of change in Cp distribution on the airfoil pressure side indicates that as AOA increases and the underside “faces” the flow more, due to the favorable pressure gradient the fluctuations in oncoming pitch angle and velocity have a significantly reduced impact. The influence of Reynolds number was also investigated and no notable changes were found in smooth and turbulent conditions.

Figure 87 shows the time-averaged pressure distribution over the airfoil at higher turbulence intensities by bringing together measurements made at the four spanwise stations. The delayed bubble formation along with its impaired growth when subjected to higher levels of turbulence intensity can be observed. Unlike in smooth flow, the region of constant mean Cp and region maximum Std.Dev can be seen to overlap in elevated levels of turbulence, implying a change in flow structure.

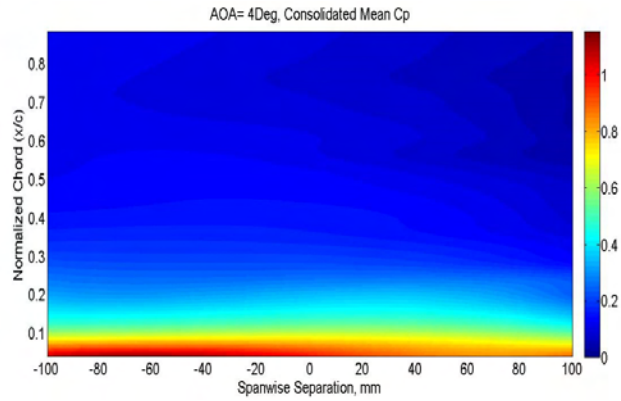
AOA= 4Deg, Consolidated Mean Cp
Normalized Chord (x/c)
Spanwise Separation, mm

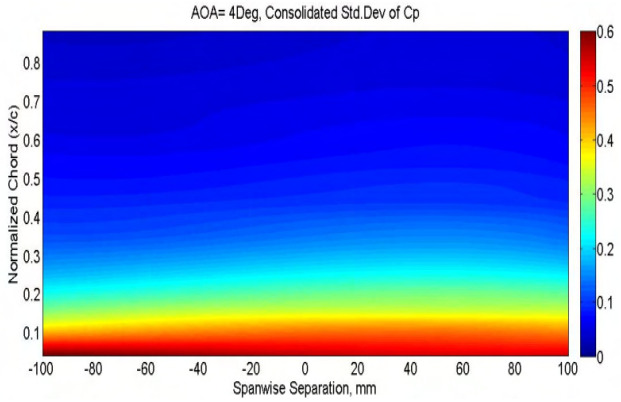
AOA= 4Deg, Consolidated Std.Dev of Cp
Normalized Chord (x/c)
Spanwise Separation, mm

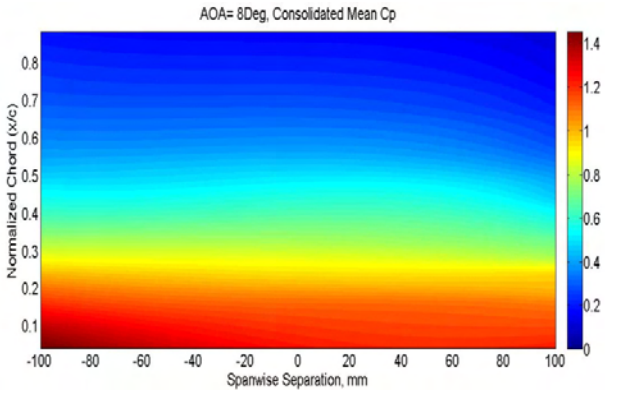
AOA= 8Deg, Consolidated Mean Cp
Normalized Chord (x/c)
Spanwise Separation, mm

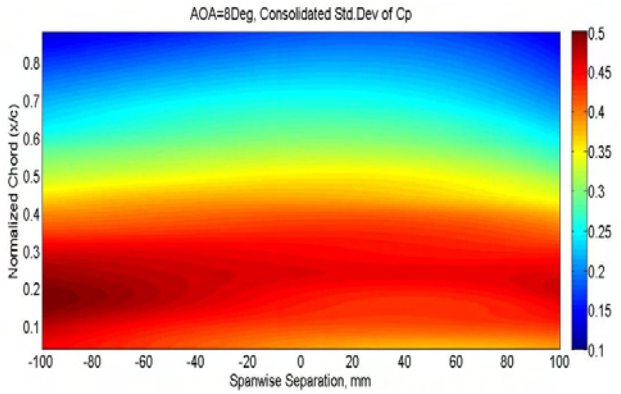
AOA=8Deg, Consolidated Std.Dev of Cp
Normalized Chord (x/c)
Spanwise Separation, mm

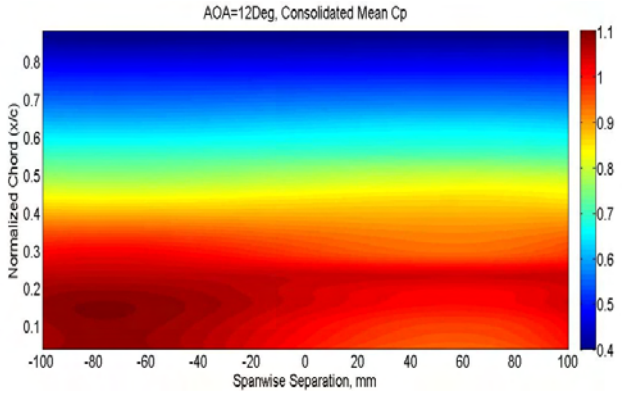
AOA=12Deg, Consolidated Mean Cp
Normalized Chord (x/c)
Spanwise Separation, mm

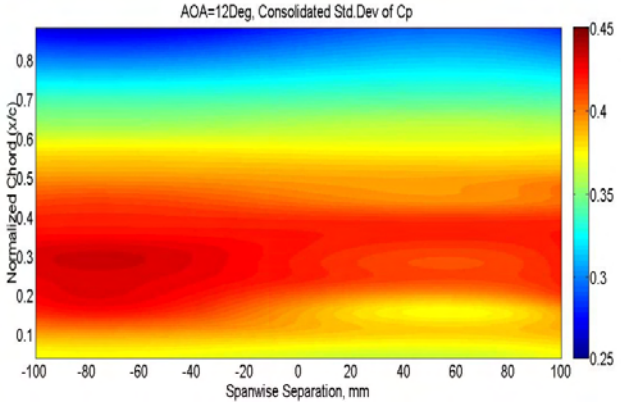
AOA=12Deg, Consolidated Std.Dev of Cp
Normalized Chord (x/c)
Spanwise Separation, mm

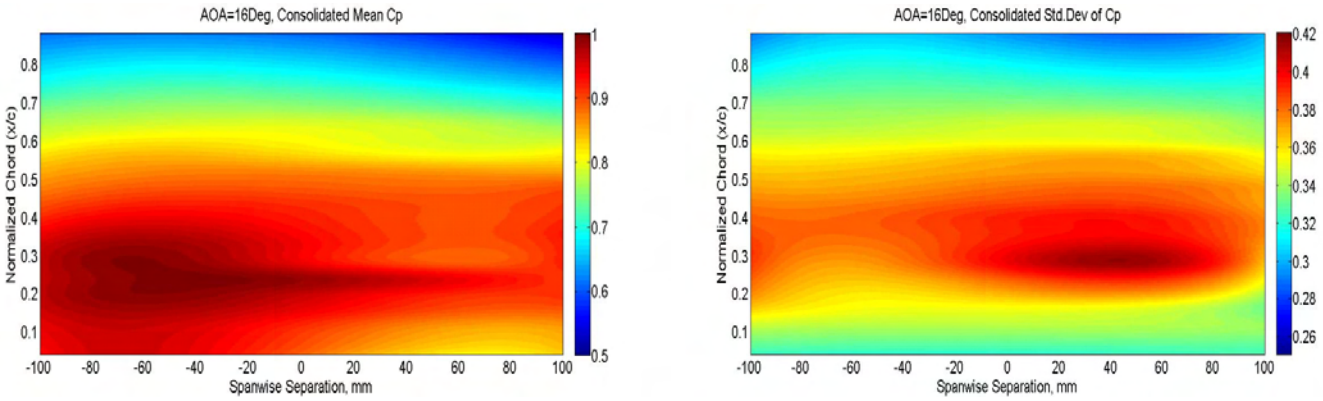

Figure 87: Series of figures showing spanwise distribution of inverted mean and Std.Dev of Cp at various AOA when Ti=7.15% and Lxx=0.14m. Refer plot title for AOA and pressure property.

3.3.2 Influence of Turbulence Length Scale on Pressures

In order to investigate the influence of turbulence length scale, comparisons were made between measurements obtained in the following flow conditions; Ti=7.15% Lx=0.15m, Ti=7.2% Lxx=0.22m and Ti=7.22% Lxx=1.3m. Comparisons were also made between measurements made in Ti=12.3% Lxx=0.15m and Ti=12.6% Lxx=0.31m to further understand the influence of length scale at higher turbulence intensities.

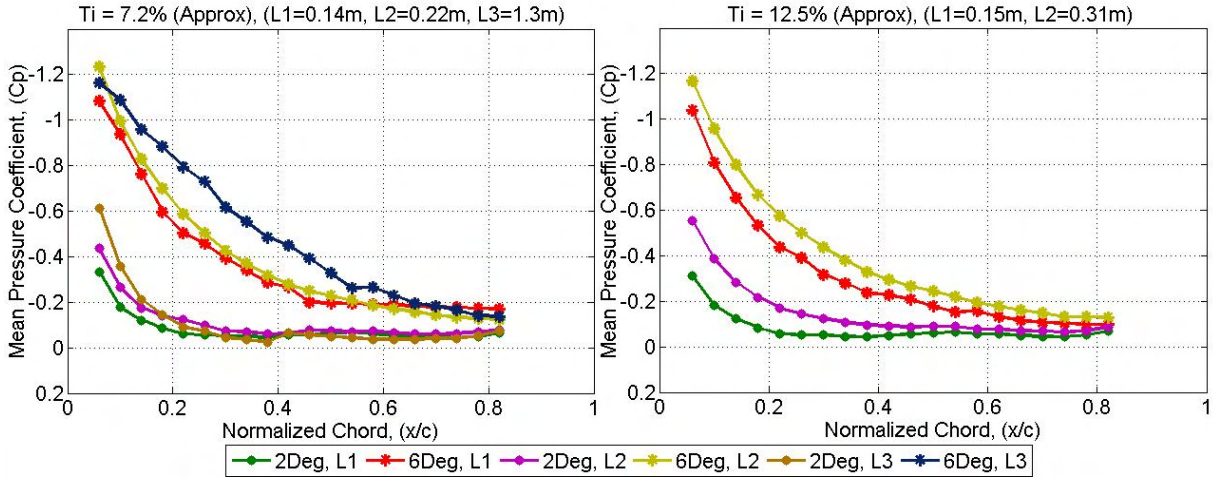

Figure 88: Mean Cp distribution over the airfoil top surface for AOA =2Deg and 6Deg at different length scales. For both figures, Re=75000.

At low AOAs, the suction produced was observed to be greater in longer length-scales and this trend was consistent even at higher turbulence intensities as seen in Figure 88. The plot of Std.Dev of Cp in Figure 90 shows that the magnitude of fluctuations experienced is also higher at longer length scales. This result is somewhat contrary to the findings of Li & Melbourne (1999), where the mean suction was found to decrease when a blunt flat plate was exposed to longer length scale flows, see Figure 89.

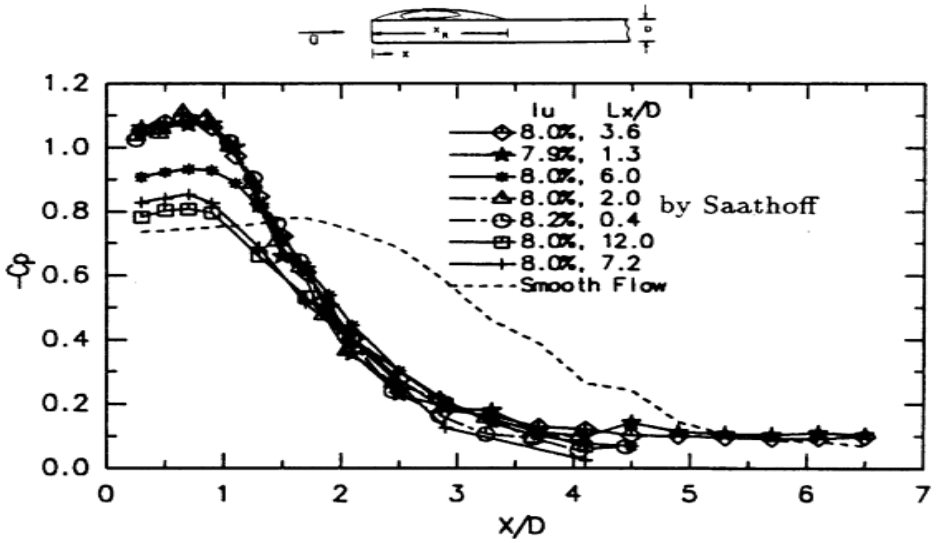

Figure 89: Mean Cp distribution over blunt flat plate exposed to different relative length scales at nominally constant Ti. Li & Melbourne (1999)

The reason for the difference in findings on the influence of length scale on time-averaged Cp distribution is unclear. However, the mean pressure distribution over blunt flat plates when subjected to varying levels of turbulence is different to that noticed over the airfoil used here. A greater mean suction was noticed over the airfoil in smoother conditions in comparison to the suction at higher levels of turbulence while the opposite can be seen to occur over blunt flat plates (see Figure 89). It is also believed that the manner of turbulence generation and the effect of the actual size of turbulence eddy

(i.e. the actual value of Lxx) and not the L_{xx}/D ratio would have a bigger impact on the results obtained. Elaborating, the peak energy in the flow would continually increase with increase in turbulence integral length scale (see spectra in Figure 51) while this would not be the case if the geometry of the testing object was altered. The results from this research however consistently indicated a greater suction was generated at larger length scales even as AOA increased past 10Deg as seen in Figure 90. It should be

noted that in spite of the noticed changes in Cp with change in length scale is small, the inferences derived here are well removed from the associated error bounds, refer Appendix A.

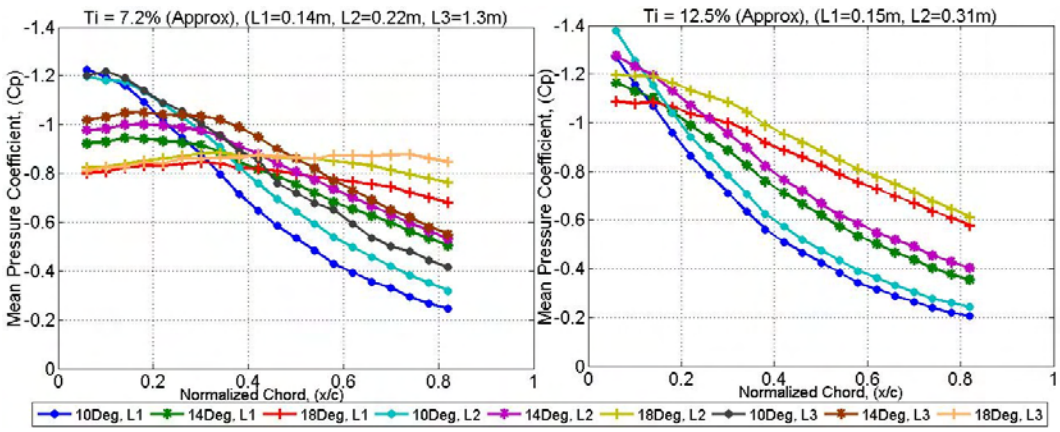

Figure 90: Mean Cp distribution over the airfoil top surface for AOA =10Deg, 14Deg and 18 Deg at different length scales. For both figures, Re=75000.

The findings here and the findings of Li & Melbourne (1999) however concurred with the fact that the mean Cp distribution at the longest length scale has closest resemblance to that observed in nominally smooth flow conditions. Similarly both finding indicated that a larger magnitude of fluctuations was experienced at longer length scales; see Figure 92 and Figure 93. Refer Figure 91 for Li & Melbourne's (1999) results.

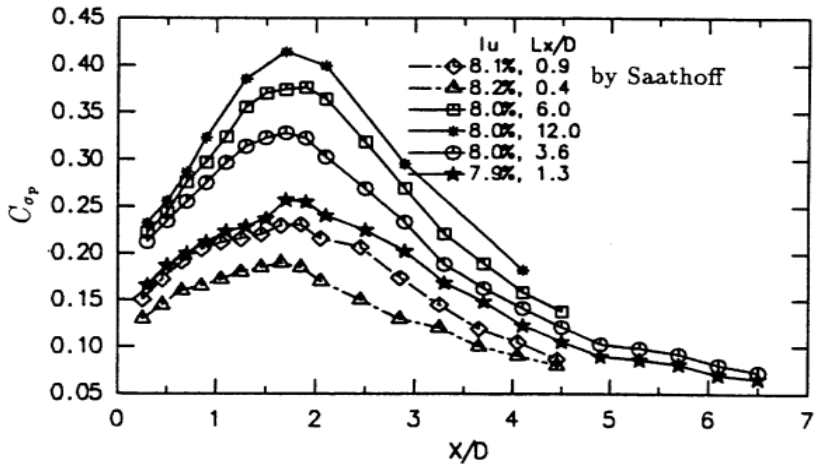

Figure 91: Std.Dev of Cp distribution over blunt flat plate exposed to different relative length scales at nominally constant Ti. Li & Melbourne (1999).

Therefore, findings in this research suggested that a greater suction was produced over an airfoil when exposed to longer length scales; however the fluctuations experienced also increases considerably. When compared to shorter length scale flows, at longer length scales the fluctuations in flow speed and pitch angle are relatively small at the higher frequencies whereby more oscillations occur in the lower frequency range. Therefore, the flow structure over the airfoil remains consistent for longer periods of time (be it fully attached, with LSB's or detached) since fluctuations occurred at a relatively slower rate. This sort of flow structure has a closer resemblance to the smooth flow condition and hence the suction generated is higher, similar to smooth conditions. However, as the peak energy of the oscillations in the oncoming flow is greater at longer length scales, the actual magnitude of fluctuations imparted is considerably higher, which in turn increases the Std.Dev. See Figure 51, for a consolidated view of spectra for all turbulence generated in this research. For the turbulence intensities generated, the peak energy (at the lower frequencies) is notable higher at longer length scales.

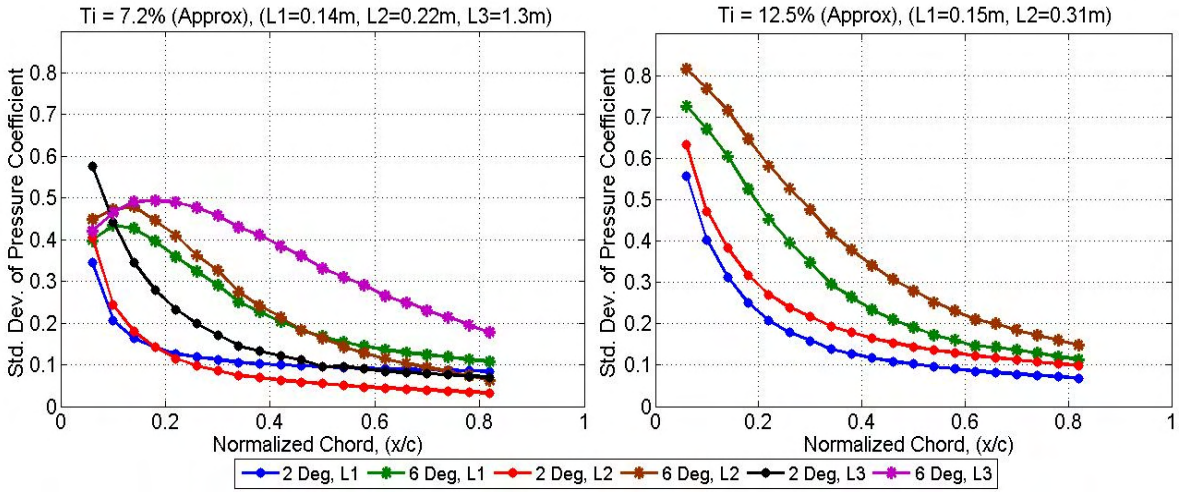

Figure 92: Std.Dev of Cp distribution over the airfoil top surface for AOA =2 and 6 Deg at different length scales. For both figures, Re=75000.

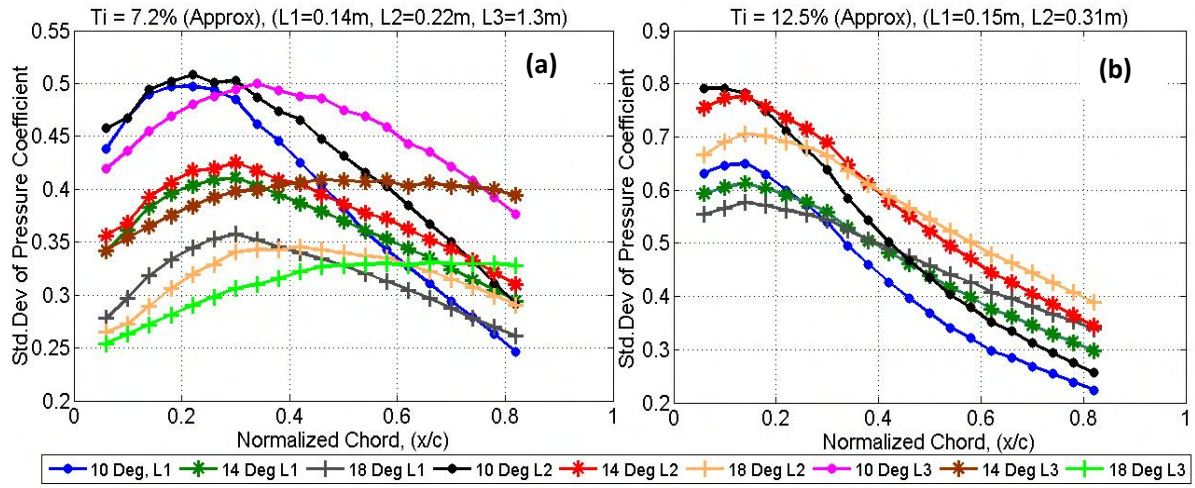

Figure 93: Std.Dev of Cp distribution over the airfoil top surface for AOA =10Deg, 14Deg and 18Deg at different length scales. For both figures, Re=75000.

At higher AOAs for longer length scales, the region of maximum Std.Dev can be seen to become wider, see Figure 93. This is believed to be because the flow structure over the airfoil remains consistent for longer periods (i.e. staying attached, with LSB or detached). At the higher turbulence intensity case, a lot more variation is seen in the fluctuations experienced, see Figure 93b. As for the influence of length scale at negative AOAs (i.e. the airfoil underside); since turbulence intensity itself did not have a large impact on the mean and Std.Dev of pressures experienced by the bottom surface due to the favorable pressure gradient, changes in length scale, which imparted comparatively lesser influence on the pressures, has an almost negligible effect on the airfoil lower surface as seen in Figure 94.

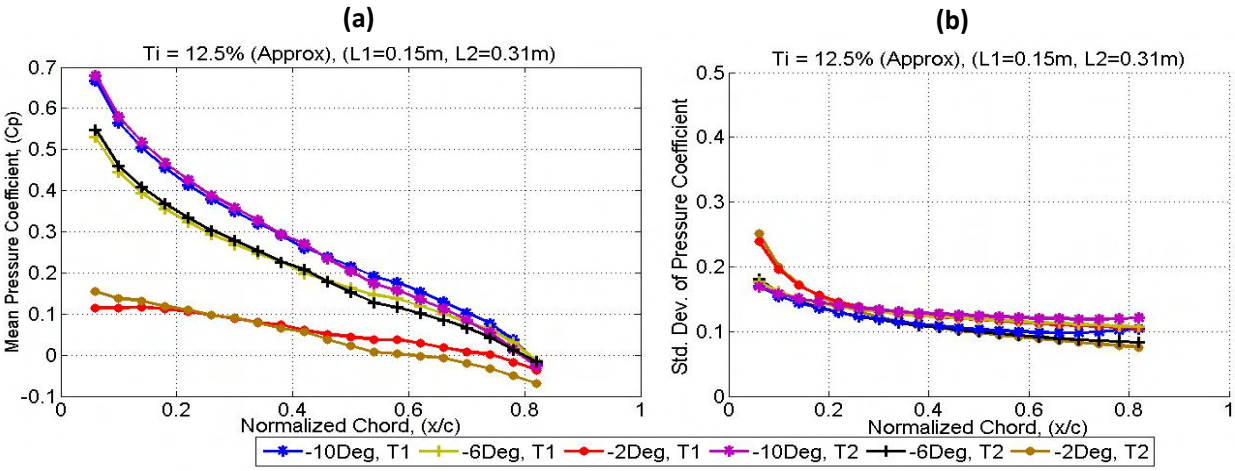

Figure 94: Mean (a) and Std.Dev (b) of Cp distribution over the airfoil bottom surface for AOA =2Deg, 6Deg and 10 Deg at different length scales. For both figures, Re=75000.

3.4 A Consolidated View of Pressure Distributions in Turbulence

Figure 95 provides a consolidated view of the mean and Std.Dev of Cp distribution over the airfoil across a wide range of AOAs. Comparing the figures below provides a global view of the influence of intensity and length scale on the pressure distributions.

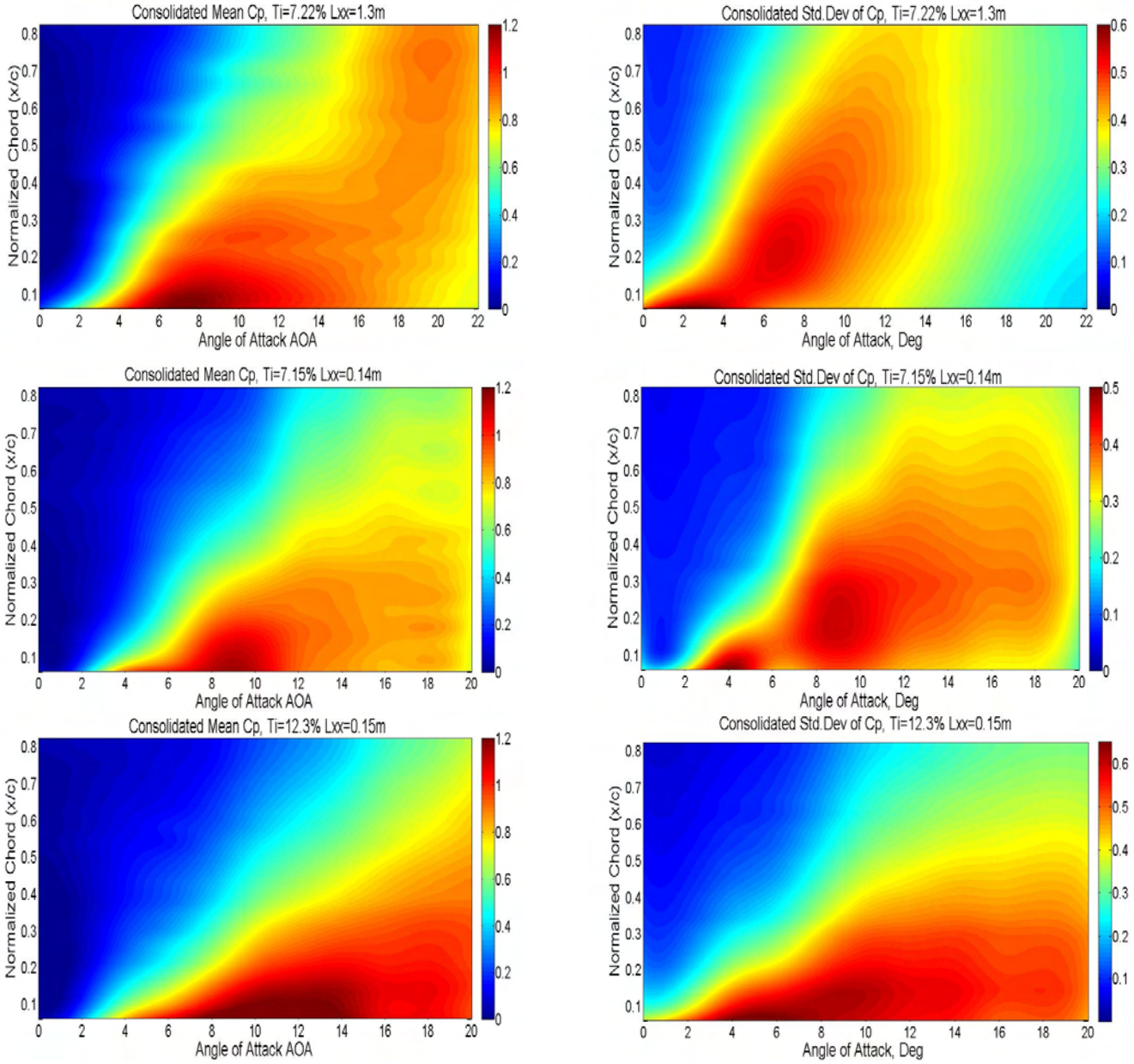

Figure 95: Consolidated view of inverted mean and Std.Dev of Cp over airfoil at different turbulence conditions. Refer plot titles for turbulence properties.

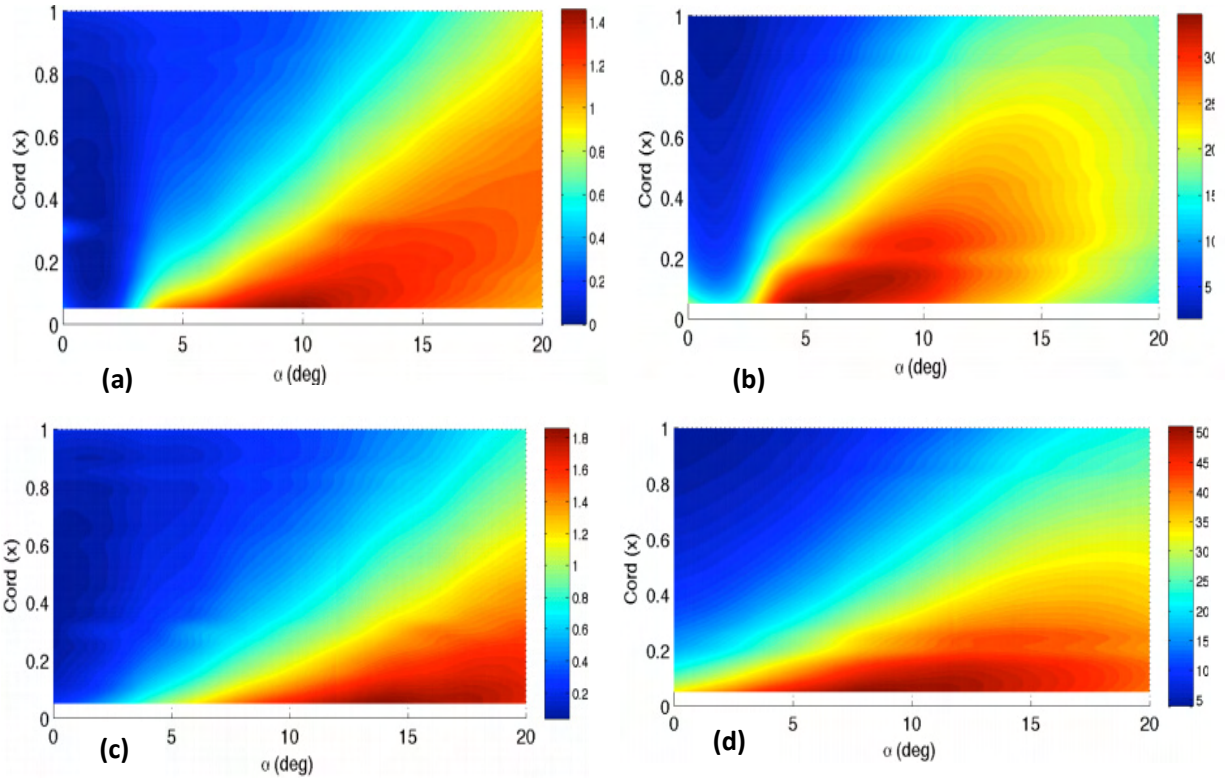

Figure 96: Consolidated view of inverted mean and Std.Dev of Cp over wing with AR=2 at different turbulence conditions. (figures a&b) Ti=7.3% Lxx=0.23m and (figures c&d) Ti= 12.6% and Lxx=0.31m. Loxton et al (2009)

As turbulence intensity increases, the rate of growth of the bubble can be seen to decrease considerably while the fluctuations experienced also increase. At the longer length scale the mean Cp as well as the Std.Dev contours become steeper having closer resemblance to distribution experienced in smooth flow. A similar trend was noticed over a wing with similar airfoil section and AR=2 by Loxton et al (2009).

3.5 Chapter Conclusion and Discussion

In the lowest turbulence intensities tested (nominally smooth flow), flow over the airfoil was found to remain attached till 2Deg AOA after which leading edge separation occurred along with subsequent reattachment leading to the formation of a LSB. The bubble then grew rapidly with increase in AOA until stall which occurred at 10Deg. Flow visualization indicated that only a section of the fluid in the shear

layer rolled up as recirculating fluid within the bubble, while some of the fluid passed over the same. The point of reattachment of the shear layer however did vary with time, whereby the reattachment point moved back and forth over the airfoil chord. Estimating the bubble length using the region of constant mean Cp was found to give a consistently lower length than by locating the point of maximum fluctuations. Flow visualization agreed well with the latter approach implying that to obtain an accurate estimate of the length of the LSB and its influence on pressures, time-varying pressure measurements must be taken.

In turbulence however, the flow-field was considerably different in that a larger section of the shear layer rolled up leading to the formation of vortical cores. These structures were different to LSBs whereby significantly higher circulation was present within the vortex cores and pulsating patterns of rapid growth and dispersion were also noticed. No such behavior was seen in LSBs, where the flow remained mostly chordwise until high AOAs. With increment in Ti, the magnitude of fluctuations experienced increased substantially along with the shortening of the bubble. At low AOAs, the peak suction produced was also higher at lower Ti due to the longer region of low pressure experienced beneath the bubble, while the opposite was noticed at high AOAs due to the increased resistance to an APG at higher Ti. The curtailed length of the bubble in turbulence significantly delayed stall.

Influence of turbulence length scale was comparatively limited; a slight increase in suction along with earlier attainment of stall was noticed at the longer integral length scales. This was due to the flow over the airfoil bearing relatively closer resemblance to smooth flow conditions. Due to the higher peak energy (at lower frequencies) in the oncoming flow fluctuations at longer length scales, the magnitude of fluctuations imparted was also higher.

CHAPTER 4

Further Statistical Analysis of Time-Varying Pressure and Velocity Fluctuations

The results presented in Chapter 3 showed the presence of a number of unsteady phenomena within the flow over the airfoil. In order to gain an understanding of the influence of turbulence on MAV flight dynamics, an understanding of the unsteady flow characteristics is required. In this chapter, the surface pressure and velocity fluctuations when the airfoil is exposed to different turbulence conditions will be analyzed with the aid of various other statistical processes and techniques. Effective comparisons will also be made between nominally smooth and turbulent flow to highlight the salient flow features in each condition.

4.1 Pressure and Velocity Fluctuations over Airfoil in Smooth Flow

A sample time series of fluctuating pressures measured at two locations over the airfoil chord is shown in Figure 97. It is evident that fluctuations of varying amplitude and frequency are experienced as AOA and on-coming flow conditions change. Significantly greater amplitude of fluctuation can be noticed at the location of reattachment as opposed to an arbitrary location when the flow remains fully attached. While the fluctuations appear to be random, distinct low-frequency oscillations can also be observed at reattachment in Figure 97. The formation and manifestation of these oscillations in pressure and velocity over the airfoil when subjected to nominally smooth flow will be analyzed in this sub-section.

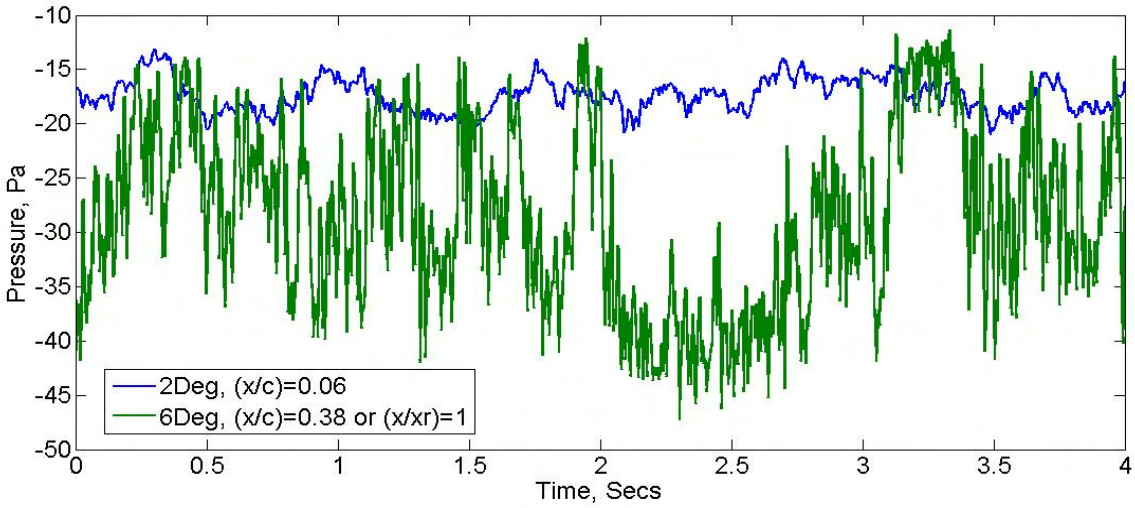

Figure 97: Sample Time series of fluctuating pressures measured close to LE at 2Deg AOA and at mean reattachment point when AOA=6Deg. Ti=1.2% and Re=75000

At low AOAs, in relatively smooth flow (Ti=0.5% and 1.2%), the flow remains attached throughout the airfoil and this is evident from smoke flow visualization. To identify any repeating patterns in the flow, velocity fluctuations were measured utilizing the Cobra Probe at center-chord and 10mm (z/c=0.066) above the surface for AOAs 0Deg & 2Deg. As expected, no peak in spectrum was observed in any of the orthogonal directions implying the fluctuations were fully random.

As indicated by the Std.Dev plots in the previous chapter, in comparison to attached flow condition the pressure fluctuations increased significantly when a separation bubble formed, the sample time series in Figure 97 concurs with this. A consolidated spectrum of all the pressure fluctuations over the chord at 4Deg AOA is presented in Figure 98. It should be recalled from the time-averaged results that a small LSB forms at this AOA. Figure 98 can be interpreted in the following manner; for each pressure tap along the chord (y-axis), the spectrum is plotted on the "x-z" plane, whereby the color intensity represents power (z-coordinate) at each frequency (x-axis).

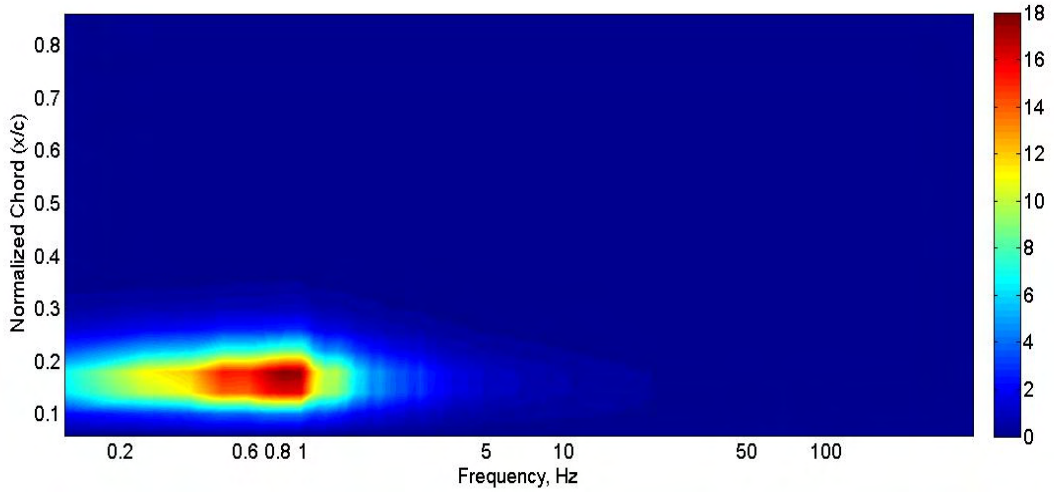

Figure 98: Consolidated PSD of pressure fluctuations over the suction side of the airfoil at 4Deg AOA. Ti=1.2% and Re=75000

A peak at around 0.9Hz in the spectrum of the pressure taps located between (x/c)=0.1-0.2 can be observed in Figure 98. This region of elevated power corresponds well with the region of oscillation of the shear layer reattachment point. Detailed checks confirmed that this peak in energy was not due to changes in oncoming flow or background noise, (refer appendix A), but a genuine flow phenomenon. At 4Deg AOA, the size of LSB was very small, hence velocity measurements over the airfoil were not considered. At 6Deg however, where the bubble size was significantly larger in height and length, velocity measurements were taken using the Cobra Probe. The spectrum of the velocity measurements taken at half length of the bubble ((x/c)=0.2) and (z/c)=0.1 above the airfoil, is presented in Figure 99. A peak at 0.9Hz and a weaker peak ("bump") between 150Hz-160 Hz can be seen in the spectra. The higher frequency peak is believed to be the frequency at which instabilities developed within the shear layer. Since no significant fluctuations in velocity was noticed in the spanwise direction (lateral axis, v), the spectra presented are only for fluctuations in the longitudinal (u) and vertical (w) directions.

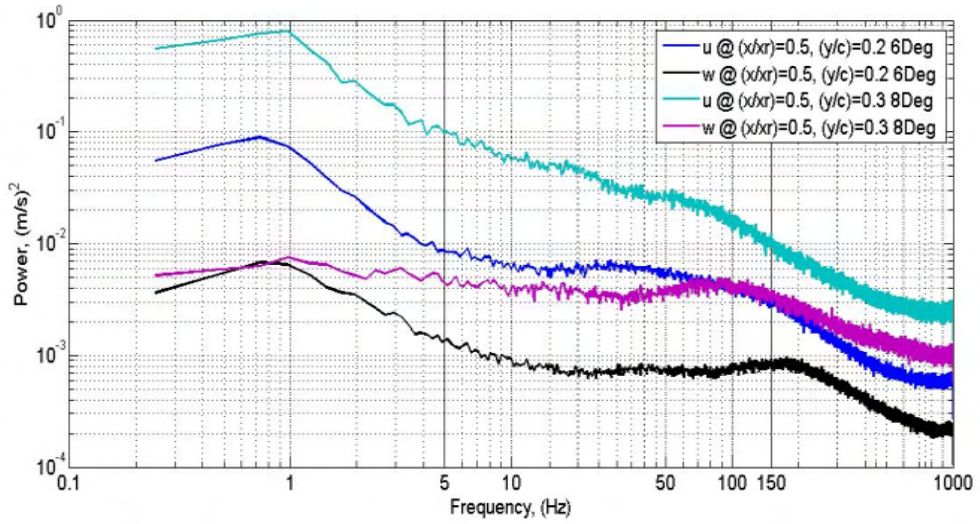

Figure 99: PSD of velocity measured at (z/c)=0.1 and (x/x_r) =0.5. AOA=6Deg and 8Deg, Ti=1.2% and Re=75000

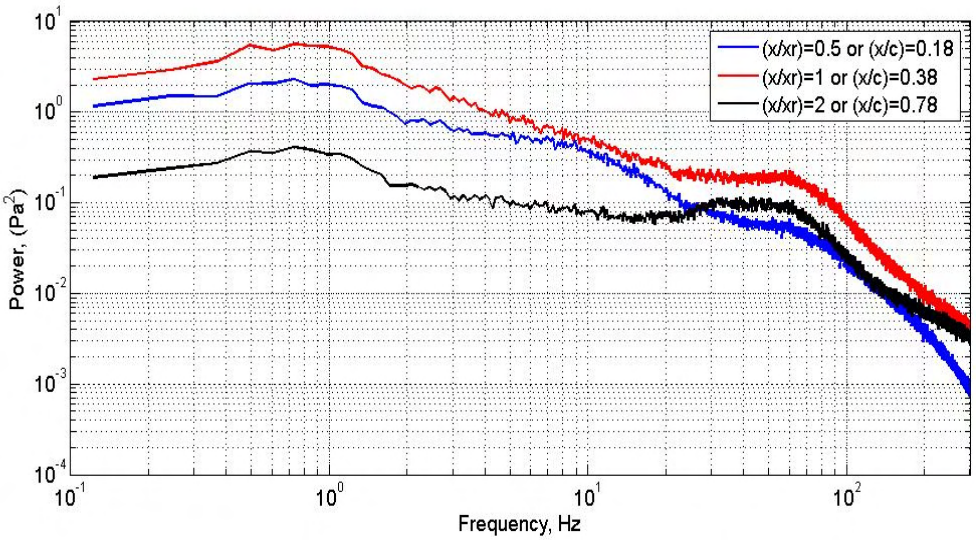

Figure 100: PSD of pressure fluctuations of a few pressure taps, AOA=6Deg, Ti=1.2% and Re=75000

It is generally accepted that a separated shear layer undergoes transition from laminar to turbulent flow through the amplification of initial disturbances. Smoke flow visualizations suggested that the separated shear layer in this case behaved like a free shear layer whereby Kelvin-Helmholtz-like (K-H) instabilities could be seen to develop in the lower regions, see Figure 101. Due to lack of velocity distribution data over the airfoil, it could not be determined with definite certainty that the observed instabilities in the separated shear layer here (Figure 101) were in fact K-H instabilities. However the instabilities seen in

Figure 101 resembled the K-H instabilities observed to develop in free shear layers that form over blunt flat plates (Abdalla & Yang (2004)) and over airfoils, where laminar separation close to the LE occurs (Hu & Yang (2008)), see Figure 102. The higher frequency peak (150Hz-160Hz) seen in the velocity spectra is therefore believed to be the rate of formation of the instabilities in the detached shear layer. The velocity measurements and flow visualization provide strong evidence suggesting that in this case transition occurs through the formation of K-H instabilities in the detached shear layer however velocity surveys with a high degree of spatial and temporal resolutions would be required to verify this. The flow visualizations indicate that the instabilities amplify (grow larger) as the flow advects downstream, leading to the rollup or curling inward of the shear layer. This rollup is however limited only to a section of the shear layer whereby fluid in the upper regions of the layer appear to pass over the re-circulating region. The fact that extremely limited smoke is seen within the bubble indicates that fluid entrainment into the bubble is very limited.

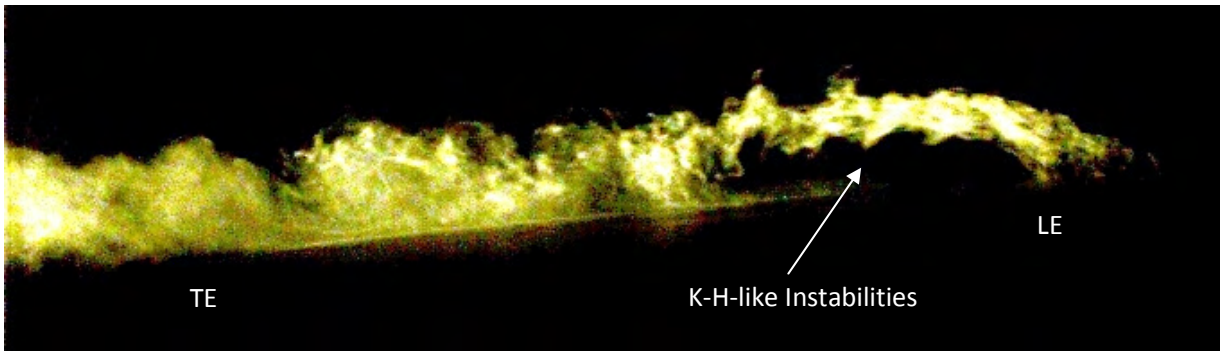

Figure 101: Instantaneous view of smoke flow showing the growth and amplification of K-H-like instabilities when AOA=6 Deg. Ti=1.2% and Re=75000

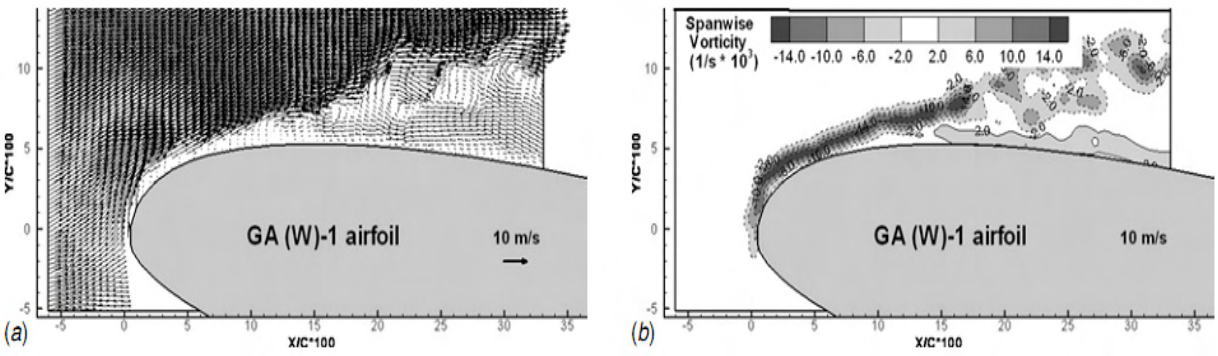

Figure 102: (a) Instantaneous velocity vectors and (b) instantaneous vorticity distribution close to the LE obtained through PIV measurements. Hu & Yang (2008)

Spectra of the pressures measured at some of the pressure taps at AOA=6Deg are presented in Figure 100. The frequency peak seen in velocity fluctuations at around 150Hz-160Hz (Figure 99) is absent here but the low-frequency high-energy oscillation, at the same frequency (around 0.9Hz) as seen in the spectra at 4Deg AOA, is distinctly present. The absence of the peak between 150Hz-160Hz in the pressure spectra could be because the fluctuations present in the detached shear layer diffuse rapidly at the onset of turbulence just prior to reattachment, Yarusevych et al (2008). These high frequency fluctuations however rendered oscillations of significantly lower energy as seen from the velocity spectra in Figure 99, as opposed to the lower frequency fluctuations which imparted much larger changes. The influences of these low-frequency high-energy fluctuations are of particular interest here.

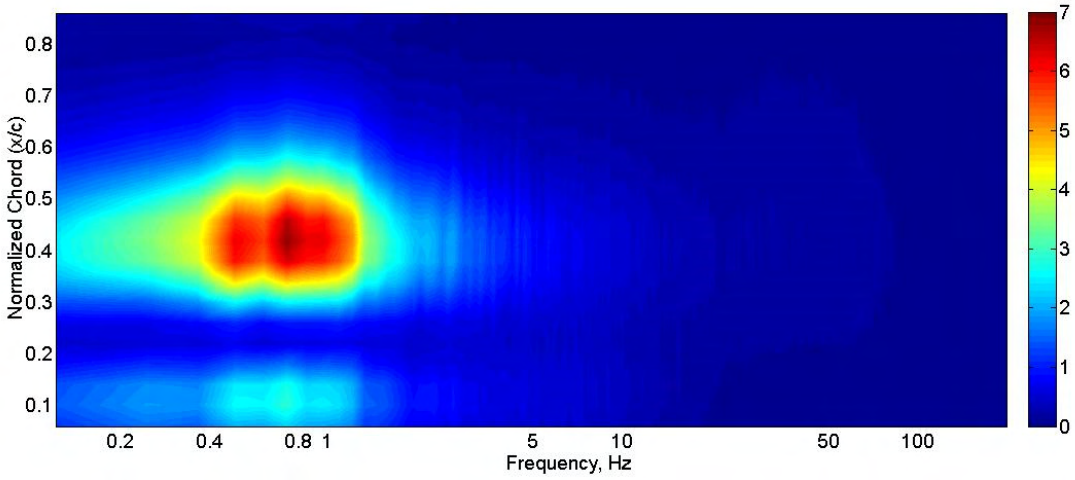

Figure 103: Consolidated PSD of pressure fluctuations over the airfoil at 6Deg AOA. Ti=1.6% and Re=75000

The consolidated spectra for the fluctuations experienced at all pressure taps over the chord at 6Deg AOA is presented in Figure 103. Here too, a peak can be noticed around 0.9Hz, but compared to 4Deg AOA the region is located further downstream, corresponding to the increase in bubble length. The increase in the chordwise region of peak fluctuations suggests an increase in length of reattachment point oscillation concurring with the Std.Dev plots presented earlier. Though the peak frequency of fluctuation agrees well with Loxton et al (2009)'s findings (Figure 104), the location of reattachment is much closer to LE in Loxtons's results. The time-varying influence of the disturbances due to the presence of wing tip vortices on the 3D airfoil (wing) can be clearly seen by comparing Figure 104 and Figure 103. The increased spread in elevated frequencies in Loxton et al (2009)'s results is believed to be

due to the higher Reynolds number at which tests were conducted and the increased ambient disturbances present in Loxton's experiments.

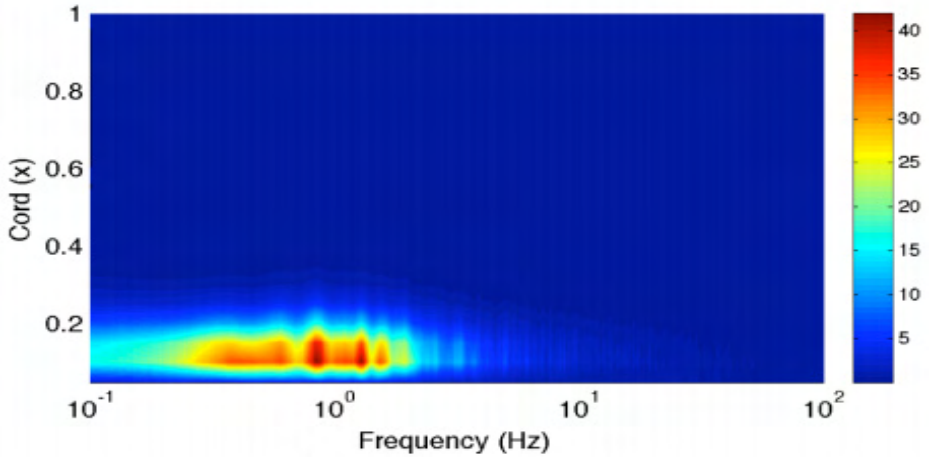

Figure 104: Consolidated PSD of pressure fluctuations over wing with AR=2 at 6Deg AOA. Loxton et al (2009)

In Figure 103, a secondary weaker peak at the same frequency can be noticed close to the LE. After careful analysis of the smoke flow visuals, this region was identified to be the other end of the recirculation region within the bubble where flow direction changes for circulation to occur. As the flow was tangential to the airfoil chord between those two regions, no peak was noticed in the spectra of pressure taps located there. To aid visualization, a schematic of the structure of a typical LSB is reproduced in Figure 105.

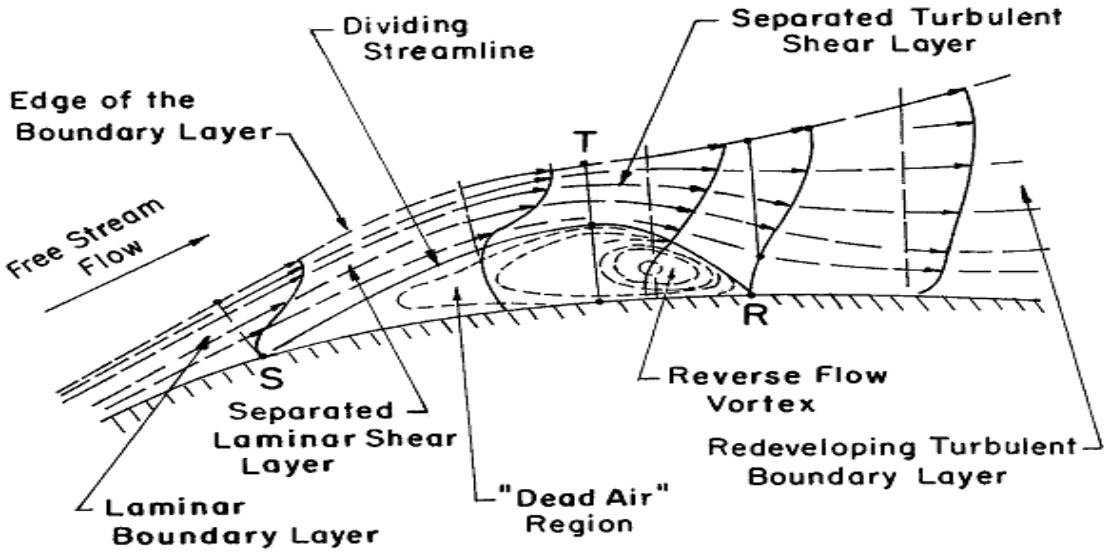

Figure 105: Anatomy of a typical laminar separation bubble. Horton (1968)

Apart from the low-frequency oscillations, a plateau can be seen between 30Hz and 60Hz in the spectra of the pressure fluctuations measured at, and downstream of, the region of reattachment, see Figure 100. Large-scale vortical structures can also be seen to form after reattachment of the shear layer, see Figure 106. The vortices observed after point of reattachment are believed to be responsible for the noticed increase in energy between 30Hz-60Hz in the pressure spectra. While the formation of these large-scale vortices have been observed in reattaching free shear layers present over blunt flat-plates (Cherry et al (1984), refer Figure 107), it is still unclear if they are a result of pairing of the initially formed instabilities. It is however believed that the large-scale vortices here formed due to the reattachment of the "rolled up" shear layer.

As these large-scale vortices moved over the remaining chord, due to viscous dissipation and other energy losses, they appeared to become weaker and hence more dispersed. The reduction in their intensity can be seen in the form of the drop in energy of fluctuations at the shedding frequencies at the downstream pressure taps, see Figure 100. As Figure 106 shows, the flow past the reattachment point consists mainly of these vortices that are shed in an unsteady manner. Even when turbulence intensity is low, the location of transition and hence reattachment of the shear layer changes, leading to the reattachment point moving back and forth, because of which an unsteady rate of formation of vortices occurred. A survey of the airfoil wake revealed that some of these vortical structures were still present in the near wake. Further analysis of the wake structure will follow later in this chapter.

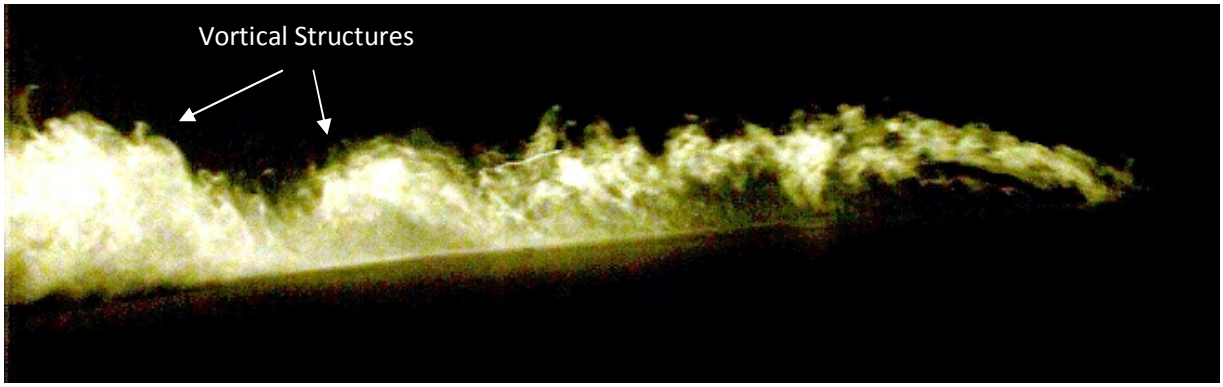

Figure 106: Instantaneous view of smoke flow showing large-scale vortical structures created at reattachment point when AOA=6Deg. Ti=1.2% and Re=75000

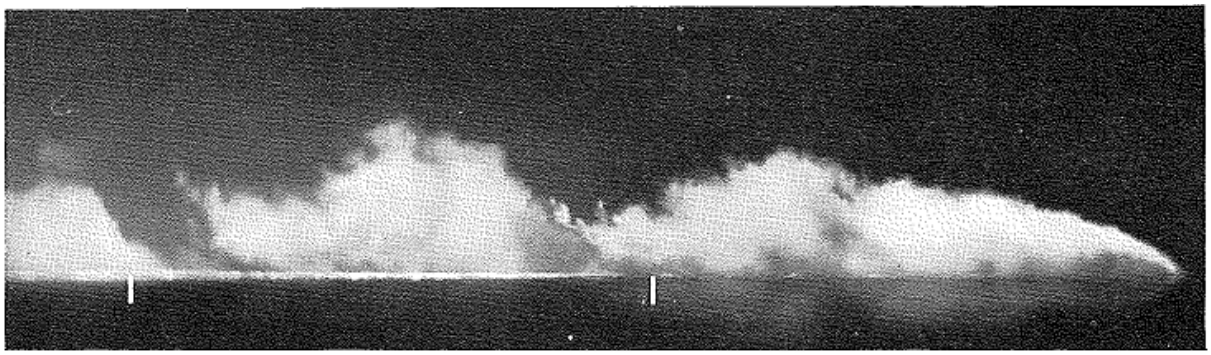

Figure 107: Instantaneous view of smoke flow showing large-scale vortices forming at reattachment point over a blunt flat plate. Cherry et al (1984)

By the time these vortical structures reached the trailing edge they become dispersed. However, circulating fluid could still be noticed in their center. At the trailing edge, due to the shear between the streamline from the top and bottom surfaces, another set of K-H-like instabilities formed, see Figure 108. The presence of these instabilities may indicate a difference in circulation between the top and bottom streamlines at the TE. This is contrary to the Kutta condition of flow circulation, which states that the circulation of the top and bottom should be equal at TE. Hence, traditional vortex-panel method and other potential flow methods are likely to have reduced accuracy when predicting airfoil performance in this flow regime.

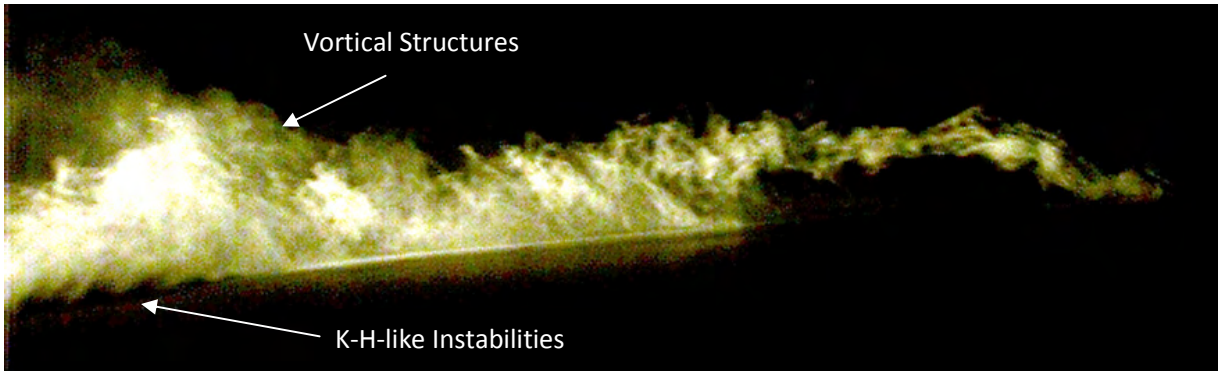

Figure 108: Visualization of the development of K-H-like instabilities in the near wake when 6Deg AOA. Ti=1.2% and Re=75000

Therefore, in attached flow, unsteadiness in the wake appears to consist of a mix of oscillations originating from the roll-up of the shear layer, the low-frequency high-energy fluctuation present within the LSB and K-H-like instabilities originating from the TE. The wake structure will be addressed in detail later on in this chapter.

With further increase in AOA to 8Deg, the low-frequency oscillation peak moved downstream indicative of a further increase in bubble length. A larger portion of the chord exhibited this increase in fluctuation as compared to the spectrum at lower AOAs, implying a further downstream shift in reattachment point. A relative increase in intensity and width of the secondary peak located close to the LE can be seen at 8Deg (see Figure 109) and this gives an insight as to the size of the recirculation region within the bubble. While an increase in bubble length occurred, the strength of the recirculation dropped, this can be inferred from the continuous drop in spectral energy as AOA increased. This concurred well with the Std.Dev of Cp distribution where highest Std.Dev was observed at 4Deg. The change in size and intensity of the bubble can be seen by comparing the color-bars in Figure 98, Figure 103 and Figure 109.

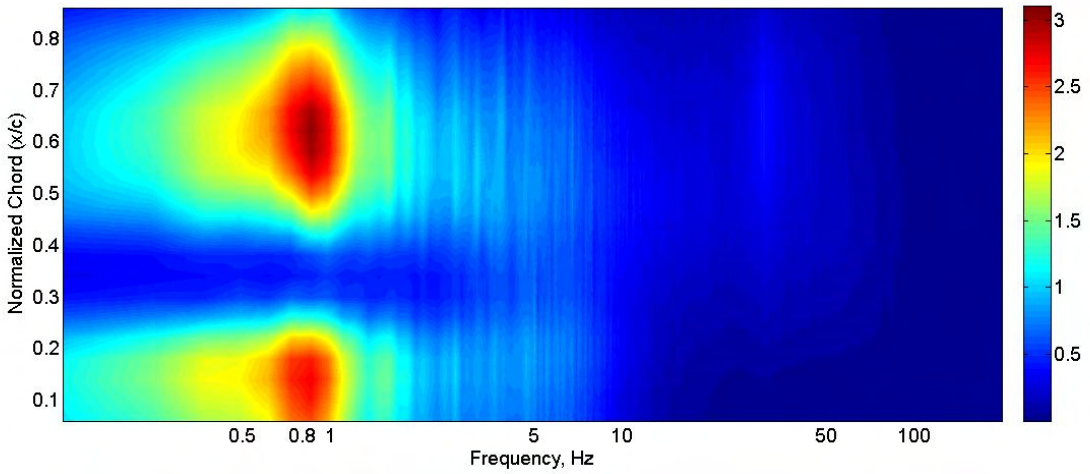

Figure 109: Consolidated PSD of pressure fluctuations over the airfoil at 8Deg AOA. Ti=1.2% and Re=75000

Unlike at 6Deg where a "plateau" in the surface pressure spectra was noticed over a range of frequencies (30Hz-60Hz) at and after the point of reattachment, at 8Deg along with a similar increase in energy between 30Hz and 60Hz, a distinct peak at around 30Hz is also present, see Figure 110. Though this peak also appeared to be the result of unsteady vortex formation due to rollup of the shear layer, a peak at the same frequency was present in the spectrum of the pressures measured on the pressure side (top surface at AOA=-8Deg), see Figure 110. Previous analysis indicated that the unsteady shedding on the top surface did not significantly influence the fluctuations at the bottom surface therefore the 30Hz peak may be due to a new flow feature. There is strong evidence to suggest that the 30Hz peak at 8Deg is due to characteristic bluff-body-like vortex shedding. This implied than even in attached flow condition i.e. pre stall AOAs; von Karman-like vortex shedding took place. From 8Deg onwards, the wake therefore consisted of not only the shedding of vortex structures from the shear layer, but also characteristic bluff body shedding. (N.B. in Figure 110, the difference in spectral resolution between the top and bottom surface is due to the reduced sampling duration used for measuring the pressures on the pressure side).

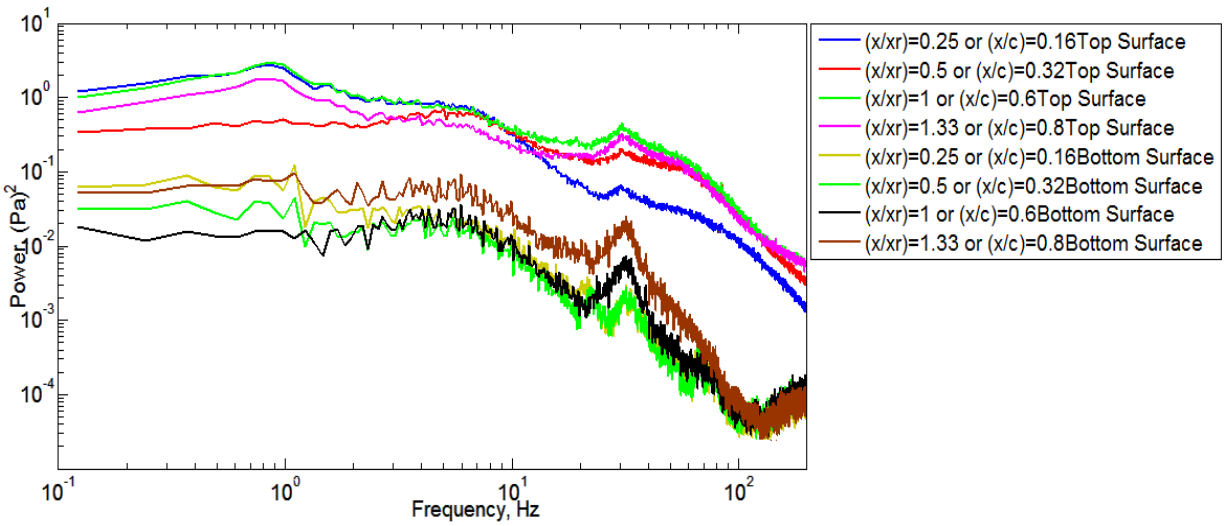

Figure 110: PSD of pressures from selected pressure taps on top and bottom of airfoil at 8Deg AOA. Ti=1.2% and Re=75000

Increasing the AOA further to 10Deg induced stall, whereby the shear layer failed to reattach. As expected, the spectrum remained centered on the von Karman-like vortex shedding frequency which was around 31Hz for this case, see Figure 113.

Comparing plots in Figure 111, while stall was noticed in the airfoil tests here, the 3D airfoil (wing with AR=2) used in Loxton et al's (2009) experiments still experienced attached conditions. The secondary peak is still visible in the pressures over the 2D and 3D airfoils implying that recirculation still takes place even though the shear layer is just detached.

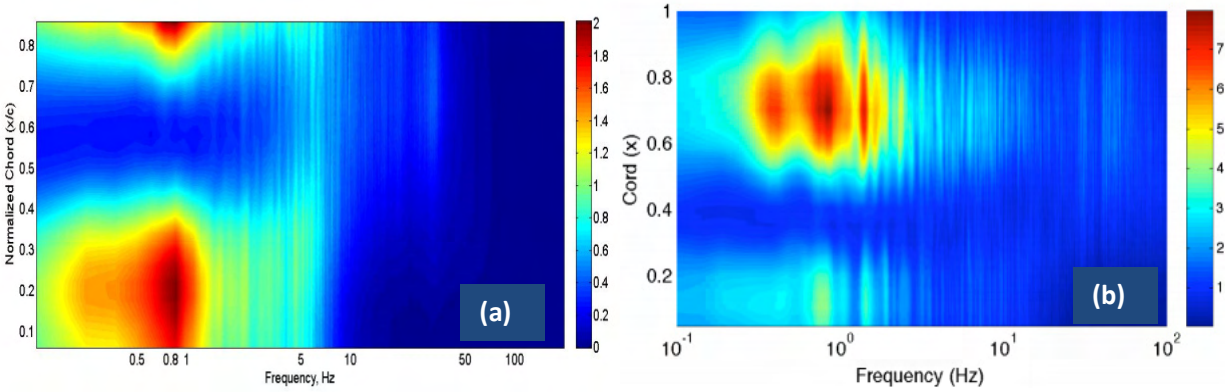

Figure 111: Consolidated PSD of pressure fluctuations over the airfoil (a) and (b) wing with AR=2 at 10Deg AOA. Ti=1.2% and Re=75000. Loxton et al (2009)

At 10Deg AOA, since the shear layer is open ended (remains detached, see Figure 112), large quantity of smoke is noticed under the same. While the shear layer remained detached it appeared to become vulnerable to undergo transition. It was observed that attempts at reattachment took place during instances when the ambient disturbances instantaneously increased, enabling better mixing within the BL. At such times, what appeared to be amplified K-H-like instabilities developed in some sections of the detached shear layer; see Figure 112. These structures further increased the fluid entrained under the shear layer, leading to a slight bulging in the size of the layer.

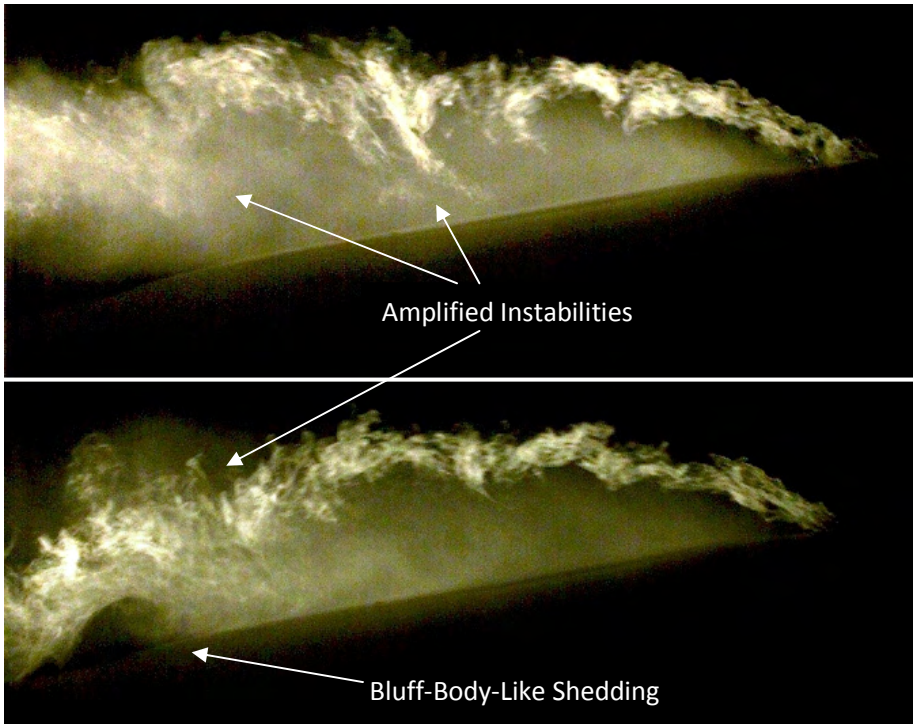

Figure 112: Instantaneous view of smoke flow showing the development of instability waves in detached shear layer while attempts of reattachment take place. Characteristic vortex shedding from the lower surface can also be seen. Airfoil at 10Deg AOA. Ti=1.2% and Re=75000

When reattachment does not occur, these amplified instabilities appear to cause the separated shear layer to roll up creating detached vortices. These vortices appeared to be shed in a non-uniform manner as they depended on the amplification of instabilities within the shear layer. Flow visualization also indicated that the characteristic bluff-body-like vortex shedding from the airfoil originates from the pressure side (bottom surface), refer Figure 112. The increase in energy of oscillations at shedding frequency in the pressure taps closer to trailing edge supports this, see Figure 113a.

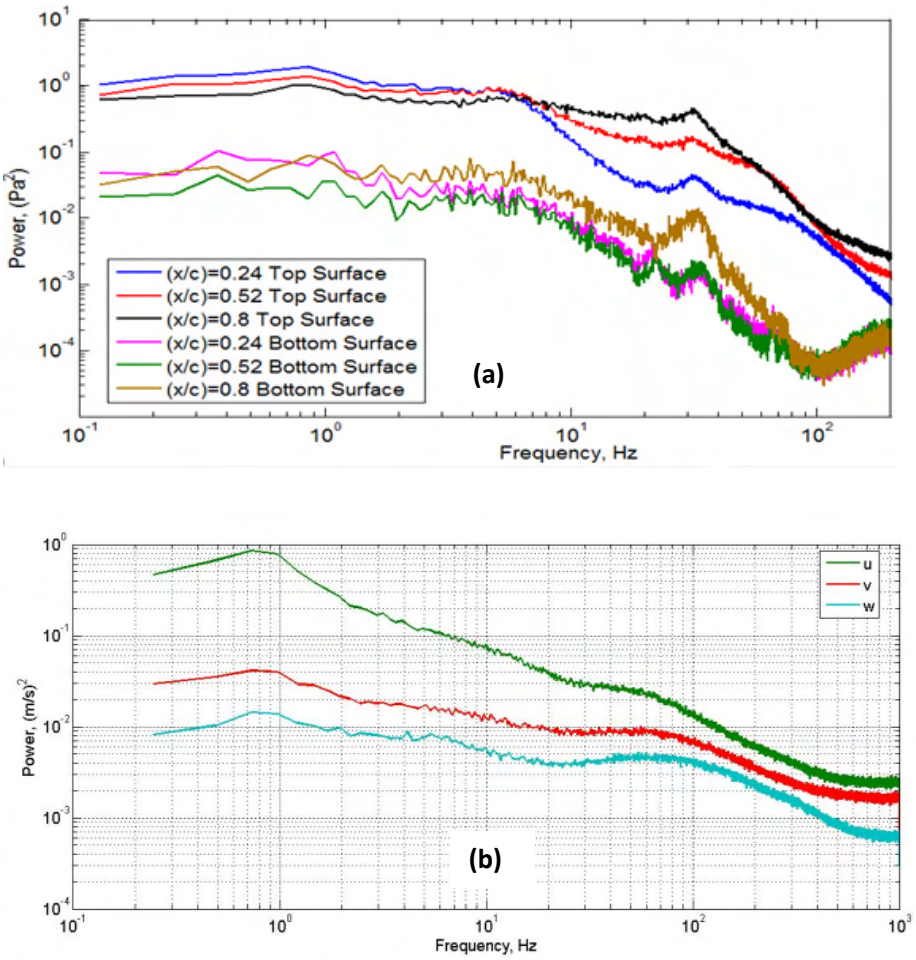

Figure 113: (a) PSD of pressures from selected pressure taps on top and bottom surfaces of the airfoil. (b) PSD of velocity measured at (z/c)=0.15 and (x/c) =0.15. For both AOA=10Deg, Ti=1.2% and Re=75000

The detached shear layer at 10Deg also possesses the low-frequency oscillation occurring at around 0.7Hz-0.9Hz as seen in Figure 113a. Using the frontal width as reference length, Cherry et al (1983) found the shear layer that developed over a blunt flat plate displayed a “flapping like” motion at a wave number of around 0.012. This flapping property has also been reported by Kiya & Sasaki (1983) at around the same wave number. They found this fluctuation to be different from the higher frequency shedding originating at the reattachment point which they considered was the result of small disturbances in the flow. Due to the flow structure being very similar here, the low-frequency fluctuation noticed here is also believed to be due to flapping of the shear layer. Since shear layer flapping occurs at, or very close to the point of separation (Abdalla & Yang (2004)), and since separation occurs at the same point and in a similar manner here from 4Deg AOA onwards, the flapping rate also

does not change with AOA. As the flapping rate of the shear layer is not influenced by change in AOA, the chord length was used as reference length here. The 0.9Hz shedding therefore resulted in a wave number of 0.021. The difference in wave number found here and Cherry et al (1983)'s finding is believed to be due to the difference in reference length used and the difference in section geometry. Though the exact reason for the shear layer to display this flapping motion is still unclear, it has been attributed to the consequence of large-scale unsteadiness within the shear layer, Kiya & Sasaki (1983) and Abdalla & Yang (2004).

Above 10Deg AOA, the pressure fluctuations and flow visualization revealed that the airfoil behaves like a bluff-body as the shear layer remains detached at all times. From this AOA onwards, large von Karman-like vortex shedding occurs from the airfoil. The fluctuations in pressure and velocity over this range of AOAs will be addressed later along with the study of the wake structure.

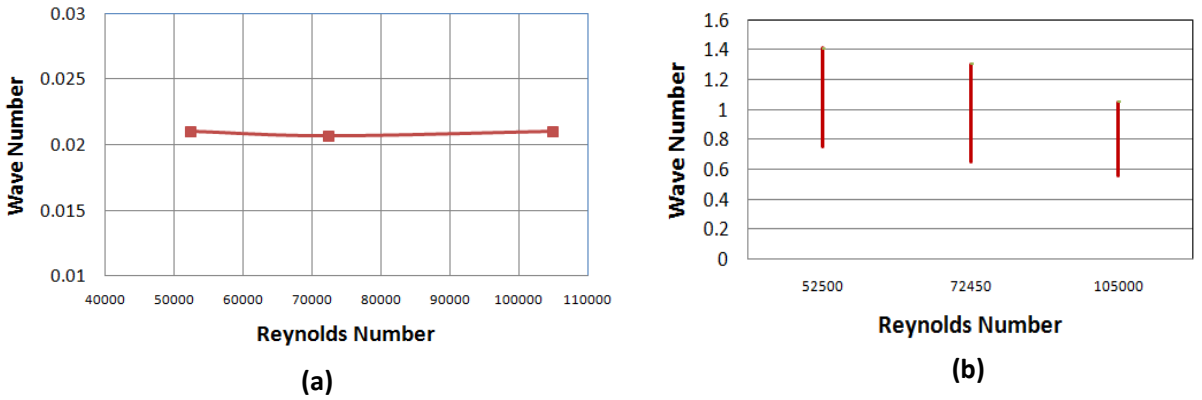

Figure 114: Reynolds number sensitivity of shear layer flapping (a) and vortex shedding on reattachment due to shear layer roll up (b). (Wave number = c.f/v) AOA=6Deg and Ti=1.2% for both cases.

Experiments were conducted to study the Reynolds number sensitivity of the pressure fluctuations over the airfoil. Figure 114a shows that the rate of flapping of the shear layer (as non-dimensionalized by the wave number) remains nominally unchanged at a wave number of 0.021 over the range tested. As the rate at which the vortices were shed on reattachment varied over a range of frequencies (see Figure 100), the wave number for the shedding frequency range was plotted against the different Reynolds numbers. It was found that the higher frequencies in the shedding range were relatively more sensitive to change in Reynolds number as seen in Figure 114b. The shedding rate was found to increase with an increase in Reynolds number, but not at the same rate as the wave number trend indicated. The reason

for such a trend could not be determined since detailed velocity survey was not conducted at higher Reynolds numbers.

Thus, based on the nominally smooth flow results presented so far it can be inferred that the flow-field on the suction side in smooth flow depends primarily on the structure of the shear layer and hence its profiles (i.e. attached, with LSB or fully detached) have a significant influence on the flow-field. Though the exact process of transition from laminar to turbulent flow is unclear, it is firmly believed to originate from amplification of K-H-like instabilities that developed in the lower sections of the separated shear layer soon after detaching from the LE. Only a section of the shear layer was found to roll-up, resulting in limited fluid entrainment within the bubble. On reattachment the rolled-up shear layer formed large-scale vortices which were shed over a range of frequencies. The shear layer also displayed a "flapping-like" motion which consisted of high-energy low frequency fluctuation in pressure and velocity at a wave number of around 0.02. This wave number was much the same over the range of Reynolds numbers tested. Due to the velocity difference between the streamlines from the top and bottom surfaces of the airfoil, K-H-like instabilities also formed in the near wake. Fluctuations measured on the pressure side of the airfoil were considerably lower in magnitude and remained largely random until characteristic vortex shedding began from 8Deg AOA onwards.

4.2 Pressure and Velocity Fluctuations over Airfoil in Turbulence

Following identification of various flow features that persist over the airfoil when subjected to smooth flow, this section will deal with identifying the changes to flow structure in the presence of elevated levels of freestream turbulence. Statistical and qualitative metrics used previously will be used here as well in order to identify the salient features of the flow over the airfoil.

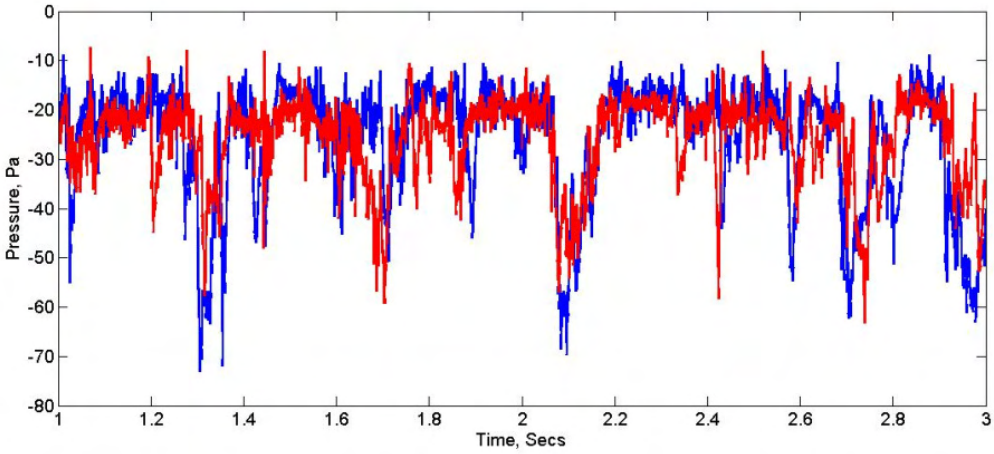

Figure 115: Pressures measured at nominally same chordwise location (x/c)=0.3 (blue) and (x/c)=0.32(red) with 200mm spanwise separation. AOA=6Deg, Ti=7.3%, Lxx=0.22m and Re=75,000

As stated in Chapter 3, even at low AOAs where fully attached flow is present in smooth flow, instances occurred when large LSBs formed over the airfoil in the presence of freestream turbulence. Figure 115 shows a sample time series of pressures measured at nominally the same chordwise station but with 200mm spanwise separation, when exposed to turbulence with properties Ti=7.3% and Lxx=0.22m. The rapidly changing oncoming pitch angle generates continuously varying on-coming flow conditions. For this reason, the sample pressure data in Figure 115 show periods of high fluctuation, alongside periods of relatively mild fluctuations. Further in-depth analysis will be conducted in this section to identify the various flow features that develop in turbulence.

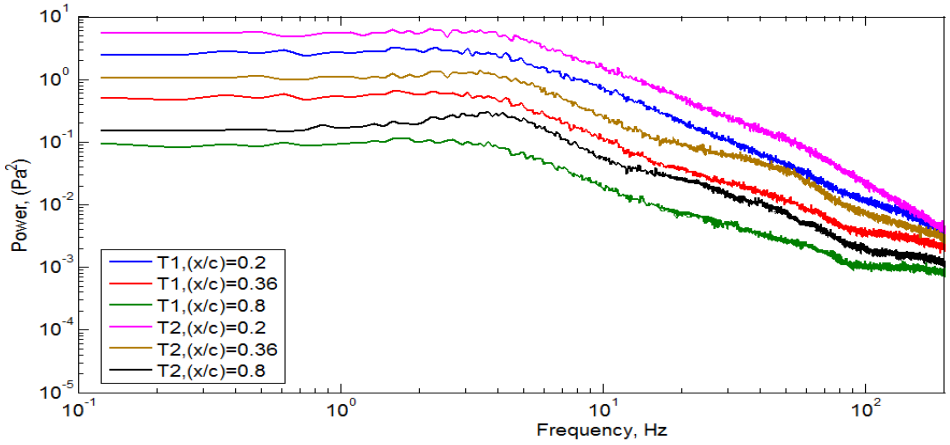

Figure 116: Spectra of selected pressure taps when AOA=2Deg, where T1 (Ti=7.15%, Lxx=0.14m) and T2 (Ti=12.3%, Lxx=0.15m). Re=75000 for both cases.

At low AOAs, no periodicity appears to be present in the fluctuating pressures measured at various chordwise locations in the turbulence intensities presented in Figure 116. Given the fluctuations in pitch angle and velocity were stochastic it is likely that the pressure fluctuations would also be random. A small bump can however be seen at around 3-4Hz at the furthermost located pressure tap in the higher turbulence intensity case. An elevation in power can be seen at around the same frequency in the consolidated spectra plot of the pressure fluctuations over the airfoil at 6Deg AOA in Figure 117.

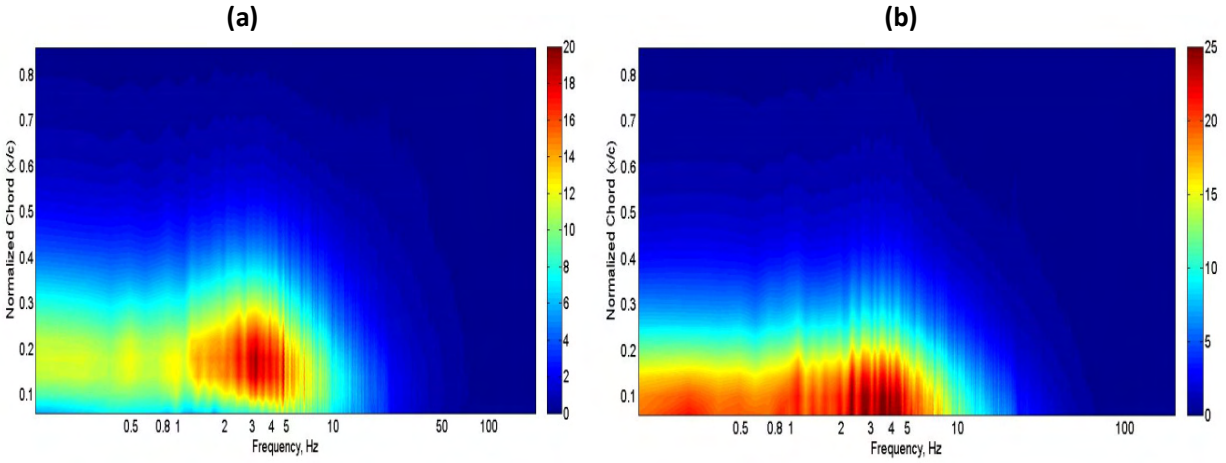

Figure 117: Consolidated spectra of pressure fluctuations occurring over airfoil at AOA=6Deg subjected to freestream turbulence with properties Ti=7.15%, Lxx=0.14m (a) and Ti=12.3%, Lxx=0.15m (b). Re=75000 for both cases.

The location of maximum fluctuation moved closer to LE with increase in turbulence intensity, refer Figure 117 and Figure 118. An overall increase in energy was also noticed in the spectra, implying an increase in magnitude of the fluctuations which seems to occur mainly at the lower frequencies. It was found that in nominally smooth flow, flapping of the shear layer was uninfluenced by change in AOA until the shear layer separated completely (AOA>12Deg). Therefore, in spite of the rapidly fluctuating AOA in turbulence, this flapping motion of the shear layer might be expected to still be present in higher levels of turbulence when the instantaneous AOA<12Deg. This is however not the case, as seen from Figure 117 and Figure 118 where no peak was present at the flapping frequency indicating that in turbulence the flow structure undergoes significant changes. The secondary peak that was earlier seen at the same AOA in smooth flow is also absent here. These results are similar to Loxton's findings on a wing, however Loxton's experiments were at a slightly longer length scale and conducted at a higher Reynolds number.

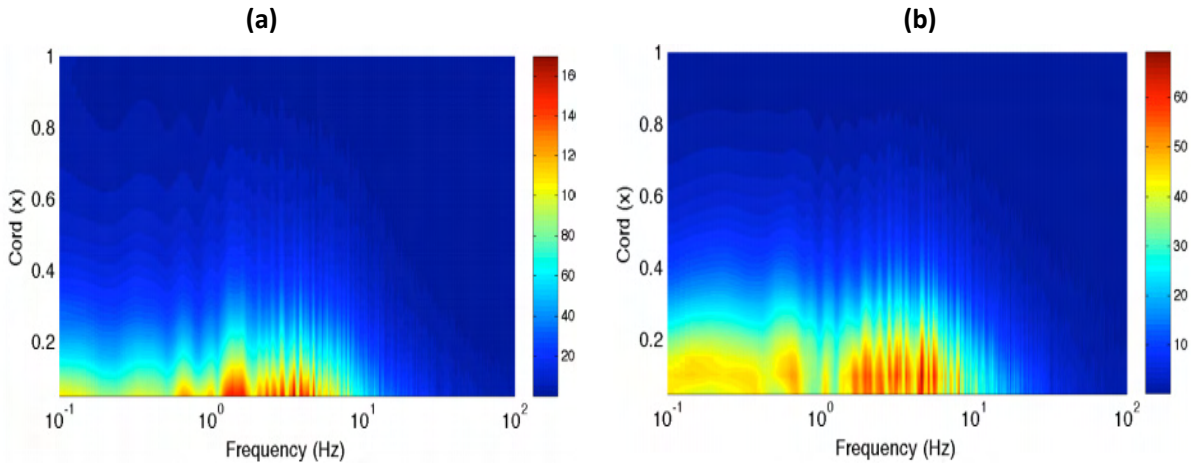

Figure 118: Spectra of pressure fluctuations measured by Loxton et al (2009) over wing with AR=2 at AOA=6Deg subjected to freestream turbulence with properties Ti=7.3% Lxx=0.22m (a) and Ti=12.6% Lxx=0.31m (b)

Smoke flow visualization revealed that in turbulence, when the airfoil's LE encounters an increase in instantaneous AOA, flow separation occurs in the presence of an APG, similar to smooth flow conditions. Instabilities then developed in the lower part of the shear layer because of the velocity difference. At higher turbulence intensities, these instabilities were noticed to develop much earlier. The significant increase of ambient disturbances brought about by not only velocity fluctuations in the chordwise plane but also from the spanwise variation of instantaneous flow properties, appear to amplify the instabilities resulting in the rolling up of a larger portion of the shear layer. It rendered reattachment of the shear layer close to the LE. This is unlike in smooth flow where only a relatively smaller section of the shear layer rolled up.

At low AOAs (AOA>6Deg) when Ti=7.2%, the shear layer rolled up forming vortices similar to that noticed in nominally smooth flow but with what appears to be significantly higher vorticity, compare Figure 106 and Figure 119. However at higher AOA when Ti=7.2% and for all AOAs at the highest turbulence intensity (i.e. Ti=12.3%), the increased instability rendered the roll up of the entire shear layer soon after separation from LE, see Figure 120a. Due to the roll up of the entire shear layer, on reattachment, the streamwise velocity vector seems to point inwards rapidly increasing fluid entrainment within the bubble presumably leading to the formation of strong vortical cores evident in Figure 120. The vortex cores consisted of fast recirculating fluid and moved downstream at a rate visibly lower than the mean freestream velocity. This reduction in velocity is believed to be due to the changing direction of the velocity vector of the shear layer. The time-averaged influence of these vortical cores on

the pressure distribution has been addressed in the previous chapter. Gartshore (1973) and Melbourne (1993) also noticed a reduction in curvature of the separated shear layer with increase in turbulence intensity from their experiments studying the influence of turbulence intensity on bluff bodies.

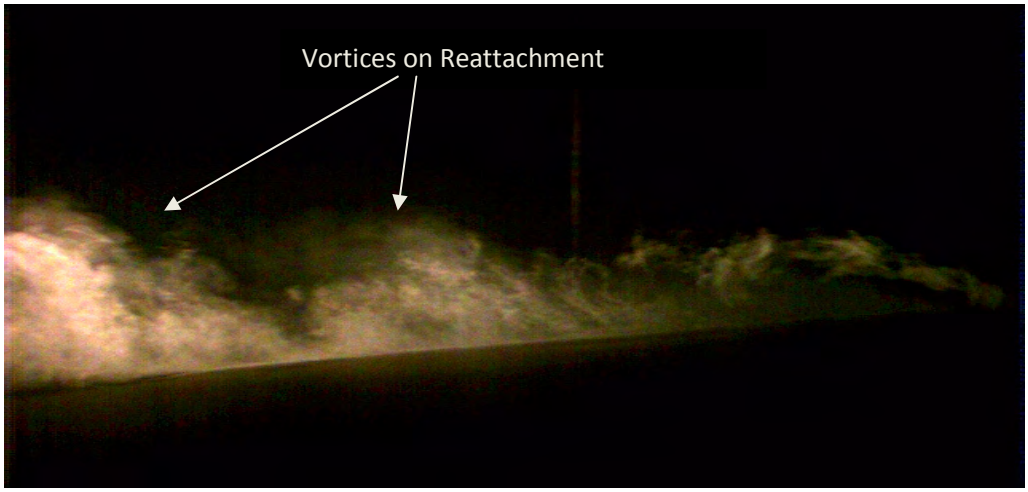

Figure 119: Vortices created due to shear layer rollup are much larger in turbulence in comparison to smooth flow. AOA=6Deg and Ti=7.3% Lxx=0.22m.

As the vortex core translated downstream, due to the significantly increased fluid entrainment, more fluid can be seen to be injected into the bubble resulting in an expansion of the same, refer Figure 120b. Therefore, along with the vortex core, the point of reattachment also moved downstream, however since the magnitude of the fluctuations were largest at the location of vortex core formation, the downstream translation of the reattachment point is not reflected in the pressure spectra in Figure 117. This is unlike in smooth flow where the reattachment point oscillated over a much smaller region. The absence of a secondary peak in the pressure spectra in elevated levels of turbulence is believed to be due to the lack of a constant region of recirculation over the airfoil.

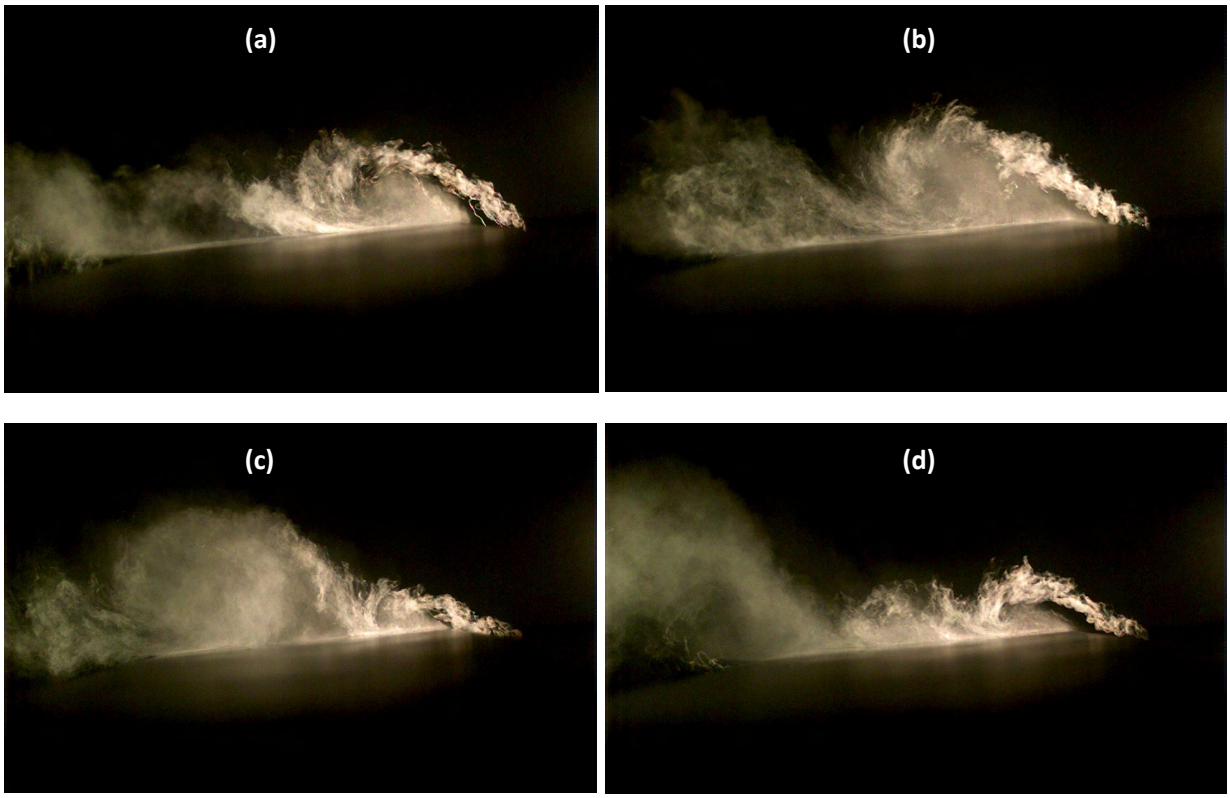

Figure 120: In turbulence, the amplified instability structures render the entire shear layer to rollup creating vortical cores (a) which rapidly increases the fluid entrained under the bubble. A large quantity fluid is hence injected into the bubble leading to an expansion of the same (b). Due to losses, by the time the vortical core reaches the TE, it is very large and dispersed, hence a new vortex core forms at the LE and the process repeats (c&d). Bluff-body-like vortex shedding can also see noticed close to trailing edge in (d). AOA=10Deg and Ti=12.6%, Lxx=0.31m

While the vortex core increased in size as it advected downstream, instances occurred when sections of the shear layer formed amplified instability structures well before the location of reattachment. These instabilities appeared to inject fluid against the direction of circulation within the vortex core, leading to a drop in vorticity, see Figure 121. The strength of vorticity also appeared to reduce due to the spanwise incoherence of fluctuations as the sample data presented in Figure 115 indicates. Therefore, by the time the vortex core reached the TE, it becomes very large, weak and dispersed. At this point, depending on oncoming flow conditions, a new vortex core was seen to develop at the LE and the process repeats, see Figure 120. A pulsating trend of the vortex core forming, growing and being shed is thus evident when freestream turbulence intensity is high. The increase in energy noticed in the pressure spectra at around 3.5Hz (refer Figure 117) is believed to be the average rate at which the vortex cores were formed and shed when AOA=6Deg. Just like the flapping of the shear layer, the 3.5Hz peak seen here is believed to be a characteristic rate of vortex core development dependent of airfoil geometry and AOA.

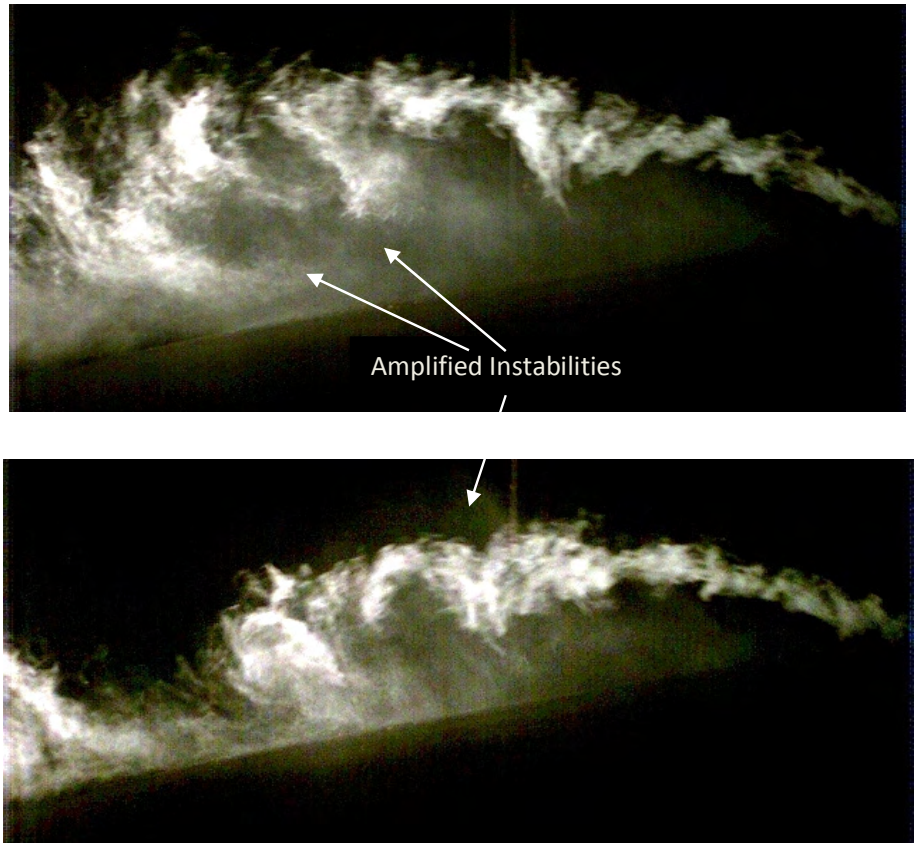

Figure 121: Amplified instabilities forming in the detached shear layer before the reattachment point inject fluid against the direction of circulation within the vortex core leading to a drop in vorticity in the core. AOA=10Deg and Ti=7.3% Lxx=0.22m

While a vortex core was developing, if the LE encountered a large reduction in instantaneous pitch angle brought about by a turbulent gust, immediate cessation of the vortex development was observed. Subsequently the flow assumed a more stable structure while the previously terminated vortex proceeded downstream until it eventually dispersed. At low AOAs (AOA<6Deg) when Ti=7.2%, instances, though rare, were also noticed when the flow resembled smooth flow conditions. This was believed to occur during periods when the oncoming flow fluctuations were relatively small.

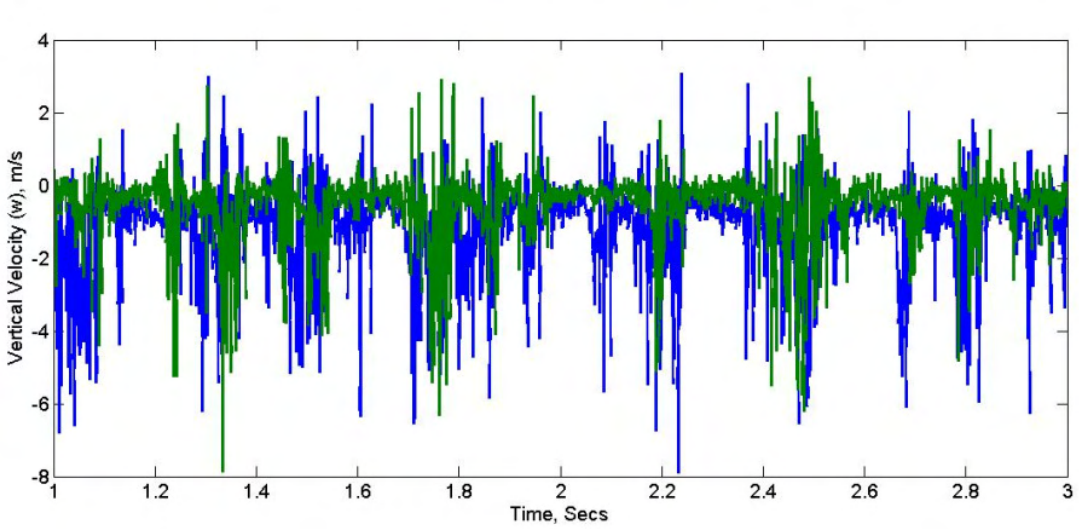

Figure 122: Simultaneously measured velocity at nominally same chordwise location (x/c)=0.3 (blue) and (x/c)=0.32(green) with 200mm spanwise separation. The probes were held 15mm ((z/c)=0.1) above airfoil surface. AOA=6Deg, Ti=7.3%, Lxx=0.22m and Re=75,000

Similar fluctuations in pressure and velocity were noticed over the airfoil though the two were not measured simultaneously, compare Figure 122 and Figure 115. The large pressure and velocity fluctuations alongside regions of mild fluctuations are believed to be due to the formation and downstream advection of the vortex cores. The times of milder fluctuations in Figure 122 could either be due to a reduction in instantaneous pitch angle or they may be the time between the earlier advected and oncoming vortex core influenced pressure and velocities at the location of interrogation. Though the velocity fluctuations at the two points in Figure 122 appear to be reasonably coherent, given that the distance between the probes is larger than the spanwise length scale, instances can be seen (for example at t=1 or 2.1secs) when large fluctuations are present at one point and not at the other. The presence of such large changes in fluctuations indicated that in turbulence, sections of the airfoil might experience grossly varied flow conditions at different spanwise locations at the same time instant.

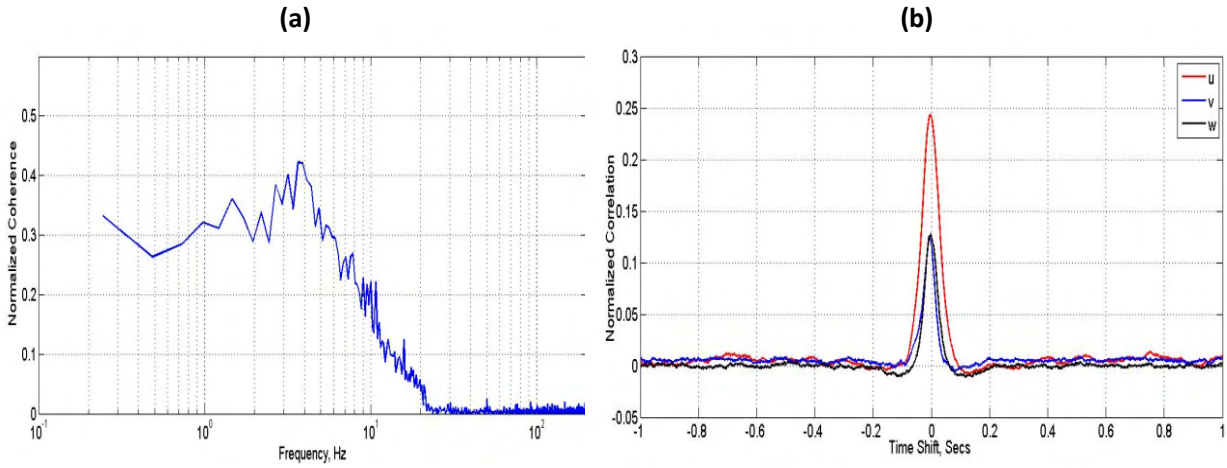

Figure 123: (a) The coherence between the velocity measurements presented in Figure 122 and (b) cross-correlation between the velocities in the u, v and w directions measured at the same locations as in Figure 122

Comparing the velocities measured simultaneously in Figure 122 revealed that fluctuations occurring above 20Hz are incoherent as they might be due to local changes occurring in the flow, refer Figure 123a. Maximum coherence is also seen at around the same frequency (around 3.5Hz) where a peak in energy was noticed in pressure spectra for AOA=6Deg. This further implicates the presence of a larger, more coherent oscillation occurring due to vortex core formation over the airfoil amongst fluctuations that are due to local changes. In Figure 123b, reasonable correlation is seen in the fluctuations in v and w directions however a significantly higher correlation is noticed in streamwise direction, probably due to the larger spanwise length scale of the same. Detailed comparison of the pressure and velocity fluctuations occurring at different spanwise stations will be presented later.

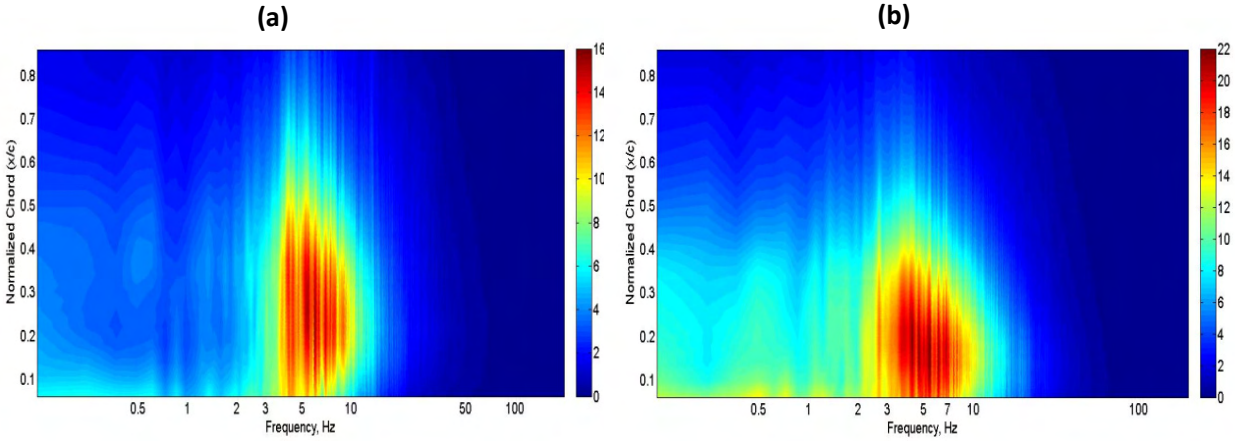

Figure 124: Consolidated spectra of pressure fluctuations occurring over airfoil at AOA=10Deg subjected to freestream turbulence with properties Ti=7.15%, Lxx=0.14m (a) and Ti=12.3%, Lxx=0.15m (b). Re=75000 for both cases.

With further increase in AOA, an elevation in the spectra is noticed at around 5.5Hz at both turbulence conditions, compare Figure 124a&b. This frequency is slightly higher than at 6Deg AOA where the peak was at around 3.5Hz, compare Figure 117 and Figure 124. However the peak frequency increases only marginally with further increase in AOA, as seen in Figure 125, where the spectra of pressures measured at location of maximum oscillation for various AOAs are plotted. Figure 125 also shows that the location of the peak in frequency increases steadily with AOA till 10Deg AOA after which it remains nominally constant. It should be recalled that the airfoil stalled at 10Deg in smooth flow and only a small change in the pressure distribution was noticed with further increase in AOA. The shedding frequency wave number and Strouhal number (St) versus AOA for both turbulence intensities is plotted in Figure 126. The projected frontal width was used as the representative length to estimate the St while the chord was used to estimate the wave number. The rate of vortex core formation was dependant on the AOA hence the effective frontal length (also a function of AOA) was used as the characteristic length to estimate the St. A number of other workers (Hoarau et al (2003), Sicot et al (2006)) have used this method to normalize the shedding observed behind airfoils. Due to the diminished spectral resolution, a line of best fit was passed through the spectra to effectively determine the most appropriate spectral peak for each AOA in Figure 125. The Increase in vortex core formation frequency with increase in AOA is believed to be due to the presence of higher instantaneous AOAs and the increased instability of the shear layer in the presence of a stronger APG. This change in vortex core formation rate with change in AOA is also believed to be a property of the airfoil geometry and the fact that a similar trend is noticed at higher turbulence intensity further supports this.

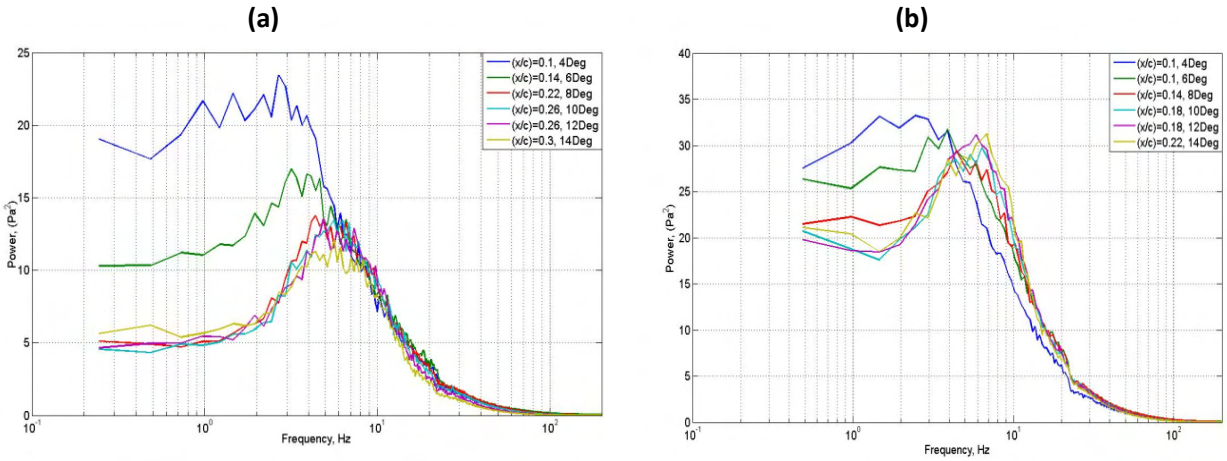

Figure 125: Spectra of pressures measured at location of maximum oscillation at various AOAs where T1 is when Ti=7.15%, Lxx=0.14m (a) and T2 is when Ti=12.3%, Lxx=0.15m (b).

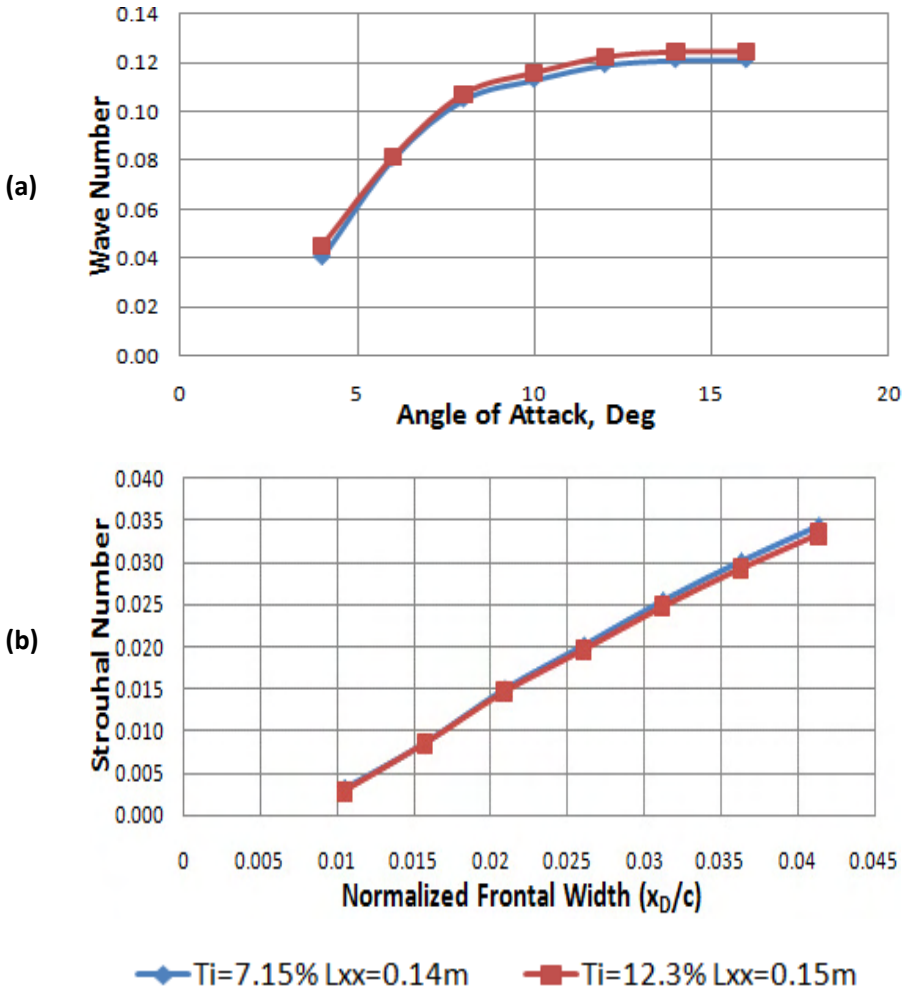

Figure 126: (a) Wave number at which vortex cores formed at different AOA using chord as representative length. (b) Strouhal number of vortex core formation at different AOAs using projected frontal width x_D=(c x (sine(AOA)) as reference.

Time-averaged pressure measurements showed that the airfoil stalled at 16Deg when Ti=7.2%, however the spectra in Figure 127 show that the pressures fluctuated with a peak at around 6.5Hz when AOA=18Deg. Flow visualization showed that vortex cores still formed at such high angles when the instantaneous velocity fluctuations rendered a reduction in AOA. At higher AOAs, due to a stronger APG, a larger distance would be required for the shear layer to undergo transition and roll up and therefore the location of maximum fluctuation, which represents the location of vortex core formation, moves downstream as well.

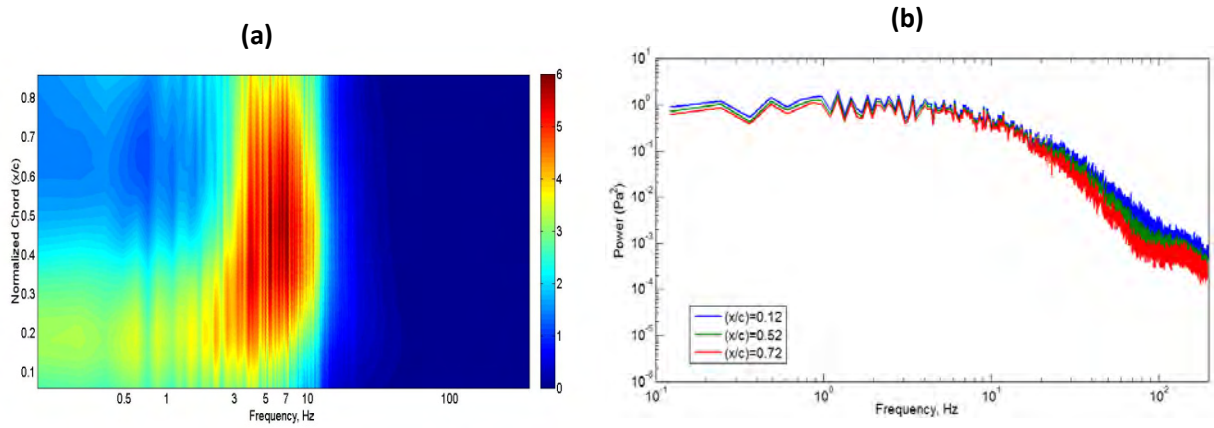

Figure 127: (a) Consolidated spectra of pressure fluctuations over airfoil at AOA=18Deg. (b) spectra of pressures measured at various chordwise stations when AOA=-18Deg. For both cases freestream turbulence is Ti=7.15%, Lxx=0.14m and Re=75000.

It should be recalled that in smooth flow conditions, bluff-body-like vortex shedding was noticed from the airfoil from 8Deg onwards. In turbulence however, even at 18Deg AOA no distinct peak is visible, see Figure 127b. Flow visualization however showed that bluff-body-like vortex shedding occurred intermittently, i.e. when the instantaneous AOA was high enough to enable the same, see Figure 120d. This implied that the wake structure in turbulence changed considerably with time but mainly consisted of a mix of vortical cores, von Karman-like shedding and instabilities that form at the TE. Discussion on the flow structure in the airfoil wake will be presented later in this chapter.

The spectrum in Figure 128 shows that a change in longitudinal length scale does not significantly alter the flow structure. Comparing Figure 117, Figure 124 & Figure 128 shows that only a small change in fluctuations is noticed with change in integral length scale whereby an overall increase in energy was noticed along with the location of peak fluctuations moving slightly downstream. The overall increase in energy could be attributed to the increase in magnitude of fluctuations experienced at longer length scales.

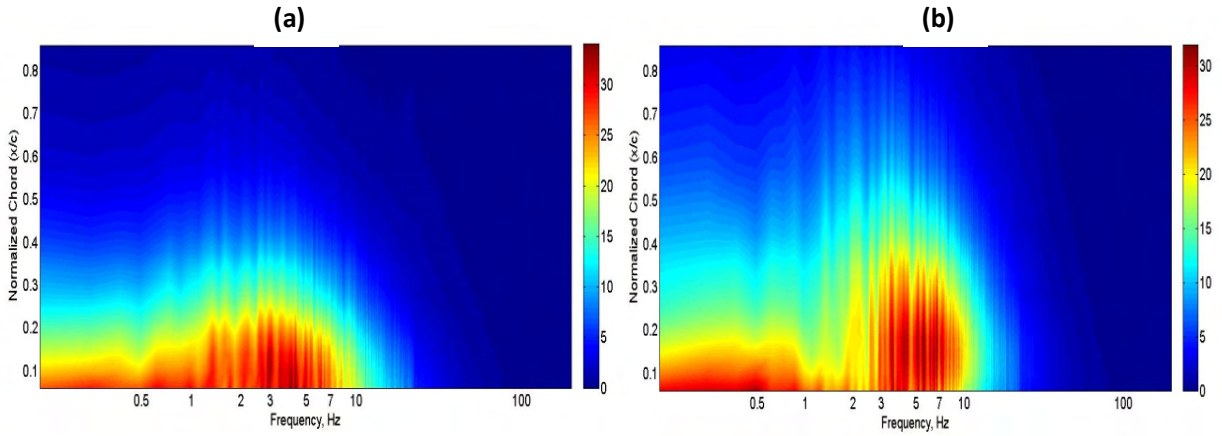

Figure 128: Consolidated spectra of pressure fluctuations when airfoil is at AOA=6Deg (a) and AOA=10Deg (b). Freestream turbulence Ti=12.6%, Lxx=0.31m and Re=75000 for both cases.

Figure 129 shows that when Lxx was around 10c (Lxx= 1.3m) at 6Deg AOA, peak fluctuations occur at around 0.9Hz which is similar to that found in nominally smooth flow. The peak indicates that the shear layer flapping takes place in this flow condition (while it was absent at the lower length scales). Since only a limited number of tests were conducted within this turbulence condition, a detailed survey of pressure and velocity fluctuations was not feasible, therefore further insights on the flow structure in this turbulence conditions could not be obtained. The high frequency shedding of vortices on reattachment, noticed in smooth flow is, however, not present here but along with shear layer flapping, it is believed that vortex cores also formed in this turbulence condition. Figure 129 also shows that above 6Deg AOA, no elevation in power is noticed at 0.9Hz which suggests that possibly due to the increased instability of the shear layer, the flapping motion ceases past 6Deg AOA. Above 10Deg AOA, except for an overall increase in energy and the point of reattachment moving slightly downstream, the pressure fluctuations were similar to that noted at lower length scales. Here too, no signs of the presence of bluff-body-like vortex shedding taking place was observed.

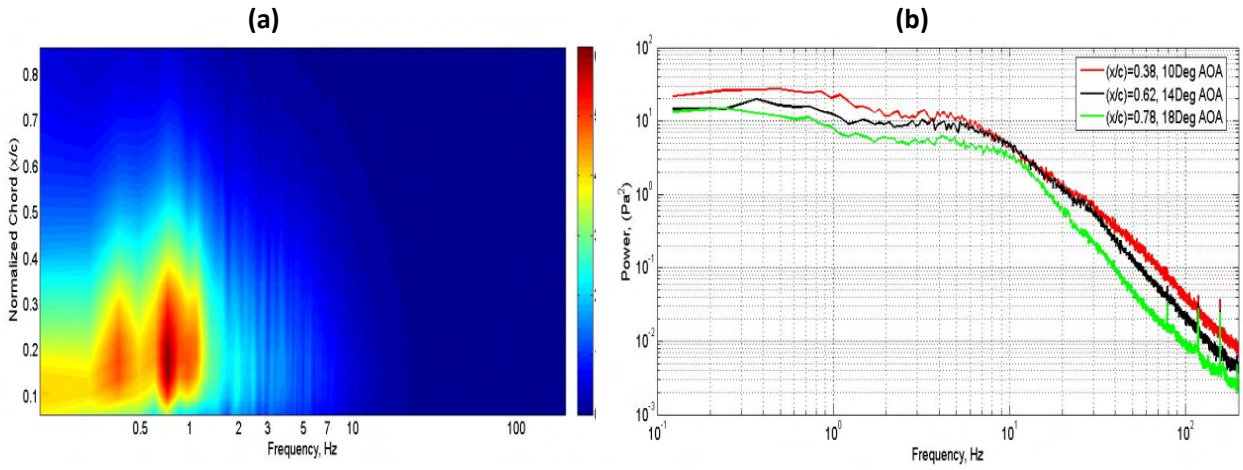

Figure 129: (a) Consolidated spectra of pressure fluctuations over airfoil at AOA=6Deg. (b) spectra of pressures measured at different AOAs at various chordwise stations. For both cases freestream turbulence is Ti=7.22% Lxx=1.3m and Re=75000.

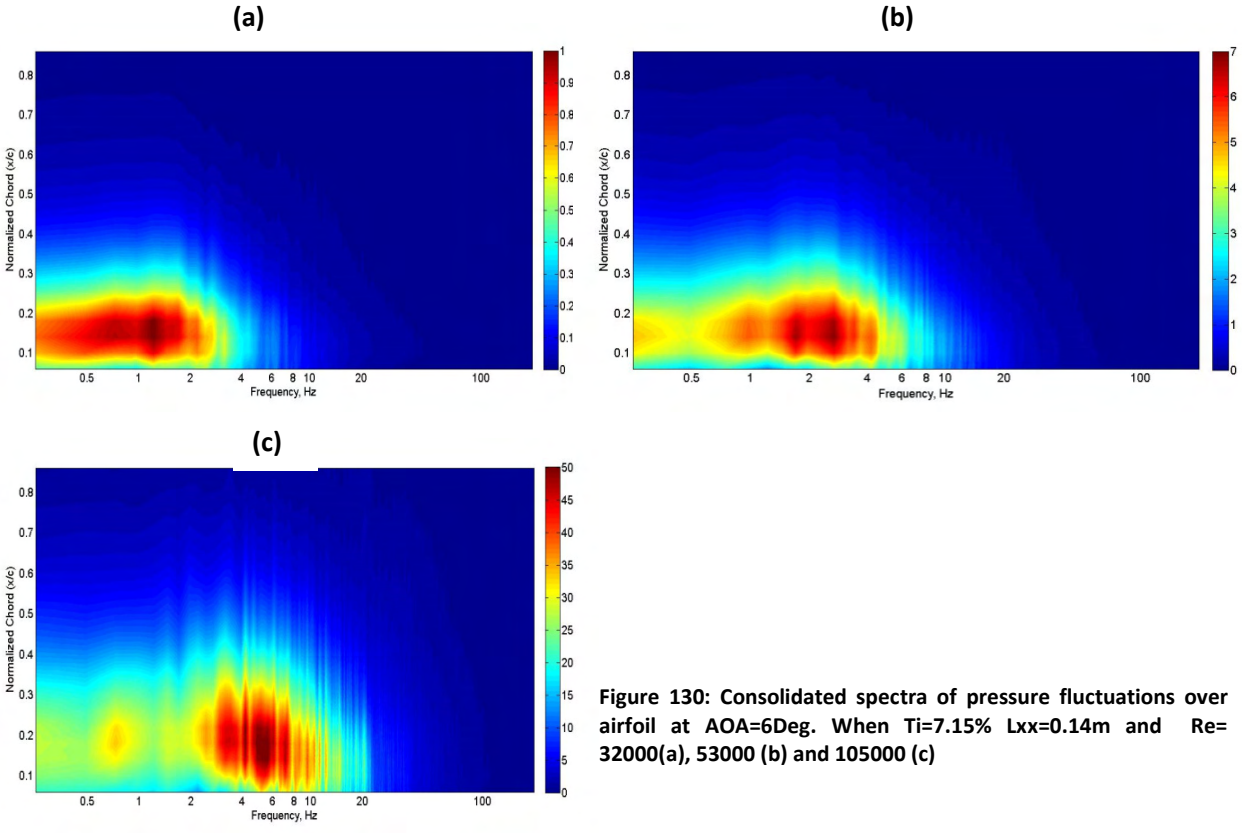

Figure 130: Consolidated spectra of pressure fluctuations over airfoil at AOA=6Deg. When Ti=7.15% Lxx=0.14m and Re= 32000(a), 53000 (b) and 105000 (c)

Tests were conducted at different Reynolds numbers to determine the dependence of pressure fluctuations over the airfoil to Reynolds number. It can be inferred from Figure 130a,b&c that the

location of reattachment moves downstream with increase in Reynolds number and this agreed well with the time-averaged results. By comparing the three figures, the increase in rate of vortex core formation, along with increase in the overall magnitude of fluctuations, can clearly be seen. The wave number for the rate of vortex core formation is plotted against the different Reynolds numbers tested in Figure 131. It shows that frequency of vortex core formation, at both low as well as high AOA, is sensitive to Reynolds number changes in that both increase at around the same rate. This trend in Figure 131 can be attributed to the increased susceptibility of the shear layer to undergo transition and hence roll up as velocity increases. It is also conjectured that with further increase in Reynolds number, a critical wave number will be reached whereby the vortex core formation cannot occur any faster.

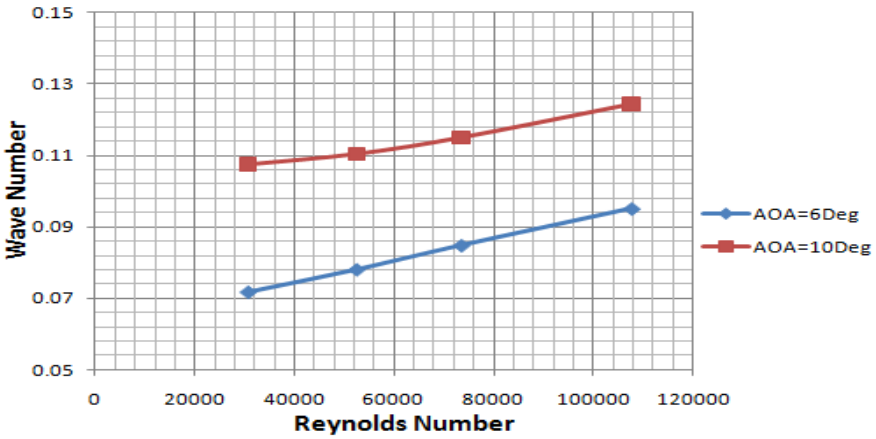

Figure 131: Wave number for the rate vortex core formation plotted against the Reynolds number for AOA=6Deg and 10Deg. Ti=7.15% and Lxx=0.14m

The results presented so far indicated that in higher levels of turbulence the shear layer separates from the LE and instabilities develop much earlier. This is believed to be due to increase in ambient disturbances a larger portion of the shear layer rolled up in turn rendering the vortices shed to be considerably stronger. At higher turbulence intensities the instabilities amplified after shear layer separation, leading to the entire shear layer rolling up. Strong vortical cores were created due to this roll-up and a fluctuating trend of the vortex cores forming, growing and being shed was observed. The rate of vortex core formation increased with AOA until AOA=10Deg, after which it remained nominally constant at a wave number of 0.12. Fluctuations of large magnitude were imparted over the airfoil due to the formation and advection these vortical cores. At high AOAs (>10Deg), bluff-body-like vortex shedding occurred only intermittently, presumably due to the constantly changing flow conditions,

hence no peak in spectra was present at the higher frequencies. Except for the longest length-scale tested, the influence of increase in length scale on the pressure fluctuations was limited to an overall increase in energy of fluctuation along with a slight downstream movement of reattachment point. When Lxx=10c, evidence of shear layer flapping was present at low AOAs, but was absent at AOA>10Deg. The fact that vortex cores also formed at this length scale at AOA>=10Deg was indentified from the pressure spectra.

4.3 Chordwise Comparisons of Surface Pressure Fluctuations

In this section the fluctuations experienced at different chordwise locations will be analyzed with respect to each other in order to further identify various properties of the transient flow structures that develop over the airfoil in smooth and turbulent flow. This will be accomplished by analyzing the time-varying pressure data acquired at the various points as well as by computing their correlation and coherence functions. Figure 132 shows the zero time shifted correlation in the pressure fluctuations between the pressures at location of reattachment and all remaining pressure taps.

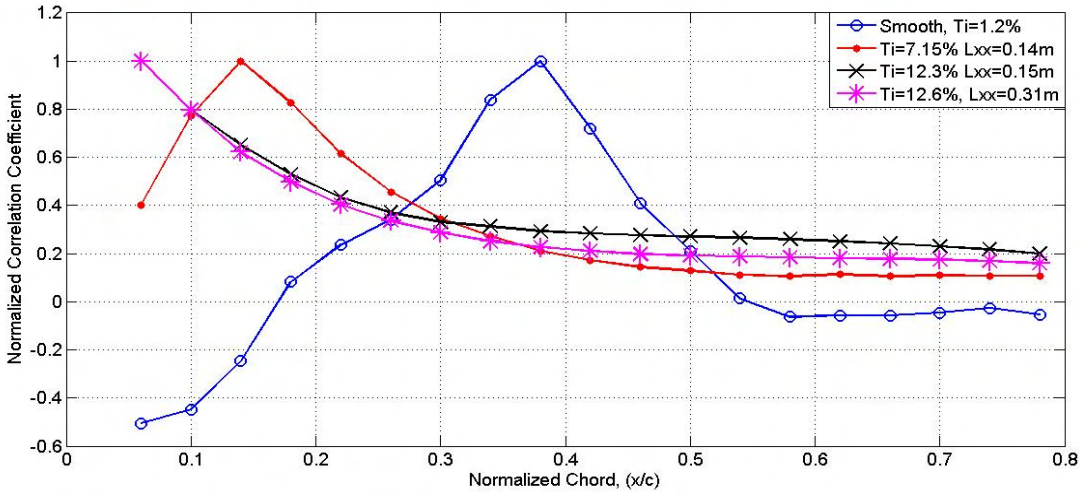

Figure 132: Zero time shifted correlation between reattachment point and the other pressure taps in different turbulence conditions. AOA=6Deg and Re=75,000 for all cases

A high negative correlation is seen near to the LE in smooth flow conditions while this region is absent in turbulence, see Figure 132. The high negative correlation is due to the anti-phase relation between the

pressures measured at either ends of the bubble. This is not noticed in turbulence because of the absence of a constant recirculation region over the airfoil. The fact that correlation drops rapidly after the reattachment in smooth flow once again suggests that the transient flow structures that develop after reattachment are relatively less correlated and dependant on local influences. In contrast, the correlation in turbulence reduces at a much slower rate and a slightly higher correlation can be noticed at the higher turbulence intensity. The diminished decay of correlation in elevated levels of turbulence can be attributed to the development of the large vortex cores which advect downstream influencing the pressures measured across a relatively larger section of the chord. The increase in correlation at higher turbulence intensities is believed to be due to the relatively larger size of vortical cores created at higher intensities. Though the influence of change in integral length scale is limited as seen in Figure 132, the comparative drop in correlation suggests a reduction in vortex core size having closer resemblance to smoother conditions.

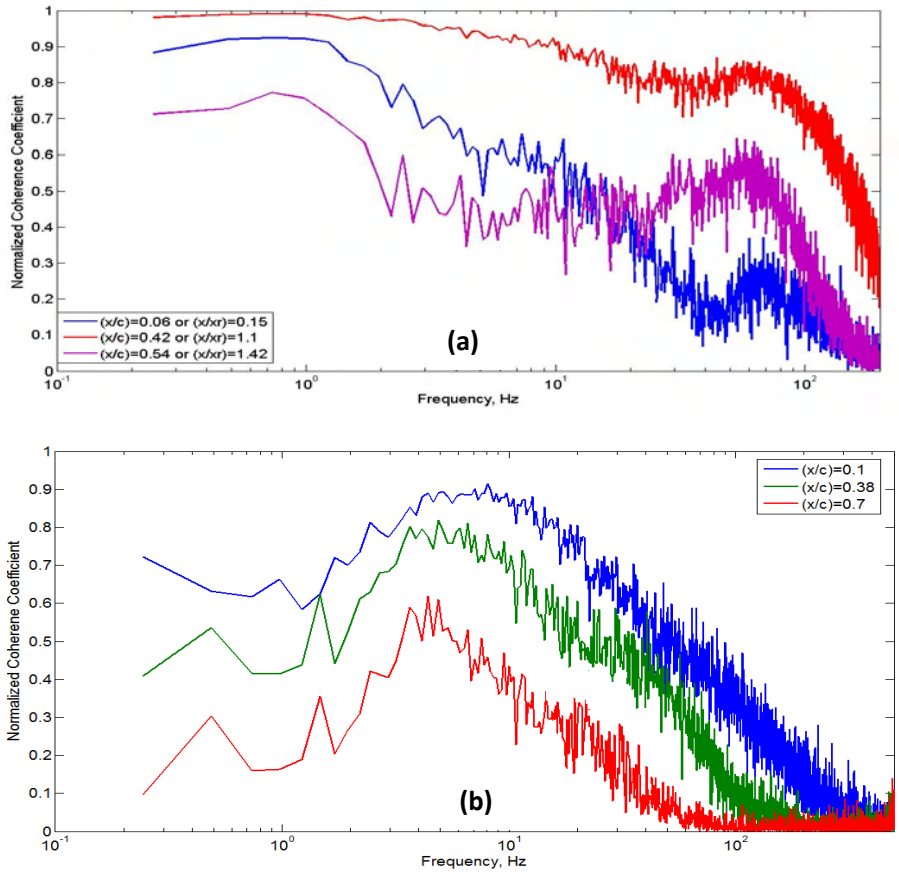

Figure 133: Coherence between pressure fluctuations at reattachment and selected pressure taps when (a) Ti=1.2% and AOA=6Deg and (b) AOA=10Deg and Ti=12.3% Lxx=0.15m.

The coherence fluctuation between point of reattachment and other chordwise locations in nominally smooth flow is plotted in Figure 133a. It shows that the fluctuations upstream of reattachment ((x/c)=0.06) under the bubble, are very coherent at the shear layer flapping frequency, while the fluctuations downstream of reattachment ((x/c)=0.54) are very coherent at the roll up vortex formation frequencies (30Hz-60Hz). Though slightly elevated coherence in the locations downstream and upstream of reattachment is seen at flapping and rollup vortex frequencies respectively, the fact that both curves cross each other in Figure 133a indicates that the fluctuations experienced on either side of reattachment are dependent on different flow phenomenon, viz. shear layer flapping and vortices on reattachment respectively. The reattachment point, through which both these flow phenomena influence the airfoil, is therefore a very influential point which separates the two sides while possessing a governing influence on the fluctuations experienced on either side.

To provide better insight on the size and rate of translation of the various flow structures that developed, the time shifted correlation with respect to reattachment point for all pressure taps is plotted in Figure 134. The figure is to be interpreted as follows; for each chordwise station along the y axis, the normalized time shifted (along x axis) correlation with respect to the reattachment point is plotted on the x-z plane whereby the color intensity represents the coefficient magnitude. The time-shift was normalized with respect to the velocity and chord. By analyzing the regions of high spatial and temporal correlations in the composite plots, insights on the rate of advection and size of the different flow structures can be obtained.

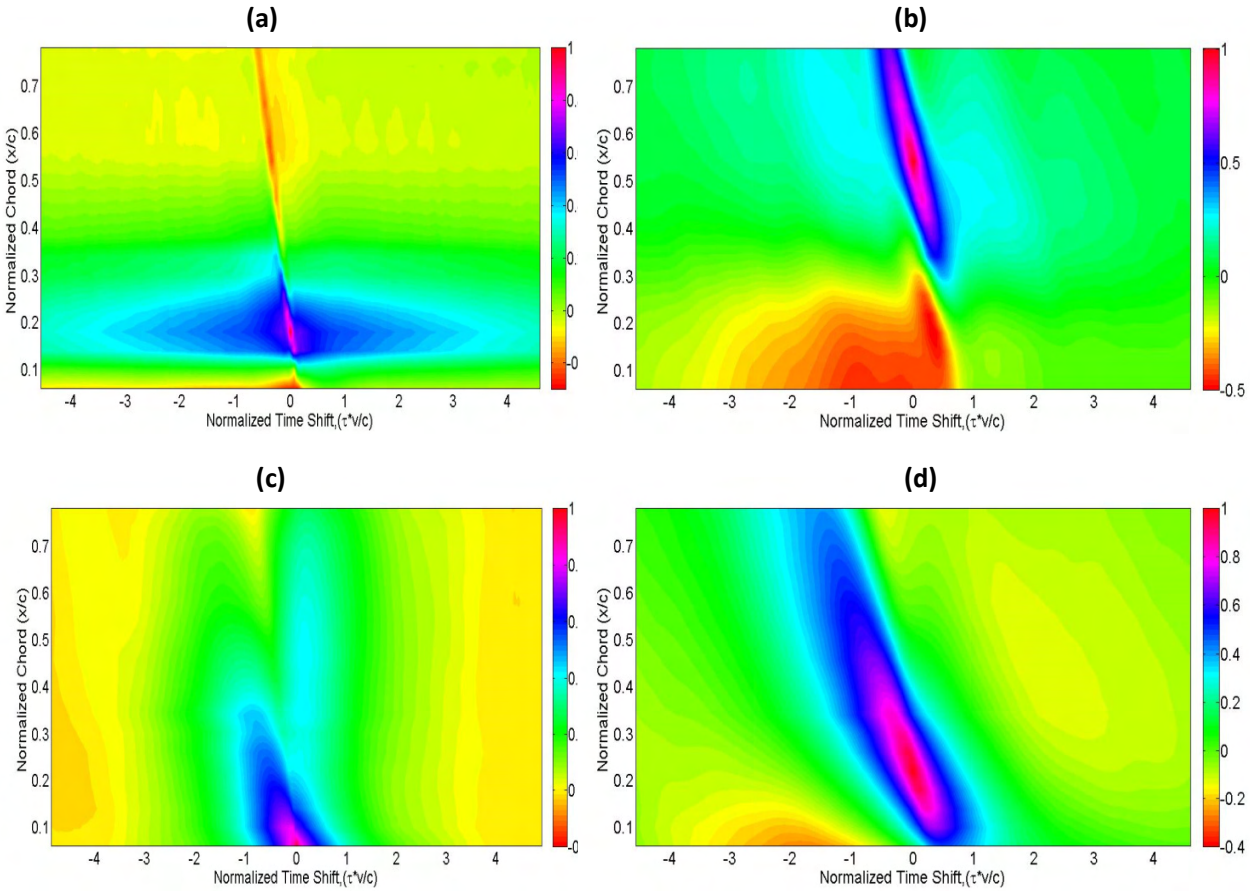

Figure 134: Consolidated correlation between reattachment point and all pressure taps as a function of normalized time shift whereby a&b when Ti=1.2% and AOA=4&8Deg respectively. c&d when Ti=7.15% Lxx=0.14m and AOA=4&8Deg respectively.

The increase in size of the flow structures between 4Deg and 8Deg in smooth flow can clearly be seen by comparing Figure 134a&b where the region of high temporal and spatial correlation is much larger at AOA=8Deg. The sharp peak seen in the correlation in a&b represents the high correlation close to reattachment while the long tail of nominally high temporal correlation (along the x-axis) upstream of point of reattachment and close to leading edge is due to the low-frequency shear layer flapping. The rate of advection of the vortices can be seen to decrease with increase in AOA (i.e. larger time-shift is required to obtain maximum correlation). This is considered to be due to the increased rollup in the shear layer due to the larger velocity difference in the presence of a stronger APG.

Relatively better coherence at the vortex core formation frequency is noticed across all the pressure taps in turbulence, see Figure 133a&b. In turbulence, the correlation peak is much wider temporally, due to the large size of the vortex cores and it decays much lower compared to smooth flow, refer

Figure 134c&d. The consolidated correlation plots in c&d also show that the rate of advection of the vortex cores is much smaller than in smooth flow.

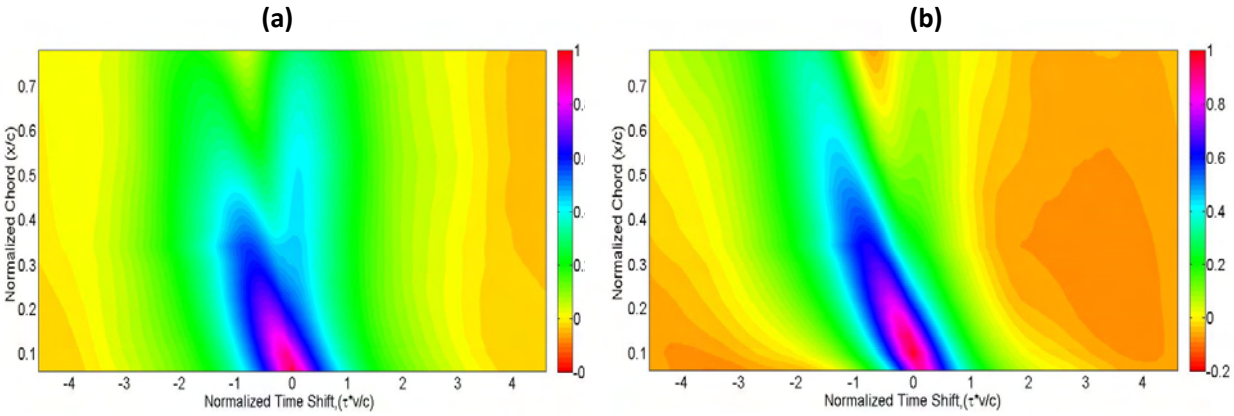

Figure 135: Consolidated correlation between reattachment point and all pressure taps as a function of normalized time shift whereby a & b when Ti=12.3% Lxx=0.15m and AOA=4&8Deg respectively

It was identified in the earlier sub-section that the rate of vortex core formation did not change significantly with change in turbulence intensity because it appeared to be a characteristic of the airfoil section geometry. This is seen once again in the Figure 134c&d and Figure 135a&b where turbulence intensity has a relatively small influence on the rate of vortex core formation and downstream advection.

Except for the case when Lxx=10c (around 1.3m), changes in length scale over the range tested only showed only a very small influence on the correlations. To highlight the influence of the largest length scale, the consolidated correlations when Lxx=0.22m and Lxx=1.3m is plotted in Figure 136a&b respectively. Significantly larger correlation is noticed both spatially and temporally at the longest length scale. This might be due to the higher peak energy in the lower frequencies at the longer length scales having a larger impact on the fluctuations experienced in comparison to the higher frequency lower energy fluctuations at the smaller length scales. It can be deduced from the steeper high correlation region in Figure 136b that the rate of advection of flow structures over the airfoil when Lxx=1.3m is slightly higher than when Lxx=0.22m.

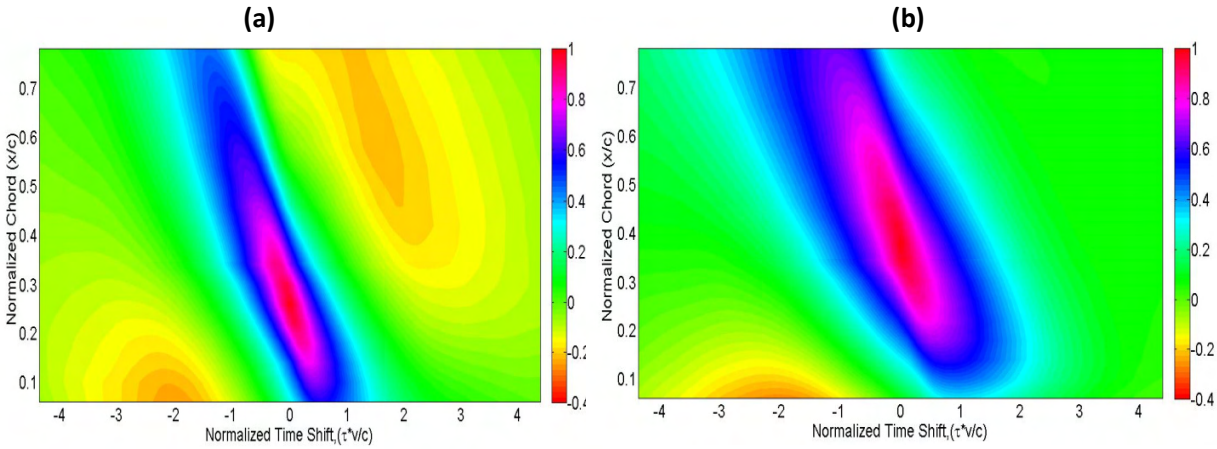

Figure 136: Consolidated correlation between reattachment point and all pressure taps as a function of normalized time shift whereby Ti=7.3% Lxx=0.22m (a) and Ti=7.22% Lxx=1.3m (b). AOA=10Deg for both cases.

4.4 Spanwise Comparisons of Surface Pressure Fluctuations

The simultaneously measured pressures at two spanwise stations separated by 50mm and 200mm permitted the comparison of pressure fluctuations occurring at one spanwise location with respect to another. Analysis of the spanwise correlations of the pressure fluctuations should provide insights on the degree of two dimensionality of the flow over the airfoil. The rolling moment fluctuations that the airfoil might experience can also be gauged from this analysis. In Figure 137 the maximum correlations between pressure taps across two spanwise stations over the chord for different AOAs in nominally smooth flow (Ti=1.2%) are presented.

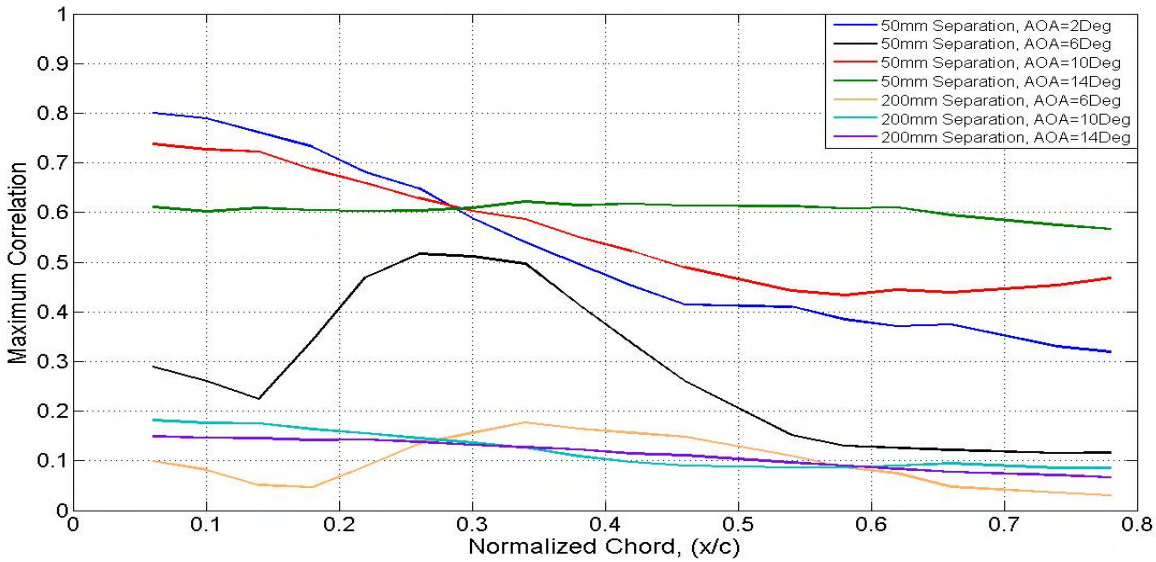

Figure 137: Maximum correlation between pressure taps across the spanwise stations which were 50mm and 200mm apart for different AOAs in nominally smooth flow (Ti=1.2%).

When spanwise separation was 50mm between the pressure measuring stations, a high correlation can be seen at low AOAs (AOA=2Deg) close to the LE, but it drops downstream, refer Figure 137. In the same figure, for both separations (50mm and 200mm) the general trend of the correlations show that relatively higher correlation is present at the location of reattachment for AOAs where LSBs form (see AOA=6Deg). The reduced correlation present downstream of reattachment implies that the structure and shedding rate of the vortices that form on reattachment are governed by local effects and hence they are relatively uncorrelated over the span. Figure 137 also shows that for the AOAs when LSBs are present, the correlation of the time-varying pressures over the span is quite low even when the separation distance is only 50mm. The reduced correlation for this range of AOAs suggests that the flow profile associated with the presence of LSBs is very sensitive to local disturbances.

For the 50mm spanwise separation, at the post-stall AOAs, the correlation increases once again whereby, for AOA=14Deg it is relatively low and nominally constant over the entire chord (Figure 137). It indicates that for AOA>10Deg where the shear layer remains detached, the size of flow structures within the recirculation occurring between the detached shear layer and the airfoil is larger and correlates reasonable well over the 50mm. As expected, the correlation drops considerably as the separation distances increases to 200mm. The low spanwise correlation of surface pressures in smooth flow is believed to be due to the very small eddy size present in the oncoming nominally smooth flow. The

smaller eddies in the oncoming flow influence only a smaller section of the airfoil resulting in the pressure fluctuations over the span at larger separations to be uncorrelated.

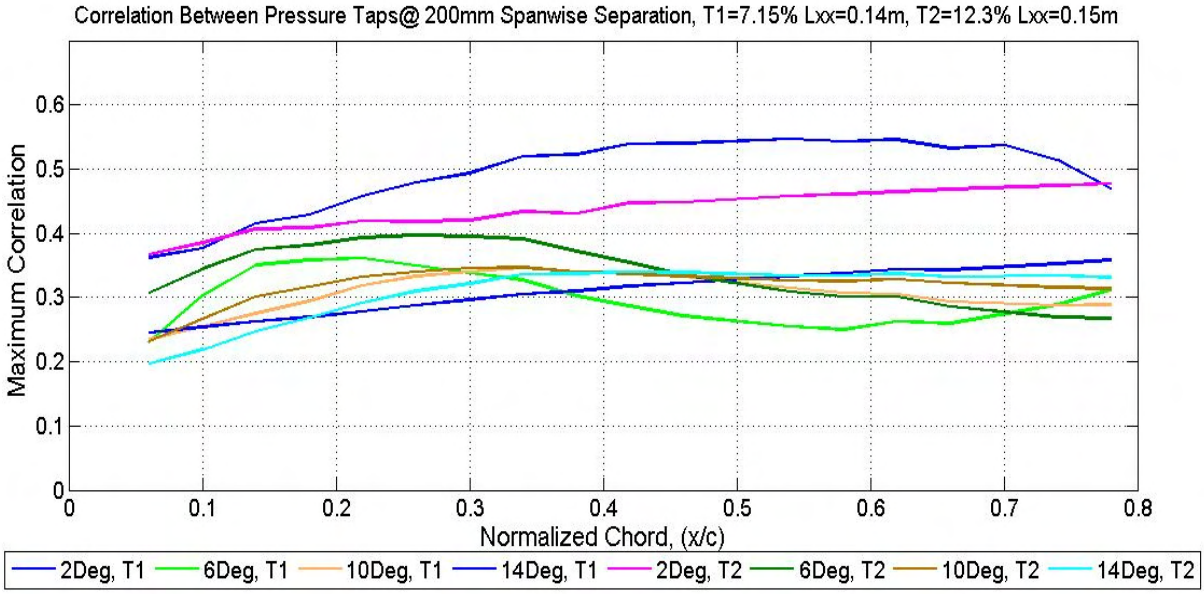

Figure 138: Maximum correlation between pressure taps across the spanwise stations which were 50mm and 200mm apart for different AOAs in Ti=7.15% and 12.3% at Lxx=0.15m approx

In Figure 138, the maximum correlations between the spanwise stations at 200mm separation at two turbulence intensities with nominally the same integral length scale are plotted. Comparing Figure 137 and Figure 138, considerably higher correlation can be noticed in higher levels turbulence as compared to that present in nominally smooth flow, the reason for this is believed to be twofold. Firstly, a greater spanwise correlation of oncoming fluctuations is present in turbulence hence the oncoming forcing frequencies have a greater influence over a large portion of the airfoil span resulting in an increase in spanwise pressure correlation. Secondly, the various flow structure that formed over the airfoil in turbulence were larger in size and intensity, hence they can be expected to have higher correlation over the span.

In Figure 138, high spanwise correlations can be seen to be present over the entire chord at 2Deg AOA in both Ti presented, however the correlation at the lower Ti was marginally higher towards the TE. At higher AOAs, the correlation can be seen to increase with downstream distance from the LE, till a point of maximum correlation is reached. After this point, a gradual reduction in spanwise correlation of

fluctuation occurs. The location of maximum correlation corresponds well with the location of vortex core formation for the respective AOA. Therefore, similar to smooth flow, the regions of reattachment and vortex core formation are best correlated over the airfoil span. At very high AOAs (>14Deg), the spanwise correlation remains nominally the same over the entire chord.

Figure 138 shows that for a given Ti, only a small variation in correlation was present over the range of AOAs except for 2Deg, where correlation was higher. A similar trend was noticed at the same spanwise separation in nominally smooth flow, see Figure 137. Only a small change in correlation is seen to occur when Ti was increased from around 7% to around 12%, suggesting that Ti does not have a significant influence on the spanwise correlation of pressure fluctuations.

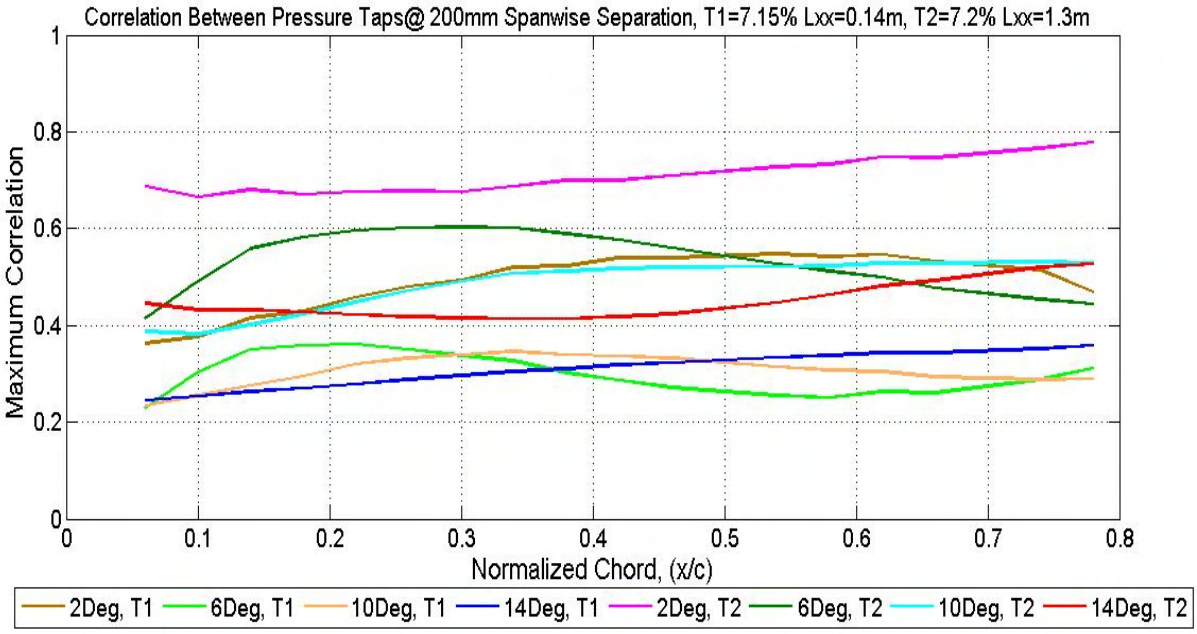

Figure 139: Maximum correlation between pressure taps across the spanwise stations which were 50mm and 200mm apart for different AOAs in Lxx=0.14m and 1.3m at Ti=7.2% approx

The spanwise correlations of pressure fluctuations over the chord at different AOAs when the airfoil was subjected to nearly the same Ti and different length scale are presented in Figure 139. In the figure, a significant increase in spanwise correlation can be noticed over the entire range of AOAs when the airfoil was subjected to the longer length scale. However the chordwise trend of the spanwise correlation appears to remain the same for the two turbulence conditions presented in the Figure 139.

The rate of increase in correlation is higher with change in integral length scale as compared to changes in Ti, compare Figure 138 and Figure 139. This is consistent with the fact that as the oncoming disturbances becomes more correlated, they influence the pressures over a larger portion of the span hence the correlation of pressures is higher. Therefore, comparing results presented in Figure 138 and Figure 139, the spanwise correlation of pressures seem to be more influenced by changes in turbulence length scale as opposed to changes in Ti.

Since spanwise correlations here show the linkage between the pressure fluctuations occurring at one chordwise point with respect to another at a finite spanwise distance away, the possible rolling moments experienced can be gauged from analysis of the spanwise correlation trends. Due to similar spanwise correlation of pressures noticed when Ti was around 7% and 12%, the rolling moments are expected to be higher in the latter condition. This is because analysis of surface pressure fluctuations revealed that the magnitude of pressure fluctuations experienced was significantly higher at the higher Ti, consequently the induced rolling moments would also be high. Though the Std.Dev of pressures over the chord showed that a greater magnitude of pressure fluctuations was experienced by the airfoil when subjected to turbulence of same Ti but with longer integral length scales, analysis of spanwise correlations showed that the induced pressure fluctuations at longer length scales are more correlated over the span. The increased spanwise correlation suggests that the rolling moment experienced at longer length scales will be lower in comparison to those experienced at shorter length scales even though the magnitude of lift fluctuations was lower in the latter condition.

Only detailed investigation of the overall relative lift fluctuations will reveal the exact influence of Ti and length scales on the rolling moments experienced. This was also conducted and the results of the same will be presented in the next chapter.

4.5 Airfoil Wake Structure in Smooth and Turbulent Conditions

Velocity measurements were made downstream of airfoil to better understand the interaction between the different flow structures that formed over the airfoil. The Cobra Probe was used for all wake velocity measurements. Due to high circulation in the flow, data dropouts occurred at certain times during velocity measurement when the flow direction fell outside the probe's ±45° cone of acceptance. In the

data analysis, only sections of data that had extremely limited (0.05% of total data) or no dropouts were used. Spectra of streamwise and vertical velocity fluctuations measured in the airfoil wake when AOA=2Deg and 6Deg when subjected to smooth flow are presented in Figure 140. A distinct peak is noticed at around 450Hz when AOA=2Deg in the velocity fluctuations. Since the Cobra Probe has a flat frequency response well over 2.5kHz, the frequency peak seen in Figure 140 falls well within this range.

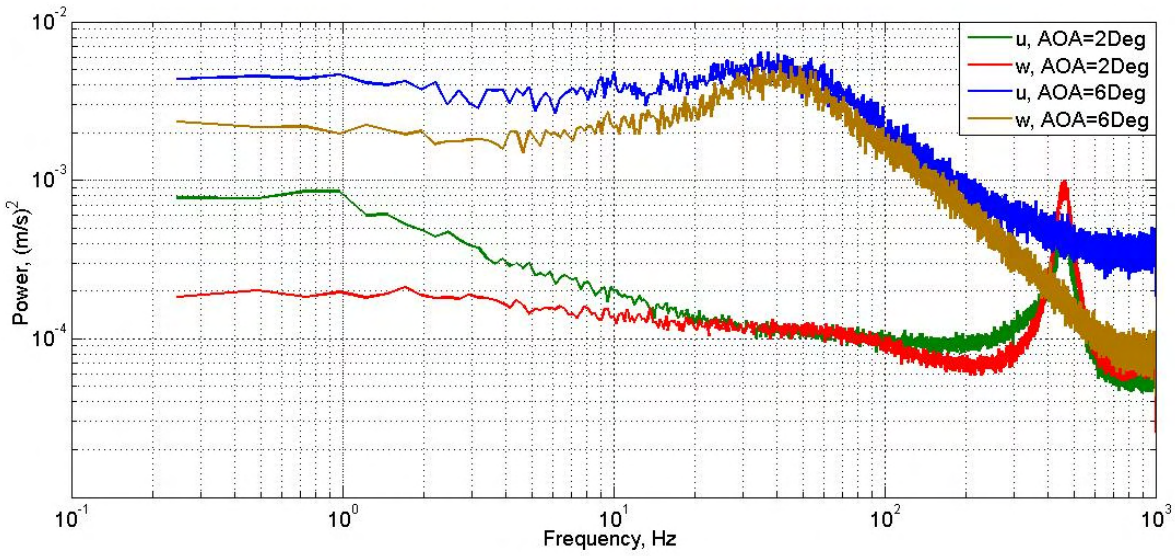

Figure 140: Spectra of velocity in the streamwise (u) and vertical (w) directions measured at (x/c)=1.25 for AOA=2Deg and (x/c)= 0.5 for AOA=6Deg. Ti=1.2% and Re=75000 for both cases.

The 450Hz peak at2Deg AOA could be the rate of K-H-like instability formation at the TE, but since no peak is noticed at such frequencies when AOA=6Deg where the K-H-like instabilities also formed suggests that the 450Hz peak is due to a different flow feature. While it is not possible to definitively identify the fluctuation which resulted in the 450Hz peak, it is strongly believed to be the rate at which the TE streamline oscillates due to the circulation difference between the streamline from top and both surface. Since the field of view was not large enough in the flow visualization experiments, it was not entirely possible to capture this oscillation. The origin of this oscillation can however be seen by comparing the Figure 141a&b where the time difference between the two photos is 0.002s.

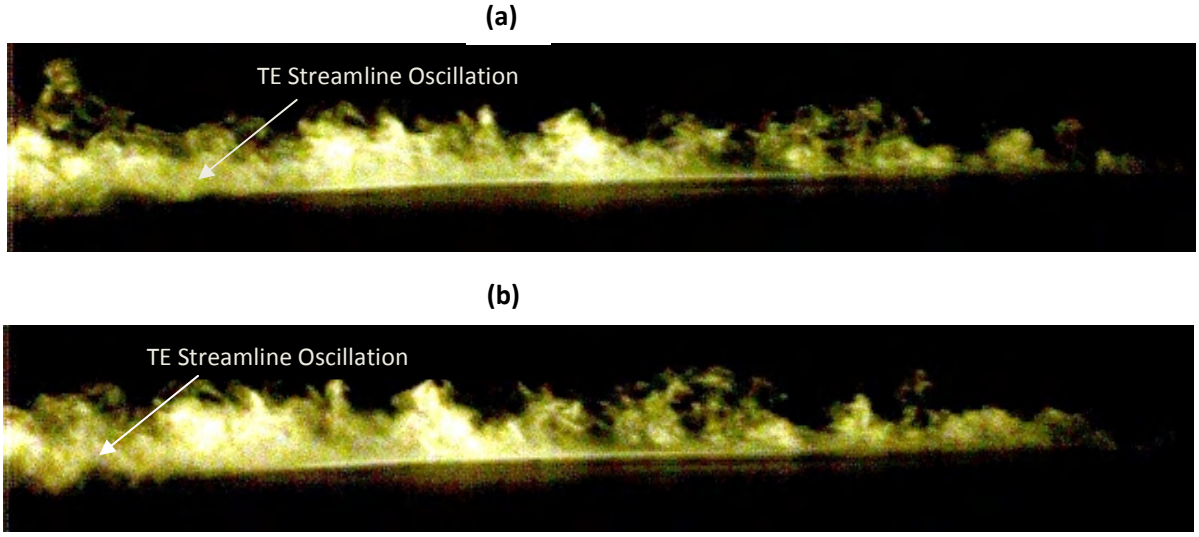

Figure 141: Instantaneous flow visualization showing high frequency oscillation of the TE streamline. Time difference between (a&b) is 0.002seconds.Ti=1.2%, AOA=2Deg and Re=75000.

The wake when AOA was 6Deg is different to at 2Deg AOA as seen in the spectra in Figure 140. The elevation in energy between the 30-60Hz seen in the pressure fluctuations in Figure 100 reduces to oscillations centered around 40Hz in the wake. While the reason for the reduction in peak frequency range is unclear it is suggested that certain rates of shedding dispersed relatively quickly, while certain other shedding rates were characteristic. Since no frequency peak was noticed in the lower surface at this AOA, this fluctuation noticed in the wake is believed to occur due to shedding from shear layer reattachment. Shear layer flapping is not noticed in the wake since it is a LE phenomenon and becomes very weak by the time the flow reaches the TE. The shedding St therefore drops considerably at this AOA as seen in Figure 144.

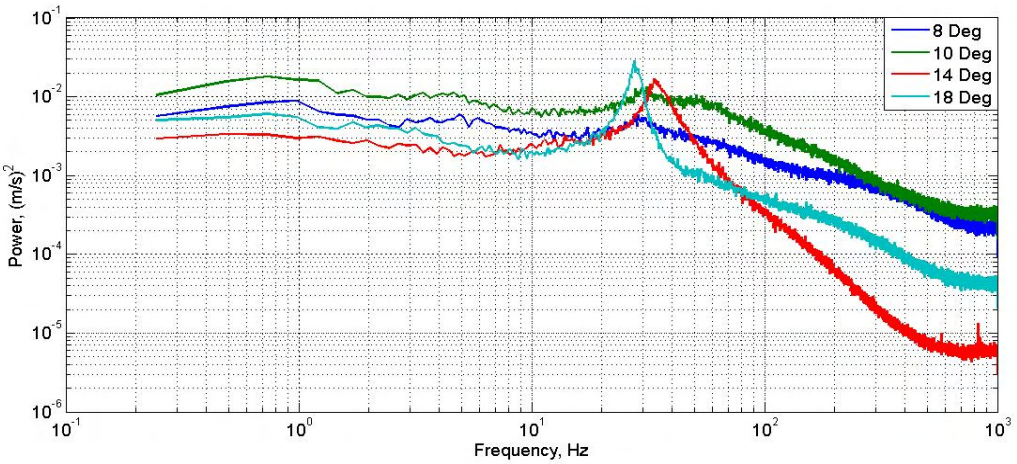

Figure 142: Spectra of velocity fluctuations in vertical direction (w) measured at (x/c) =1.5. Ti=1.2%, Re=75000 for all cases.

Another change in wake structure is noticed with further increase in AOA, see spectra of vertical velocity fluctuations when AOA=8Deg & 10Deg in Figure 142. Firstly, a slight elevation in energy is noticed at the shear layer flapping frequency; this is because the reattachment point is much close to the TE when compared to lower AOAs hence having a greater presence in the wake. At 8Deg & 10Deg AOA, a plateau between 30-60Hz and a small peak at around 30Hz is also noticed in the spectra. Since the point of reattachment is close to TE for these AOAs, the vortices shed on reattachment were still present at the measurement location (1.5(x/c) from LE). The peak at around 30Hz is due to the bluff-body-like vortex shedding. Bluff-body-like vortex shedding from AOA>8Deg result in an increase in shedding St, see Figure 144.

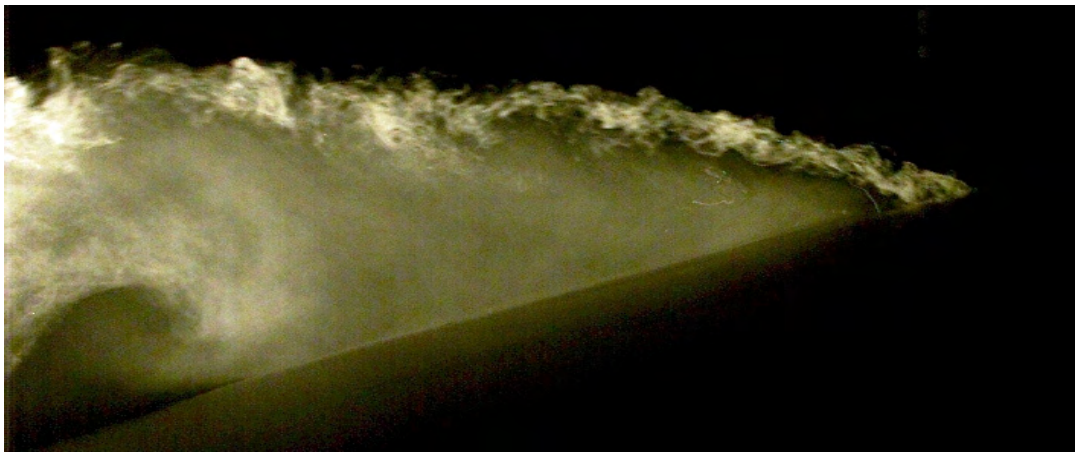

Figure 143: Instantaneous flow visualization showing large vortices being shed from TE when AOA=18Deg, and Re=75000

At AOAs well above 10Deg, the wake was consisted primarily of bluff-body-like vortices, Figure 143. The shedding rate at these high AOAs followed general vortex shedding laws whereby as the AOA increased, the rate of shedding was found to drop, refer Figure 142. Using the projected frontal width as reference, at 14Deg, the shedding occurred at a Strouhal number of 0.19. At these AOAs the surface pressure fluctuations were also centered on the shedding frequency. This was also noticed by Nishimura & Taniike (2001) where the lift force over a circular cylinder was found to fluctuate at the von Karman shedding frequency. Hoarau et al (2003) and Sicot et al (2006) found the same to occur in their experiments on airfoils at high AOAs. Though the exact reason for the vortex shedding frequency at 8Deg to be lesser than at 14Deg is still unclear, it is however believed to be because of the presence of a LSB at the lower AOA which has a significant effect on the interaction between the streamlines from top and bottom surface leading to a drop in shedding rate. The influence of LSB formation on the wake structure can clearly be seen in the Figure 144.

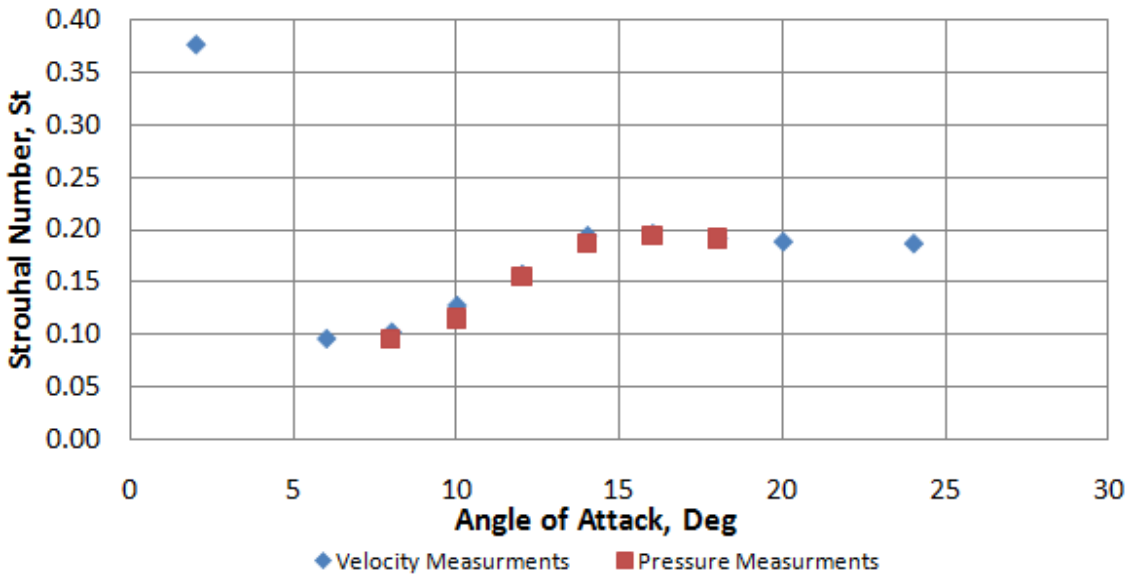

Figure 144: Shedding Strouhal number (St=f*c(sine(AOA))/v) for each AOA based on surface pressure and wake velocity measurements. Wake velocity was measured at (x/c)=1.5 for all AOA, except for 2Deg where (x/c)=1.25. Re=75000 and Ti=1.2% for all cases.

Roshko (1961) and Vickery (1966) reported shedding to occur at around 0.2 and 0.13 for circular and square cylinders respectively. Sicot et al (2006) conducted experiments on a NACA 65_4-421 airfoil and found the characteristic shedding rate at high AOAs to be around Strouhal number of 0.18. The 0.19 shedding Strouhal number noticed here is indeed similar to that reported in earlier studies.

As seen in the earlier section, the wake structure is considerably different in turbulence due to the large variations in flow over the airfoil. Even though the instantaneous AOA varied over a large range, flow visualization revealed that large-scale bluff-body-like vortex shedding from the airfoil when AOA=0 or 2Deg was extremely rare. The surface pressure spectra revealed that vortex cores began forming from 4Deg AOA when Ti=7.2% and for all AOA when Ti=12.3%, however velocity measurements in the airfoil wake, even when AOA=10Deg showed that the wake was fully turbulent with no periodicity present, see Figure 145.

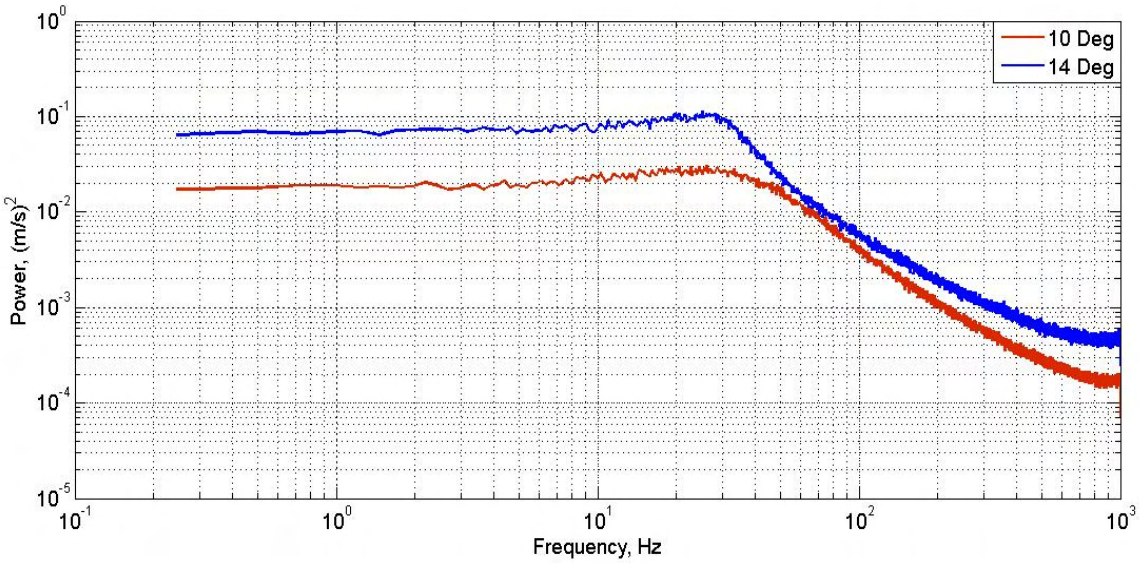

Figure 145: Spectra of velocity fluctuations in the airfoil wake when subjected to turbulence with Ti=7.3% Lxx=0.22m.

The reason for the absence of the any periodicity in the wake is believed to be twofold; the rapidly fluctuating oncoming AOA at relatively high turbulence conditions implied that shedding at a constant rate cannot take place and secondly, numerous instances were seen during flow visualization when the interaction between an advecting vortex core and a vortex being shed from the TE resulted in the nullification of either due their opposing circulation, see Figure 146. It is therefore believed that the combined influence of both these aspects resulted in the wake of the airfoil to be fully turbulent. Sicot et al (2006) however did find characteristic shedding from a NACA 65_4-421 airfoil subjected to turbulence to occur at the same Strouhal number as in smooth flow however at AOA well above 35° when Ti=4%. Since it is improbable for MAVs to be flying at AOA above 25Deg, all testing conducted in

this research was at and below this AOA. Wake velocity measurements were therefore not conducted above 25Deg.

Figure 146: The interaction between vortex cores on the top surface and the bluff-body-like shedding at the TE resulting in the nullification of circulation of either.

Understanding the airfoil wake structure in turbulence also provided insights about the flow experienced by sections of the MAV that may be behind its wings (e.g. empennage). Turbulence intensity and length scale of the flow in the airfoil wake was evaluated since the spectra revealed that the wake is fully turbulent. For the two AOAs (10Deg & 14Deg) presented in Figure 145, the Ti in the wake was 21% and 24% and Lxx was 0.02m and 0.03m respectively. This implied that the interactions between the vortex cores and the vortices shed like bluff-bodies resulted in a significant increase in turbulent energy but the lack of circulation in the wake resulted in an extremely small integral length scale. It is hence conjectured that if the tail plane of the MAV is designed such that it is fully submerged in the airfoil wake, it would be relatively immune to upstream flow speed and direction fluctuations as it would always be within the fully turbulent wake of the wing. High fluctuations in the forces over the tail plane are also expected since it would be exposed to very high Ti.

4.6 Chapter Conclusions and Discussion

Analysis of surface pressure and flow visualization revealed that flow separation occurred at the leading edge at AOAs above 4Deg in smooth flow. On separation, the shear layer transition to turbulence occurred through the amplification of K-H-like instabilities that formed in the bottom sections of the

detached shear layer, leading to the roll up of the layer. The K-H-like instabilities developed much earlier at higher turbulence intensities while length scale did not have a significant influence. In smooth flow pressure fluctuations on the airfoil was dominated by the low-frequency shear layer flapping and higher frequencies vortices being shed on reattachment. Only a small spanwise correlation between the pressure fluctuations over the span was present. This was due to the fact that eddies present in smooth flow were very small and hence they had an influence only over a smaller section of the airfoil span. Velocity measurements in the wake revealed that the characteristic bluff-body-like shedding occurred from AOA=8Deg onwards, but due to its interaction with the LSB and the vortices shed on reattachment of the shear layer, the Strouhal number changes considerably with AOA. The projected frontal width (c(sin(AOA)) was used as the reference length for St estimation. The shedding assumes a more constant Strouhal number from 12Deg onwards of around 0.19, comparable to shedding rate of circular cylinders.

In turbulence however, large vortex cores developed at reattachment point which was very close to LE. These vortex-cores imparted large fluctuations in velocity and pressure over the airfoil and the surface pressure spectra revealed that the rate of vortex core formation was a characteristic of the airfoil and AOA. Due to their large size and higher vorticity, the rate of translation of the vortex cores was much lower than the vortices present in smooth flow. By the time the vortex cores reached the TE, they became very large and weak hence dispersed quickly. Numerous instances occurred when the interaction between the vortex shed from the TE and the vortex core resulted in the nullification of both due to their opposing circulations. This resulted in the airfoil wake to becoming completely turbulent. A comparatively higher spanwise correlation of pressure fluctuations was noticed in turbulence due to the presence of a higher lateral correlation in the oncoming flow fluctuations (forcing frequencies). The spanwise correlation of the pressure fluctuations were also found to be more influenced by changes in integral length scales as opposed to changes in turbulence intensity.

CHAPTER 5

Airfoil Performance in Smooth and Turbulent Flow

This section will bring together the time-averaged and time-varying properties of the flow over the airfoil in smooth and turbulent conditions in terms of their influence on the overall performance. Coefficients of lift, drag and moments were analyzed as both time-averaged and time-varying quantities, as a function of AOA. The measured surface pressures were integrated and transposed to calculate the lift and drag produced by the airfoil. The lift and drag axis orientation used is shown in Figure 147.

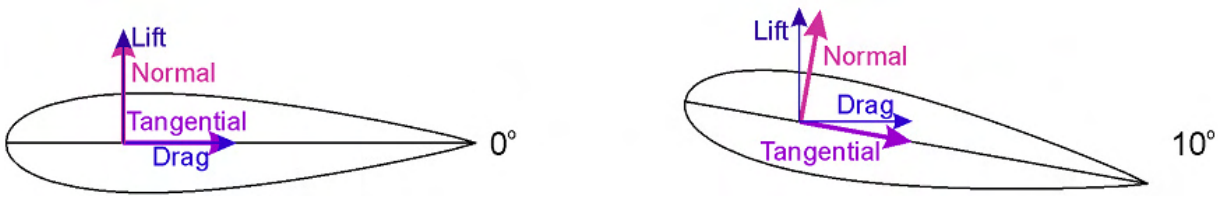

Figure 147: Lift and drag axis orientation used for force calculations. Swalwell (2005)

Since pressure measurements were taken only at finite locations over the airfoil, certain assumptions had to be made to accurately estimate the total lift and drag generated by the entire airfoil section. On the top surface of the airfoil, except for the pressure tap located just downstream of the tap located on the LE, all taps were located in the central section of the airfoil which was planar (i.e. constant thickness). The lift contribution of the pressure taps located in the planar region of the airfoil was relatively straight-forward to calculate since the pressure distribution over the same was normal to airfoil chord. However for the LE of the airfoil, the pressures had to be resolved to account for the local

angles. This was done by dividing the airfoil into small panels of width (x/c)=0.04 and the angle of these panels with respect to the airfoil chord was used. The actual airfoil section, along with the modified top surface is plotted in Figure 148. Having calculated the angle with respect to chord for all panels, the pressure at each panel was resolved to determine its contribution to total lift and drag. For the first panel just rear of the LE, the time-averaged pressures were interpolated between the pressure at the LE and the remaining taps. Even though high suction was produced close to LE, the estimation of the time-averaged pressure at the first pressure tap through interpolation was deemed sufficient since the section width was very small (x/c=0.04), refer Figure 148.

The stagnation point had to be identified for the non-zero AOAs to accurately estimate the total lift generated. While the stagnation point was located at the LE when AOA=0Deg, the point moved towards the TE along the pressure side of the airfoil with increase in AOA. A number of computational as well as experimental methods have been previously adopted to accurately locate this point as a function of AOA, Kang & Altman (2006). However experimentally it was extremely difficult to locate the stagnation point to high accuracy here. Hence the point was estimated by dividing the airfoil lower surface into a large number of smaller panels (x/c=0.01) and the center of the panel to which the mean flow was directly perpendicular for each AOA was assumed to be the location of stagnation point. Once the stagnation point had been identified, one panel was used to connect the LE to the stagnation point, while another was used to connect the stagnation point to the panel containing the first pressure tap from the LE. The planar section of the airfoil on the pressure side was also divided into panels with a width of 6mm (x/c=0.04).

Since the airfoil was thin and the LE was elliptical, for the AOA range tested here, the stagnation point was found to stay very close to the LE. Though this method of stagnation point estimation was not ideal, it offered a manner through which the point could be located quickly and with reasonable accuracy. For example, when AOA=-18Deg the pressure tap closest to the LE ((x/c)=0.06) measured a Cp of around +0.8 and the stagnation point estimated though this method was found to be at (x/c)=0.045. It was therefore considered that by using this method the stagnation point could be located to reasonable accuracy. Moreover, it was found that slight variation in the location of the stagnation point did not significantly influence the overall performance estimation of the airfoil. The actual airfoil section and the modified bottom surface for this AOA are plotted in Figure 148.

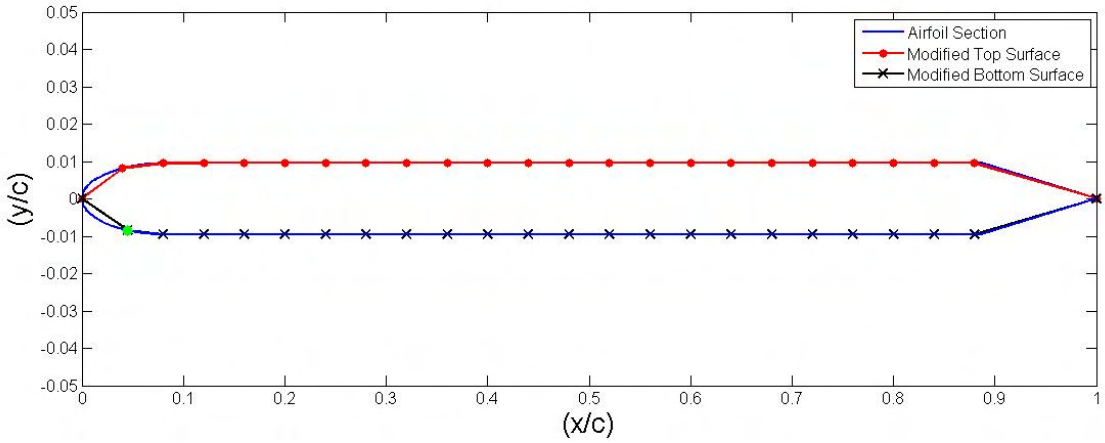

Figure 148: Actual and modified airfoil section divided into a number of panels is plotted one over the other. The second point on the bottom surface (green dot) corresponds to the stagnation point for AOA=18Deg.

The final point required for closing the Cp plot over the airfoil top and bottom surface was the Cp at the TE. It should be recalled from the earlier chapter that K-H-like instabilities formed at the TE implying a difference in circulation between the top and bottom surface at the TE. As pressure taps were not located in the converging rear portion of the airfoil, certain assumptions had to be made in estimating the Cp at TE. It was difficult to accurately measure the velocity at the top and bottom surface at the TE, hence it was assumed that the Cp here is halfway between the Cp of the last pressure tap on the suction and pressure sides. Though this assumption somewhat contradicted what was seen in the flow visualization experiments, it is believed that the difference in circulation is small and its influence on the total lift estimation will also be negligible. The closed Cp plot was resolved appropriately and numerically integrated using the trapezoidal rule to evaluate the lift, drag and moments.

5.1 Influence of Turbulence Intensity and Scale on Time-Averaged Lift, Drag and Moment Coefficients

Even though low spanwise correlation of instantaneous pressure fluctuations was noticed in smooth flow at higher AOAs, higher correlation was present in the time-averaged lift estimated at various spanwise stations, see Figure 149. At post-stall AOAs (AOA>10Deg) however, a slight difference in the lift

estimated is visible but this is only small (i.e. variation of ±1.5% of total lift estimated for the respective AOA). Good similarity across the span indicates that the pressure measuring locations were well removed from end effects.

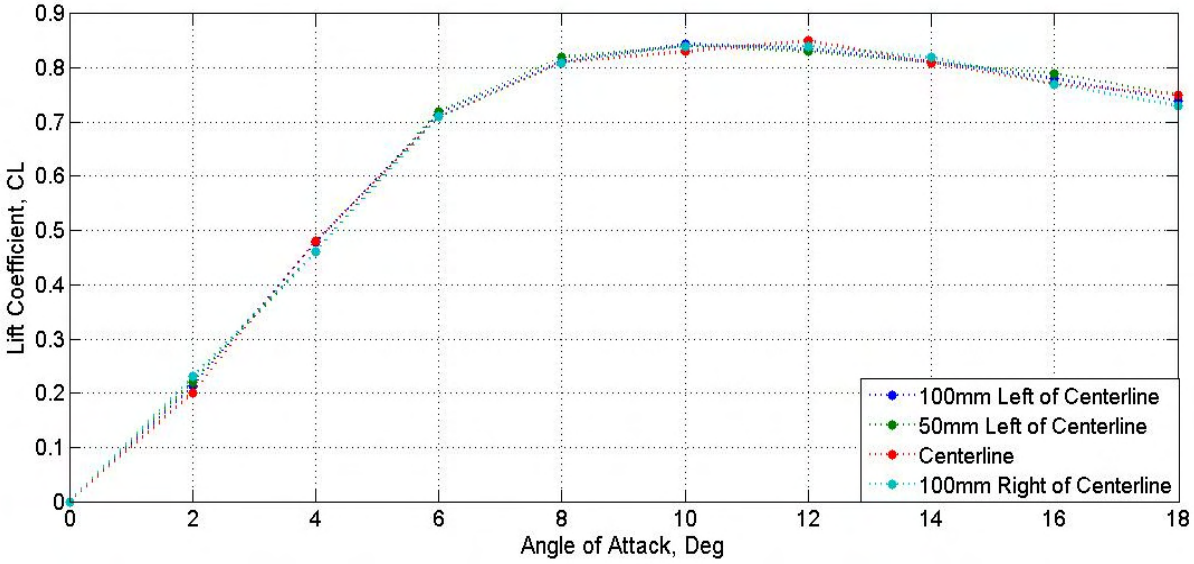

Figure 149: CL vs. AOA measured various spanwise stations in nominally smooth flow (Ti=1.2%).

In Figure 150, the integrated mean Cp (lift coefficient) of only the top surface as a function of AOA at the lowest turbulence intensities (smooth flow) is plotted. Analyzing the lift produced by the top surface of the airfoil from a negative to positive AOAs provided better insight on the lift produced by the pressure and suction sides of the airfoil. Comparing the lift produced at the lowest turbulence intensities i.e. Ti= 0.5% & 1.2% in Figure 150, it can be seen that a slightly steeper CL Vs AOA curve is present along with a marginally lower Maximum CL (CLmax) at the lower Ti. However, the difference in the lift produced by the top surface in the two conditions is quite small. This is similar to Mueller's (1999) finding where no significant influence of turbulence intensity at such low levels was noticed, see Figure 152 from Mueller (1999). In Mueller's work the turbulence intensity was varied from 0.25% to 1.3%, which is of the order of turbulence intensity generated here, however the lift produced was measured through force measurements.

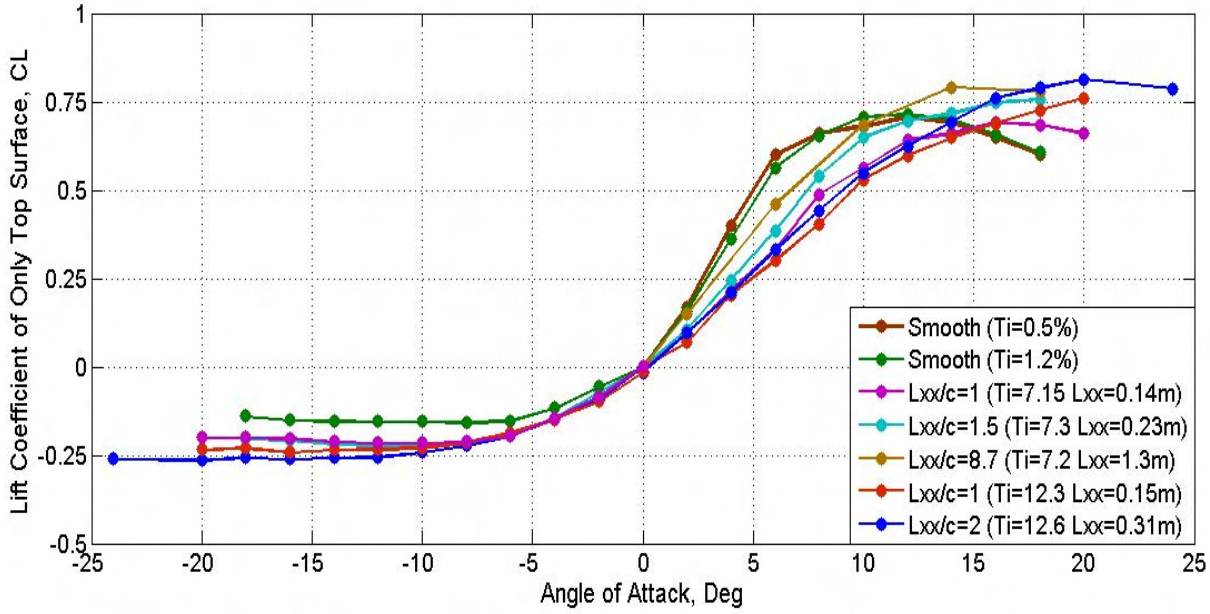

Figure 150: CL vs. AOA of airfoil top surface for different turbulence intensities and turbulence length scales

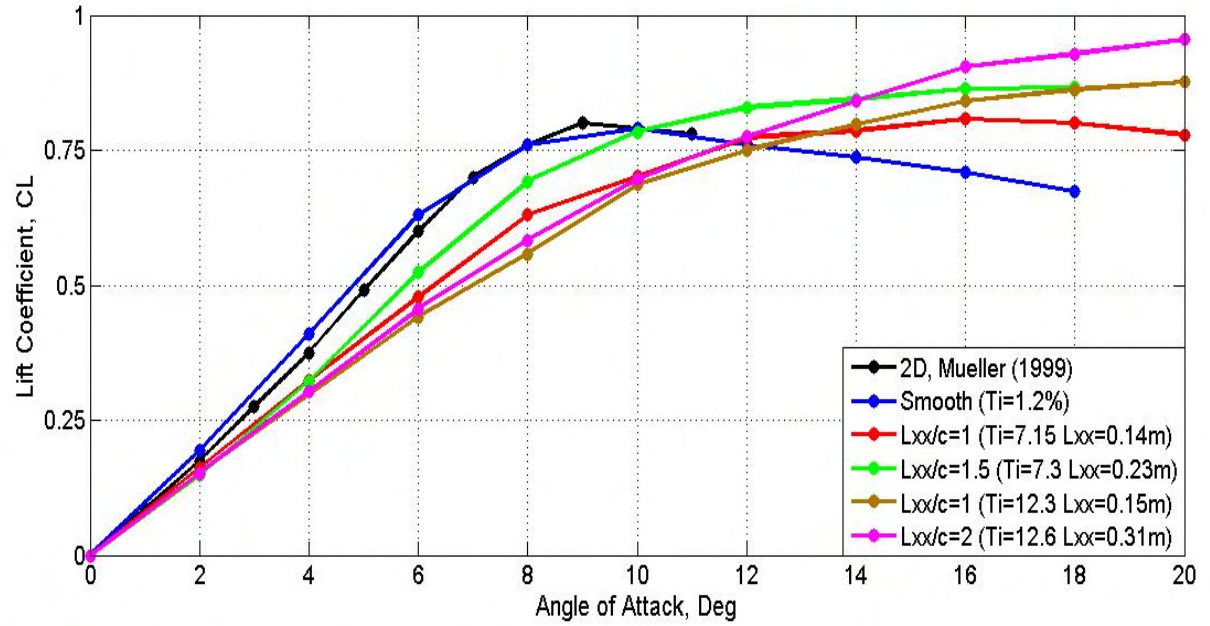

Figure 151: CL vs. AOA of combined suction and pressure sides of the airfoil in different turbulence intensities and length scales. Mueller's (1999) airfoil results at Reynolds number=80,000 in smooth flow is also plotted.

Comparing the estimation of the total lift generated by the airfoil measured through pressure measurements here to Mueller's estimation of the total lift (through force measurements) shows good

similarity. However, the lift estimated here is higher than Mueller's estimation for 4Deg<AOAs<8Deg. It should be recalled that the pressure measurements revealed that in nominally smooth flow LSBs form between 4-8Deg AOA. The variation in the CL estimation obtained here and by Mueller (1999) could be attributed to the fact that LSBs are extremely complex and 3D in nature hence, integration of pressures across one chordwise station would be inadequate to estimate the overall airfoil lift. It is also believed that errors associated, however small, with reading data-points from Mueller's graphs also contributed to the difference in lift estimations. Winkelmann (1982), Swalwell (2005) and a number of other workers had demonstrated the presence of various non-uniform flow phenomena like stall cells over airfoils and reported that lift estimation of the entire airfoil through single row of chordwise pressure measurements would be inaccurate. Therefore, it is believed that in the range of AOAs where LSBs form the time-averaged flow over the airfoil was generally not completely 2D even in nominally smooth ambient conditions. This agrees well with the comments made by Winkelmann (1982) and Swalwell (2005). The spanwise variaince in flow properties over the airfoil in smooth flow under the influence of LSBs has been reported by Sathaye (2004), Burgmann et al (2006, 2008), etc.

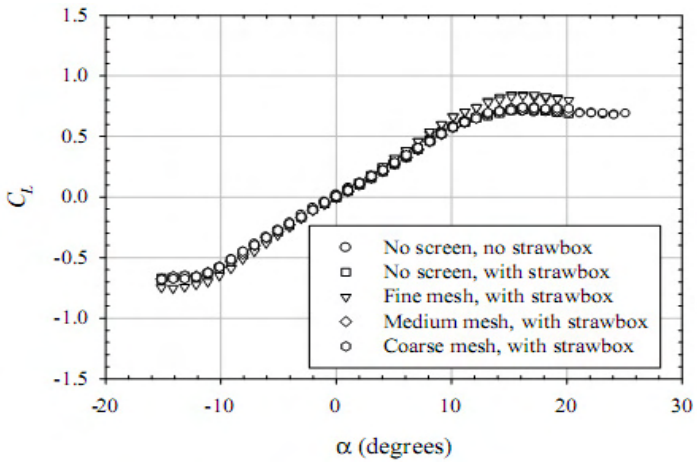

Screen	Mesh size (meshes/cm)	Wire diameter (mm)	Turbulence %
Fine	7.09	0.245	0.25
Medium	3.15	0.508	0.45
Coarse	0.64	1.397	1.3

Figure 152: Effect of freestream turbulence on time-averaged lift coefficient for a wing with semi AR of 1.5 at Re=60000, Mueller (1999). The airfoil section is similar to the one used in this research.

It has also been demonstrated that the interactions between the airfoil end-plates, oncoming flow and the airfoil LE has a large influence in the flow structure over the entire airfoil. McCroskey (1982) and Carr (1988) in their reviews however suggested that further studies were required to deterime the exact degree of influence of these interactions. The slight variation between the results presented here and Mueller (1999)'s finding, where airfoils with an AR of 6 and 2 was used respectively, indicated that the

influences due to flow and side wall interaction was small however further investigation in needed to acertain its exact influence.

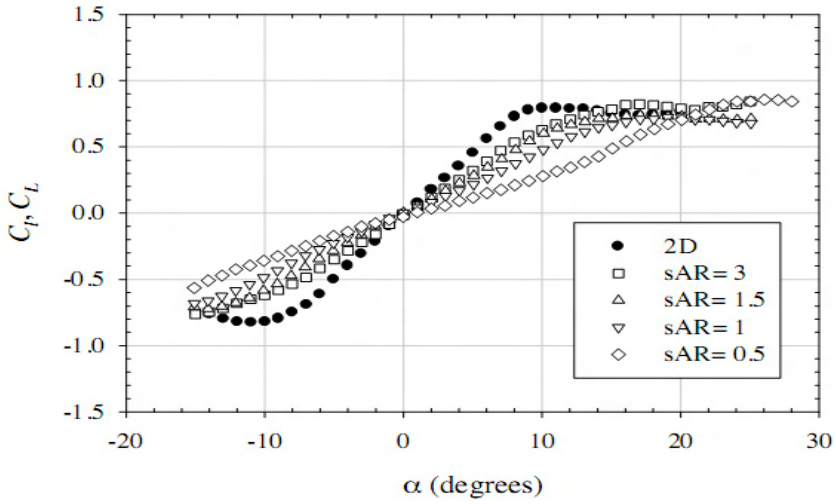

Figure 153: CL vs. AOA for the same airfoil section measured through force measurements by Mueller (1999).

Similar to smooth flow, the time-averaged lift measured at various spanwise locations correlate well in increased levels of turbulence (Figure 154). In Figure 150 and Figure 151 a large change in lift generated is however noticed as the turbulence intensity increases; compare the CL vs. AOA for smooth flow, Ti=7.14 Lxx=0.14m and Ti=12.3 Lxx=0.15m conditions. In the figures, a progressive but considerable reduction in the lift-curve-slop is also noticed as Ti increases. The reduced slope at higher Ti implied that for a given AOA, the time-averaged lift generated in smoother flow was greater than in increased levels of turbulence, however, in the same figure it can be seen that stall was experienced much earlier in smoother conditions.

The steeper lift-curve-slope present at lower Ti is believed to be due to a "pseudo-camber" effect experienced by the airfoil. When oncoming flow was subjected to an APG over the airfoil, flow separation from airfoil leading edge occurred; however a region of high suction was also noticed to form from the LE till the location of reattachment in the LSB or over a region of vortex core formation in smooth and turbulent flow respectively (refer mean Cp plots in smooth and turbulent conditions). Therefore, the LSB in the smooth flow condition, or the vortex core in its formative stage in higher levels of turbulence, can be considered to act as a small appendage to the airfoil top surface that altered its geometry by creating a cambering effect on the top surface. Since the velocity attained in the top region

of the shear layer in smoother flow was greater than in turbulence (where higher mixing was present), it rendered the suction to also be greater in the former case. Hence in smooth flow for the range of AOAs where LSBs were present (pre stall AOAs) the airfoil appeared to have a higher camber (pseudo-camber) resulting in an increase in lift generated for a given AOA.

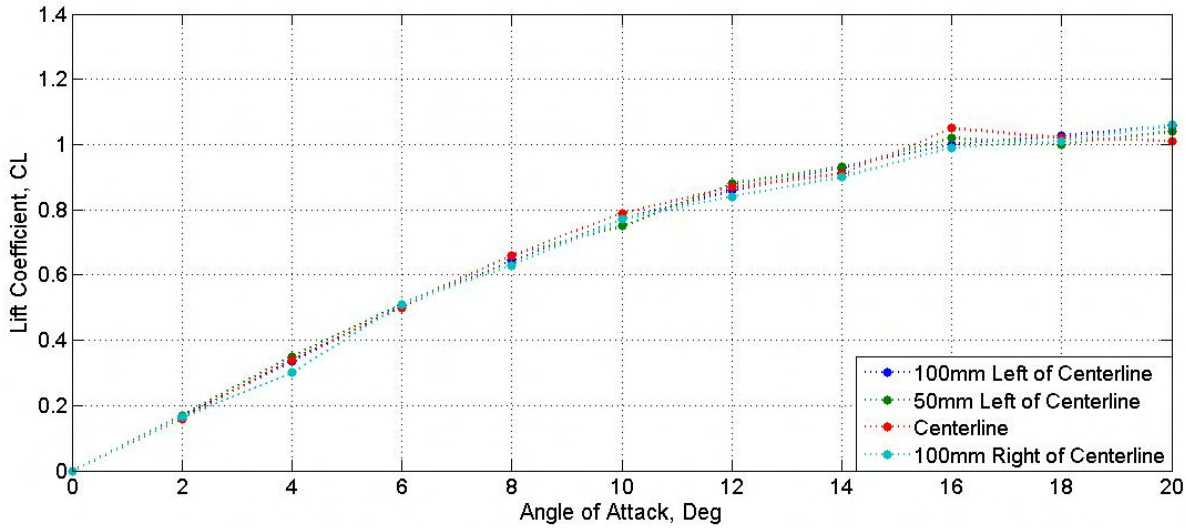

Figure 154: Combined top and bottom surface CL vs. AOA measured various spanwise stations in turbulence (Ti=12.6% Lxx=0.31m)

In smooth flow the pseudo-camber effect had the highest effect on the total lift generated due to the increased acceleration of the flow just above the shear layer. Due to the reduced acceleration of the flow just above the shear layer because of increased mixing and the absence of a constant region of circulation over the airfoil in higher levels of turbulence, the pseudo-camber effect had a significantly lesser influence as Ti increased. This resulted in a relative reduction in the lift generated at higher Ti. The reduction in the lift-curve-slope can be seen in Figure 150 and Figure 151 as turbulence intensity is increased.

While a higher lift was generated in smoother flow conditions at lower AOAs, the presence and growth of LSBs at lower Ti implied that stall was experienced much earlier as well. The delay in stall with increase in Ti is clearly seen in Figure 150 and Figure 151. On stalling, the lift produced in smooth flow begins to drop, not because of a large drop in suction, but due to a combined effect of a small drop in suction and a reduction of the suction component along the lift axis (i.e. flow normal direction). The

small change in pressure distribution over the airfoil in the post-stall AOAs in smooth flow supports this fact. In the presence of high freestream turbulence, earlier transition and the formation of vortex cores resisted the strong APG even at very high AOAs (AOA>12Deg), allowing the airfoil to experience attached flow and significantly delaying stall. While it is not ideal to characterize the vortex core formations over the airfoil as an attached condition, the fact that the shear layer does attach to the airfoil surface leads to an increase in lift. Due to the increased curvature of the shear layer and a stronger resistance offered to the APG at higher AOAs, the maximum lift (CLmax) was much higher at higher turbulence intensities. Delayed stall indicates that the airfoil's operational range, in terms of time-averaged lift generation, increases as turbulence intensity increases.

Therefore, increase in turbulence intensity resulted in a reduction of the lift curve slope along with a delay in stall and an increase in maximum CL. This is very similar to the findings by Devinant et al (2002), Jancauskas (1983) and Swalwell (2005)'s findings as seen in Figure 20, Figure 19 and Figure 155 respectively. Two points must be noted while comparing with Swalwell (2005)'s results shown in Figure 155. Firstly, the experiments conducted by Swalwell were at a much higher Reynolds number (Re>300,000) as they were relevant for turbine blade research. Secondly, the turbulence length scale was not constant for all Ti presented in Figure 155. Hence results in Figure 155 consisted of an intermigled influence of both turbulence length scale and intesnity. As for the results from Jancauskas (1983) and Devinant et al (2002)'s expreiments, the Reynolds number was higher in both and no mention of the length scale was made in the latter.

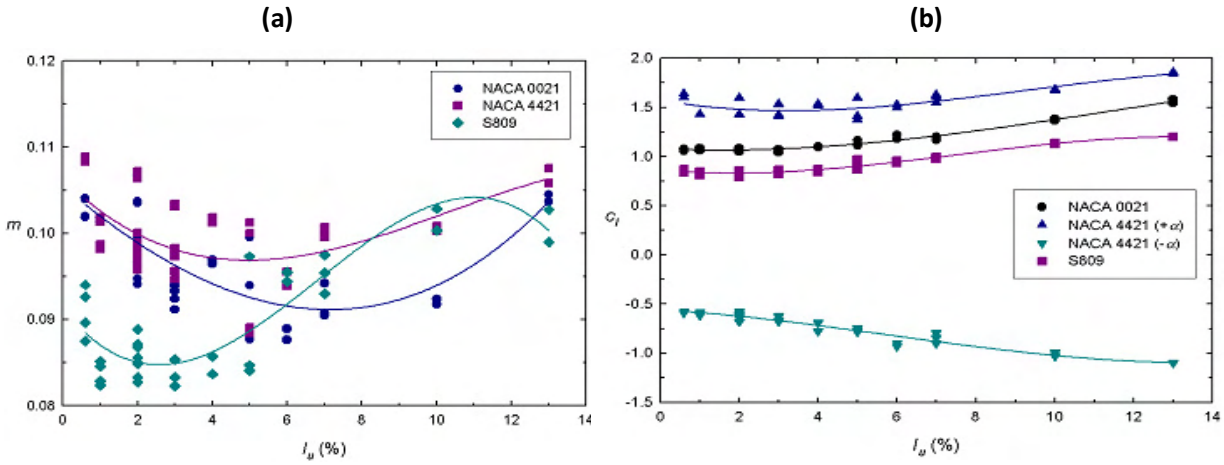

Figure 155: Variation of (a) lift-curve-slope and (b) CLmax with turbulence intensity. Swalwell (2005)

Stack (1931) found the lift curve slope to increase in the presence of a turbulence grid at Re=53,000 (see Figure 18), this is just below the Reynolds number at which tests were conducted here. However Stack (1931) also found the opposite to occur at Re=83,000, just above the Reynolds number at which testing was conducted here (Re=75000). As mentioned in the earler chapter, this discrepancy is believed to be due to the improper characterization of turbulence in the flow by Stack at that time. Loxton et al (2009) also reported a similar trend for a 3D wing with same airfoil section as used here albeit with AR=2 subjected to turbulence.

In general, good similarity is present between the findings here and other research in terms of overall trends on the influence of turbulence intensity on the lift generated. By plotting the lift over the top surface of the airfoil in various flow conditions, the results here offer a unique perspective on the influence of fluctuations in oncoming flow speed and direction on the pressure and suction sides of the airfoil at different AOAs. Figure 150 also shows that turbulence intensity has a significatly smaller influence on the pressure side as opposed to the suction side where a number of different flow features develop. The pressure side can be seen to contribute around 25% to the total lift generated by the airfoil in both smooth and turbulent conditions.

The individual lift produced by top surface of the airfoil, as well as the entire airfoil, when subjected to turbulence of varying length scale and intensities is also plotted in Figure 150 and Figure 151, respectively. To identify the influence of length scale on lift, comparisons will be made between the CL vs AOA obtained when Ti was around 7% and Lxx was 0.14m, 0.22m and 1.31m, and when Ti was around 12.5% and Lxx were 0.15m and 0.31m. Figure 150 shows that similar to the influence of Ti, the influence of changes in turbulence length scale is most noticable on the suction side, while only a small change in the lift produced by the pressure side is present. From both figures it can be seen that as the length scale decreases, a reduction in the lift-curve-slope and a small decrease in CLmax occurs. The increase in lift-curve-slope with increase in length scale is believed to be due to the fact that at longer length scales, more energy is present at the lower frequencies hence the flow has a closer resemblence to smoother flow condition where the “pseudo-camber” effect has a larger influence. This in turn results in an increase in lift generated at longer length scales concequently leading to an increase in CL vs AOA slope. This is evident in Figure 150 where the lift-curve-slope for the longest length scale has closest resemblence to that obtained in smooth flow. Along with an increase in the lift- curve-slope, the CLmax is also marginally higher at the longer length scale. The lift-curve-slope varies in a similar manner for changes in length scale when nominally Ti=12%, see Figure 151. However, there appears to be a larger

influence of length scale when the Ti was nominally 12% as opposed to the nominally 7% condition. The change in lift produced in the post-stall region across the different length scales is also much higher here when compared to the Ti nominally 7% condition.

Extremely limited literature was available to make effective comparisons with findings here on the influence of length scale on mean lift generated by the airfoil. The only available source was work conducted by Swalwell (2005) where, of the many turbulence conditions studied, only for a few conditions the turbulence intensity was held constant and the length scale was varied. The turbulence intensity for these conditions were however quite low (Ti=2% & 5%). In Figure 156, Swalwell's findings on the variation of lift-curve-slope and maximum CL with turbulence length scale is plotted. While comparing with these results, the earlier-mentioned precaution with respect to Swalwell's (2005) findings must be kept in mind. The presence of large scatter and small range in the data rendered accurate inference difficult, but based on the trendlines, it appears that the findings presented by Swalwell correlates resonably well with results obtained here. In general good similarity is noticed between results here and the limited literature on the influence of turbulence length scale on lift.

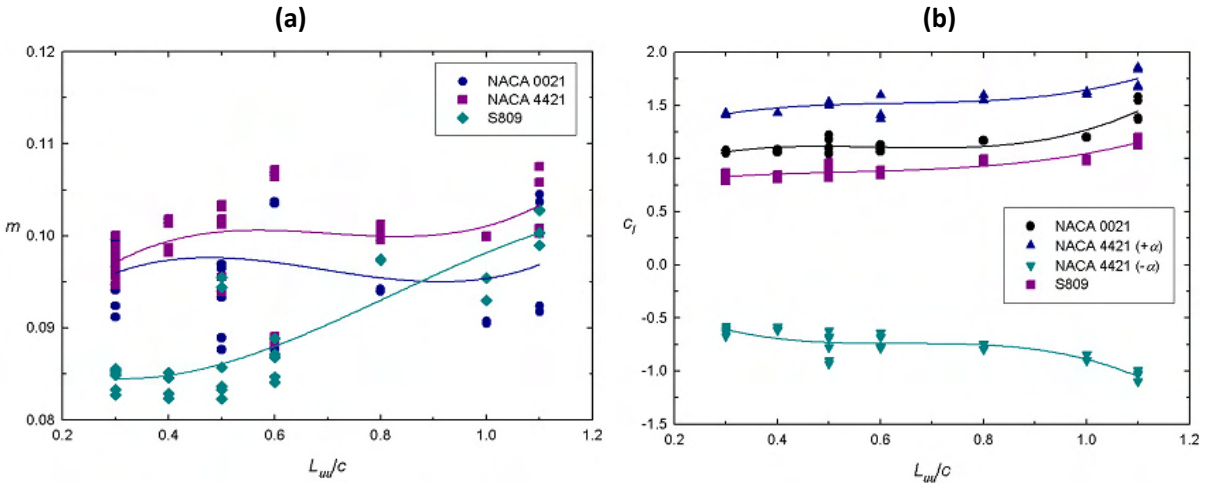

Figure 156: Variation of (a) lift-curve-slope and (b) CLmax with turbulence length scale. Swalwell (2005)

Having indentified the influence of turbulence intensity and length scale on lift, the CD vs AOA for various flow conditions was investigated and is plotted in Figure 157. Since the drag was estimated through the pressure measurements, only the pressure drag coefficient could be estimated. It can be seen that due to the reduced lift curve slope in higher levels of turbulence, the pressure drag at lower

AOA is lesser than in smoother flow while the opposite occurs at higher AOAs due to the delay in stall and a greater CLmax in turbulence, see Figure 157.

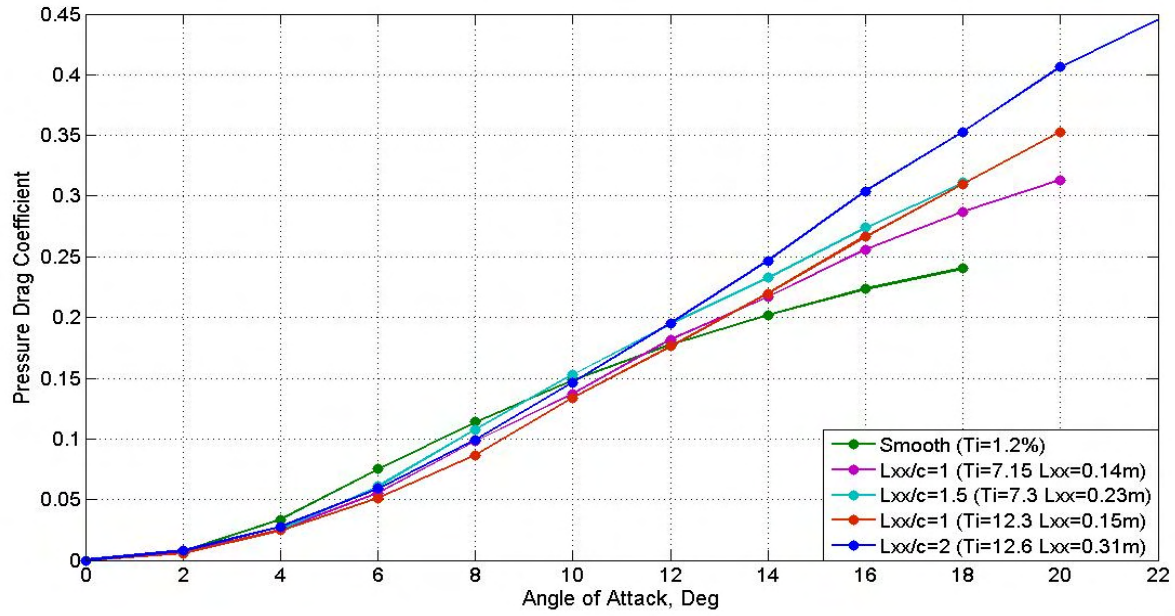

Figure 157: Combined top and bottom surface CD vs. AOA of airfoil top and bottom surface in different turbulence intensities and length scales

The drag coefficient estimated in smooth flow here can be compared to the drag measured by Mueller (1999) through force measurements on the same airfoil. Mueller (1999)'s results are presented in Figure 158. Comparing Mueller (1999)'s estimation of CD vs AOA to the plot in Figure 157 shows that the majority of the drag in the range of AOAs presented is due to pressure drag contribution. The reason for this is however unclear, as it would be expected that the presence of separation bubbles would significantly increase the overall drag (form+parasite drag). Swalwell (2005) too estimated the pressure drag on three different airfoils and found turbulence to have a considerable influence especially around the stalling AOA. For the airfoils tested by Swalwell (2005), in smooth flow a significant drop in CL along with a sharp increase in CD occurred at stall. In turbulence however, the extent of drop in CL and increase in CD was much smaller. Since stall occurred more gradually for the airfoil here, increasing turbulence resulted in an even smoother change in CL and CD with AOA. Swalwell (2005)'s estimation of pressure drag coefficient on NACA0021 airfoil is presented in Figure 159.

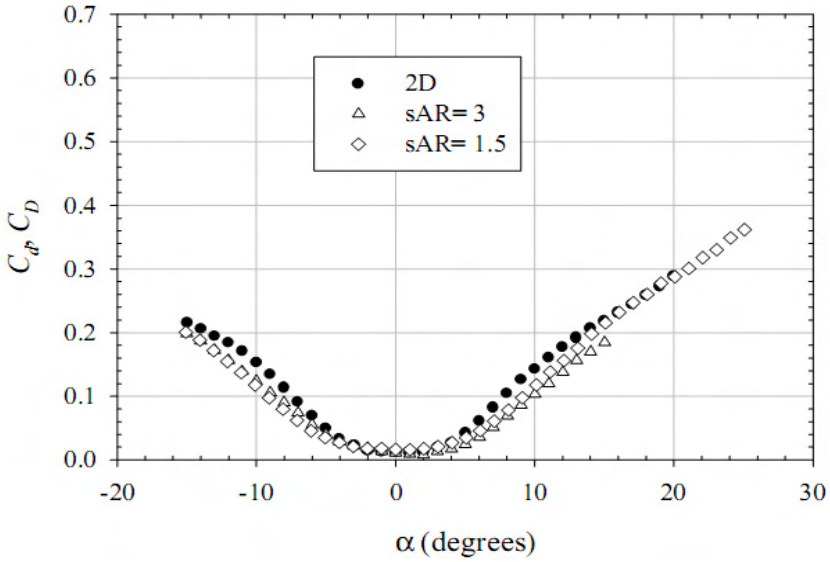

Figure 158: CD vs. AOA for the same airfoil section measured through force measurements by Mueller (1999).

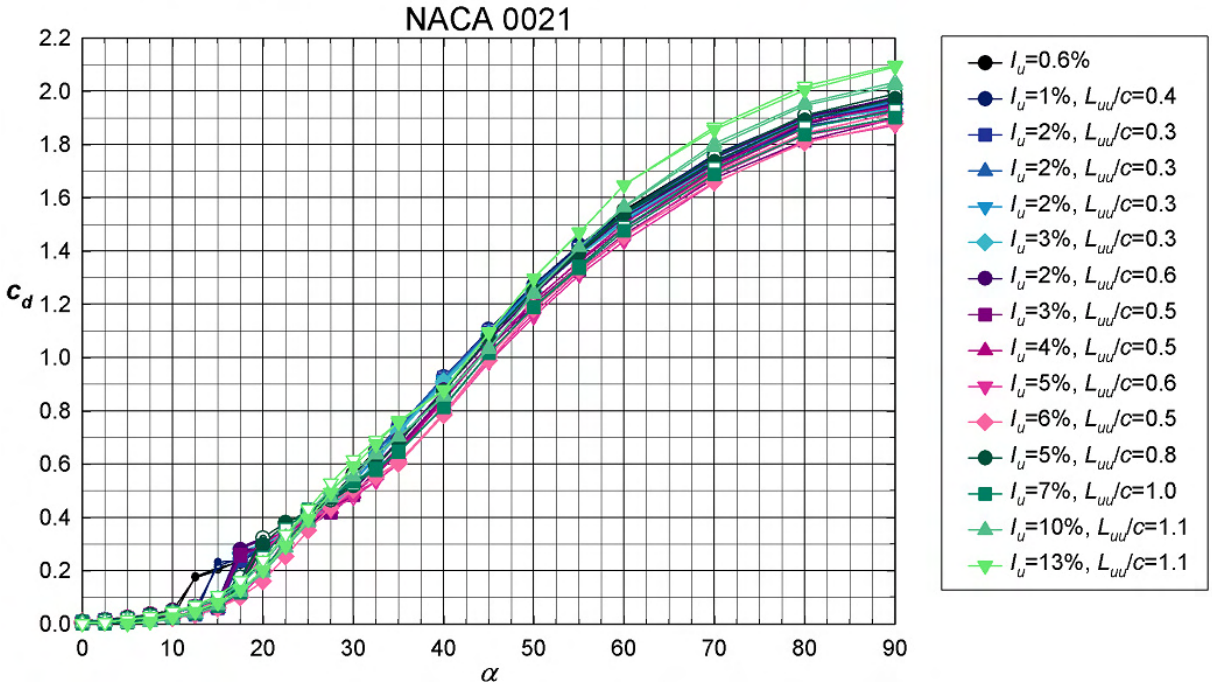

Figure 159: CD vs. AOA for NACA0021 airfoil section in different turbulence conditions. Swalwell (2005)

In Figure 160, CL vs CD for the different flow conditions is plotted. Though the estimated airfoil drag is not complete since only the pressure drag is accounted for, the figure nevertheless provides insight on the variation of drag and lift when exposed to various flow conditions. A large difference in the variation

between CL and CD is noticed between smooth and turbulent flow. Comparing Figure 160 and Figure 151, for a particular AOA, shows a large variation in CL, depending on oncoming flow condition, but for a particular CL the coresponding pressure drag is very similar over the various turbulence conditions. It would have been ideal if the total drag could be estimated for exact performance analysis, however since only pressure measurements were taken, this was not feasible.

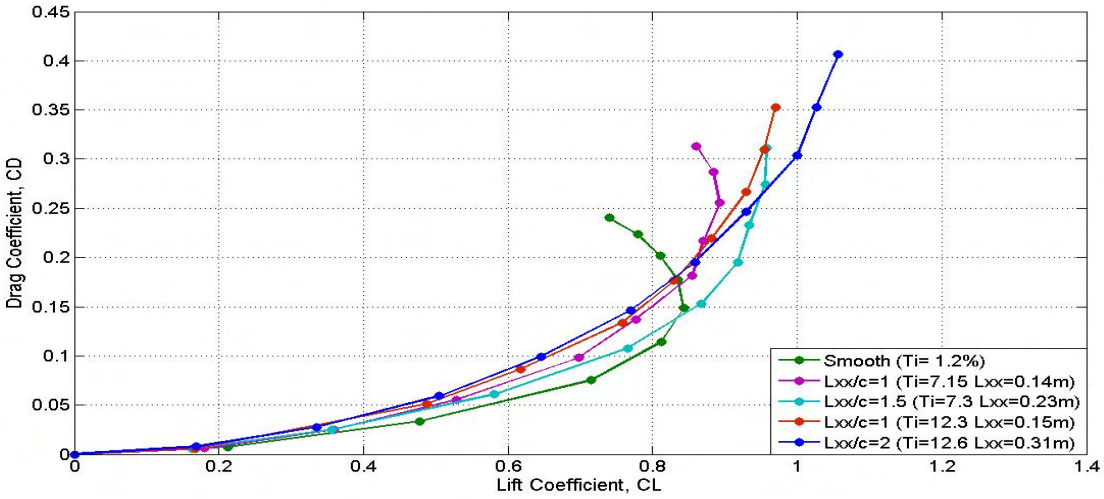

Figure 160: Pressure CD vs. CL of airfoil in different turbulence intensities and length scales

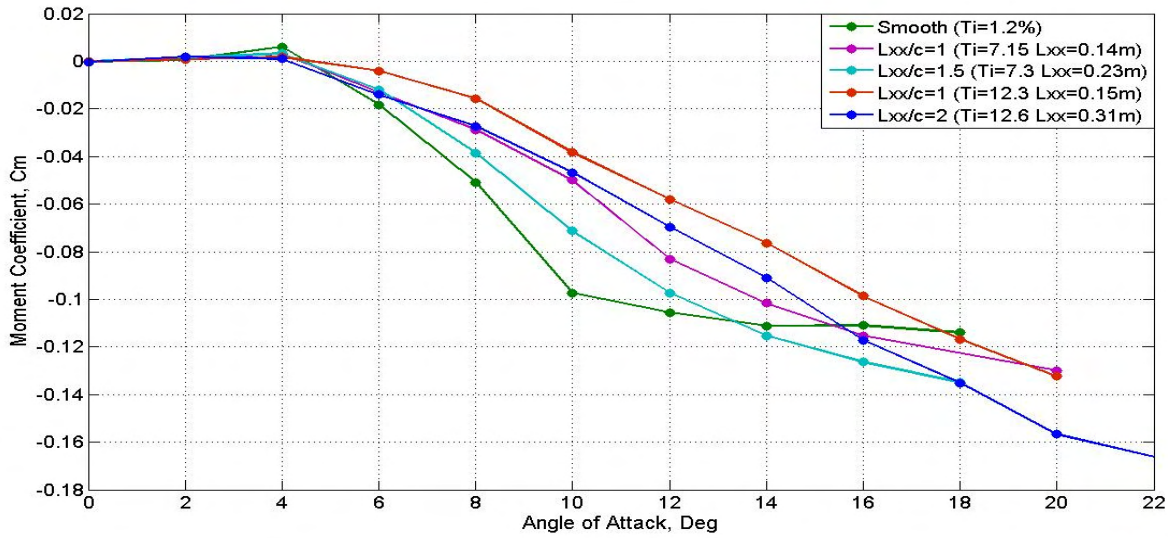

Figure 161: CM vs. AOA of airfoil in different turbulence intensities and length scales

The variation of pitching moment coefficient at quarter chord with AOA in various flow conditions is plotted in Figure 161. The figure shows that turbulence length scale and intensity have an influence on CM as well. In smooth flow, the pitching moment can be seen to increase slightly from CM=0 at 0Deg AOA until LSBs form (4Deg AOA), after which the pitching moment decreases steadily until stall occurs. Therefore, when the airfoil is experiencing an attached flow condition, it attains a slightly longitudinally unstable condition. The presence of a LSB however seems to enforce higher longitudinal stability whereby a decrease in CM ensues with further increase in AOA till the point when the airfoil stalls completely, after which the CM remains nominally constant. A similar trend was noticed by Mueller (1999) as seen in Figure 162.

When subjected to higher levels of turbulence (see Figure 161), CM remains constant at around CM=0 for a longer range of AOAs because the airfoil experiences attached condition until a significantly higher AOA. The slight increase in CM at the lower AOAs noticed in smooth flow is not seen in higher levels of turbulence. Further increase in AOA (AOA>6Deg) shows that the CM begins to decrease but the rate of decrement seems to be determined by both turbulence intensity and length scale. With increase in turbulence intensity the rate of decrement of CM is lower due to earlier attainment of transition and reattachment of the flow. An increase in length scale however resulted in the airfoil attaining a state closer to smooth flow condition, hence for particular turbulence intensity, the increase in length scale resulted in an increase in the rate of reduction of CM. The influence of length scale and turbulence intensity is well captured in Figure 161. In turbulence, unlike in smooth flow, the CM appears to follow this decreasing trend even at high AOAs. Based on the findings here, the turbulence intensity and length scale appear to have an opposing influence on the airfoil's pitching moment coefficent at higher AOAs.

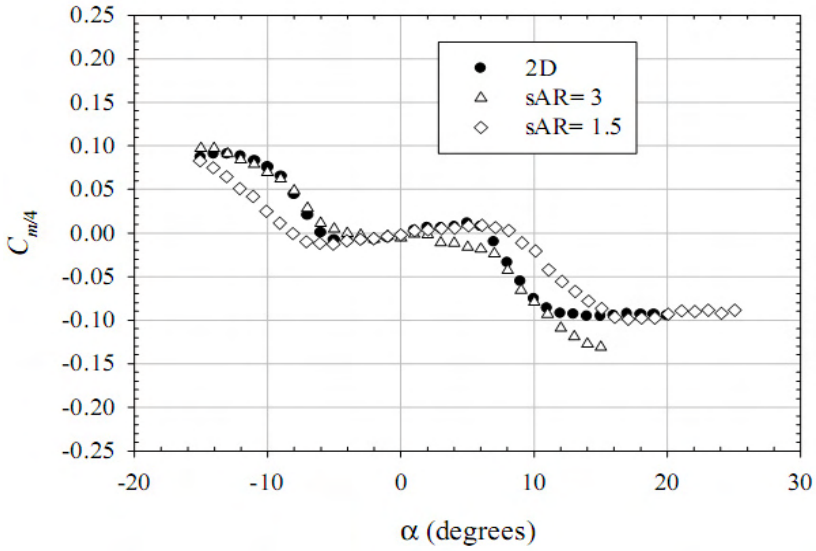

Figure 162: CM vs. AOA for the same airfoil section measured through force measurements by Mueller (1999)

Thus the analysis of various time-averaged aerodynamic coefficients revealed that turbulence has a considerable influence on CL, CD and CM of the airfoil. The increase in CLmax and a reduction in pressure drag at the lower AOAs implied that turbulence has a positive effect on overall airfoil performance. To understand the influence turbulence has on the transient aerodynamic properties of the airfoil, the time-varying fluctuations of forces like lift and rolling moments were investigated. The results of this investigation is presented in the next sub-section.

5.2 Analysis of Lift Fluctuations

While an understanding of time-averaged properties might suffice for relatively smooth flow, where changes in flow speed and direction are very small, it is not the case in higher levels of turbulence where rapid changes in flow speed and direction occur. An understanding of the time-varying fluctuations of the lift generated by the airfoil is also useful for the development of an effective control system to maintain steady flight in turbulence.

The instantaneous pressures over the chord were resolved and integrated in a similar manner to the time-averaged force analysis to estimate the time-varying lift generated. The spectra of the lift fluctuations were calculated using a method similar to that adopted during the time-varying pressure analysis. Spectra of lift fluctuations over the top surface at various AOAs in smooth flow are plotted in Figure 163a. Except for a peak present at the shear layer flapping frequency there does not appear to be any other distinct peaks in the spectra at lower AOAs (AOA<6deg). Though a number of transient flow features were identified over the top surface over this AOA range, they do not seem to have a significant influence on the overall lift fluctuations experienced by the airfoil. This may be due to the fact that the energy associated with the flapping of the shear layer is much higher than the energy within the other flow features that developed. Moreover shear layer flapping was always present over the airfoil whereas other flow features (e.g. vortices that develop on reattachment) were transient in nature. At higher AOAs (AOA>10 Deg), though the airfoil had stalled and bluff body like shedding was noticed in the pressure trace, no peak is noticed in the lift spectra. This is probably because the shedding is not strong enough at AOA<10Deg to significantly influence the fluctuations over the airfoil. At these higher AOAs, an increase in energy can be seen at the lower frequencies, see spectra at 10Deg and 12Deg in Figure 163. With a further increase in AOA, it is believed that the fluctuations induced by bluff-body-like shedding will have a greater influence.

As for the spectra of lift fluctuations on the pressure side, at lower AOAs no peak was observed. However at higher AOAs, a peak was noticed at the respective shedding frequency. Flow visualization and pressure measurements indicated that shedding vortices when AOA>8Deg originated from the bottom surface at the TE.

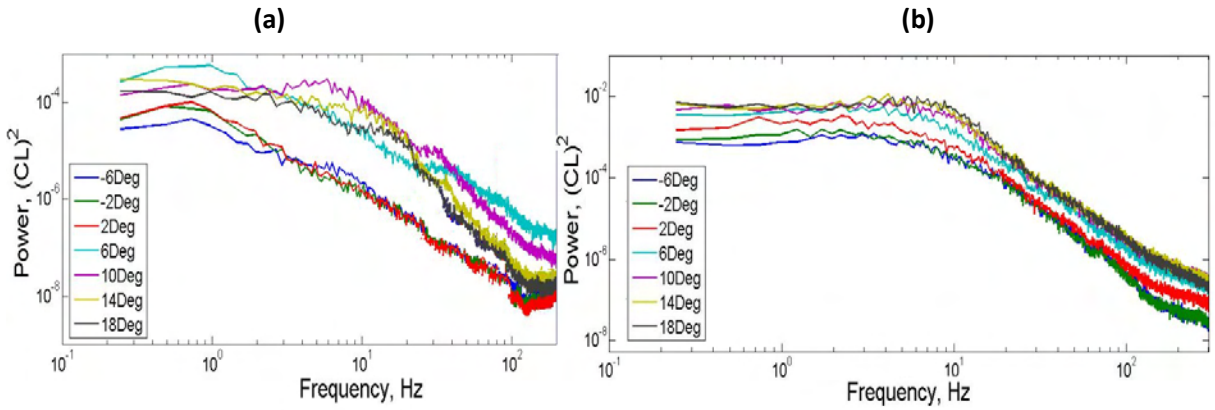

Figure 163: Spectra of lift fluctuations at various AOAs in (a) nominally smooth (Ti=1.2%) and (b) turbulent flow (Ti=12.6 Lxx=0.31m).

The spectra of lift fluctuations in turbulence is quite different in comparison to smooth flow, see Figure 163b. Analysis of pressure fluctuations and flow visualizations revealed that vortex cores form over the airfoil top surface in turbulence and create large fluctuations in forces. Since the vortex cores form close to LE and sweep over the airfoil chord creating large pressure variations, the spectra of the lift fluctuations in turbulence possesses a small increase in energy at the vortex core formation frequency. However, due to the presence of other random fluctuations the peak is not distinctive, see Figure 163b. As for lift fluctuations on the bottom surface in turbulence, since no particular oscillations were noticed in the pressure fluctuations the lift fluctuations also appear to be random. At high AOAs since no peak was indentified in the wake velocity or pressure fluctuations indicating the presence of bluff-body-like shedding in turbulence, the lift fluctuations also appears random in that frequency range. At AOA>30Deg, Devinant et al (2002) and Sicot et al (2006) found the lift fluctuations to be centered on bluff-body-like shedding occurring at a wave number of 0.2. This range of AOA however was not tested here.

To further understand the time-varying lift over the top surface of the airfoil, histograms of the lift oscillations measured in various flow conditions along with a histogram of typical pitch angle fluctuations present in the respective turbulence condition is presented in Figure 164. The instantaneous CL was calculated by appropriately transposing and integrating the instantaneous pressure coefficient distributions. The CL fluctuations (CL') were used for the histogram analysis in Figure 164. For the construction of the histograms, a bin size of 0.2Deg was used for the pitch angle fluctuations while the bin size for lift coefficient was 0.05 and 0.1 for smooth and turbulence flow respectively. In all the histograms the occurrences at each bin were normalized with respect to the total number of samples.

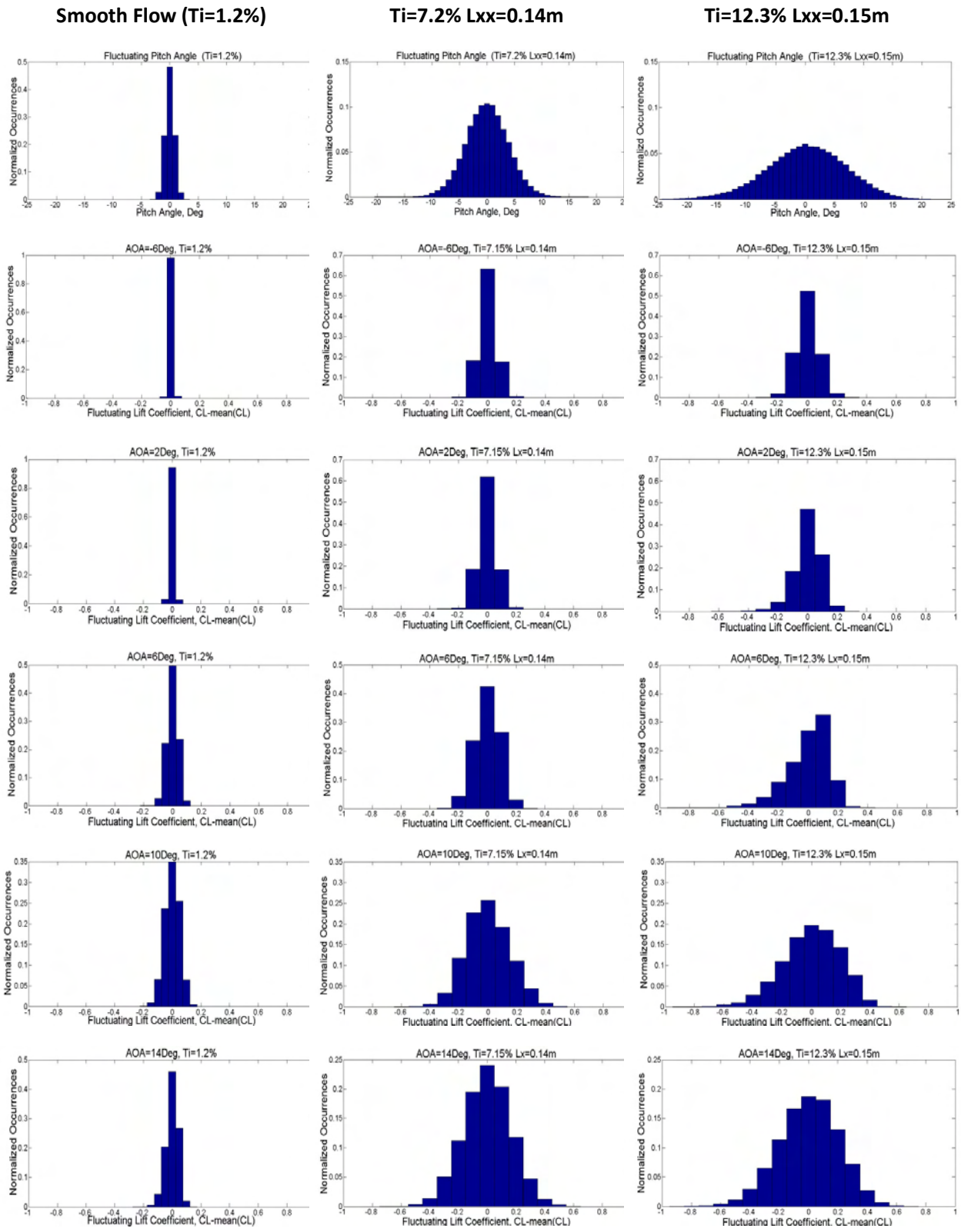

Figure 164: Histograms of typical pitch angle in three different flow conditions and corresponding lift fluctuations over airfoil top surface over a range of AOAs.

The instantaneous pitch angle in Figure 164 was estimated by taking into account velocity fluctuations in the streamwise as well as vertical directions. As expected, the pitch angle fluctuations are nominally symmetric about the mean i.e. a Gaussian distribution is present indicating that the turbulence is well mixed. The increasing spread of pitch angle fluctuations over a wider range as Ti increases is clearly seen in the histograms.

As for the CL fluctuations, it can be seen in the histograms that the fluctuations at the negative and very small positive AOAs (-6<AOA>2Deg) over the different turbulence conditions also closely follow a Gaussian distribution. This indicates that over this AOA range, a nominally linear relationship exists between the fluctuations in the oncoming flow and the corresponding CL fluctuations over the airfoil. A continually increasing spread of CL fluctuations is also noticed with increase an in Ti.

With further increase in AOA (AOA>=6Deg), the range of CL fluctuations increases considerably along with a deviation from the Gaussian distribution that was present earlier. However, the deviation from a Gaussian distribution (see histograms of CL fluctuations above 6Deg AOA) is only small in this case. This deviation is believed to be due to the nonlinear relationship between CL and AOA at higher AOAs. The nonlinear CL vs. AOA relationship implied that if the airfoil was exposed to consistently mixed turbulence over different runs, the resulting lift fluctuations would also remain consistent but with a non-Gaussian distribution. Hence, airfoils that stall abruptly or experience sudden changes in lift with changes in static AOA, when exposed to turbulence, are expected to possess a CL fluctuation distribution that is very unlike a Gaussian distribution along with experiencing large changes in the instantaneous CL due to rapid changes in oncoming AOA.

Investigation on the degree of influence of hysteresis and other time-varying phenomena of the airfoil pressures and forces in smooth and turbulent flow was not possible. However a number of workers have reported that such phenomena are prevalent and have a relatively high influence in this Reynolds number regime in smooth flow conditions. The influence of turbulence on hysteresis and other dynamic properties of the flow over the airfoil is still unclear. Based on the results obtained here it is speculated that these phenomena exert only a limited influence on this airfoil. This is because, only a marginal deviation from Gaussian distribution is noticed in the histograms for AOA>6Deg in Figure 164 where the variation in the histograms for a particular AOA over different runs is also small, see Figure 165.

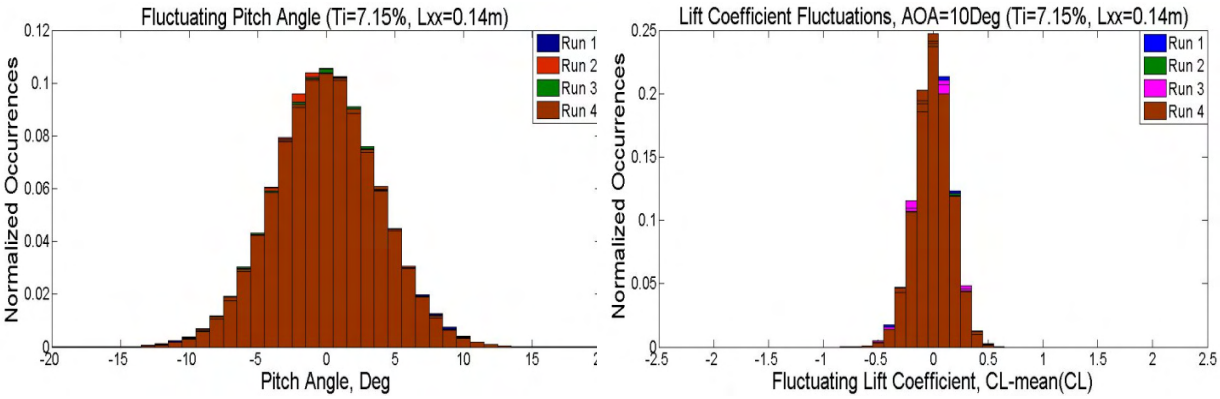

Figure 165: Overlapped histograms of time-varying pitch angle and CL fluctuations taken over different runs.

Figure 166 shows the influence of length scale on the CL fluctuations and the dependency of CL fluctuations on the pitch angle fluctuations of the oncoming flow. As expected, only a small difference is noticed in the pitch angle histograms of the two length scale conditions. However, the small difference between the histograms is thought to be due to slight variations in the Ti at the two length scales. A large difference is however present in the corresponding CL fluctuations experienced. In spite of the flow over the airfoil having closer resemblance to smooth flow conditions at longer length scale, the increased energy at the lower frequencies in the pitch angle fluctuations appears to impart a greater magnitude in CL fluctuations, this is seen in Figure 166. A similar trend was noticed on comparing different length scales at the lower Ti (i.e. Ti approx =7%).

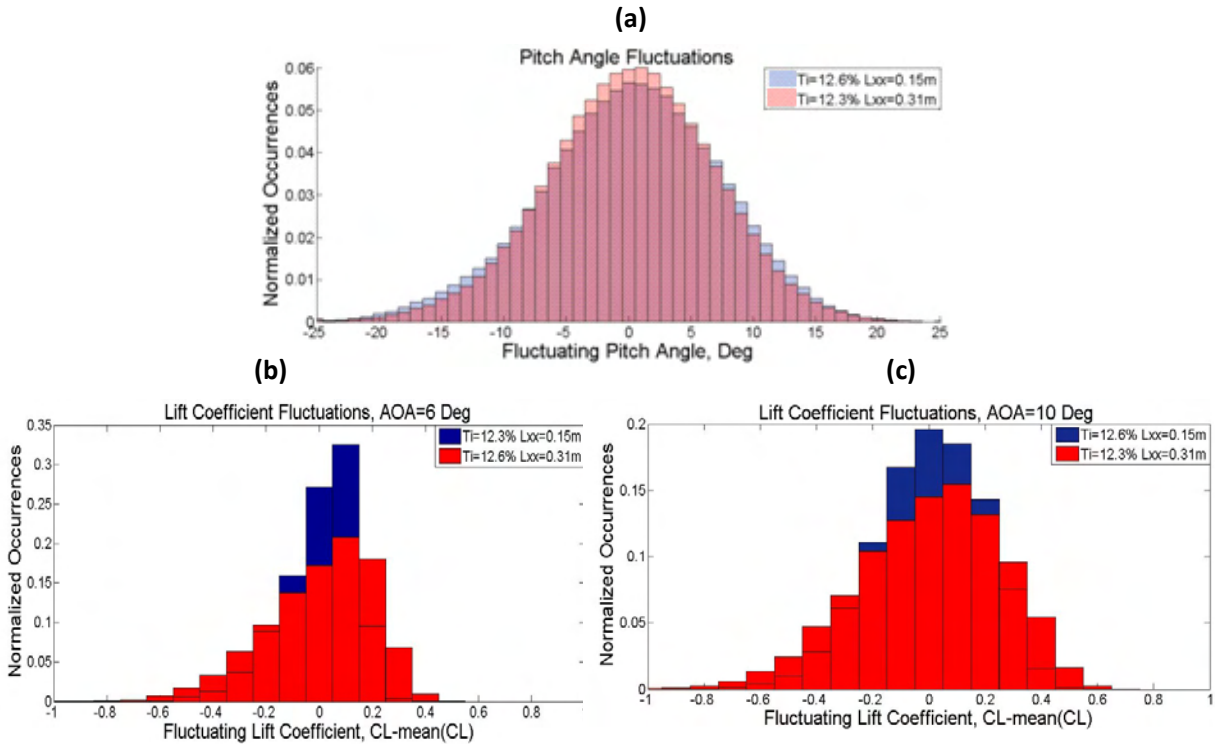

Figure 166: Overlapped histograms of (a) typical pitch angle fluctuations at two different turbulence length scales. Corresponding (b&c) overlapped CL fluctuations at the two length scale at AOA=6Deg and 10Deg respectively.

In order to obtain a better understanding of the range of lift fluctuations experienced in smooth and turbulent flow, a box-plot of the lift-per-unit-span fluctuations (Lift/unit span=0.5ρV^{2}cCL') occurring over the airfoil top surface across a range of AOAs is presented in Figure 167. Box-plots offer a convenient means of representing large datasets whereby the top and bottom edges of the box corresponds to the 25th and 75th percentiles respectively while the center-line of the box corresponds to the median and generally the width of the box has no statistical significance. The top and bottom markers (whiskers) in the box-plot are placed at the 1st and 99th percentiles respectively. The Std.Dev of the lift fluctuations experienced for each turbulence condition over the range of AOAs is also plotted in the same figure.

To add perspective to these fluctuations, the possibility of predicting the range of lift fluctuations that an airfoil might experience in different turbulence conditions based on the airfoil's time-averaged performance and time-varying longitudinal velocity data was investigated. For each turbulence condition, the static lift-per-unit-span was calculated from the time-averaged CL vs. AOA data assuming three longitudinal velocity conditions viz.; $V=V_{Mean}$, $V=V_{Mean} - V_{Std.Dev}$, $V=V_{Mean} + V_{Std.Dev}$. In Figure 167, along with the box plots and the Std.Dev of the actual lift fluctuations, the calculated static lift-per-unit-span vs. AOA for each longitudinal velocity condition is plotted. Estimating the lift from the time-

averaged CL vs. AOA using the three different velocity conditions provides a prediction of the possible range of CL fluctuations the airfoil can be expected to experience when exposed to the particular turbulence condition.

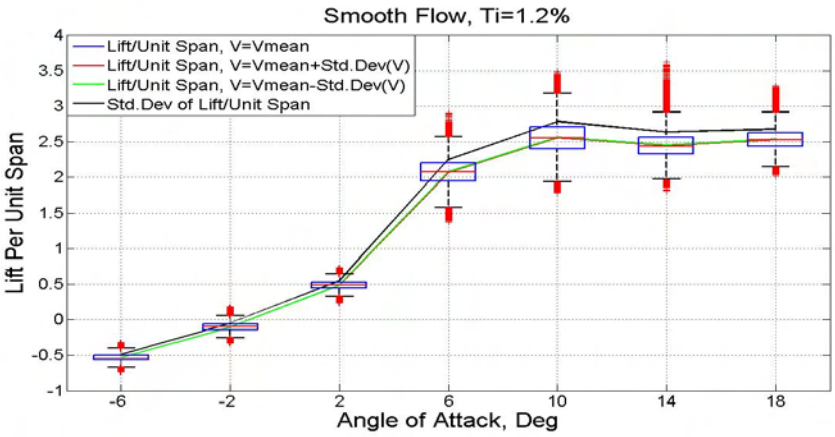

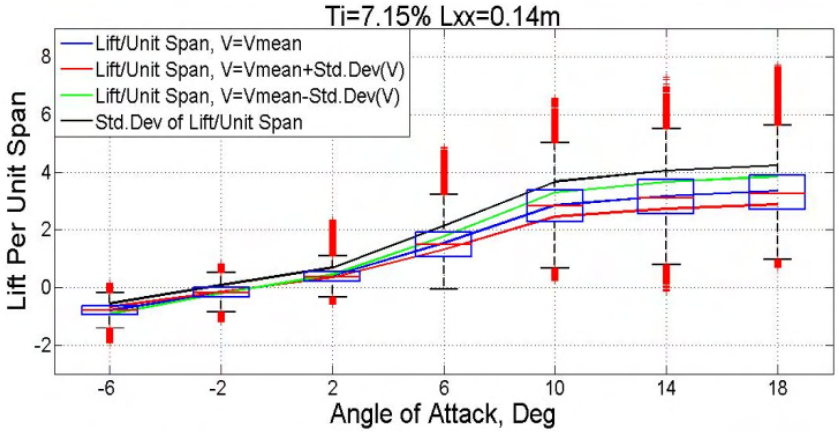

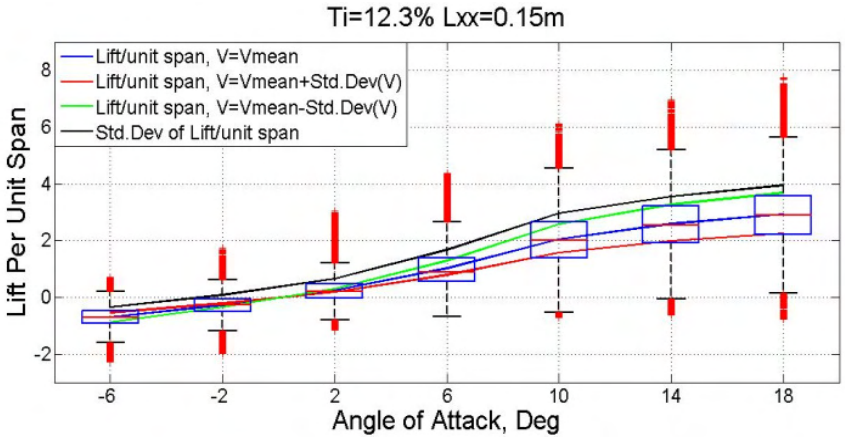

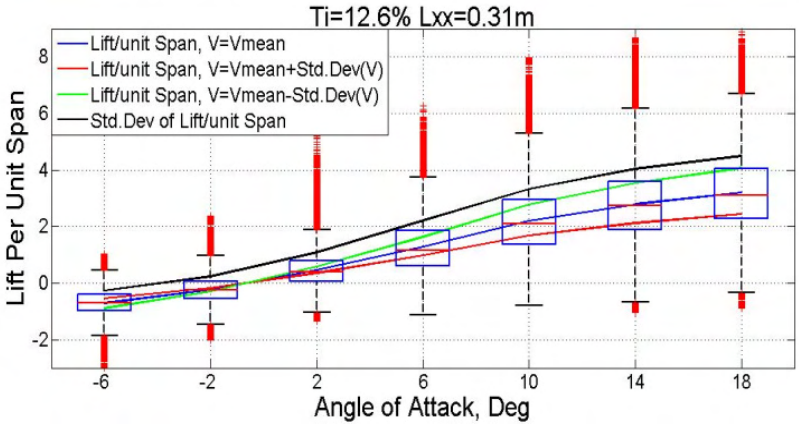

Figure 167: Series of overlapped box plot of lift/unit span fluctuations over a range AOAs in different turbulence conditions. Refer plot title for details on turbulence properties.

Due to very small magnitude of the velocity fluctuations present in smooth flow, the lift predictions at the three velocity conditions almost overlap, see Figure 167. In smooth flow at AOAs>6Deg a significant difference is noticed between the predicted and actual range of lift fluctuations experienced, in that the latter is much larger, refer Figure 167. This suggests that the lift fluctuations experienced in nominally smooth flow is not entirely due to influences of oncoming longitudinal velocity fluctuations but it is only one of the contributing factors. Lift fluctuations are believed to originate from other LSB related flow fluctuations like shear layer flapping, vortices shed on reattachment, etc. A steadily increasing range in the lift fluctuations with increase in AOA is also noticed in the box-plots. The presence of a larger number of outliers at higher AOAs indicates the shear layer becomes more susceptible to induce large changes in lift over the airfoil as AOA increases.

In higher levels of turbulence, at negative and low positive AOAs similar to smooth flow, the predicted range of lift fluctuations was very small in comparison to the actual range of fluctuations experienced. As seen in Figure 167, the Std.Dev of the actual fluctuations is also consistently higher than the static lift estimated for the condition when $V=V_{Mean} - V_{Std.Dev}$ however with respect to the total range of fluctuations for the particular turbulence condition, the static lift estimation when $V=V_{Mean} - V_{Std.Dev}$ appears to be relatively closer to the Std.Dev at higher turbulence levels. Across the different turbulence conditions, at higher AOAs (AOA>=10Deg) the predicted range seems to coincides well with the 25^{th} and 75^{th} percentile (top and bottom edges of the box) of lift fluctuations implying that around 50% of the possible lift fluctuations that the airfoil might experience can be predicted using this method. This trend of under-predicting the possible CL fluctuations suggests that apart from fluctuations in oncoming

streamwise velocity, other factors like fluctuations induced by the formations of vortex cores also have a considerable influence. It should be noted that the velocity fluctuations only in the streamwise axis has been accounted in predicting the range of possible lift fluctuations in Figure 167.

To obtain closer estimate of the transient lift experienced in turbulence, unlike the previous method, changes in velocities both in the streamwise and vertical directions were taken into consideration. The time-varying pitch angle calculated for each turbulence condition was converted to a corresponding CL based on the time-averaged CL vs. AOA data of the airfoil for the particular turbulence condition. Histograms of the predicted and actual CL fluctuations for certain AOAs are presented in Figure 168 where a large difference between the actual and predicted CL fluctuations can be observed. This method seems to grossly under predict the fluctuations experienced at higher AOAs while over-predicting the fluctuations at lower AOAs. The noticed trend in the predicted CL fluctuations is due the reducing slope of the time-averaged CL vs. AOA curve as AOA increases. Reduced similarity between the predicted and actual fluctuations highlights the necessity to further investigate the relationship between fluctuations in the oncoming flow and the corresponding fluctuations in lift.

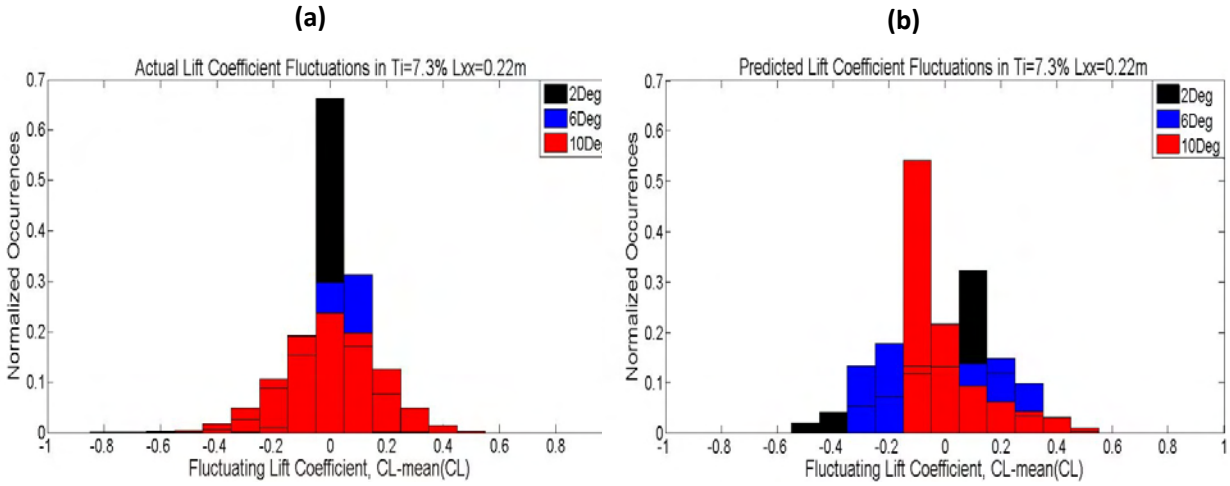

Figure 168: (a) Actual and (b) predicted CL fluctuations experienced in turbulence (Ti=7.3% Lxx=0.22m) when AOA = 2Deg, 6Deg and 10Deg.

The analysis of time-varying fluctuations of lift has revealed that turbulence has a very complex yet significant influence on the instantaneous lift generated by the airfoil. Increase in Ti and length scale resulted in an increase in the range of lift fluctuations experienced. Attempts at predicting the range of fluctuations in turbulence revealed that knowledge of the airfoil's time-averaged performance and time-

varying data of the oncoming flow is inadequate in order to obtain accurate estimates on the transient performance of the airfoil in turbulence. This suggests that a spectral link between the lift and oncoming flow fluctuations might be required to obtain closer predictions. Based on the analysis conducted here, it is also believed that airfoils that stall abruptly and that are subjected to large influences of hysteresis might be relatively less suitable for MAVs as they would experience large variations in lift distribution when exposed to higher levels of turbulence. Their lift fluctuation distribution is also expected to be very unlike the preferred Gaussian distribution. In the next chapter, the relationship between oncoming gust and corresponding force fluctuations over the airfoil will be further explored through analysis of the simultaneous measurement of up-field velocity and surface pressures.

5.3 Analysis of Rolling Moment Fluctuations

It has been identified in previous studies that for conventional fixed-wing MAVs destabilization in the rolling axis is the most significant disturbance encountered in flight when a MAV is subjected to freestream turbulence, Watkins et al (2006) and Thompson & Watkins (2010). In this sub-section, analysis of the rolling moments experienced by the airfoil in the different flow conditions will be presented. The rolling moment was calculated by estimating the resultant of moments created by the fluctuating lift measured at two spanwise stations with separations of 50mm and 200mm. The rolling moment was calculated with respect to the center point of the two spanwise pressure measuring locations. Though there was a chordwise offset in the pressure taps across the two spanwise stations, this offset was small ((x/c)=0.02) and hence the measured pressures and lift at the two locations was nearly identical, refer Appendix B&C for further clarification.

The correlation between the lift fluctuations experienced at the two spanwise separations over a range of turbulence conditions is presented in Figure 169. As earlier seen in the spanwise correlations of individual pressure taps, the lift fluctuations also correlate better in higher levels of turbulence than in smoother conditions. This is due to the presence of a stronger and better correlated forcing frequency in the oncoming flow and also due to the increased size of the different flow structures that develop over the airfoil in higher levels of turbulence. As expected, the correlation drops considerably at 200mm separation implying that the rolling moments experienced would be significantly greater. At 200mm

separation, the correlation noticed at the longest length scale is however considerably higher than those noticed at the smaller length scales at the same spanwise separation. The increased correlation suggests that the rolling moments experienced at the longest length scale would be smaller. The Std.Dev of the rolling moments experienced in the different turbulence conditions is presented in Figure 170.

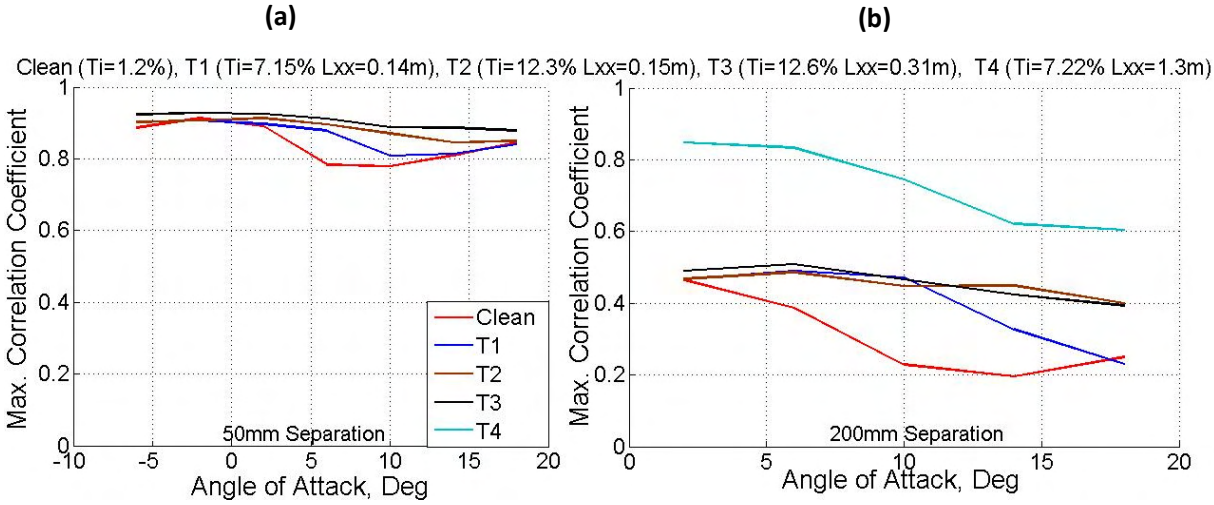

Figure 169: Correlation between the lift fluctuations experienced at the two spanwise separations ((a) 50mm and (b) 200mm) over a range of turbulence conditions

To effectively capture the relative fluctuations in lift between the 50mm and 200mm spanwise separations, the rolling moment per unit lift and per unit moment arm was computed. This was done by firstly resolving and integrating the fluctuating pressures at both spanwise stations into lift fluctuations through the aforementioned method. The resultant time-varying moments created by the lift fluctuations was then calculated assuming a unit moment arm. Assuming a unit moment arm highlighted the rolling moments created purely due to changes in relative lift fluctuations (changes in flow structure) and not due to an increase in arm-length. Viewing upstream (facing the airfoil), a clockwise rolling moment was assumed positive.

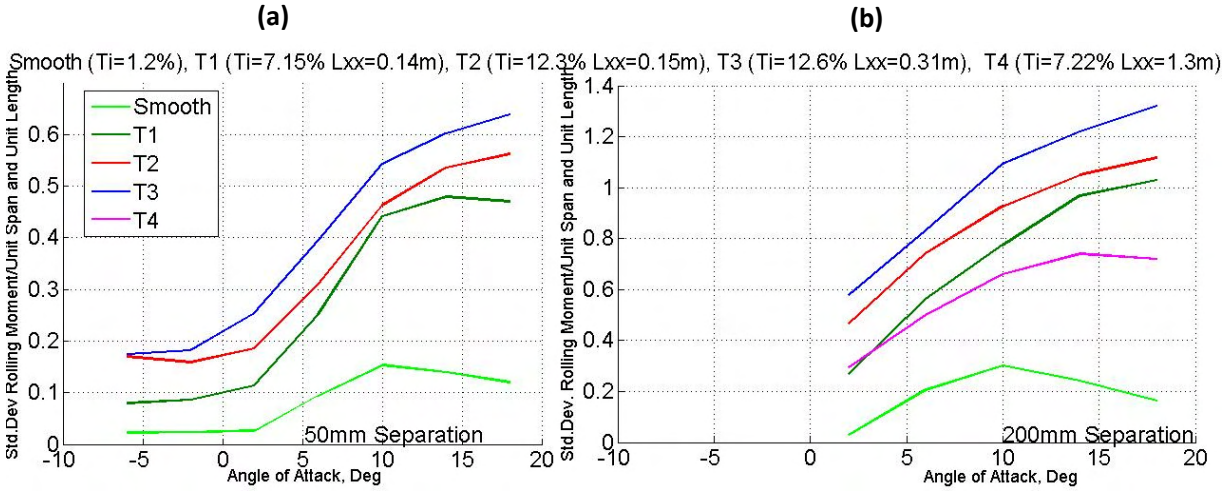

Figure 170: Std.Dev of the rolling moments experienced in the different turbulence conditions

Due to the similarity in test setup and Reynolds number across all turbulence conditions tested, direct comparison of the rolling moments across all flow conditions was possible. Comparing the Std.Dev of the rolling moments per unit span and moment arm at the two spanwise separations in Figure 170, it can be seen that the Std.Dev of the rolling moment that is experienced only due to the relative lift fluctuations at 200mm separation is over two times greater than that experienced when the separation was only 50mm. A further difference between the rolling moments experienced at the two separations is expected considering the moment arm for the latter case was four times longer. When spanwise separation was only 50mm, at AOAs<10Deg, the rolling moment fluctuations increased steadily till around 10Deg after which a slight stabilization seems to occur, see Figure 170. It can be recalled that the rate of vortex core formation too stabilizes at 10Deg AOA above which the shedding rate remains nominally unchanged.

Apart from an overall increase in moment fluctuations noticed when spanwise separation was 200mm, the rate of increase in fluctuations with AOA appears to be nominally similar to that found when separation was 50mm. In both cases, an increase in turbulence intensity results in an increase in rolling moment fluctuations, but the overall trend with AOA remained unchanged at both Ti tested. An increase in turbulence length scale when Ti=12%approx. led to an increase in rolling moment fluctuations however the opposite was found to occur when Ti=7%approx (refer Figure 170). The variation in trend noticed at the two Ti suggests that the range of length scales tested when Ti=12%approx. was inadequate to accurately obtain the influence of length scale on rolling moment fluctuations experienced. It is believed that the increased correlation of lift fluctuations over the span at the longest

length scale (Lxx=1.3m) manifests as the reduction in rolling moment experienced, this is can be seen in Figure 170.

Earlier conducted analysis of the time-averaged and time-varying pressures revealed that the pressure and consequently lift fluctuations experienced in the longest turbulence length scale were higher due to the flow possessing higher energy at the lower frequencies. Analysis of the rolling moment indicates that when subjected to longer length scales the induced fluctuations in pressure and forces are high but are better correlated over the span resulting in a reduction in rolling moment. Figure 170 also shows that the reduction in rolling moment fluctuations is only evident at the higher AOAs whereby at AOAs<6Deg, the Std.Dev of rolling moments at both length scales are very similar.

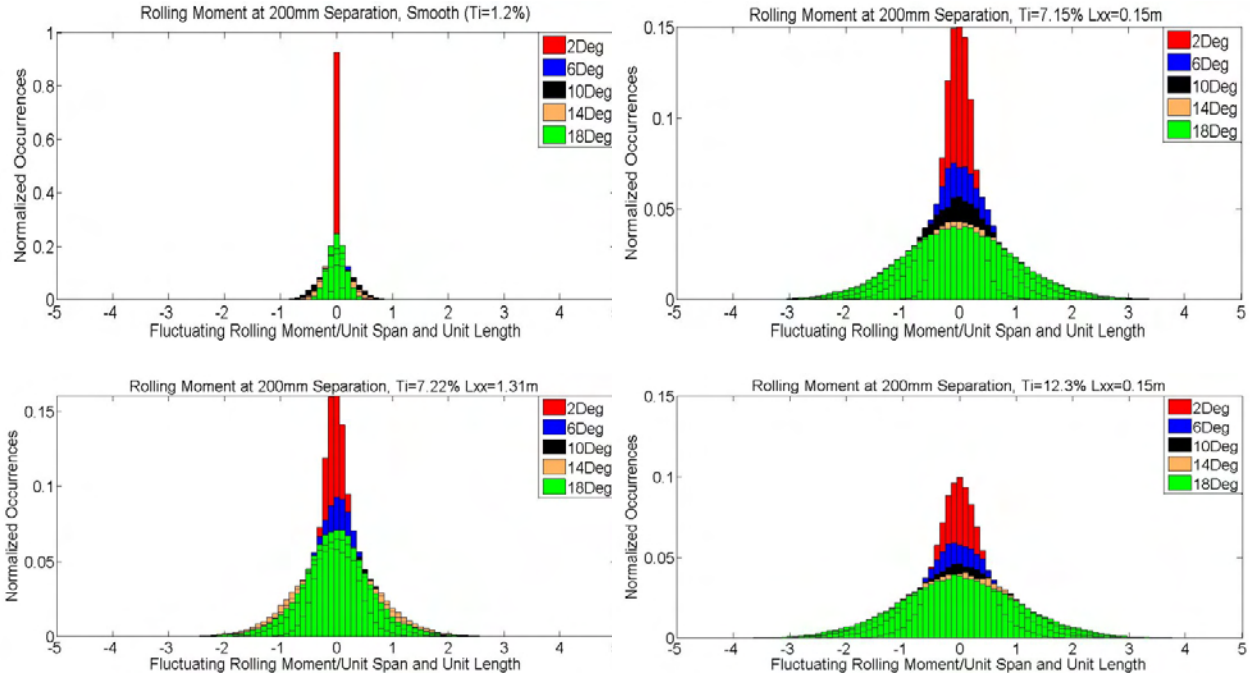

Figure 171: Histograms of rolling moment/unit span and unit length at different AOAs when subjected to turbulence of varying intensity and length scale.

The overall influence of turbulence intensity and length scale on the range of rolling moment fluctuations can be seen in the histograms in Figure 171. The bin size used in the construction of the histograms in Figure 171 was 0.1N/m^2. Comparing the histograms for nominally smooth flow and Ti=7.15% Lxx=0.14m, shows large change in fluctuation with change AOA, however a significantly larger spread of fluctuations is noticed in the higher turbulence condition. A further spread of the fluctuations

is noticed as Ti increases to 12.3% (Lxx=0.15m). The reduction in rolling moment fluctuations at significantly longer length scale can be seen by comparing the histograms when Ti=7.15 Lxx=0.14m and Ti=7.22% Lxx=1.31m. While the fluctuations at the lower AOAs appear to be similar, a distinct reduction in the range of fluctuations is evident at higher AOAs. The fact that the relationship between the lift and oncoming pitch angle fluctuations is complex and nonlinear suggests that the resulting rolling moment fluctuations too would possess a distribution that is not exactly Gaussian. Hence slight deviations from the ideal Gaussian distribution can be witnessed in the histograms.

Similar to the analysis conducted in the previous sub-section, here too the possibility of predicting the range of rolling moments that might be experienced from knowledge of the airfoil's time-averaged Lift Vs AOA was investigated. Within the same experimental setup, the airfoil was removed and simultaneous velocity measurements in the three orthogonal directions were taken at exactly the same stations as the pressure measurements. The measured velocities were converted to pitch angle and from the time-averaged airfoil Lift vs. AOA data, the instantaneous local pitch angle was converted to local lift. Using the same sign convention, the rolling moment due to variation in instantaneous lift was calculated. Since the mean pitch angle was zero in the velocity measurement, to compare the predicted and actual rolling moments, before estimating the rolling moments the respective AOA was added to the measured fluctuating pitch angle. The predicted and actual rolling moments for a few AOAs is presented in Figure 172. Similar to the previous sub-section, this method grossly under predicts the range of rolling moment fluctuations experienced. It further suggests that a better understanding of the interaction between the time-varying pitch angle and lift fluctuation is required such that a closer estimate of the fluctuating forces and moments can be made.

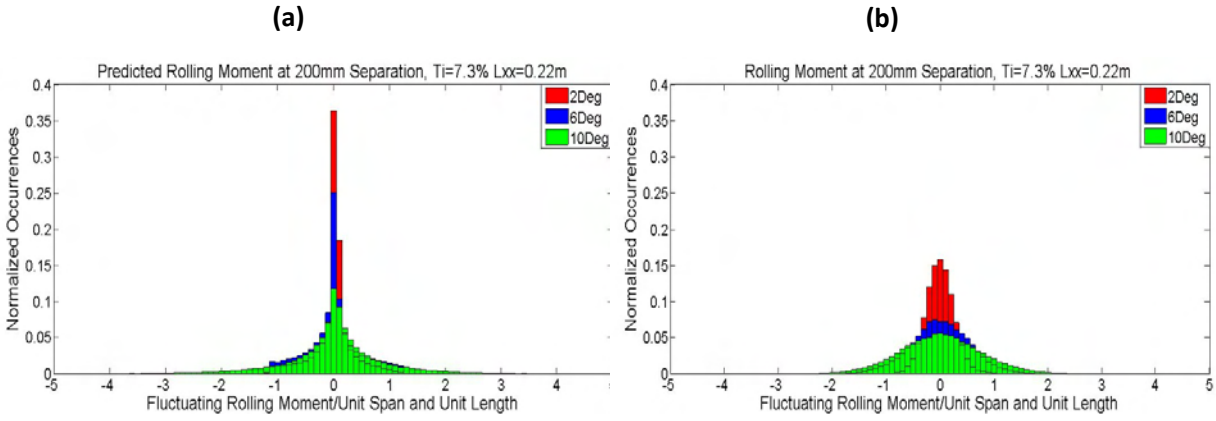

Figure 172: (a) Predicted and (b) actual rolling moment fluctuations experienced in turbulence (Ti=7.3% Lxx=0.22m) at AOA= 2Deg, 6Deg and 10Deg.

The spectra of the fluctuating rolling moments in nominally smooth and turbulent flow is presented in Figure 173. While the fluctuations appear to be random, for AOA>=10Deg a very weak elevation in energy is present at around the vortex core formation frequencies at higher levels of turbulence. Due to large fluctuations in pressure induced by the vortex cores, slight time-varying differences in the structure of the vortex cores over the airfoil span would lead to large rolling moments. As for the rolling moment spectra in nominally smooth flow, the fluctuations were found to be mostly random except for 6Deg and 10Deg AOA. At 6Deg AOA a small elevation in energy was noticed at the shear layer flapping frequency, at 10Deg however a small peak was present at around 5Hz. The origin of this oscillation is unclear. In both nominally smooth and at higher levels of turbulence, majority of the energy is present at the low-frequency range (<20Hz), implying that by developing an effective control and auto-pilot system to negate the low-frequency fluctuations, nominally steady flight can be achieved.

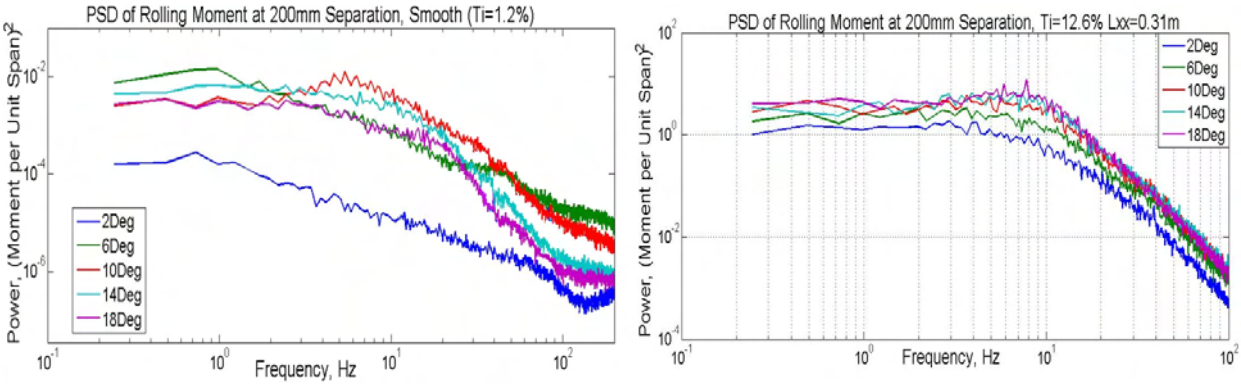

Figure 173: spectra of the fluctuating rolling moments in nominally smooth and turbulent flow. Refer plot tile for turbulence properties

5.4 Chapter Conclusions and Discussion

The analysis conducted here revealed the individual influence of turbulence intensity and length scale on the various aerodynamic properties of the airfoil. Analysis of the time-averaged lift showed that increase in turbulence intensity resulted in a reduction in the lift-curve-slope of the airfoil. This reduction has been attributed to an increased influence of a “pseudo-camber” effect experienced by the airfoil at lower Ti. At higher Ti, a delay in stall AOA and an increase in the time-averaged maximum CL

was also noticed. Turbulence length scale has a relatively less profound influence on the Cl Vs AOA of the airfoil, but increase in the same resulted in an increase in the CL vs. AOA slope and CL maximum.

A slightly longitudinally unstable condition was attained by the airfoil at lower AOAs in smoother flow conditions, but this did not occur at higher levels of Ti. As for the influence of turbulence on CM of the airfoil, at higher AOAs, turbulence Intensity and length scale were found to have opposing influences on the CM vs. AOA of the airfoil.

Statistical analysis of the lift and rolling moment fluctuations showed that large fluctuations occurred in turbulence. Due to the complex interactions between oncoming flow and the airfoil, and due to the large range of fluctuations experienced, prediction of the possible range lift fluctuations based on the airfoil's time-averaged properties and time-varying oncoming flow-field data was found to be grossly inaccurate. This suggested that a spectral link between the lift and oncoming flow fluctuations might be required for more accurate predictions. Spectra of lift and rolling moment showed that at higher levels of turbulence, the airfoil experiences fluctuations at around the vortex core forming frequency however the majority of the fluctuations were found to occur only at the lower frequencies (<20Hz). It was also suggested that airfoils that stall abruptly and that are influenced by hysteresis and other dynamic stall effects might be unsuitable for MAVs as they would experience large changes in lift with changes in oncoming AOA.

CHAPTER 6

Relationship between Incoming Turbulence and Airfoil Lift Fluctuations

In this section the interactions between oncoming fluctuations in pitch angle and the corresponding lift fluctuations induced over the top surface will be explored further through the analysis of simultaneous upstream velocity and surface pressure measurements. This analysis will aid in investigating the possibility of using control inputs from surface pressure fluctuations and/or upstream flow measurement as a means to negate disturbances induced by turbulence. The most optimum location for pressure taps on the airfoil chord such that they may be held most representative of lift fluctuations occurring over the entire airfoil will also be suggested.

6.1 Comparisons between Surface Pressure and Incoming Velocity Fluctuations

Current autopilot systems use variations in acceleration along the different axis as control inputs to attempt to maintain steady flight in turbulence. However, the rapid fluctuation in flow speed and direction imparts force and moment fluctuations over the aircraft and by the time an induced acceleration is detected through the respective accelerometers and a suitable correction is made, its effectiveness may become reduced. As an alternate means to attain steady flight, the possibility of using a combination of surface pressure fluctuations and upstream flow velocity and direction fluctuations as

a control input was evaluated. Simultaneously measured upstream flow and surface pressure fluctuations will assist in this analysis.

Analysis of the time-varying lift and rolling moment fluctuations in the previous chapter revealed that interaction between the airfoil and oncoming gust is very complex. Predicting the time-varying aerodynamic properties of the airfoil based on knowledge of its time-averaged characteristics was also found to be very difficult. To provide insight on the interaction between oncoming pitch angle and airfoil lift fluctuations, upstream velocity and surface pressures were measured simultaneously. Velocity measurements were taken at different distances (multiples of longitudinal integral length scales) upstream of the airfoil using the Cobra Probe. The Cobra Probe was aligned with the pressure taps along the airfoil centerline and in line with the airfoil LE for each AOA at various upstream distances. Simultaneous measurement of pressure and velocity were made by connecting the four output channels of the Cobra Probe to the four auxiliary inputs in the Digital Pressure Measurement System (DPMS) interface box. Refer Chapter 2 for further information on either system.

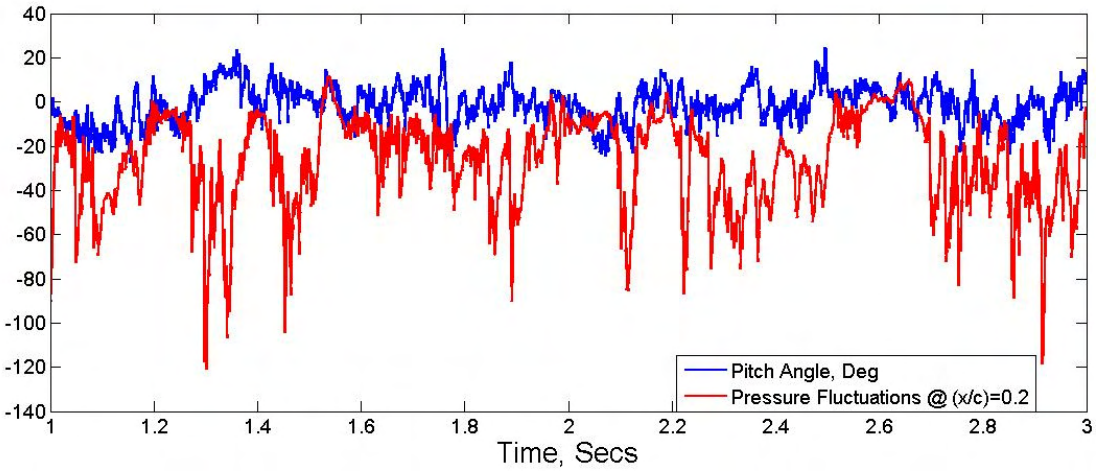

Figure 174: Sample time series of simultaneously measured pitch angle one length scale upstream and pressure fluctuations on the suction side at (x/c)=0.2. Ti=7.3% Lxx=0.22m

A sample time series of simultaneously measured pitch angle and pressure fluctuations at an arbitrary pressure tap close to the LE is presented in Figure 174. Though there would be a small temporal difference between the instant a gust was measured by the velocity measuring probe upstream to it having an influence on the pressures over the airfoil, the simultaneously measured time series

presented in Figure 174 appear to be uncorrelated. The maximum correlation coefficient between upstream velocity fluctuations in the three orthogonal directions and pressure fluctuations at each pressure tap was computed for AOA=10Deg and is presented in Figure 175. Refer Appendix F for more information on correlation function used.

The figure shows that relatively good correlation is present between surface pressure and velocity fluctuations in the vertical direction (w axis). However, in spite of the increased magnitude of turbulent energy present in the velocity fluctuations occurring along the streamwise axis (u axis), it has a relatively lesser influence on the pressure fluctuations over the airfoil. This is evident from the limited negative correlation present with respect to the pressure fluctuations. This correlation trend with respect to velocity fluctuations along the u axis is believed to due to the inverse relationship between the local static pressure and velocity. As expected the surface pressure fluctuations were not correlated with the velocity fluctuations along the lateral axis (v axis). The best correlation was obtained with respect to the fluctuating pitch angle however it was only marginally higher than the correlation obtained with respect to velocity fluctuations along the vertical axis.

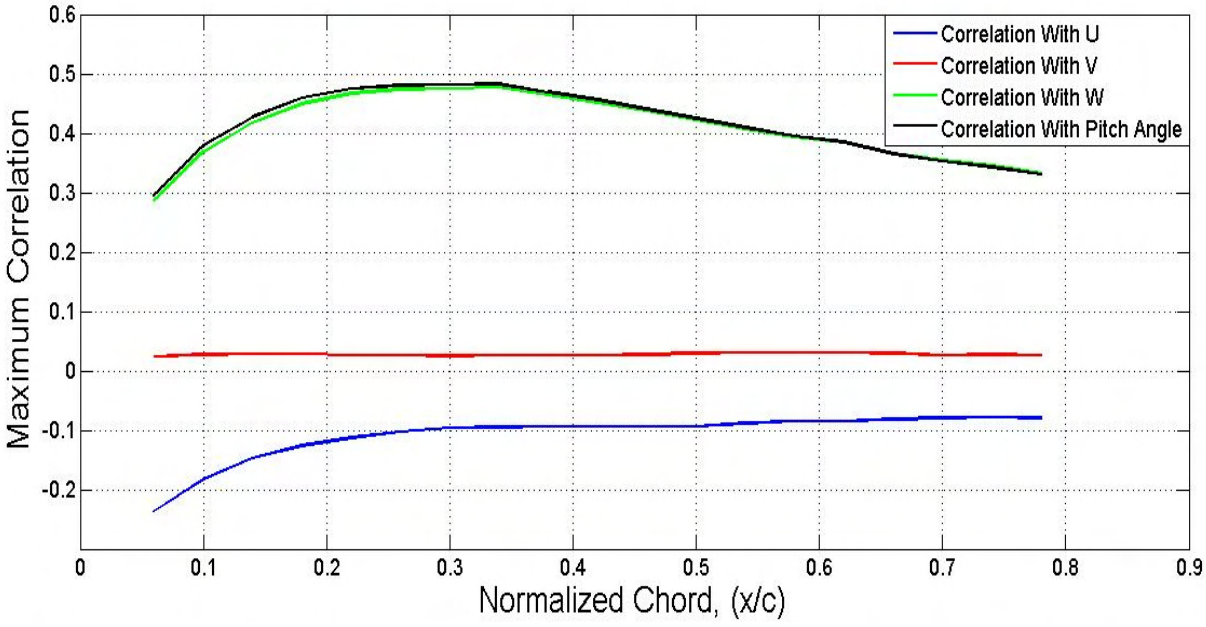

Figure 175: Maximum correlation between oncoming flow fluctuations measured one length scale upstream and pressure fluctuations at each pressure tap. AOA=10Deg Ti=7.3% Lxx=0.22m

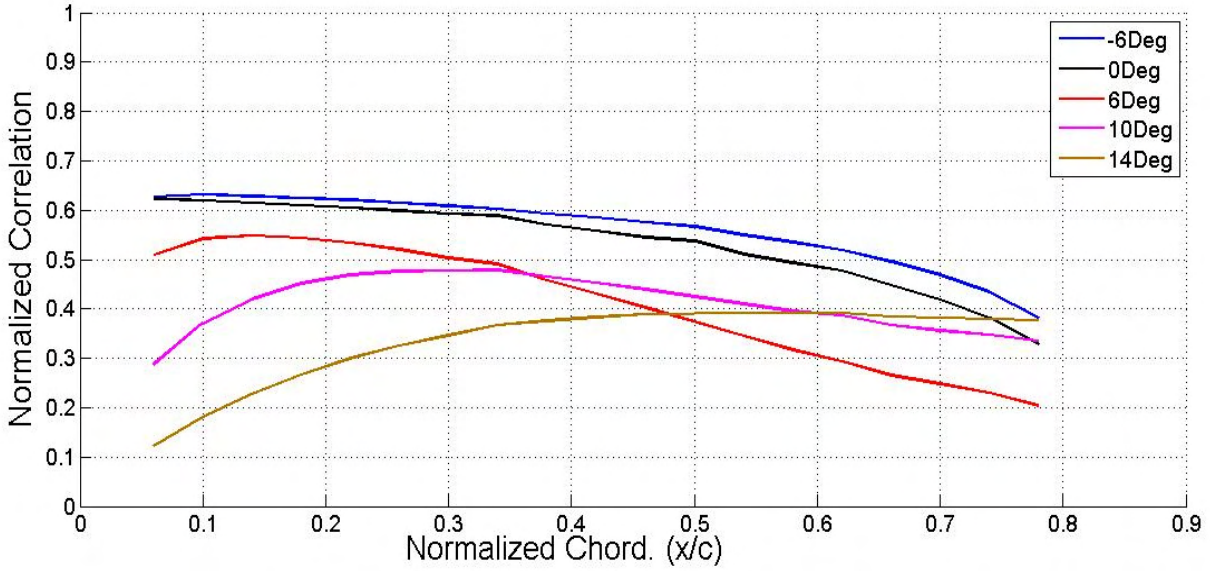

Figure 176: Correlation between pitch angle fluctuations measured one length-scale upstream and surface pressure fluctuations, at various AOA. Ti=7.3% Lxx=0.22m

In Figure 176 the correlations between pitch angle fluctuations measured one length-scale upstream (Lxx=0.22m) and surface pressure fluctuations at various AOA are presented. The figure again shows that there exists relatively good correlation between oncoming pitch angle and surface pressure fluctuations. For a given positive AOA, the correlation steadily increases along the chord till a region of max correlation is attained, it then gradually decreases towards the TE. As AOA increases the maximum correlation drops and the region of maximum correlation nears the TE. This reduction suggests that at higher AOAs the shear layer became relatively more influenced by fluctuations induced by other factors like local disturbances induced during transition and reattachment.

The reduced correlation close to the LE is believed to be due to the fact that when flow separation occurs, the region close to the LE lies under the separated shear layer and thus remains relatively shielded from oncoming fluctuations. As separation occurs frequently when the airfoil is exposed to turbulence, the correlation between pressure fluctuations in this region and oncoming velocity fluctuations remains low. The correlation plots in Figure 176 also agree well with the Std.Dev plots presented in Chapter 3 which suggests that the vortex core formation region correlates best with oncoming gusts. To indentify the variation in pitch angle correlation with overall lift fluctuations in different turbulence conditions, in Figure 177 and Figure 178, the CL' vs. pitch angle correlations for

different upstream distances and CL' vs. upstream measuring distance correlations for different AOAs are presented respectively.

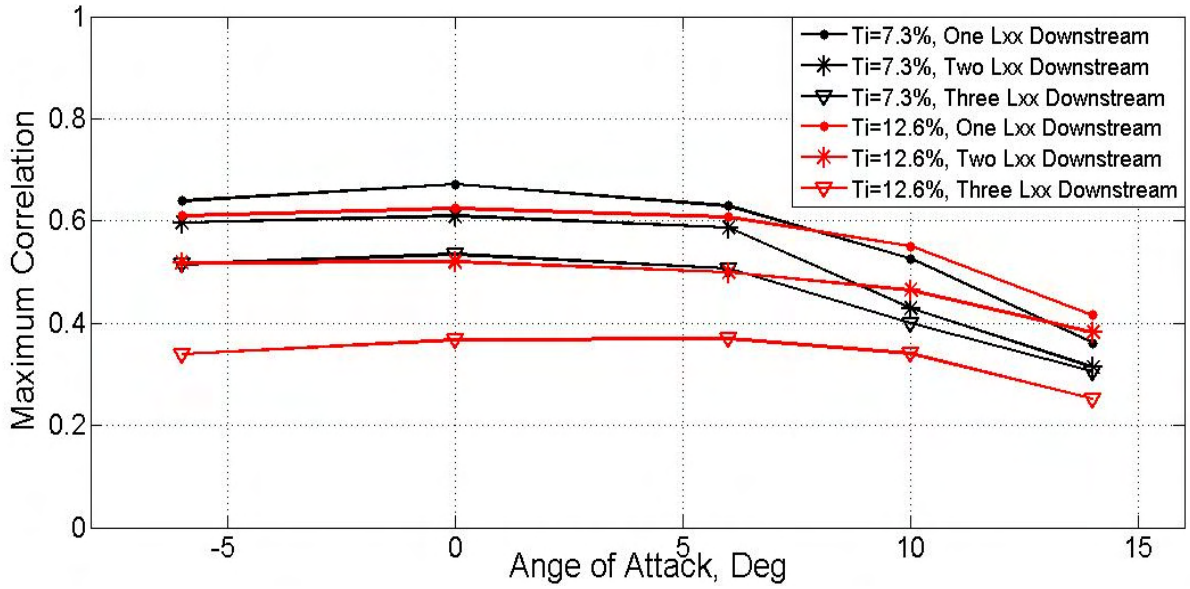

Figure 177: Maximum correlation between CL and pitch angle fluctuations, measured at different distances upstream, at different mean AOAs. Lxx for Ti=7.3% and 12.6% were 0.22m and 0.31m respectively.

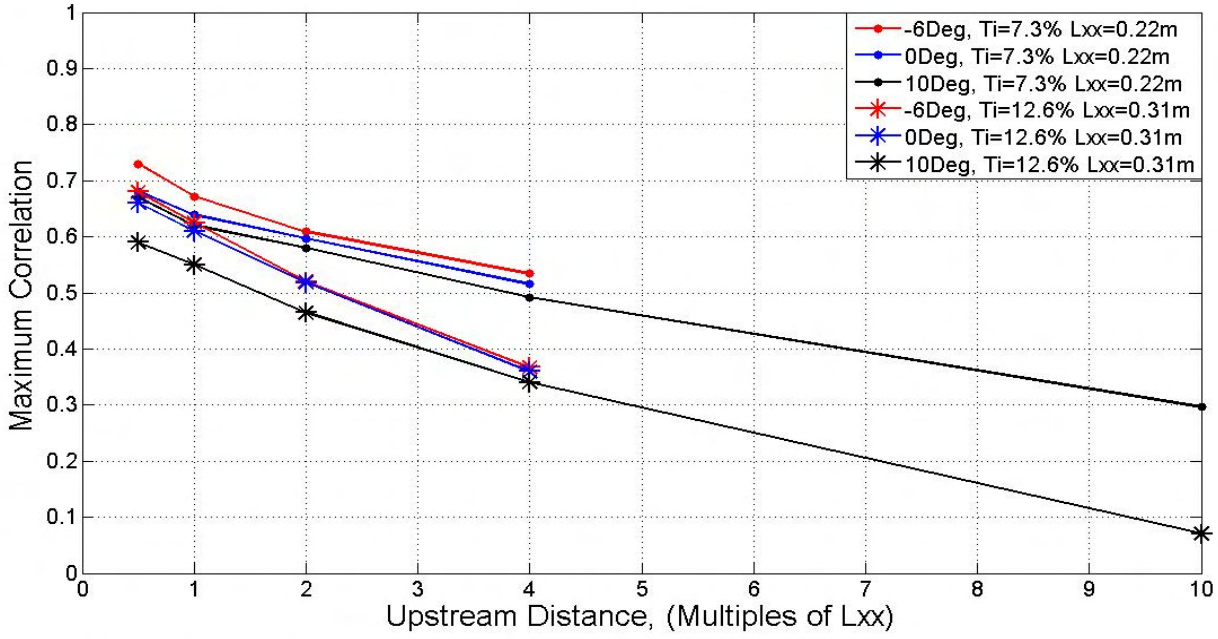

Figure 178: Correlations between CL and pitch angle measured at different upstream distance for different AOAs

At the lower AOAs there seems to be around 60% correlation between CL fluctuations occurring over the airfoil top surface and pitch angle fluctuations measured one length scale upstream, see Figure 177. The lift correlations also reveal that at the lower AOAs only a small change in the correlation is noticed at higher Ti when the upstream flow measuring location is less than one length scale from the airfoil, see Figure 177 and Figure 178. However, as the location of flow measurement moved further upstream, a larger difference is noticed between the correlations obtained at the two Ti, in that a consistently higher correlation was obtained at the lower Ti, see Figure 178. In Figure 177 the correlation between CL and pitch angle can be seen to remain nominally the same until AOA=8Deg approximately, above which the correlation gradually reduces.

Figure 177 and Figure 178 also serve as an indication of the validity of Taylor's hypothesis. The presence of high correlations serve as a validation of the hypothesis but its limits in the turbulence generated here can clearly be identified from the reducing correlation noticed as location of velocity measurement moves further upstream. When AOA=10Deg, at the higher Ti almost all correlation is lost when the velocity measuring point is ten length scales upstream, see Figure 178.

Comparing the turbulence conditions developed here to the turbulence encountered in the ABL away from local effects, the correlation coefficients are expected to be slightly different in the outdoor environment compared to those reported here. This is mainly due to the fact that the turbulence generated within wind-tunnels is generally still developing as compared to the relatively well-established state of turbulence present in the outdoor environment. It is therefore believed that the correlations measured here are on the conservative side as better correlation between lift fluctuations and upstream pitch angle fluctuations would be obtained outdoors due to the presence of well established longer length scales of turbulence in the ABL. However, for higher levels of turbulence in the ABL (e.g. in cities) it is postulated that, during instances when Ti is very high (Ti>20%), a reduced level of correlation is likely to be present.

The simultaneous measurement of upstream flow and surface pressure fluctuations have demonstrated that a reasonable correlation exists between the two. However, to maintain steady flight in turbulence using upstream flow measurements as a control input requires the development of a suitable autopilot system. An aerodynamic admittance function (transfer function) linking upstream velocity and surface pressure fluctuations must in turn be developed for the autopilot system to predict the influence of oncoming disturbances such that corrective measures can be taken. While the development of an accurate admittance function is beyond the scope of this work, the simultaneous upstream velocity and

surface pressure measurements permitted the assessment of the possibility of its development. The aerodynamic admittance function is generally derived and presented in the frequency domain hence the interaction between pitch angle and the airfoil lift fluctuations at varying frequencies was investigated. This was done by passing the simultaneously measured pitch angle and CL through band-pass filters of varying ranges and the cross correlation between the two was calculated. A 2nd order Butterworth filter was used for the filtration process. In the Figure 179 the results of this operation is presented.

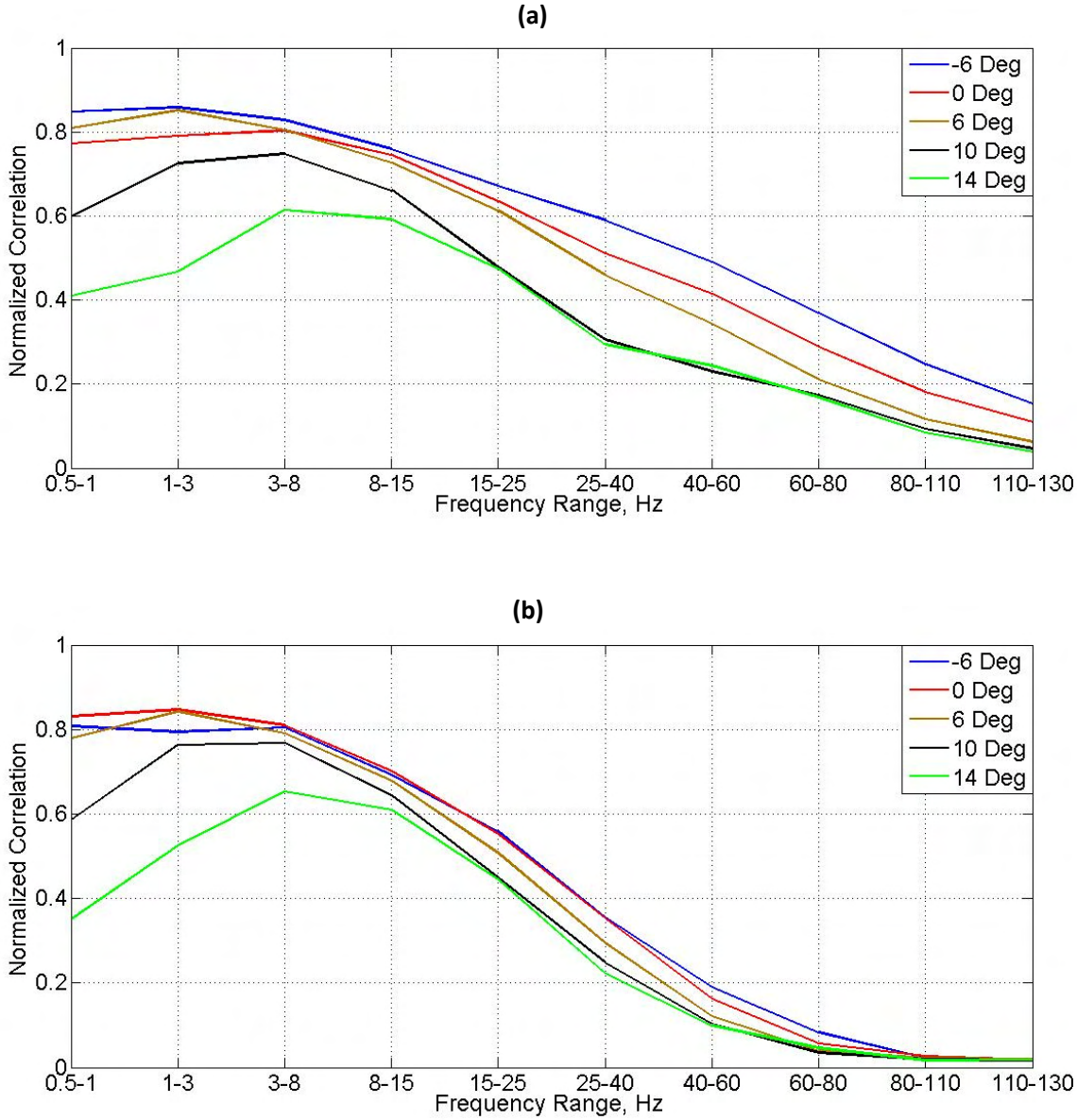

Figure 179: Correlation between band passed upstream pitch angle fluctuations measured one length scale upstream and integrated pressure (lift) fluctuations over the airfoil. (a) Ti=7.2% Lxx=0.22m, (b) Ti=12.6% Lxx=0.31m.

Figure 179 shows that for both turbulence conditions at negative and 0Deg AOA, high correlation between pitch angle and lift fluctuations exists till around 10Hz above which frequency the correlation drops steadily. However, as AOA increased further, a lower correlation is present at frequencies below 1Hz, but it increases with increase in frequency. Maximum correlation was reached in the range of frequencies where vortex cores formed for the respective AOA. This can be clearly seen from the fact that as AOA increased, maximum correlation was present at a higher frequency range. The location of maximum correlation present at the same frequency range for both turbulence levels once again suggested that within the turbulence range tested here, the rate of vortex core formation was not dependent on oncoming turbulence conditions. It also supported the fact that the rate of vortex core formation was dependent on AOA. In Figure 179, at higher frequencies (40Hz<), in spite of higher energy present at the higher turbulence intensity, a distinctly lower correlation was present. This is believed to be due to the location of flow measurement being further upstream at the higher turbulence intensity condition since the length scale was larger in the same.

This correlation analysis between the pitch angle and lift fluctuations over various ranges of frequencies has some resemblance to an admittance function as it provides a spectra link between upstream velocity and airfoil lift fluctuations. The trends presented here indicate that a suitable aerodynamic admittance function can be generated by taking simultaneous upstream velocity and surface pressure fluctuations. But a considerably more rigorous spectral comparison and analysis is required to enable development of an accurate version of the same.

6.2 Optimum Chordwise Locations for Pressure Taps

It is likely that a MAV using surface pressure fluctuations as a control input will possess a limited number of surface pressure taps. It would be desirable if the force fluctuations over the airfoil/wing can be appropriately gauged using only a few pressure taps that are optimally placed. Therefore the regions over the airfoil that are most suitable for placing pressure taps need to be identified. These regions should be representative of fluctuations occurring over the entire airfoil as well as being well responsive to changes in oncoming flow fluctuations. In Figure 180 and Figure 181, the correlation between overall

lift fluctuations and surface pressure fluctuations occurring at each pressure tap over the top surface is presented.

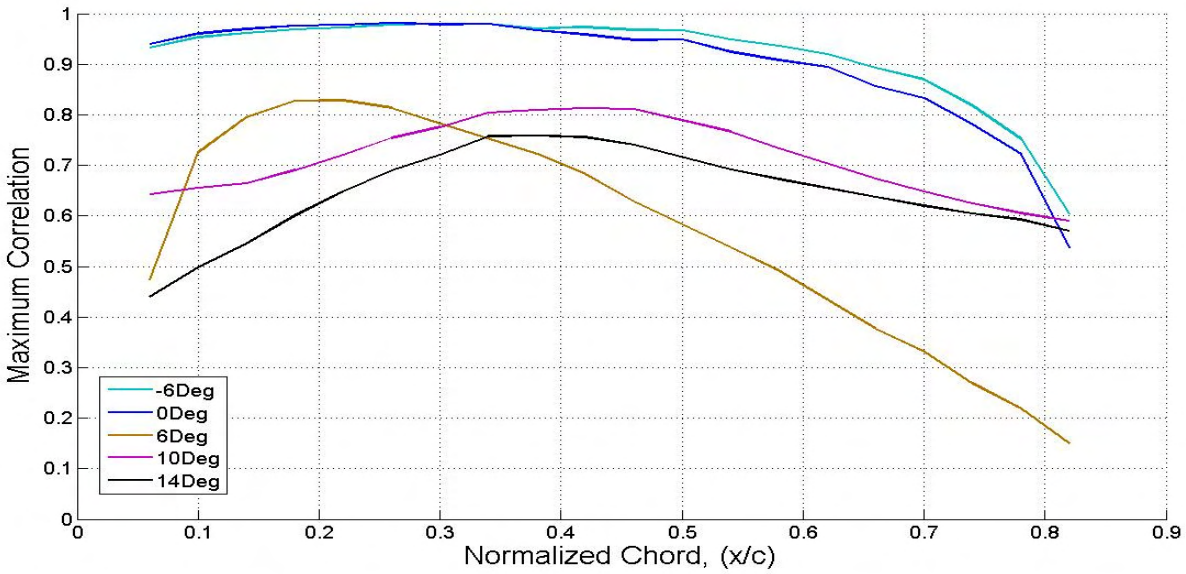

Figure 180: Correlation between overall lift fluctuations and surface pressure fluctuations occurring at each pressure tap. Ti=7.2% Lxx=0.22m

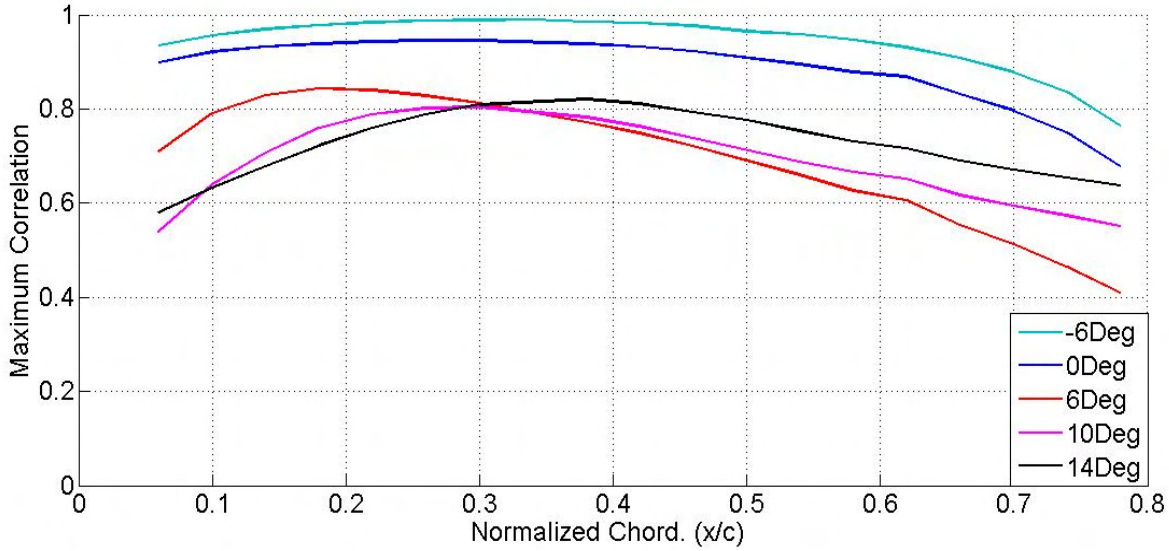

Figure 181: Correlation between overall lift fluctuations and surface pressure fluctuations occurring at each pressure tap. Ti=12.6% Lxx=0.31m

The correlation plots in Figure 180 and Figure 181 show that at lower AOAs the lift fluctuations are very well correlated with all pressure taps in both Ti conditions. At higher AOAs however (6Deg<AOA<10Deg) the correlation close to LE is lower but increases rapidly till the point of maximum correlation is reached, after which a gradual reduction ensues. This trend indicates that, similar to oncoming pitch angle fluctuations, the lift fluctuations are also most correlated with the pressure fluctuations occurring in the vortex core formation region. At very high AOAs, the correlation distribution assumes a flatter trend. The correlation distribution of the lift vs. pressure taps is similar to the distribution present in upstream pitch angle vs. pressure tap correlations.

Based on the analysis conducted here, for airfoils that experience leading edge separation when exposed to higher levels of turbulence the most optimum location for pressure taps appears to be the region of vortex cores formation i.e. close to the LE. In smooth flow however, greatest correlation was found to coincide with the reattachment point oscillation region. Though a pressure tap was located on the LE, time-varying analysis of the pressure measured there was not possible due to the presence of a sharp bend in the tubing system which influenced the time-varying pressures measured. It is however strongly believed that the fluctuations experienced at the LE would also correlate very well with both lift as well as pitch angle fluctuations. Therefore, specifically for this airfoil, it was found that the most optimum locations for placing pressure taps in both smooth and turbulent flow would be between 0.2(x/c) – 0.5(x/c) and on the LE.

6.3 Chapter Conclusions and Discussions

The interaction between upstream velocity and surface pressure fluctuations was further investigated in this chapter. Good correlation between upstream pitch angle and pressure fluctuations was noticed at lower AOAs, however the correlation dropped as AOA increased. The CL and pitch angle correlation was nominally the same for both the turbulence conditions when flow measurements were taken one length scale upstream. This indicated that reasonably accurate prediction of the CL fluctuations can be made by taking upstream flow measurements close to the LE, so long as the flow over the airfoil was not significantly influenced by the velocity measuring probe. The correlation between pitch angle and CL computed for different frequency ranges indicated that best correlation occurred at the vortex core

formation frequency while the correlation was very low for frequencies occurring above 40Hz. The significant variation in correlation of pitch angle and lift fluctuations at different frequencies highlighted the necessity to develop a suitable admittance function. Regions of vortex core formation and the location of reattachment were identified to be the most sensitive locations for pressure taps as a sensory input for a turbulence-rejection control system.

CHAPTER 7

Conclusions, Discussion and Recommendations

7.1 Conclusions & Discussion

The key research questions this work sought to answer were:

1) How do the time-averaged and time-varying surface pressures over the airfoil change between smooth and turbulent flows?
2) What are the salient flow features that develop over the airfoil in smooth and turbulent conditions, in particular the LSB?
3) How does the airfoil performance change in turbulence and what is the specific influence of turbulence intensity and integral length scale on the same?
4) How well do upstream velocity fluctuations correlate with surface pressure and lift fluctuations and could upstream velocity measurements be used as a control input to attain steady level flight?

Based on the data gathered from the experimentation and subsequent detailed analysis, the following conclusions were derived to answer the specific research questions.

7.1.1 Mean and Standard Deviation of Pressures over the Airfoil

The distributions of the mean and Std.Dev of pressures over the airfoil was analyzed for different turbulence conditions and consequently the following conclusions were derived:

In nominally smooth conditions, attached flow was present over the airfoil until 2Deg AOA, above which LE separation with subsequent reattachment occurred. The LSB rapidly grew with further increase in AOA till the airfoil stalled at 10Deg. For the range of AOAs where LSBs formed, the region of constant high suction was found to represent the region of recirculation within the LSB, while the location of maximum Std.Dev correlated well with the location of reattachment of the shear layer. Above the stalling AOA, a nominally constant mean pressure was noticed over the airfoil chord while the Std.Dev was also relatively low.

The distribution of mean and Std.Dev of pressures over the airfoil was significantly different at higher levels of turbulence. Maximum suction was noticed close to the LE and a rapid pressure recovery ensued. A decreasing trend of maximum suction generated also occurred with increase in Ti. An increase in the mean suction over the airfoil was however noticed with increase in length scale at nominally the same turbulence intensity. The Std.Dev was also considerably higher at higher Ti in comparison to that present in smooth flow. For a given Ti, the magnitude of pressure fluctuations experienced over the airfoil increased with increase in length scale. This was considered to be due to the presence of higher energy at the lower frequencies in the oncoming flow at longer length scales.

7.1.2 Time-Varying Properties of Flow over the Airfoil

Considerable variation in the distribution of mean and Std.Dev of pressures over the airfoil suggested that the flow structure was quite different between smooth and turbulent conditions. In smooth flow, flow visualization revealed that shear layer transition occurred through the amplification of K-H-like instabilities that formed in the lower part of the shear layer. Fluid entrainment within the bubble was limited as only a section of the shear layer rolled-up. The rollup of the shear layer led to vortices being shed on reattachment over a range of frequencies. Pressure fluctuations over the majority of the chord were however dominated by the flapping of the shear layer which occurred at a wave number of around 0.02. At AOAs greater than 8Deg, bluff-body-like vortex shedding was found to occur at the TE. The rate of vortex shedding at the TE was dependent on the AOA up to around 10Deg, above which the shedding rate was constant at a Strouhal number of 0.19.

At elevated levels of turbulence a significantly different flow structure over the airfoil evolved. Higher levels of ambient disturbances resulted in the shear layer to undergo transition to turbulence much earlier. Amplified instabilities formed that led to a significant portion of the shear layer to rollup. The enhanced rollup formed vortex cores resulting in a considerable increase in flow entrainment under the separated shear layer. A pulsating trend of vortex core formation, advection and dispersion was noticed in the pressure and velocity fluctuations over the airfoil. The rate of vortex core formation was found to be dependent on the AOA until 12Deg, above which AOA the formation rate remained nominally constant at a wave number of 0.12. The rate of vortex core formation was also found to remain the same within the test range of elevated freestream turbulence conditions generated here.

Comparison of the chordwise correlation of the pressure fluctuations revealed that the rate of advection of the vortex cores was lower than the advection rate of the flow structures in smoother conditions (Ti<1.2%). The velocity and pressure fluctuations indicated that the vortex cores imparted large fluctuations over the airfoil. Higher spanwise correlation was noticed at higher turbulence levels due to the increased spanwise correlation of the oncoming forcing frequencies and due to the larger size of the flow structures that formed over the airfoil. In elevated levels of turbulence, bluff-body-like vortex shedding occurred only intermittently even at high AOAs (>18Deg) due to the constant changes in oncoming flow speed and direction. The interactions between the advecting vortex cores and vortices shed from the TE resulted in the nullification of circulation in either rendering in a fully turbulent wake.

7.1.3 Airfoil Performance in Smooth and Turbulent Conditions

The time-averaged and time-varying properties of coefficients of lift, drag and moments were analyzed and the following conclusions were derived:

Analysis of the lift produced independently by the suction and pressure sides of the airfoil in smooth and turbulence conditions revealed that turbulence has a considerably larger influence on the suction side as opposed to the pressure surface. An increase in Ti from the nominally smooth conditions led to an increase in the maximum CL, a reduction in the lift-curve-slope and a delay in stall. For a particular Ti, an increase in length scale resulted in an increase in the lift-curve-slope and maximum CL. This implied that for a given AOA (in the pre-stall region) the lift generated in smooth flow was higher than in turbulence,

but at higher AOAs the opposite trend occurred. The noticed trend in the time-averaged CL variation was due to the high suction present under a LSB, or under a forming vortex core, resulting in the airfoil experiencing a pseudo-camber effect. This effect had greater influence on CL in smoother conditions (due to the higher suction present under a LSB than under a forming vortex core). Increased resistance to an APG, even at high AOAs, led to a delay in stall and an increase in CL max at higher levels of turbulence.

The opposite trend was noticed in the pressure drag coefficient variation with AOA, whereby a lower drag was measured in turbulence at low AOAs. The pressure drag at higher AOAs was, however, higher in higher levels of turbulence as compared to smooth flow. Turbulence intensity and length scale also had a significant influence on the CM vs. AOA variation of the airfoil. An extended range of AOAs, where pitching moment coefficient remained zero was noticed at higher levels of turbulence. At higher AOAs however, Ti and length scale had an opposing influence on the rate of reduction of pitching moment coefficient with increase AOA.

Analysis of the time-varying lift and rolling moments revealed that the interactions between the oncoming flow and the airfoil were complex. Due to the complexities of interaction and large range of fluctuations experienced, prediction of the possible range of lift and moment fluctuations based on the airfoil's time-averaged properties was found to be significantly incorrect. At higher levels of turbulence, the airfoil experienced lift and moment fluctuations at around the vortex core forming frequency and the majority of the fluctuations were found to occur only at the lower frequencies. It was also suggested that airfoils that stall abruptly were influenced by hysteresis and other dynamic stall properties, thus may be unsuitable for MAVs as they would experience large changes in lift with changes in oncoming AOA.

The surface pressure fluctuations correlated best with the upstream pitch angle fluctuations at lower AOAs, however the correlation dropped as AOA increased. Therefore, reasonably accurate prediction of the CL fluctuations could be made by taking upstream flow measurements close to the LE so long as the flow over the airfoil was not significantly influenced by the velocity measuring probe. The best correlation between upstream pitch angle and lift fluctuations occurred at the vortex core formation frequency while the correlation was very low for fluctuations occurring above 40Hz (Wave number = 0.85). The significant variation in correlation between pitch angle and lift fluctuations at different frequencies highlighted the necessity to develop a suitable aerodynamic admittance function. Regions of

vortex core formation and location of reattachment were identified to be the most suitable locations for pressure taps to be used at as control inputs.

7.2 Recommendations

As a result of the experiments and subsequent analysis conducted in this research, the following areas have been identified for future work;

- To obtain further understanding of the flow-field over the airfoil in turbulent conditions, it is recommended that a detailed survey of the flow is conducted using PIV systems. This would shed more light on the mechanism of transition and vortex core formation in turbulent conditions.

- Further airfoil testing should be conducted in flow with integral length scales that are many orders larger than typical MAVs (Lxx>1.5m). Particular emphasis should be given to the change in flow structure over the airfoil in such conditions. There has been negligible prior work investigating the influence of length scales and it has been shown to have a significant influence on the rolling moments experienced. Therefore this area is thought worthy for further investigation.

- The pressure measurements conducted here provided insights on the flow structure but only over a limited section of the airfoil. Therefore, it is recommended that the time-varying force and moment fluctuations (lift, drag, pitching/rolling moment, etc) are measured directly as they will provide an integrated view on the influence of Ti and length scale over the entire airfoil. A high frequency balance system would be needed for this.

- Analysis of the relationship between oncoming turbulence and lift fluctuations revealed that a suitable admittance functions needs to be developed such that a relatively accurate prediction of the transient forces experienced by the airfoil can be made. It has also been demonstrated that the function can be developed through spectral comparisons between oncoming turbulence and lift fluctuations. The development of a suitable aerodynamic admittance function is hence suggested.

References and Bibliography

Abdalla, I. E. & Yang, Z., “Numerical study of the instability mechanism in transitional separating-reattaching flow”. Intl J. Heat Fluid Flow, vol. 25 no. 4 (2004): 593–605.

Aberle, B., “Clean and Quiet – The Guide to Electric Powered Flight”. Douglas Charles Press, 1995.

Anderson, F. H., “An Encyclopedia of the Golden Age of Model Airplanes, Volume 1, The Dawn of American Aeromodeling 1907–1935”. Palm Bay, Florida 32907-1604: published by Frank H. Anderson, 1998.

Anon., “UAVs Applications are Driving Technology – Micro Air Vehicles”. UAV Annual Report, Defense Airborne Reconnaissance Office, 1993.

Batchelor, G.K. and Townsend, A.A., "Decay of vorticity in isotropic turbulence." Proceedings of the Royal Society. 1947. 534–550.

Batchelor, G.K. and Townsend, A.A. "Decay of isotropic turbulence in the initial period." Proceedings of the Royal Society . 1948. 539–558.

Bastedo, W.G.Jr. and Mueller, T.J., "The Spanwise Variation of Laminar Separation Bubbles on Finite Wings at Low Reynolds Numbers." AIAA Paper No. 85-1590, presented at the AIAA 18th Fluid Dynamics, Plasma Dynamics, and Laser Conference, July 1985.

Bergh, H. and Tijdeman, H., “Theoretical and experimental results for the dynamic response of pressure measuring systems”. Technical Report NLR-TR F238, National Aerospace Laboratories, 1965.

Broeren, A.P. and Bragg, M.B., "Unsteady stalling characteristics of thin airfoils at low reynolds number." Edited by Thomas J. Mueller. Progress in Astronautics and Aeronautics. Vol. 195 (2001): 191 – 213.

Burgmann, S., Brucker, C. and Schroder, W., "Scanning PIV measurements of a laminar separation bubble." Exp. Fluids. Vol. 41 (2006): 319–326.

Burgmann, S., Dannemann, J. and Schroder, W., "Time-resolved and volumetric PIV measurements of a transitional separation bubble on an SD7003 airfoil." Exp. Fluids. Vol 44 (2008): 602–622.

Carmichael, B.H., "Low Reynolds Number Airfoil Survey." Volume I, NASA Contractor Report 165803, 1981.

Carr, L. W., "Progress in Analysis and Prediction of Dynamic Stall." Journal of Aircraft. Vol 25, no. 1 (1988): 6-17.

Chen, J., Haynes, B. S., and Fletcher, D., "Cobra probe measurements of mean velocities, reynolds stresses and higher-order velocity correlations in pipe flow." Experimental Thermal and Fluid Science. Vol 21 (2000): 206–217.

Chen, W.F., "Handbook of Structural Engineering". Boca Raton: CRC Press, 1997.

Cherry, N. J., Hillier, R. and Latour, M.E,M.P., "Unsteady measurements in separating and reattaching flows." Journal of Fluid Mechanics. Vol 144 (1984): 13-46.

Cherry, N.J., Hillier, R., Latour, M.E.M.P., "The unsteady structure of two-dimensional separated and reattaching flows." Journal or Wind Engineering and lndustrial Aerodynamics, no. 11 (1983): 95-105.

Comte-Bellot, G. and Corrsin, S., "The use of contraction to improve the isotropy of grid generated turbulence,." Journal of Fluid Mechanics. Vol. 25, no. 4 (1966): 657 – 682.

Crompton, M.J. and Barrett, R.V., "Investigation of the separation bubble formed behind the sharp leading edge of a flat plate at incidence." Proceedings of the Institution of Mechanical Engineers, Part G: Journal of Aerospace Engineering (Professional Engineering Publishing). Vol. 213, no. 3 (2000): 157-176.

Cruz, E G., Watkins, S., Loxton, B., Watmuff, J., "A flat plate rectangular wing subjected to grid-generated turbulence." 26th AIAA Applied Aerodynamics Conference. Honolulu, Hawaii, 2008.

Cruz, E., Watkins, S. and Loxton, B., "A study of the effects of turbulence on airfoils at low reynolds numbers". Interim Report AOARD-06-4037, Melbourne: RMIT University, 2007.

Cruz, E., Watkins, S. and Loxton, B., "A study on the effects on turbulence on airfoils at low Reynolds numbers". Interm Report : USAF Project No: AOARD-06-4037, RMIT, 2008.

Devinant, P., Laverne, T. and Hureau, J., "Experimental study of wind-turbine airfoil aerodynamics in high turbulence." Journal of Wind Engineering and Industrial Aerodynamics. Vol. 90 (2002): 689-707.

Dryden H.L., Schubauer G.B., Mock W. C. and Skramstad H. K., "Measurement of Intensity and Scale of Wind-Tunnel Turbulence and their Relationship to the Critical Reynolds Numbers of Spheres." NACA Report No. 581, 1936.

Flay, R.G.J., "Structure of a Rural Atmospheric Boundary Layer Near the Ground". PhD. Thesis, New Zealand: Dept. of Mech. Eng., University of Canterbury, 1978.

Foch, R. J. and Ailinger, K. G., "Low Reynolds Number Long Endurance Airplane Design." 1992.

Gartshore, I.S., "The effects of freestream turbulence on the drag of rectangular two dimensional prism." BLWT, University of Western Ontario, Canada , 1973, 4-73.

Gaster. M., "The structure and behaviour of laminar separation bubbles". AGARD CP-4, 1966, 813–854.

Ghosal, M., "7.8.5 Vertical Wind Speed Gradient" Alpha Science International, 2005.

Good, W., ""History of RC Flying," Model Aviation, Part 1". 56–129. 1986.

Gopalarathnam,A., Broughton, B.A., McGranahan, B.D. and Selig, M.S., "Design of Low Reynolds Number Airfoils with Trips." Journal of Aircraft. Vol. 40 No.4, 2003

Grant, H. L. and Nisbet, I.C.T., "The inhomogeneity of grid turbulence". Journal of Fluid Mechanics. Vol. 2 (1957): 263-272.

Grusovin, M., "Modelling of Atmospheric Boundary Layer in RMIT Industrial Wind Tunnel". Undergraduate Thesis Project, RMIT, 2006.

Hebert, A., "New horizons for combat UAVs". Air Force Magazine, 2003.

Hillier, R. and Cherry, N.J., "The effects of stream turbulence on separation bubbles." Journal of Wind Engineering and Industrial Aerodynamics. Vol. 8 (1981): 49--58.

Hoarau, Y., Braza, M., Ventikos, Y., Faghani, D. and Tzabiras, G., "Organized modes and the three-dimensional transition to turbulence in the incompressible flow around a NACA0012 wing." J Fluid Mech. Vol. 496 (2003): 63–72.

Hoerner, S.F. and Borst, H.V. "Fluid Dynamic Lift". Brick Town, NJ: Hoerner Fluid Dynamics, 1975.

Hoerner, S.F., "Fluid Dynamic Drag". Brick Town, NJ: Hoerner Fluid Dynamics, 1965.

Holmes, J. D. and Lewis, R. E., "Optimisation of dynamic-pressure-measurement system, I:Single point measurements." Journal of Wind Engineering and Industrial Aerodynamics. Vol. 25 (1987a): 249-273.

Holmes, J. D., "Wind Loading of Structures". London: Spon Press, 2001.

Hooper, J. D. and Musgrove, A. R., "Reynolds stress, mean velocity, and dynamic static pressure measurement by a four-hole pressure probe." Experimental Thermal and Fluid Science. Vol. 15 (1997): 375–383.

Horton, H.P., "Laminar separation bubbles in two and three-dimensional incompressible flow". PhD Thesis, Univ. London, UK, 1968.

Hu, H. and Yang, Z., "An Experimental Study of the Laminar Flow Separation on a Low-Reynolds-Number Airfoil." Journal of Fluids Engineering. Vol. 130 (2008).

Iberall, A. S., "Attenuation of oscillatory pressures in instrument lines." Journal of Research (National Bureau of Standards) 45(RP2115) (1950): 85–108.

Jancauskas, E. D., "The Cross-Wind Excitation of Bluff Structures and the Incident Turbulence Mechanism." Doctoral thesis, Monash University, Clayton, 1983.

Kähler, C.J., "Experimental investigation of flows at low Reynolds number using optical techniques." von Karman Institute for Fluid Dynamics, RTO-AVT-104 VKI Lecture Series on Low Reynolds number

aerodynamics on aircraft including applications in emerging UAV technology, Rhode Saint Genèse, Belgium, Nov. 24–28 2003.

Kang, H., and Altman, A., "Generalized Empirical Airfoil Stagnation Point Location Prediction." Journal of Aircraft. Vol. 44, no. 2 (2006): 698 – 701.

Kang, H.S., Chester, S. and Meneveau, C., "Decaying turbulence in an active-grid-generated flow and comparisons with large-eddy simulation." J. Fluid Mech. Vol. 480 (2003): 129–160.

Kellogg, J., Bovais, C., Dahlburg, J., Foch, R., Gardner. J., et al. "The NRL Mite Air Vehicle". Univ. Bristol, 2001, 25.1–14.

Kiya, M., and Sasaki, K., "Free-stream turbulence effects on a separation bubble." Journal of Wind Engineering and Industrial Aerodynamics. Vol. 14 (1983): 375--386.

Kiya, M. and Sasaki, K., "Structure of a turbulent separation bubble." Journal of Fluid Mechanics. Vol. 137 (1983): 83-113.

Larssen, J.V. and Devenport, W.J., "The generation of high Reynolds number homogeneous turbulence." AIAA Paper 2002-2861.

Li, Q.S. and Melbourne, W.H., "The e!ect of large-scale turbulence on pressure fluctuations in separated and reattaching fows." Journal of Wind Engineering and Industrial Aerodynamics. Vol. 83 (1999): 159-169.

Liu, R., Ting, D.S-K. and Rankin, G.W. "On the generation of turbulence with a perforated plate." Experimental Thermal and Fluid Science. Vol. 28, no. 4 (2004): 307-316.

Loxton, B., Watkins, S., Watmuff, J., Trivalio, P., Cruz, E. amd Ravi, S., "The Influence of Atmospheric Turbulence on the Aerodynamics of a Flat Plate Micro Air Vehicle Wing." 3rd Australasian Unmanned Air Vehicles Conference. Melbourne, Australia, 2009.

Makita, H., "Realization of a large-scale turbulence field in a small wind tunnel." Fluid Dynamics Research 8 (1991): 53–64.

McCroskey, W. J., "Unsteady Airfoils." Annual Review of Fluid Mechanics. Vol. 14 (1982): 285-311.

McMichael, J.M. and Francis, M.S., "Micro Air Vehicles – Toward a New Dimension in Flight". USA: DARPA, 1997.

Melbourne, W.H., "Turbulence and the Leading Edge Phenomenon." Journal of Wind Engineering and Industrial Aerodynamics. Vol. 49 (1993): 45-64.

Milbank, J., Loxton, B., Watkins, S. and Melbourne W.H., "Replication of Atmospheric Conditions for the Purpose of Testing MAVs MAV Flight Environment Project: Final Report". AFOSR Final Report (USAF Project No: AOARD 05-4075), RMIT, 2005.

Mousley, P.D., Watkins, S. and Hooper, J.D., "Use of a hot-wire anemometer to examine the pressure signal of a high-frequency pressure probe." 13th Australasian Fluid Mechanics Conference. Melbourne, Australia: Monash University, 1998.

Mueller, T.J., "Aerodynamic Measurements at Low Reynolds Numbers for Fixed Wing Micro-Air Vehicles." Proceedings of the Development and Operation of UAVs for Military and Civil Applications Short Course. Belgium: published in Rto-EN-9 by NATO, April 2000, 1999.

Mueller, T.J., Kellogg, J.C., Ifju, P.G. and Shkarayev, S. V., "Introduction to the Design of Fixed-Wing Micro Air Vehicles." AIAA Education Series, 2007.

Mydlarski, L. and Warhaft, Z., "On the onset of high-Reynolds-number grid-generated wind tunnel turbulence." Journal of Fluid Mechanics. Vol. 320 (1996): 331–368.

Nishimura, H. and Taniike, Y., "Aerodynamics characteristics of fluctuating forces on a circular cylinder." Journal of Wind Engineering Industrial Aerodynamics. Vol. 89 (2001): 713–723.

Ol, M.V., McAuliffe, B.R., Hanff, E.S., Scholz, U. and Kähler, C.J., "Comparison of laminar separation bubble measurements on a low Reynolds number airfoil in three facilities." AIAA-2005-5149, 35th AIAA Fluid Dynamics Conference and Exhibit, Toronto, Ontario, June 6-9 2005

Pagliarella, R.M., "On the aerodynamic performance of automotive vehicle platoons featuring pre and post-critical leading forms." PhD thesis, RMIT University, 2009.

Pauley, L.L., Moin, P. and Reynolds, W.C., "The structure of two-dimensional separation." J Fluid Mech. Vol. 220 (1990): 397–411.

Phillips, R,. "Wireless-controlled Mechanism for Amateurs." Cassel and Company Ltd., 1927.

Pines, D.J. and Bohorquez, F., "Challenges Facing Future Micro-Air-Vehicle Development." Journal of Aircraft. Vol. 23, no. 2 (2006): 290-305.

Raupach, M.R. and Thom, A.S., "Turbulence in and above Plant Canopies." Annual Review of Fluid Mechanics. Vol. 13 (1981): 97-129.

Ravi, S., "Analysis of wing in ground-effect using potential flow theory". Honours Thesis Project, Mlbourne: RMIT, 2007.

Roberts, W.B., "Calculation of laminar separation bubbles and their effect on airfoil performance." AIAA Journal. Vol. 18, no. 1 (1980): 25-31.

Roshko, A., "Experiments on the flow past a circular cylinder at very high reynolds numbers." J Fluid Mech. Vol. 10 (1961): 315–356.

Saathoff, P.J., "Effects of free-stream turbulence on surface pressure fluctuations in separated and reattaching flow". Ph.D. Thesis, Monash University, 1988.

Sathaye, S.S., “Lift Distributions on Low Aspect Ratio Wings at Low Reynolds Numbers”. M.Sc. Thesis, Worcester Polytechnic Institute, 2004.

Sicot, C., Aubrun, S., Loyer, S.and Devinant, P., "Unsteady characteristics of the static stall of an airfoil subjected to freestream turbulence level up to 16%." Experiments in Fluids. Vol. 41 (2006): 641-648.

Simmons, L.F.G. and Salter,C., "Experimental Investigation and Analysis of the Velocity Variations in Turbulent Flow." Proceedings of the Royal Society of London. Series A, Containing Papers of a Mathematical and Physical Character 145 (1934): 212-234.

Sims-Williams, D. B. and Duncan, B. D., "The Ahmed model unsteady wake: Experimental and computational analysis." Technical Report 2002-01-1315, Society of Automotive Engineers, Warrendale, PA, 2002.

Sinha, A.K. and Kusumo, R., "A system framework to automate design decision support of re-configurable UAVs." ICAS. 2002.

Spedding, G.R., and Lissaman, P.B.S., "Technical Aspects of Microscale Flight Systems." Journal of Avian Biology. Vol. 29, no. 4 (1998): 458-468.

Stack, J., “Tests in the Variable Density Wind Tunnel to Investigate the Effects of Scale and Turbulence on Airfoil Characteristics”. NACA-TN-364, NACA Langley Memorial Aeronautical Laboratory, 1931.

Swalwell, K., “The Effect of Turbulence on Stall of Horizontal Axis Wind Turbines”. PhD Thesis, Department of Mechanical Engineering, Monash University, 2005.

Swalwell, K. E., Sheridan, J. and Melbourne, W.H., "The Effect of Turbulence Intensity on Stall of the NACA 0021 Aerofoil." 14th Australasian Fluid Mechanics Conference. 2001.

Thompson, M. and Watkins, S., "Gust Inputs Relevant to Bees, Birds and MAVs." 25th Bristol International Unmanned Aerial Vehicle Systems (UAVS) Conference. Bristol, UK, 2010.

Thuillier, R.H. and Lappe, U.O., "Wind and Temperature Profile Characteristics from Observations on a 1400 ft Tower." Journal of Applied Meteorology. Vol. 3 (1964): 299–306.

Torres, G.E., “Aerodynamics of Low Aspect Ratio Wings at Low Reynolds Numbers with Applications to Micro Air Vehicle Design”. Department of Aerospace and Mechanical Engineering, Uni. of Notre Dame, 2002.

Van der Hoven, I., “Power Spectrum of Horizontal Wind Speed Spectrum in the Frequency Range from 0.0007 to 900 Cycles per Hour.” Journal of Meteorology, Vol. 14 (1957): 160-164.

Vickery, B.J., "On the flow behind a coarse grid and its use as a model of atmospheric turbulence in studies related to wind loads on buildings." N.P.L. Aero. Rep 1143, 1965.

Vickery, B.J., "Fluctuating lift and drag on a long cylinder of square cross-section in a smooth and in a turbulent stream." J Fluid Mech. Vol. 25 (1966): 481–494.

Vino, G., "An experimental investigation into the time-averaged and unsteady aerodynamics of the simplified passenger vehicle in isolation and in convoys." PhD thesis, RMIT University, 2005.

Walshe, D. E.J., “Wind-Excited Oscillations of Structures”. London: Her Majesty's Stationery Office, 1972.

Walter, T., Gossweiler, C., and Willson, B., “Application of an improved model for the determination of acoustic resonances in indicator passages for combustion pressure measurements in large bore gas engines”. Kistler Instruments AG, Winterthur, Switzerland: Technical Report (Kistler special print) 920-352e-02.07, 2007.

Wasko, M., “Wind Tunnel Simulation of the Turbulence Experienced by Road Vehicles Through the Use of an Oscillating, Upstream Pendulum”. M.Eng. Thesis, Melbourne: RMIT, 2003.

Watkins, S., "Wind Tunnel Modelling of Vehicle Aerodynamcis: With Emphasis on Turbulent Wind Effects of Commercial Vehcle Drag." PhD Thesis, RMIT University, Victoria, Australia, 1990.

Watkins, S., Milbank, J., Loxton, B.J. and Melbourne, W.H., "Atmospheric Winds and their Effects on Micro Air Vehicles." AIAA Journal. Vol. 44, no. 11 (2006): 2591–2600.

Watkins, S., Mousley, P. and Hooper, J., "Measurement of Fluctuating Flows Using Multi-Hole Probes." in Proceedings of the 9th International Congress of Sound and Vibration, Orlando, Florida, USA, 8-11 July, 2002.

Watmuff, J. H., "Evolution of a wave packet into vortex loops in a laminar separation bubble." J. Fluid Mech. Vol. 397 (1999): 119–169.

Weibel, R. E., "Safety considerations for operation of different classes of unmanned aerial vehicles in the National Airspace System." Massachusetts Institute of Technology. Dept. of Aeronautics and Astronautics., 2005.

Winkelmann, A. E., "An Experimental Study of Mushroom Shaped Stall Cells." AIAA/ASME 3rd Joint Thermophysics, Fluids, Plasma and Heat Transfer Conference. St. Louis, Missouri, 1982.

Winter, H., "Flow phenomena on plates and airfoils of short span." naca-tm-798, 1936.

Woods, M. I., Henderson, J. F. and Lock, G. D., "Energy requirements for the flight of micro air vehicles." Aeronautical Journal. Vol. 105 (2001): 135-149.

Wordley, S. J., “On-road turbulence”. PhD Thesis, Department of Mechanical Engineering, Monash University, 2009.

Wragg, D.W., “Flight before flying”. Frederick Fell Publishers, 1974, 191.

Yang, H., Sims-Williams, D. B., and He, L., "Unsteady pressure measurement with correction on tubing distortion." In Unsteady Aerodynamics, Aeroacoustics and Aeroelasticity of Turbomachine, edited by K. C., Kielb, R. E., and Thomas, J. P. Hall, 521–529. Springer, 2006.

Yarusevych, S., Kawall, J.G. and Sullivan, P.E., "Unsteady Separated Flow Characterization on Airfoils Using Time-Resolved Surface Pressure Measurements." AIAA Journal. Vol. 46, no. No. 2 (2008).

Zhang, W., Hain, R. and Kähler, C J., "Scanning PIV investigation of the laminar separation bubble on a SD7003 airfoil." Exp Fluids. Vol. 45 (2008): 725–743.

Zimmerman, C.H., "Characteristics of Clark Y airfoils of small aspect ratios ." NACA Tech Rep. TR 431, 1932.

Appendix A: Consideration of Errors

A.1 Consideration of Cobra Probe Errors

The Cobra Probe system at RMIT has been used in numerous research projects e.g. (Vino (2005), Pagliarella (2009)) where their errors have been assesed. No dynamic calibration of the Cobra Probes was undertaken here as the manufacturer (TFI) had conducted detailed calibration exercises in their dynamic testing facility. TFI reported that the Cobra Probe system has an accuracy of ±0.1m/s in smooth flow and up to ±0.5m/s when subjected to Ti of 30%. For the velocities here (between 7m/s to 10m/s) and the turbulence generated (maximum Ti was around 12%), the accuracy of the Cobra Probes was deemed good enough to obtain flow-field data to the required accuracy. For the time-varying measurements, the manufacturer also reported that the probes have a flat response exceeding 2.5kHz; this too was well above the frequency range of interest here. To ensure negligible errors occurred during the probe setup, time-averaged calibrations of the system were conducted against a fixed Pitot-static tube before each testing session. A sample of such an exercise is presented in Figure 182.

The probe has a ±45° cone of acceptance and hence when the probe is significantly misaligned to the mean flow direction, or when velocity was measured in regions of high circulation or turbulence, data can exceed the limits of the calibration surfaces, i.e. >±45° to the probe axis. Such instances are flagged by the software, which shows the percentage of good data. To overcome such effects, the probe head was oriented as close as possible to the oncoming flow, but small mean flow offsets of the order of ±2° could be present. The correction for this offset is described in Appendix D. All of the datasets used in this thesis had >99.95% good data. Based on the small variance in the velocities measured it is considered that the conclusions drawn from this research are entirely valid.

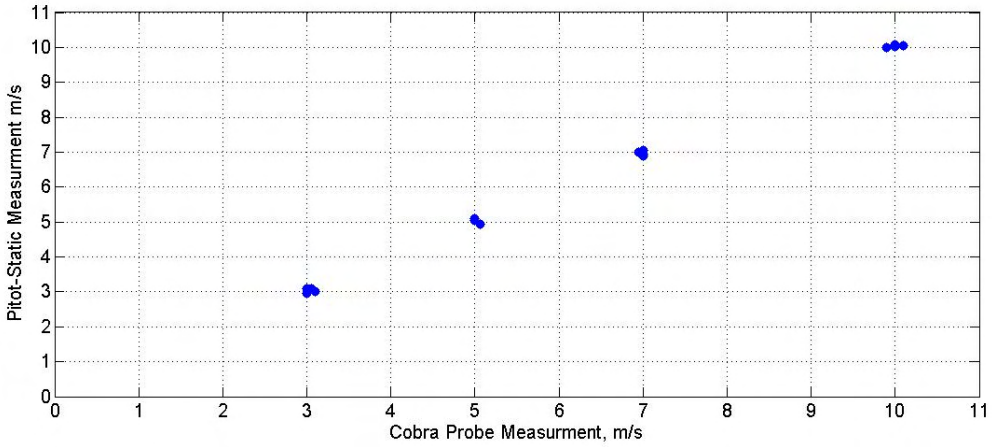

Figure 182: Comparison between Cobra Probe and Pitot-static tube measurements

A.2 Consideration of DPMS and Digitization Errors

The manufacturer (TFI) stated that the Digital Pressure Measurement System (DPMS) had a time-averaged accuracy of 98% within a range of ±35kPa. It was dynamically calibrated by TFI at their dynamic testing facility. They reported that the DPMS without any tubing added, had a flat response till over 2kHz. With tubing connected to the system as used in the experiments described in this thesis, a dynamic calibration check of the tubing system was conducted as mentioned in Appendix C. The time-averaged leak testing conducted for the airfoil (where a known pressure was added though a manometer to all pressure taps and the pressures were sampled for a finite time period) also served as a time-averaged check for the DMPS. In Figure 187 all pressure taps, and hence the DPMS system were, within 1% of the reference pressure. This provided further assurance that the DPMS system was functioning properly.

The National Instruments 6034E A/D card used to acquire the pressures from the voltages delivered by the DPMS Interface box had only one A/D channel. Therefore to sample the pressures from all pressure taps, a round-robin method of multiplexing was used. The errors in simultaneous pressure measurement, and the phase lag associated with this method of sampling, were found to be small, as the highest frequency of interest was around 100Hz. Further elaboration on this multiplexing method and the errors associated is presented in Chapter 2.

A.3 Consideration of Other Errors

The AOA of the airfoil was changed manually, however extreme care was taken to ensure all sections of the airfoil were at the same incidence. The AOA at five different positions over the span was measured using an analogue as well as a digital inclinometer. In spite of these precautions, small "variations" over different runs were noticed in the pressures over the airfoil. This variation was believed to originate from slight changes in airfoil position while exposed to turbulence and due to errors in measurement. For a given AOA, the time-averaged variation of the pressures in nominally smooth and higher levels of turbulence was of the order of ±3%. The variation in the time-varying properties i.e. Std.Dev was slightly higher at ±4.5% and ±4% in smooth and turbulent conditions respectively. The increased variation in the Std.Dev in smooth flow as compared to the variation at high levels of turbulence was believed to be due to the increased sensitivity of the shear layer to even minute changes in ambient conditions and airfoil position. At higher levels of turbulence, the variation in the Std.Dev was found to be highest close to the LE, while it reduced with downstream distance. In Figure 183 and Figure 184 variation in both mean and Std.Dev of pressures over the airfoil is respectively presented. Though the variation is higher in the time-varying properties of the pressures measured over different runs, the conclusions drawn from this research would be unaffected.

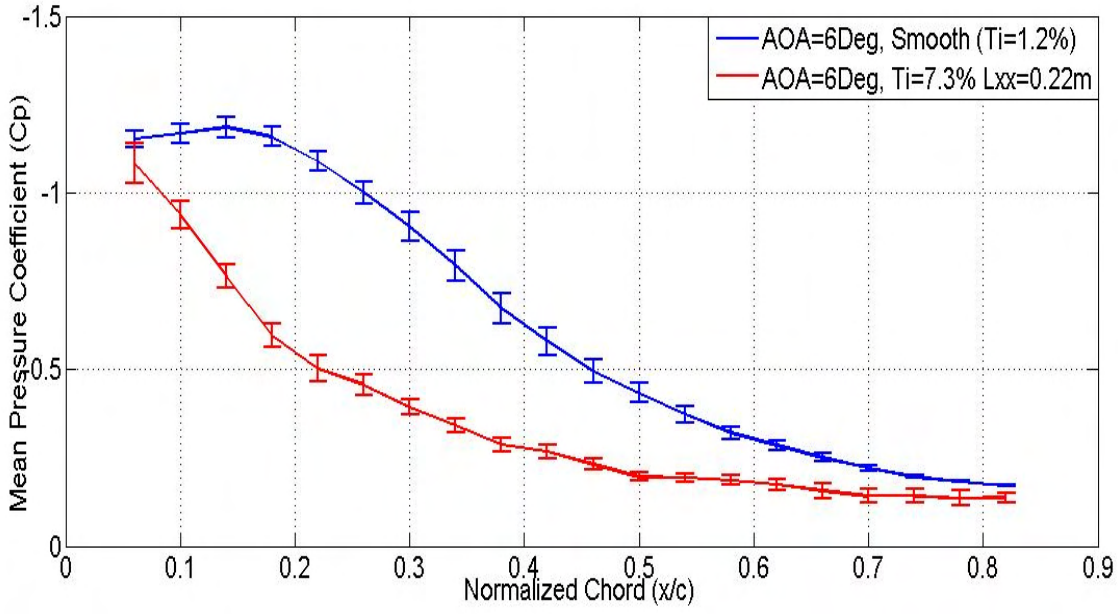

Figure 183: Variation in the time-averaged pressures measured in smooth and turbulent conditions

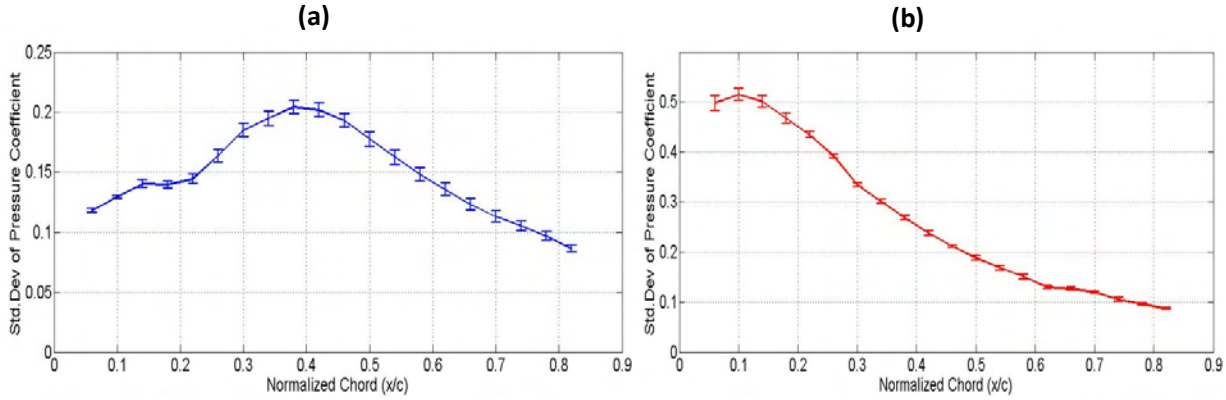

Figure 184: Variation in the time-varying pressures measured in smooth and turbulent conditions AOA=6Deg. (a) Ti=1.2%, (b) Ti=7.3% Lxx=0.22m

Other sources of errors included statistical sampling errors associated with the data gathered in this research. Due to the high sampling rate, long sampling duration, the statistical errors that were accrued during analysis were very small hence considered negligible. In spite of the fact that the frequencies of interest here were relatively low (<100Hz), the errors accrued during spectral analysis of the data (spectral bias, random errors, aliasing, etc) were considered negligible due to high sampling rate and large block-size used (block-size was equal to data-points acquired over 20secs).

A.4 Noise Consideration and Measurement

Pressure transducers generally measure the sum of hydrodynamic and acoustic pressures however they also respond accelerations, electro-magnetic noise and temperature variations. To ensure that background "noise", in the general sense of the word, within the wind tunnel did not contribute significantly to the measurements made by the DPMS and Cobra Probes, the electromagnetic and acoustic noise levels within the wind tunnel for each turbulence condition was measured. This was done by placing the DMPS module within the wind-tunnel but close to the walls and connecting it to a tube leading just outside the wind-tunnel. This way pressure transducer was close enough to be exposed to the acoustic and electromagnetic fluctuations and not to genuine flow-field fluctuations occurring within the wind-tunnel. In Figure 185 the spectra of the pressures measured in this manner are presented alongside the spectra of the pressure measured at one of the pressure taps in nominally smooth and

turbulent flow. The spectra of the pressures measured by an arbitrary pressure tap in smooth and turbulent flow are also plotted to add perspective to the contribution of background noise to the Std.Dev of pressures measured. As seen in Figure 185, the contribution of background noise to the measured pressures in all turbulence conditions was very small. The noise spectra also do not show a peak at any of the frequencies that were regarded as a genuine flow property in the analysis presented in the earlier chapters. The spectra of the velocity measured during calibration for each turbulence condition (Figure 51) also indicated that negligible acoustic or electromagnetic fluctuations were present at the frequencies of interest in the oncoming flow, with and without the grids.

N.B. The RMIT IWT has acoustically treated turning vanes fitted in order to minimize acoustic noise within the test section since it is utilized for aero-acoustic tests in a number of research and commercial projects. The DPMS and Cobra Probe systems are also shielded and grounded and there is considerable line filtering on the AC input.

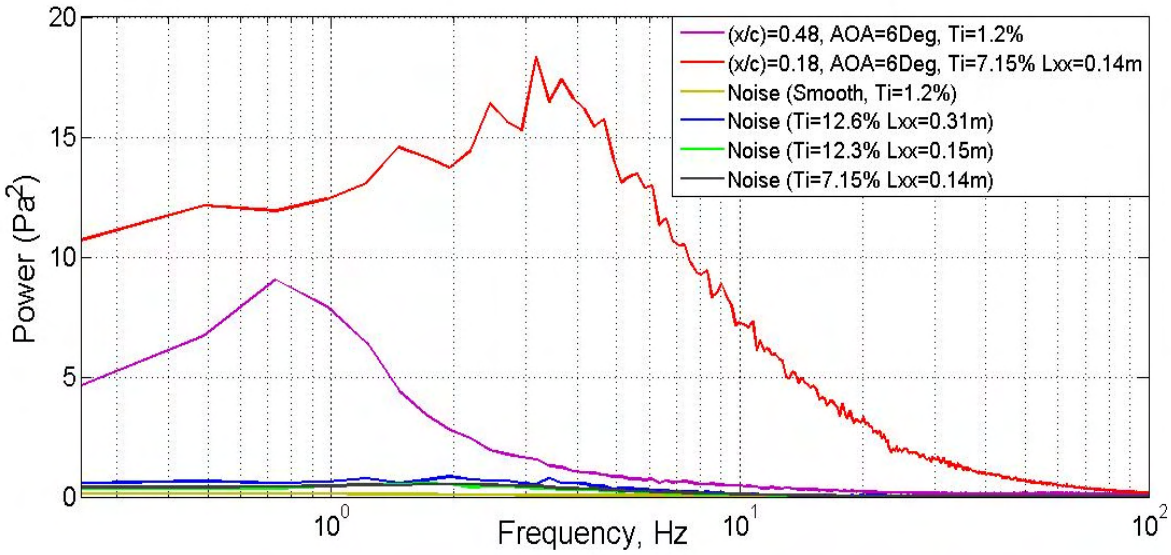

Figure 185: Spectra of background noise plotted along with pressures measured at arbitrary pressure taps over the airfoil for different turbulence conditions

Appendix B: Ensuring Flow Two-Dimensionality

When airfoil testing was conducted, it was vital to ensure that the mean flow was only along the longitudinal axis over the span of the airfoil at all times. In the presence of turbulence however, this was not entirely possible given turbulence is random and extremely three dimensional. The freestream turbulence generated in this research offered statistically repeatable conditions and hence two dimensionality of the flow was measured by examining the time-averaged properties. Though in a time-varying sense, each section of the airfoil might have experienced a unique AOA due to the random nature of turbulence, they converged to the same value when averaged over time. It should also be noted that for all tests, the reference pressure was taken twice i.e. once at the airfoil mid span without the airfoil and once inside the box with airfoil but well removed from the airfoil location. Good correlation (±2% disagreement) between the two measurements was observed.

Checks were conducted to ensure that the flow impinged over the entire span at a constant mean angle. Firstly, the AOA of the airfoil was very carefully changed using both an analogue as well as a digital inclinometer and the angle was measured at five evenly spaced positions over the airfoil. The mean and Std.Dev of the pressures measured at all four pressure measuring locations (Figure 193) were compared against one another. A sample of this study is presented in Figure 186.

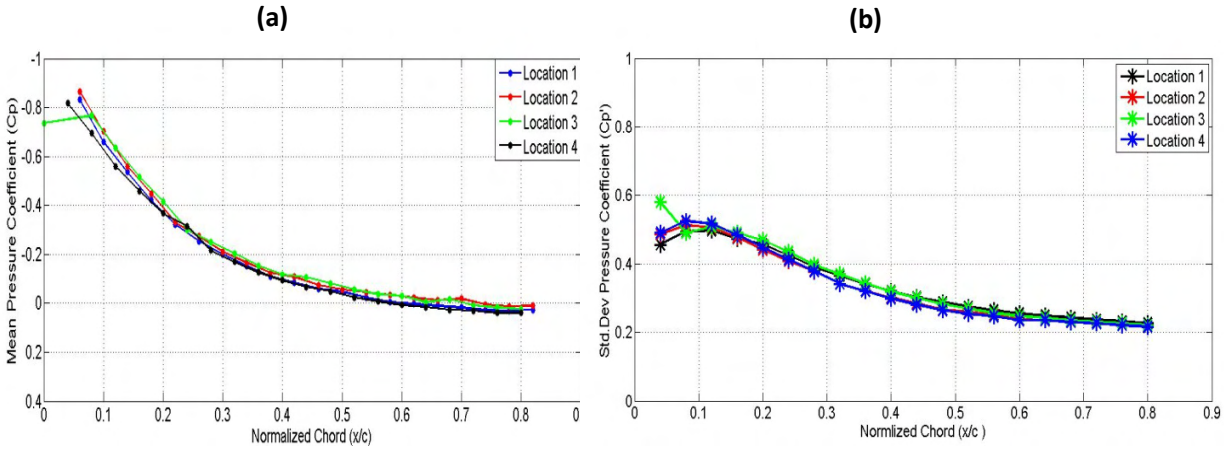

Figure 186: (a) Mean and (b) Std.Dev of pressures at the fours spanwise measuring locations over the airfoil at 6deg AOA and Re=70,000. Ti=7% and Lxx=0.15m.

It can be seen Figure 186 that both mean and Std.Dev of pressures correlate well over the four laterally locations. Slight discrepancy can be noticed in the pressure measured by tap 1 at locations 3. This is because the pressure tap was located exactly on the leading edge. The variation in mean and Std.Dev across the laterally space locations appear to be negligible here. This indicated that the small chordwise offset in the pressure taps at the different spanwise stations would have an insignificant influence on the pressure and force analysis over the span. The presence of good correlation in the pressure distribution over the airfoil span also indicates that the influence of the guy threads used to hold the airfoil rigidly did not have a significant influence on the flow structure (N.B. the threads were well removed from location of pressure taps).

Appendix C: Airfoil Leak Testing and Validation of Tubing Response

C.1 Airfoil Leak Testing

Extensive leak testing was undertaken to ensure no pressure discharge occurred at any point in the tubing system. The pressure channels were connected to an inclined manometer and a pressure of 150Pa was added into each channel of the airfoil and the pressure was monitored for 3mins. Through a T-junction, the pressure channels were also connected to pressure transducers in order to monitor pressure variations. Though this method was efficient in identifying leaks, it was very time consuming as testing had to be conducted on one pressure channel after the other. Therefore, this method of leak checking was used only on the 0.3m span airfoil tested within the RMIT Aerodynamics Wind Tunnel. As seen in Figure 187, the time-averaged drop of the pressure was less than ±0. 5%. As only time-averaged pressure measurements were conducted using this airfoil, this leak test was found to provide sufficient indication that the system was well sealed.

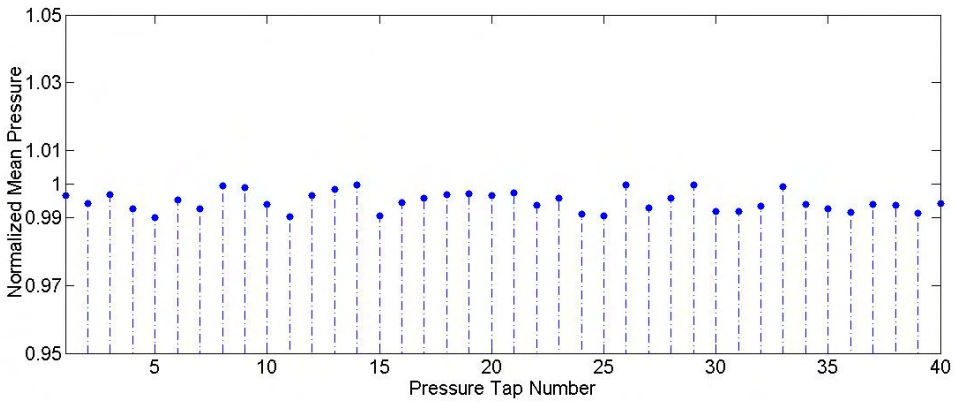

Figure 187: Result of the time-averaged leak test experiment on the smaller 0.3m span airfoil

For the larger 0.9m span airfoil which was used for testing in the other turbulence conditions, a more robust and quicker method of dynamic leak checking was adopted. In this method, the airfoil was subjected to acoustic excitation at various frequencies while pressure measurements at the taps were taken. As seen from the PSD plot (Figure 188), all sealed pressure taps possess exactly the same spectra with a peak of same energy at 100Hz, while the spectra of leaking pressure taps were considerably different. The PSD of only a few pressure taps are presented in Figure 188 for illustration. A leak was noticed in the last channel at pressure locations 1&2 and in channel 12 at locations 3&4, refer Figure 188. A stethoscope was then used to identify the exact location of the leak. A leak in former location was sealed by just adding some extra glue at the leaking location (mating point of the airfoil subsections) while the latter leak was not fixable. This rendered only 19 live pressure taps in location 3&4. During data analysis, the value of pressures at that channel was therefore interpolated based on measurements from adjacent taps.

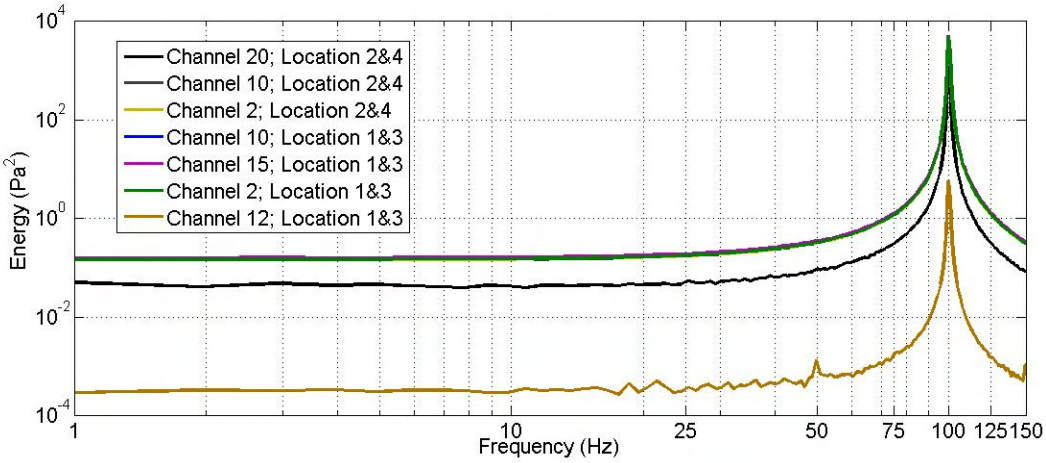

Figure 188: PSD of the leaking pressure channels clearly off compared to the sealed ones. The airfoil was subjected to sound of 100Hz.

C.2 Amplitude and Phase Response Validation of Tubing System

Studies were conducted to ensure a relatively flat frequency and phase response was present till frequencies well above the region of interest. An acoustic excitation box was used for the validation experiments. The acoustic excitation box consisted of a speaker placed within a small enclosure where a provision for placing pressure taps on top of the same was present. A reference tube was also located

close to the pressure tap location. The speaker was connected to an amplifier which was in turn connected to a computer, through which acoustic oscillations of various frequencies could be generated. Figure 189 depicts the setup.

Figure 189: Photo of the acoustic calibration box. (Courtesy Alex Fisher)

The airfoil was placed over the box such that the pressure taps aligned with the slot. All pressure taps in the airfoil were then connected to the transducers within the DPMS system. The reference tube was also connected to one of the available channels on the DPMS module. Acoustic waves were then created and a frequency sweep was performed at 10Hz intervals with 20 seconds duration at each frequency step. The sweep ranged only from 10Hz till 70Hz. The maximum frequency tested was limited to 70Hz because it was found that frequencies above 80Hz were affected by the size of the box. During the frequency sweep, pressures were measured at the pressure taps as well as at the reference point. For the first series of tests, no tubing correction was added to the tubing system within the airfoil. As the reference tube was only 30mm in length, it had a flat response till many hundred Hz. Hence, the pressure measured at the pressure taps were compared to the pressures at the reference point. The response of the airfoil pressure channels computed through this comparison is presented Figure 190.

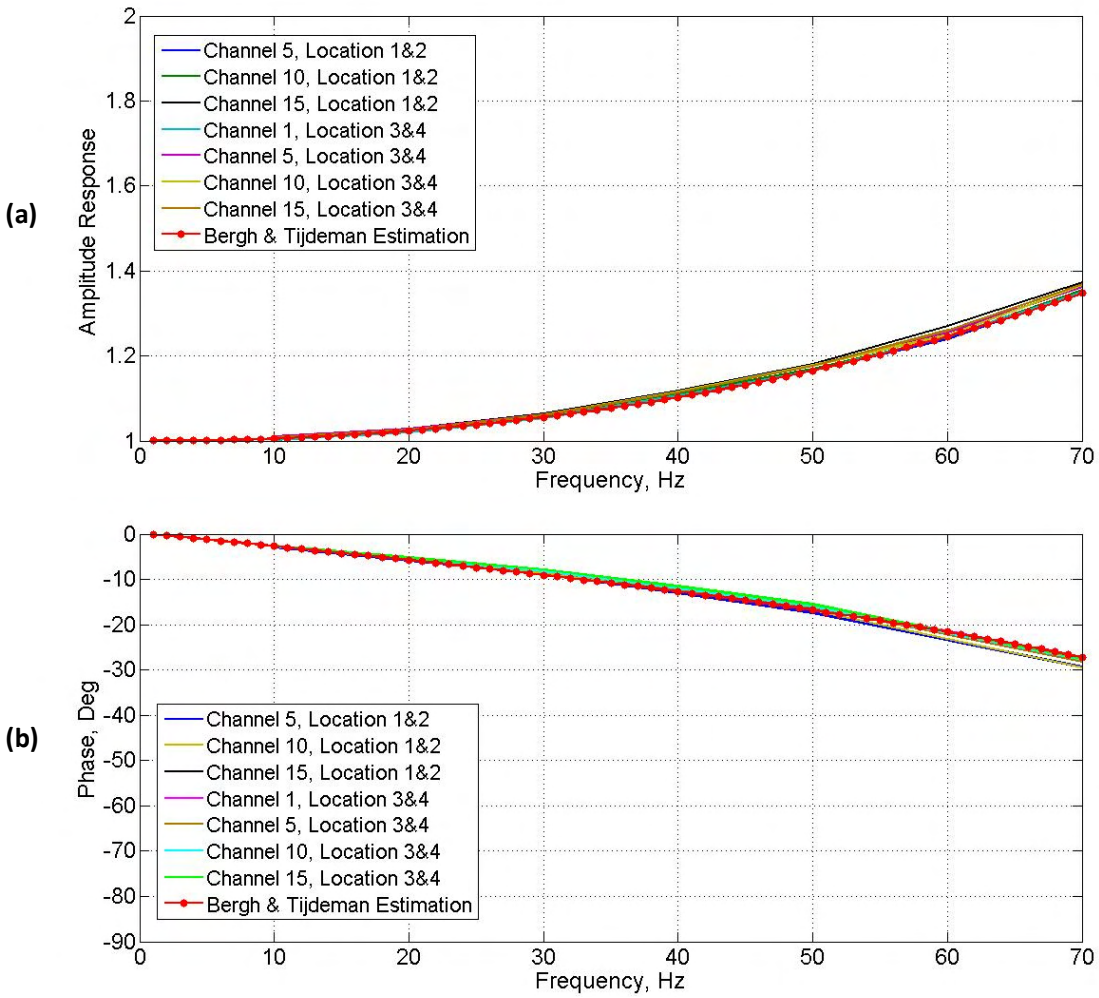

Figure 190: (a) Amplitude and (b) phase response of tubing system without any tubing correction. Bergh & Tijdeman (1965) estimation of tubing response is also plotted.

The computed response is very similar to the response predicted by Bergh & Tijdeman (1965). For the second series of tests, the sweep was repeated but with Bergh and Tijdeman tubing correction applied to the airfoil pressure tubing through the Device Control software used to run the DPMS system. No correction was applied to the tube at reference point during both runs. The response of this system was computed and is presented in Figure 191.

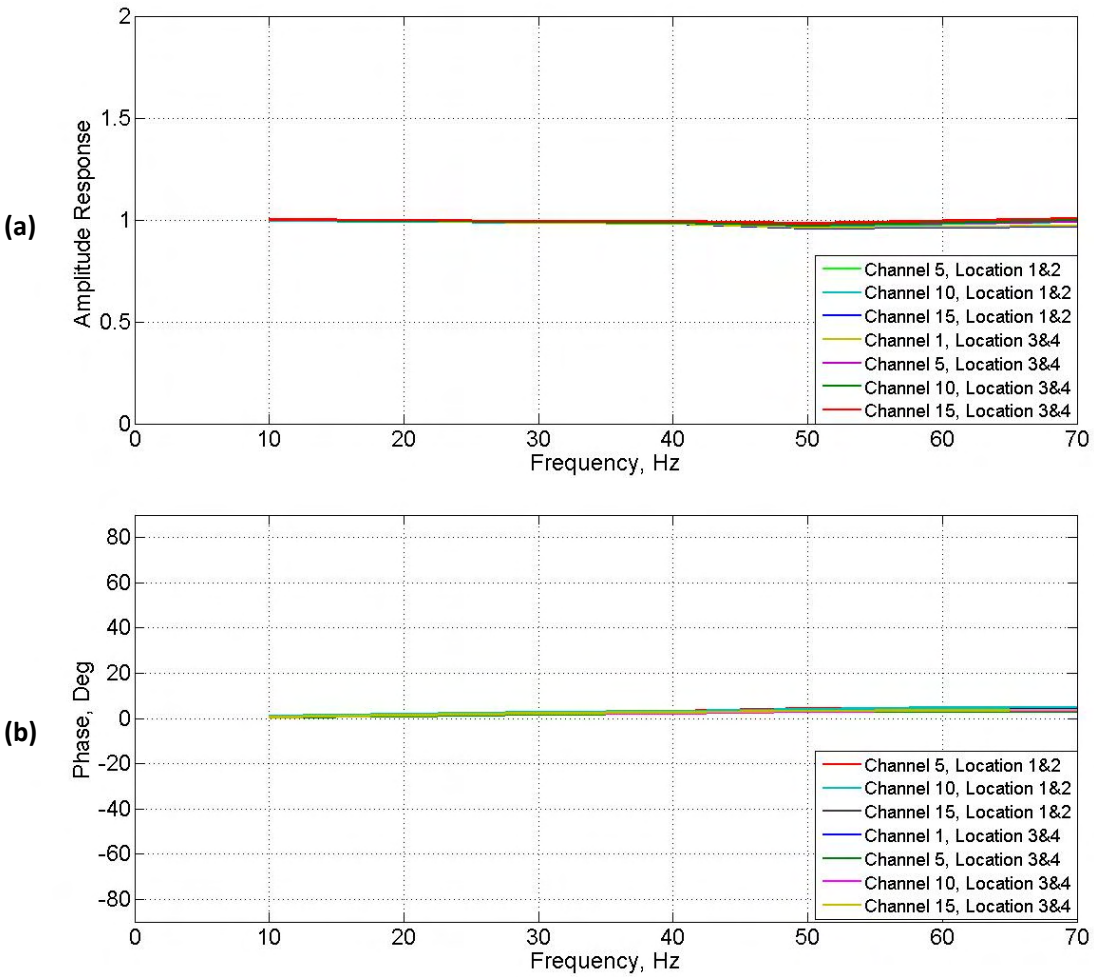

Figure 191: (a) Amplitude and (b) phase response of tubing system with tubing correction added.

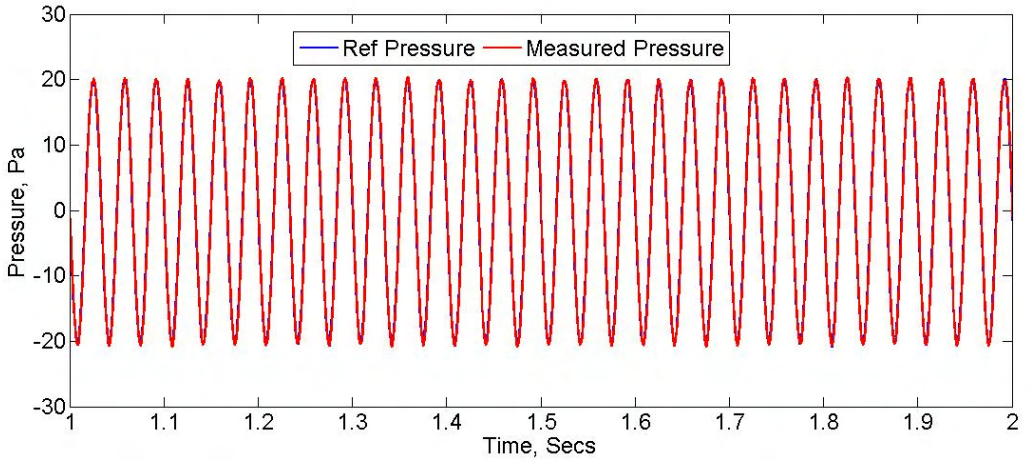

Figure 192: Time-varying pressures measured at pressure tap with tubing correction added plotted over pressures measured at reference location

Figure 191 shows that after the tubing system has been corrected for using the Bergh & Tijdeman (1965) prediction of phase and amplitude response, a nominally flat response is present for the system. The sample time series of the measured pressures with tubing correction added is presented in Figure 192 where excellent similarity with respect to the reference pressures is noticed. Hence, for all airfoil testing conducted, appropriate tubing parameters were input within the Device Control software such that the software could generate tubing correction for the specific tubing system and apply the same to the measured pressures.

C.3 Influence of Redundant Tubing at Pressure Measuring Locations 1&4

At pressure measuring locations 1&4 on the airfoil (see Figure 193), there existed redundant tubing of 50mm and 100mm respectively (i.e. the pressure channels did not terminate at the pressure taps). Some sensitivity studies were performed to ascertain the influence of this redundant tubing. As location 3&4 shared the same pressure channels with the latter having no redundant tubing, a comparison of the pressures measured at the two locations provided insight on the influence of the redundant tubing. Figure 194 is the comparison of the PSD at locations 3&4 at the same AOA.

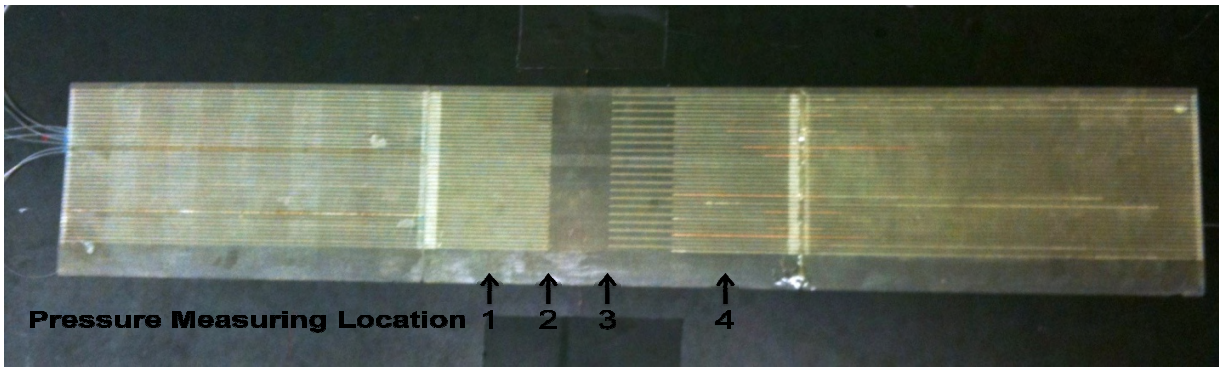

Figure 193: Photo of the final airfoil showing the pressure measuring locations.

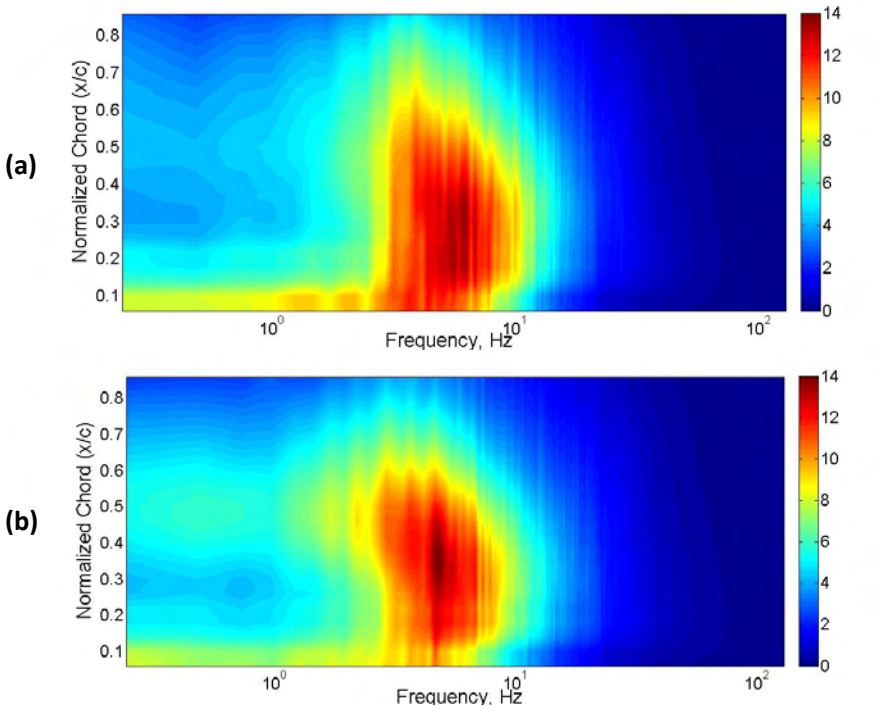

Figure 194: Consolidated PSD of pressures over the airfoil at (a) location 3 and (b) at location 4. AOA=6Deg, Ti=7.3% Lxx=0.22m.

As can be seen from Figure 194, there is not much difference between the spectra of the pressures at the two locations, indicating that the influence of redundant tubing on response is small. Only statistical comparisons were possible as the pressures at the two locations could not be measured simultaneously because they shared the same pressure channel. A similar trend was noticed when pressures at locations 1&2 were compared. Therefore no correction was made to the pressures measured at locations 1&4 for the redundant tubing.

C.4 Influence of Smoke Wand on Flow over Airfoil

To ascertain the influence of the smoke wand placed 70mm from airfoil leading edge on flow over the airfoil, a few sensitivity studies were conducted. For the first series of tests, in smooth flow conditions within the RMIT IWT (Ti =1.2%), pressure fluctuations over the airfoil surface were measured with and without the smoke wand present. No smoke was injected into the flow as there was a possibility that

the smoke would either block the pressure channels or damage the pressure transducer. Figure 195 show the time-averaged pressure distribution over the airfoil with and without the wand present.

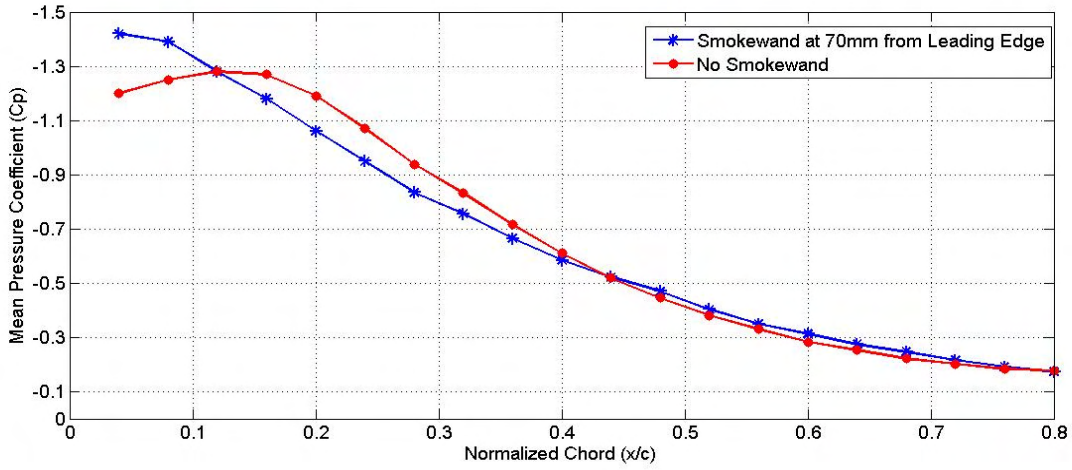

Figure 195: Influence of the smoke wand on the time-averaged pressure distribution over the airfoil at 6deg AOA and Re= 70000 in smooth flow conditions (Ti=1.2%).

Figure 195 shows that the wand does have an influence on the time-averaged flow over the airfoil however it is limited to about 40% of the airfoil. The perturbations injected into the flow by the presence of the wand seem to shorten the bubble in a similar way to small increase in freestream Ti. Nevertheless, the qualitative studies do provide valuable information on the flow-field structure in these nominally smooth flow conditions, as the time-varying oscillations over the airfoil are still present as shown in PSD plots in Figure 196.

(a)

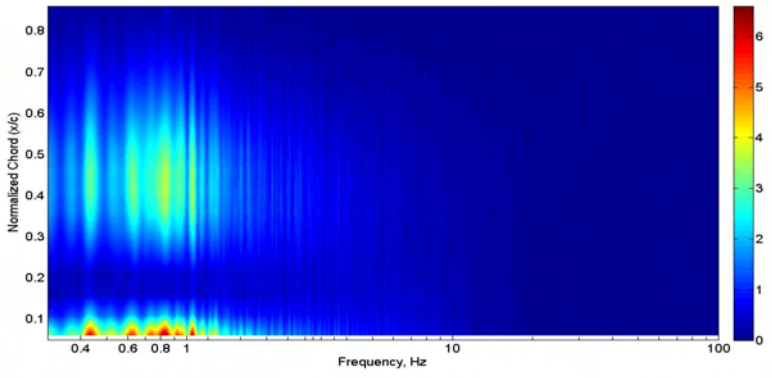

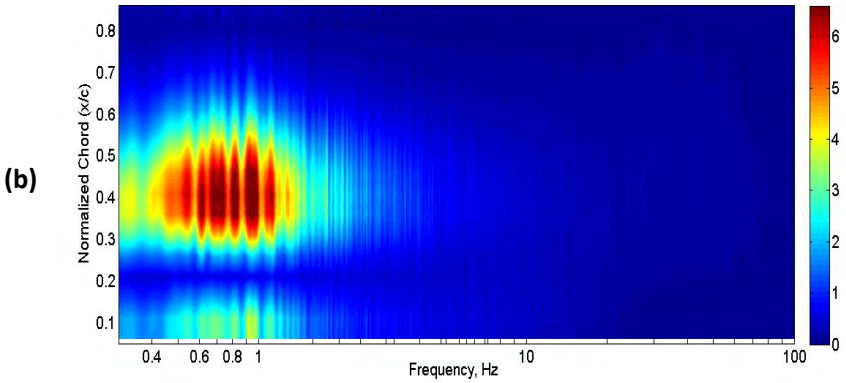

Figure 196: PSD plot of pressure fluctuations over the airfoil at 6deg AOA and Re=70,000 in smooth flow condition (Ti=1.2%), with (a) and without (b) the wand present

A similar sensitivity study was conducted in turbulent flow with following properties Ti=7.3% & Lx=0.21m. The presence of the wand has an almost insignificant influence on the time-averaged pressure distribution over the airfoil, as seen in Figure 197.

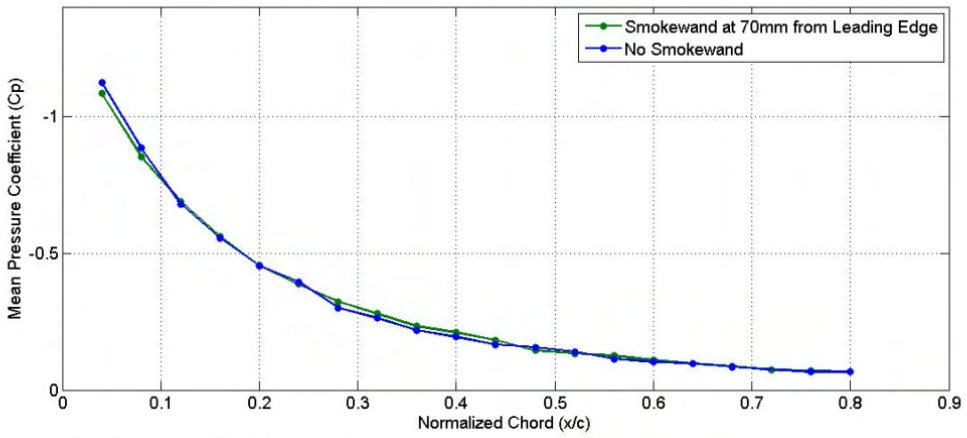

Figure 197: Influence of the smoke wand on the pressure distribution over the airfoil at 6deg AOA and Re= 70000 in flow where Ti=7.5% and Lxx=0.21m

In the presence of higher levels of ambient turbulence, the high frequency low energy oscillations created due to the wand seemed to diffuse significantly quicker than in smooth flow conditions, hence having a considerably lesser influence on the flow over the airfoil as seen in the PSD plots in Figure 198.

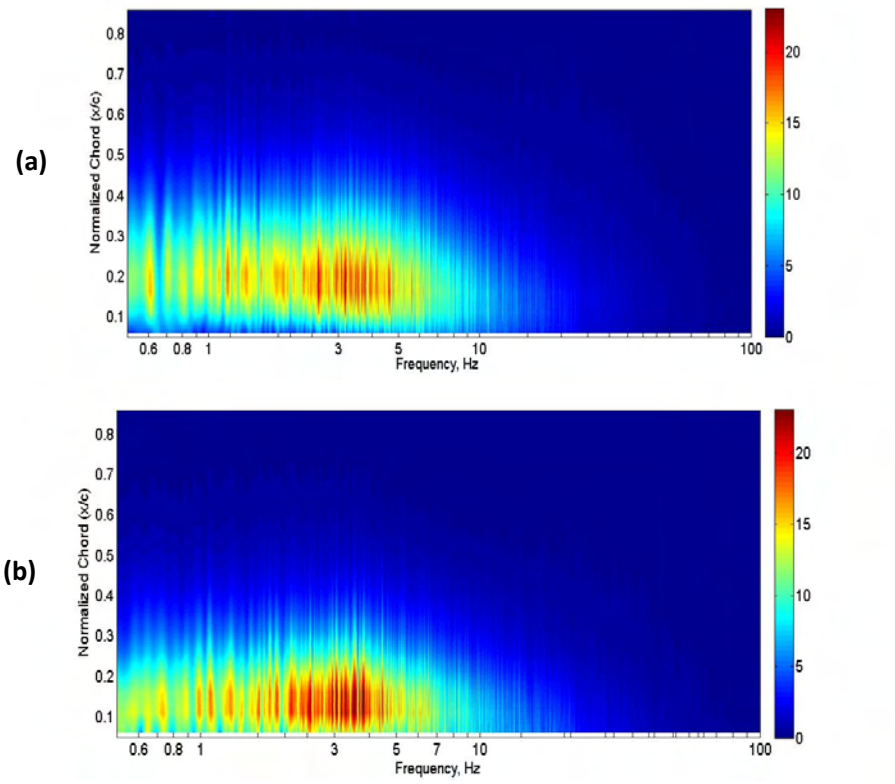

Figure 198: PSD plot of pressure fluctuations over the airfoil at 6deg AOA and Re=70,000 in turbulent flow where Ti=7.15% and Lxx=0.14m, with (b) and without (a) the wand present.

Appendix D: Correction for Cobra Probe Head Orientation

Almost all velocity measurements were made using pressure sensitive probes (Cobra Probes) because they offered a quick and reliable method of measuring velocity in the three orthogonal directions compared to hot-wire anemometers. As the probe head was only 3mm, when taking velocity measurements inside the wind tunnel, it was extremely difficult to align the probe head directly parallel to the tunnel walls. A misalignment of the Cobra Probes would result in errors in the mean flow directions. The probes were therefore placed as close to parallel to the flow as possible, however small offsets were still present. These offsets in probe alignment manifested themselves as mean velocities in the directions orthogonal to streamwise direction i.e. "v" and "w". To remove these offsets, it was assumed that the flow within the wind tunnels was only in the streamwise direction with no mean "v" and "w". This was a reasonable assumption as from previous research it was found that the mean flow angles in the "v" and "w" directions in the wind tunnels were negligibly small (<2Deg). Moreover, mean velocity in the pitch direction was corrected for through the airfoil lift distribution, while small yaw angle offsets of the flow have a negligible effect. Therefore, the mean "w" and "v" velocities were added to the streamwise "u" component in the following manner.

$$u_{Corrected} = \sqrt{u^2 + \overline{V}^2 + \overline{W}^2} \qquad \text{Equation 9}$$

$$v_{Corrected} = v - \overline{V} \qquad \text{Equation 11}$$

$$w_{Corrected} = w - \overline{W} \qquad \text{Equation 10}$$

From the above equation, the flow is assumed to travel purely in the streamwise direction, hence the turbulence intensity in the "v" and "w" directions were measured as follows;

$$Ti_v = \frac{\sigma_v}{\overline{U}} \qquad Ti_w = \frac{\sigma_w}{\overline{U}} \qquad \text{Equation 12}$$

The length scales in the respective directions are the product of the area under the autocorrelation plots and mean streamwise velocity as discussed above and described in Appendix E.

Appendix E: Estimating Turbulence Intensity and Length Scales

This subsection details the methods adopted for estimating the turbulence intensity and integral length scale present in the flow. As earlier stated, turbulence intensity is a measure of the degree of flow unsteadiness. The general equation for turbulence intensity in all three directions is given as shown.

$$Ti_u = \frac{\sigma_u}{\overline{U}} \qquad Ti_v = \frac{\sigma_v}{\overline{V}} \qquad Ti_w = \frac{\sigma_w}{\overline{W}}$$ Equation 13

Where: U, V & W are the mean velocities in the three orthogonal directions and σ is the standard deviation of the velocity fluctuation in the respective direction.

It can be noticed from the equations above that if the mean velocity tends to zero, the turbulence intensity tends to infinity hence caution should be exercised when apply these quantities to the flow. In order to estimate the total Ti of the flow, the velocity equation must first be re-written as follows;

$$V_r = \sqrt{u^2 + v^2 + w^2}$$ Equation 14

Finally the total turbulence intensity is given as;

$$Ti_{Tot} = \frac{\sigma_{V_r}}{\overline{V_r}}$$ Equation 15

Where: u, v & w are the time-varying fluctuations of velocities in the respective directions.

Estimating the integral length scale of the flow is relatively more complicated as the quantity is somewhat abstract. A given flow basically contains nine integral length scales (Lxx, Lxy, Lxz, Lyx, Lyy, Lyz, Lzx, Lzy and Lzz). The integral length scale represents the average size of the largest turbulence eddy and there are three mains ways to estimate this. The first and most explicit means of estimation is by taking

simultaneous velocity measurements at various locations in the direction in which the length scale is to be determined, for example different streamwise locations to determine Lxx, Lxy and Lxz. In grid generated turbulence within a wind tunnel, the longitudinal length scales are most relevant due to the absence of mean flow in the lateral and vertical directions. The implicit method of integral length scale estimation works under the assumption that all points inside the eddy fluctuate in the same direction, implying that a rise or fall in velocity will be noticed all through the turbulence eddy, hence by increasing the separation distance of points where simultaneous measurements are taken, a separation distance will be reached when at one point the velocity increases while it decreases at another, this indicates the point is outside the eddy. This method is complicated, time consuming and error prone. There are however two simpler methods of estimating the length scale, viz. the autocorrelation method and von Karman spectral fitting method.

E.1 Auto-correlation Technique

As per Taylor's hypothesis turbulent eddies proceed downstream in a frozen state, implying that time-varying velocity measurements at a single point can be used to predict the velocity at a point downstream. The autocorrelation method involves the calculation of the length scale by estimating the time taken for the flow to become completely uncorrelated temporally when measured at a single point. This is found by plotting the autocorrelation function of the flow with respect to time lag, a sample autocorrelation curve is presented in Figure 199. The function always starts at unity as the autocorrelation of a dataset with itself at zero time lag is maximum (one). The correlation decreases as time lag increases; at the first instant the function crosses the horizontal axis i.e. when the correlation coefficient becomes 0, the flow in that direction is assumed to have become uncorrelated. The product of area under this region to the mean velocity the direction yields the respective length scale.

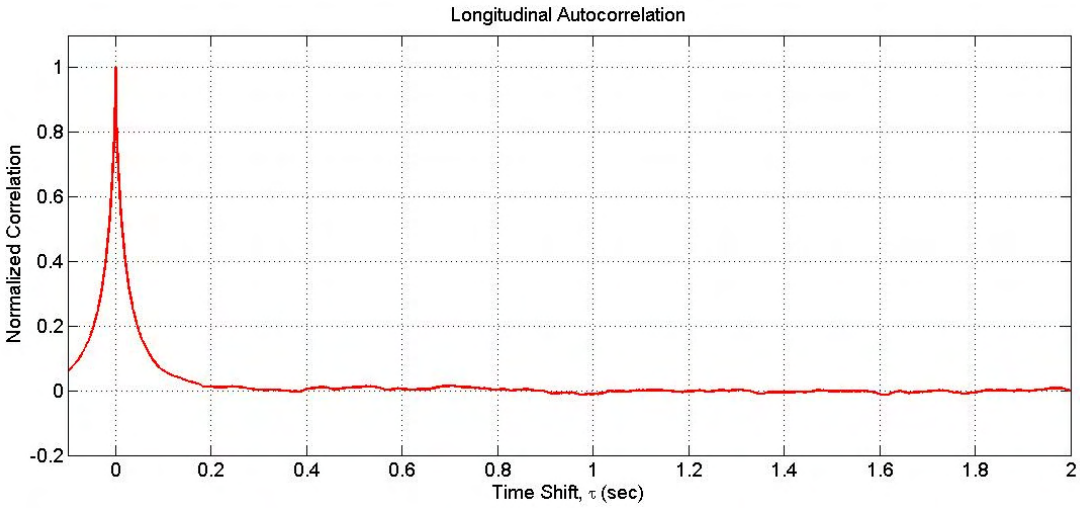

Figure 199: Autocorrelation curve of longitudinal velocity fluctuations. Ti=7.3% Lxx=0.22m.

This method of length scale estimation is very powerful and reliable Wordley (2009). A short-coming of this method is that long datasets are required such that the time is always significantly greater than length of data. Another problem with this method is that sometimes the autocorrelation function does not immediately intersect the horizontal axis since it can have an asymptotic relationship with time shift (x axis). This can lead to misestimating the length scale and for this reason a smoothing algorithm was written to remove this asymptote'ing tendency and enable quick intersection.

E.2 von Karman Spectral Fitting

Another method of estimating integral length scale is the von Karman spectral fitting method. This is an empirical method whereby the length scale is estimated by varying the value of Lxx in Equation 16 to obtain the curve of best fit to the PSD plot of the velocity fluctuation in the respective direction.

$$S(n) = \frac{\sigma_u^2}{n} \times \frac{4n_u}{\left(1 + 70.8{n_u}^2\right)^{5/6}} \qquad \text{Equation 16}$$

$$n_u = \frac{L_x \times n}{U}$$

Where: S(n) is the power(S) as a function of frequency (n), σ is the standard deviation in the subscript axis, U is the mean velocity and L is the length scale to be estimated

The above equation first appeared in the ESDU datasheets and has been derived empirically from previous measurements of turbulence within the ABL. Wordley (2009) found that the length scale estimated by this method was considerably higher than the length scales estimated through the autocorrelation method. However, for the order the length scales in this research very good similarity was found in the estimates of both methods. The reason for the difference in Wordley (2009)'s findings could be attributed to the significantly larger length scales and low-frequency trends in the ABL data measured in his research.

Due to similarity in the two methods of length scale estimation, both methods were adopted in this research, in order to estimate the integral length scale of the flow. Each method served as a check to the other. The von Karman spectral fitting was implemented through the Curve Fitting Toolbox in MATLAB whereby the line of best fit for the PSD plot was determined based on the above equation by identifying the most suitable length scale.

Appendix F: Further Details on Data Processing

In this section the various statistical methods adopted to process the data collected during experimentation will be detailed. Various assumption and corrections made to the data while data processing will also be presented here.

F.1 Software Packages

The sampling rate for pressure and velocity measurements were set as 2kHz and the sampling time varied between 1 min to 10mins. This meant that large amounts of data was collected during each run, requiring an efficient post processing software package to analyze the data. For this reason, MATLAB was chosen as the most suitable software package. Moreover, the propriety code required to open raw data files from the DPMS and Cobra Probes was written in MATLAB, hence it was convenient to perform further data processing in the same software. Microsoft Excel was also used for some of the data processing exercises.

F.2 Statistical Techniques

A number of statistical techniques were adopted for analysis of data collected, both flow-field and pressure. Due to the advancement in computing hardware and software, most of the post processing techniques used were directly called from MATLAB's command list. This section briefly discusses the various statistical quantities used for analysis here. The reader is encouraged to refer to any standard

Digital Signal Processing (DSP) and related statistics textbooks to learn further on the statistical quantities described here.

F.2.1 Mean, Standard Deviation and Variance

The arithmetic mean is defined as the sum of all observations divided by the number of observations. The "mean" function in MATLAB was called to perform this operation in this research.

Standard deviation is a measure of deviation or dispersion of data from the mean value. Standard deviation is also a gauge to the degree of fluctuation in the data. The quantity is very useful in identifying key properties in the flow, for example the region of maximum standard deviation is generally at the location of reattachment of the shear layer. Turbulence intensity was estimated by dividing the standard deviation of the velocity in the respective direction with the mean. The general equation used to determine the standard deviation of a data series is below. The "std" command in MATLAB was called to perform this operation on the data set.

F.2.2 Fast Fourier Transforms

Fourier transforms were used to transform data from the time domain to frequency domain. This transform was only applied to time-dependant data. The Fourier transform provides a measure of the power of each frequency of oscillation along with phase angle within a data-stream. It is extremely useful in identifying repeating sequences in datasets, as seen here in the case of vortex shedding or LSB flapping frequencies which were identified from the pressure time-series. A slight variation to the general Fourier transform, Discrete Fourier Transform (DFT) was used in this research, the only difference being the latter can be applied to discrete data sequences. As it was time consuming to directly apply DFT to data sequences, the transform was implemented using the Fast Fourier Transform (FFT) algorithm. This method of DFT implementation is extremely efficient and uses very little computational resources and hence used in most digital signal processing operations. FFT method is

therefore pre-programmed in most software packages and it was directly called from the MATLAB command list when required. Discussion of either general Fourier transform or the DFT will not proceed any further here, the reader may refer to any standard (DSP) textbook to learn of the fundamentals of DFT and FFTs.

In the post processing conducted here, the Welch method was found most suitable for Periodogram or PSD estimation. As per this method, the complete dataset was broken into a number of overlapping blocks, then DFT operation on each of these data block was performed and finally, all periodograms were averaged to yield the final modified periodogram of the entire dataset. This method tended to reduce the noise or variance within the PSD plot resulting in much smoother and distinct power estimate for each frequency. In order to implement this method, long datasets were required such that each data-block had enough resolution in frequencies of interest. To ensure a relatively high resolution and low variance in the spectra, the blocksize used in this work was equivalent to around the data obtained over 20secs. Generally, the sampling rate governed the highest frequency of interest while the sampling time influenced the lowest frequency of interest. The sampling time and rate used here provided sufficient resolutions over the frequencies of interest. During data processing, the data block-size was set to 20secs of data at a sampling rate of 2kHz. The “pwelch” command was called upon directly from MATLAB when required to perform this operation.

F.2.3 Auto and Cross Correlation Function

To understand the spanwise similarity of the flow or to understand chordwise structure of the separation bubble and for a number of other exercises, auto and cross correlation functions were used. By definition autocorrelation is the measure of similarity of a function over itself. Cross-correlation on the other hand is the measure of similarity between two functions. The general equation of autocorrelation of a continuous signal is as follows;

$$\varphi_{ii}(\tau) = \lim_{T \to \infty} \frac{1}{T} \int_0^T i(t).i(t+\tau)dt \qquad \text{Equation 17}$$

Where T is the length of the continuous signal and tau is the time lag. For a discrete N point function with "r" number of lags the above equation is rewritten as follows;

$$\varphi_{ii}(r) = \overline{i(n).i(n+r)} = \frac{1}{N}\sum_{n=0}^{n=N} i(n).i(n+r) \qquad \text{Equation 18}$$

As seen from the equation above the autocorrelation function is merely a statistical comparison of the function over itself but time shifted. The resulting correlation can be normalized by dividing the left hand side of the equation by the square of standard deviation. At time lag zero, the normalized autocorrelation of a function will be maximum i.e. 1.

$$\gamma_{ii}(\tau) = \frac{\varphi_{ii}(\tau)}{\sigma_{ii}^{2}} \qquad \text{Equation 19}$$

$$\gamma_{ii}(r) = \frac{\varphi_{ii}(r)}{\sigma_{ii}^{2}}$$

For cross correlation between two signals Equation 18 and Equation 19 need to be appropriately rewritten. A common problem with this operation is the drop of accuracy in the correlation coefficients as lag time increases, for this reason the total dataset taken for analysis here was significantly larger than the maximum time lag. The error due to increased time-lag was not significant here since the data length was many orders larger than the maximum time-shift. As auto and cross correlation are common operations in DSP, they are pre-programmed into MATLAB and the "xcov" command was called upon directly to apply the same to a given dataset.

F.2.4 Coherence Functions

Coherence functions were used in a number of post processing exercises for analyzing the spanwise extent of the laminar separation bubble or for understanding the link between upstream velocity fluctuations to airfoil surface pressure fluctuations. Coherence functions differ from correlation functions in that the former provides a frequency breakdown of the degree of correlation between two

signals. For example, the oscillations in two signals might be in phase or correlate well up to 10Hz, after which they might not correlate at all, this information is provided by coherence functions. The general equation to determine coherence between two signals is as follows;

$$C_{xy}(f) = \frac{|P_{xy}(f)|^2}{P_{xx}(f)P_{yy}(f)}$$ Equation 20

Where P_{xx} is the PSD of function "x", P_{yy} is the PSD of function "y", P_{xy} is the cross spectral density of functions "x" and "y" and "f" is frequency.

This function too is pre-programmed into MATLAB and hence was called when required using the "mscohere" command.